Damage progression on fiber reinforced polymer (FRP) adhesively bonded single lap joints (ABSLJ) under quasi-static tension

Implementation of a 3D continuum damage model in UMAT to predict: global behavior, damage initiation and propagation until final failure, for different adherend layup configurations

João Francisco Góis de Freitas

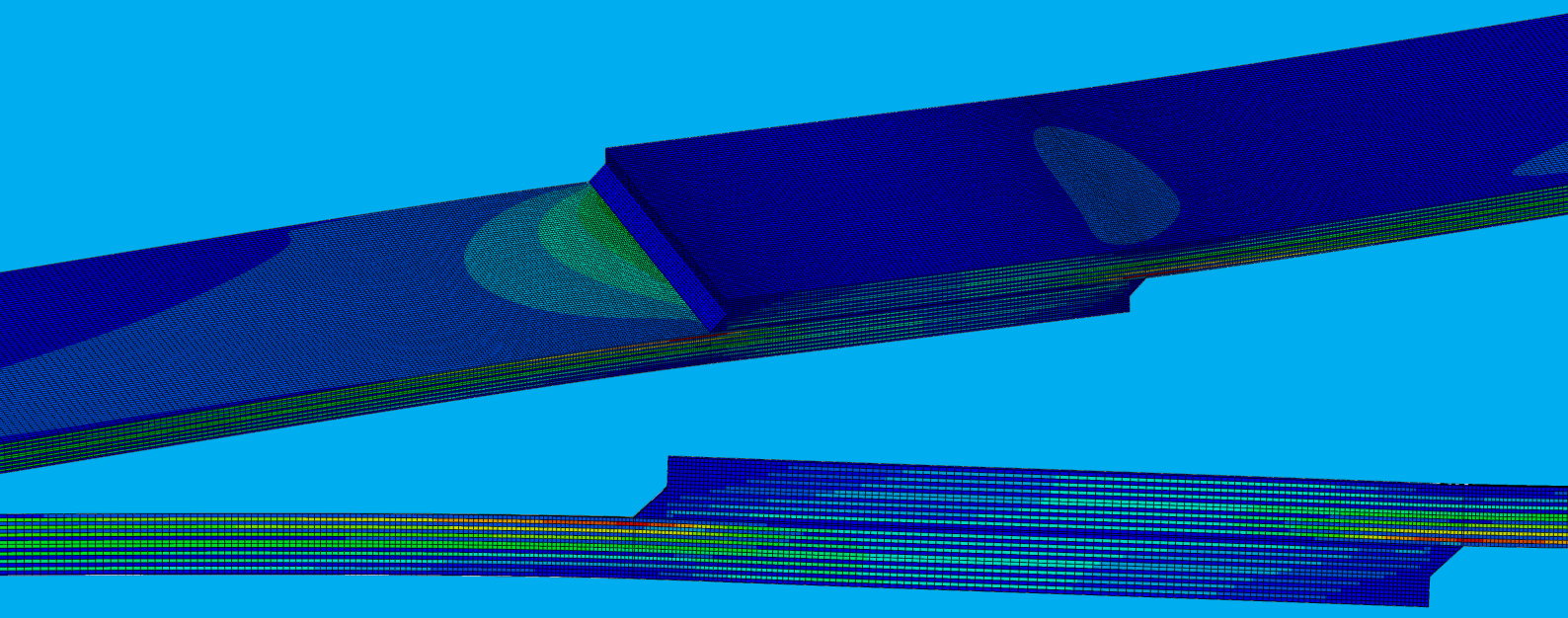

Damage progression on fiber reinforced polymer (FRP) adhesively bonded single lap joints (ABSLJ) under quasi-static tension

Implementation of a 3D continuum damage model in UMAT to predict: global behavior, damage initiation and propagation until final failure, for different adherend layup configurations

by

João Francisco Góis de Freitas

to obtain the degree of Master of Science

at the Delft University of Technology,

to be defended publicly on 30th of September, 2019 at 13:30.

Student number:	4624130	
Project duration:	18th of June, 2018 – 9th of September, 2019	
Thesis committee:	Prof. Dr. Rinze Benedictus,	TU Delft, chairman
	Dr. Marko Pavlovic,	TU Delft, external expert
	Dr. Dimitrios Zarouchas,	TU Delft, supervisor
	Dr. Sofia Teixeira de Freitas,	TU Delft, supervisor

An electronic version of this thesis is available at http://repository.tudelft.nl/.

Abstract

Adhesively bonded joints have proven to outperform their mechanically fastened joint counterparts, as they present a more structurally efficient method of load transfer, lower stress concentrations and better fatigue performance at reduced weight. In the specific case of the Adhesively Bonded Single Lap Joint (ABSLJ), bending-induced stresses that result from the load path eccentricity add up to the adherend inplane stresses. Moreover, significant peak peel and shear stresses develop at the lap ends of the adhesive and associated adherend interlaminar tensile stresses have a detrimental effect on the joint's strength. Such joints made of Fiber Reinforced Polymer (FRP) adherends bonded with an epoxy adhesive layer sustain a substantial amount of damage, from failure onset to ultimate failure. With the purpose of design structurally efficient and damage tolerant composite joints, it is essential to understand the stress distribution and to accurately predict the damage initiation and propagation events in such joints made of composite materials.

A well-established set of Damage Progression Models (DPMs) in the framework on the Continuum Damage Models (CDMs) were developed as a tool to predict the global response, damage initiation load and ultimate load of the specimens. Hashin 3D, Puck and LaRC05 were the implemented failure criteria to detect the initiation of damage in the adherends. After this point, the elastic properties of the detected damage elements were reduced according to sudden and gradual material degradation models. As for the adhesive, the von Mises criterion was used to detect the damage onset and a linear softening law modeled the material degradation. For the validation of the DPMs, the numerical results were compared against the data of an already published experimental study. Four different adherend layup sequences: $[45/90/-45/0]_{2s}$, $[90/-45/0/45]_{2s}$, $[0/45/90/-45]_{2s}$ and $[45/0/-45/0]_{2s}$ were studied based on data extracted from the mechanical testing, Digital Image Correlation (DIC) and Acoustic Emission (AE).

Good correlations between numerical predictions and averaged experimental linear stiffnesses were found, particularly for the two configurations with the outmost ply at 45°, for which the difference was lower than 5%. The initial non-linear stage of the global response seems to be governed by the longitudinal bending stiffness, while the subsequent linear behavior is controlled by the longitudinal membrane stiffness of the adherends. Regarding damage initiation, numerical predictions showed to be 11.5%, 7.5%, 29.9% and 6.1%, respectively, more conservative for the four analysed configurations, when compared to the AE results, whose established criterion should be further developed. With respect to the ultimate load, the relative differences between predictions and tests showed significant variability among the tested configurations; specifically the deviations were of: 33.2%, 37.4%, -0.4% and -13.71%.

Despite the encouraging results, an inherent shortcoming of CDMs is the representation of damage in a smeared manner due to the homogenization of the anisotropic material in the modeling process. A blended framework using CDMs to model intralaminar failure and discrete crack models to model interlaminar failure and matrix cracking might lead to more realistic damage patterns.

KEYWORDS: Adhesively bonded single lap joints; Composites; Damage progression; Continuum damage models.

Acknowledgements

I would like to express my deep gratitude to Dr. Sofia Teixeira de Freitas and Dr. Dimitrios Zarouchas, my research supervisors, for their focused guidance, enthusiastic encouragement and useful critiques of this research work.

My special gratitude to PhD candidate Julian Kupski for all the technical input and discussion moments that, I believe, we both benefited from.

(The following section of these acknowledgements is written in Portuguese considering that I feel more comfortable expressing my gratitude, using the proper words to transmit exactly what I want to express.)

Gostava de agradecer à minha mãe, Isabel de Freitas, pelo apoio emocional e financeiro incondicionais mesmo nas horas de maior tristeza e escuridão, em Lisboa e em Delft, nas quais foi certamente a pessoa que mais confiou nas minhas capacidades. Onde quer que eu chegue, nunca seria possível sem o seu apoio. A minha gratidão é eterna.

Ao meu Pai, Irmão, Patrícia, Isa e Rossana o reconhecimento do apoio ininterrupto e o agradecimento por sempre terem confiado nas minhas capacidades. Compõem a família que me proporcionou a estabilidade necessária para alcançar os meus objectivos e à qual só devo gratidão.

À já referida Patrícia, um reforço ao agradecimento por ser o controlador que garante a estabilidade do sistema.

Aos meus amigos na Madeira, em Lisboa, na Holanda e espalhados pelo mundo que me acompanharam neste percurso, com quem partilhei gargalhadas e conversas que foram desde a origem do Universo e a questão de Deus a processos agrícolas contemporâneos. Essencialmente, obrigado por me terem ajudado a crescer e 'partilhado a felicidade'.

Finalmente, uma nota de agradecimento atípica aos *so-called* Países Baixos e particularmente à TU Delft. Ao país, estou grato pela abertura, sentidos ético e de justiça que me brindaram desde o dia que cá cheguei. Após três anos, ainda sou surpreendido pela sociedade holandesa e pelo funcionamento oleado da máquina socio-político-económica. À universidade, pelos momentos de aprendizagem proporcionados junto de pessoas fenomenais, colegas e professores, providenciando também as melhores instalações, munidas de equipamento e material de excelência que proporcionam a melhor experiência de aprendizagem que um aluno de engenharia pode ter. Resta ainda agradecer aos professores da TU que depositaram confiança em mim para desempenhar funções de *teaching assistant* em três disciplinas de licenciatura e mestrado; com estes trabalhos temporários, pude pagar despesas e aliviar parcialmente o fardo financeiro dos meus pais.

"*If I have seen further it is by standing on the shoulders of Giants.*" - Isaac Newton

Contents

List of Tables xi

List of Figures xiii

List of abbreviations xxi

List of symbols xxiii

1 Introduction 1

2 Literature study 3

2.1 Adhesively bonded joints . . . 3

2.1.1 Adhesively bonded joint types . . . 3

2.1.2 Failure modes in FRP adhesively bonded joints . . . 7

2.1.3 Parameters influencing the single lap bonded joint strength . . . 8

2.2 Progressive Damage Analysis (PDA) in composites . . . 12

2.2.1 Progressive damage analysis methodology . . . 13

2.2.2 Damage modeling of composites at various scales . . . 14

2.2.3 Failure mechanisms in composites. . . . 16

2.2.4 In-situ strength properties . . . 18

2.2.5 Continuum damage models (CDM) . . . 21

2.2.6 Damage initiation criteria . . . 21

2.2.7 Material property degradation models . . . 29

2.2.8 Discussion over modeling intralaminar using the reviewed CDMs . . . 35

2.3 Conclusions . . . 37

3 Research question and objective 39

3.1 Research question. . . . 39

3.2 Research objective 41

4 Methodology 43

4.1 Computational framework 43

4.2 Finite element model definition and configurations 44

4.2.1 Coordinate system, characteristic dimensions and regions 44

4.2.2 Material properties 46

4.2.3 Boundary conditions and applied load 46

4.2.4 Assumptions 47

4.2.5 Parametric model generation - Python scripting in Abaqus 47

4.2.6 Numerical considerations 48

4.3 Preliminary studies 53

4.3.1 Adherend layup configurations 54

4.3.2 Mesh convergence study 56

4.3.3 Preliminary stress study 58

4.4 Damage progression model (DPM) 59

4.4.1 Selected failure criteria and material degradation models 59

4.4.2 User Material Subroutine (UMAT) implementation 63

4.4.3 Viscous regularization 65

4.4.4 Computational cost estimation 67

4.4.5 Verification and validation 67

5 Results and discussion 73

5.1 Preliminary mesh convergence study 73

5.1.1 Load-displacement curves 73

5.1.2 Stress distribution in the adhesive length 74

5.1.3 Stress distribution along the length of the first two adherend layers . . . 75

5.2 Preliminary stress study 77

5.2.1 Load-displacement curves 78

5.2.2 Stress distribution along the adhesive length . . . 78
5.2.3 Stress distribution along the joint thickness . . . 81
5.2.4 Stress distribution along the length of the first two adherend layers . . . 84
5.3 Verification - failure envelopes . . . 89
5.4 Validation . . . 90
5.4.1 Load-displacement curves: experimental *vs.* FE model . . . 90
5.4.2 Damage initiation and ultimate loads: experimental *vs.* FE model . . . 93
5.4.3 Strain maps: experimental *vs.* FE model . . . 95
5.4.4 Other remarks . . . 97
5.5 Failure index, degraded modulus and damage maps in the adhesive . . . 98
5.6 Failure index maps in the adherends at ultimate load . . . 99

6 Conclusions and recommendations 103

6.1 Conclusions . . . 103
6.2 Recommendations . . . 104
6.2.1 Continuum damage model . . . 104
6.2.2 Smeared representation of the crack . . . 106
6.2.3 Experimental studies . . . 107

Bibliography 109

APPENDICES 118

A Influence of the stacking sequence on the stress concentration factor around a hole in a laminate loaded in tension . . . 119
B Trade-off between adhesively bonded joints and mechanically fastened joints . 120
C Tsai *et al.* improved analytical solution: 1-D bar and 1-D beam formulations, expressions and comparison plots . . . 120
D Considerations on other parameters that influence the joint strength . . . 121
D.1 Manufacturing bonding process . . . 121
D.2 Surface preparation . . . 121
D.3 Geometric parameters . . . 122

E Effect of the adhesive and adherend properties on the joint strength 124

E.1 Effect of the adhesive ductility 124

E.2 Effect of the adherend stiffness imbalance on the adhesive peel stresses 125

F Constitutive relations for anisotropic materials: an overview 125

F.1 Stress-strain relations (3D) 126

F.2 Stress-strain relations for a thin lamina (2D): plane stress state 128

F.3 Constitutive equations of multi-directional laminates 128

F.4 2-D transformation of stresses and strains in the lamina 134

G Failure modes in FRP composites 135

G.1 Kinking bands 136

G.2 Features prone to delamination 136

H Failure criteria equations and supplementary information 137

H.1 Hashin's failure criteria equations 137

H.2 Comparison between Hashin's failure criteria and experimental results . 138

H.3 Transformation equations to obtain the stresses acting on an arbitrary sectional plane 138

H.4 Puck's master fracture surface for UD material 139

H.5 Puck's a-b-c-d fracture surface and associated failure modes to IFF failure type 139

I ABD matrices for FESALs 140

J Abaqus standard *vs.* explicit procedures 141

K Newton-Raphson implementation 141

K.1 Newton-Raphson implementation in two generic examples 141

K.2 Newton-Raphson implementation in Abaqus 143

K.3 Newton-Raphson implementation in Puck's model 145

L Hourglass control 145

M UMAT framing in an Abaqus/Standard simulation flowchart 147

N Incremental strain formulation 147

O Jacobian matrix computation 148
O.1 Isotropic material Jacobian matrix 148
O.2 Orthotropic material Jacobian matrix 148
P Preliminary FE stress study results for different layup sequences 151
Q Failure criteria code verification: failure envelopes 155
R Modulus degradation in the adhesive over time. 161

List of Tables

2.1 Definition and illustration of the failure modes classified by ASTM D5573. (Adapted from [3]). 8

2.2 Constant damage variables of Camanho and Matthews [12] sudden degradation model. 32

4.1 Characteristic dimensions of the adherends and the adhesive. 45

4.2 Material properties of the adherends - Hexply®F6376C-HTS(12K)-5-35% and the adhesive - Hysol®EA 9695^{TM} 050K AERO. (Adapted from: [55]). 46

4.3 Layup configurations used to study the stress distribution in the ABSLJ. . . . 54

4.4 Axial and bending stiffness values and relatives percentages (to FESAL1) in the main direction for the four considered layups. 56

4.5 Minimum size element and total number of elements for each mesh configuration used in the preliminary stress convergence study. 57

4.6 Overview of the selected PDA models. 60

4.7 Failure index equations and specific parameter values for each failure criteria model. 61

4.8 Degradation factor functions and specific parameter values for each material degradation model. 61

4.9 Longitudinal membrane stiffness (E_{1m}) and longitudinal bending stiffness (E_{1b}) for the four tested laminates. 69

5.1 Maximum failure index values and correspondent layers of the $[0/45/90/-45]_{2s}$ at the ultimate failure for the different failure criteria. 101

P.1 Comparison of the advantages and disadvantages between adhesively bonded joints and mechanically fastened joints. (Adapted from [5]). 120

P.2 Special laminate configurations and its consequences in the mechanical behavior of the composite structure. 134

P.3 Comparison between Abaqus standard and explicit procedures (Adapted from [1, 86, 100]). 141

P.4 Root iteration values and respective absolute errors using Newton-Raphson method for a function $y = sin(x) - 0.7$ with an initial guess of $x_0 = 1.2$. 143

List of Figures

2.1 Adhesively bonded joint types: a) different designs; b) joint strength *vs.* adherend thickness. (Reproduced from [40], copyright Kluwer, 2003). 4

2.2 Illustration of the high shear strain experience by the adhesive at the lap ends. 5

2.3 Effect of high peel on thick adherends: a) failure sequence; b) governing failure modes in function of adherend thickness. (Reproduced from [40], copyright Kluwer, 2003). 6

2.4 Tensile and shear projections of the forces acting in the adherend of a scarf joint. 7

2.5 a) Comparison of shear stress-strain curves and associated absorbed energies for brittle and ductile adhesives. (Reproduced from [39], copyright NASA, 1974); b) Actual characteristic and idealized adhesive shear stress-strain curves and parameters that characterize the idealized model. The areas bellow both plots are equal, *i.e.*, the energy absorbed by the adhesive is the same in both models. (Adapted from [39]). 9

2.6 Effects of adherend stiffness imbalance on adherend joint efficiency: a) for different adherend thickness ratio; b) for different adherend extensional stiffness ratio and bending stiffness values. (Reproduced from [38], copyright NASA, 1973). 11

2.7 Stress-strain curve of an angle-ply composite under loading, unloading and repeated loading. (Reproduced from [120], copyright Elsevier, 2004). 13

2.8 Illustration of different modeling approaches of composite materials at the a) microscale, b) mesoscale and c) macroscale. (Reproduced from [86], copyright Elsevier, 2018). 14

2.9 Scanning Electron Microscope (SEM) images of damaged E-glass/epoxy multiaxial specimens after impact showing: a) matrix cracks (1300x); b) delaminations (150x); c) interface debonding and fiber fractures (1500x). (Reproduced from [60], copyright TU Delft, 2015). d) Photograph of damaged carbon fiber woven composite showing different failure mechanisms. (Adapted from [18]). . . 16

2.10 Section cut showing the damage created in a quasi-isotropic laminate after 25J impact. (Reproduced from [52], copyright Wiley, 2015). 18

2.11 Transverse strength of the 90°oriented ply in multidirectional laminates with different numbers of 90°laminae. The dashed line represents the UD strength value. The solid line represents Dvorak and Laws prediction. (Reproduced from [26], copyright Wiley, 1987). 19

2.12 Ply classification and related in-situ strength equations. 21

2.13 Three-dimensional stresses on a UD composite element. (x_1, x_2, x_3) coordinate system is fixed to fiber direction (x_1), laminate mid-surface (x_2) and thickness direction (x_3). The (x_l, x_n, x_t) coordinate system is rotated by an angle θ_{fp} from the x_2 direction to the x_n direction which is normal to the fracture plane. The IFF is only influenced by the three stresses σ_n, τ_{nt}, τ_{nl}. (Reproduced from [84], copyright Elsevier, 1998). 25

2.14 Summary of LaRC03 failure criteria (Adapted from [21]). 27

2.15 Schematic of sudden (path OBCD) and gradual (path OBD) property degradation models. (Reproduced from [30], copyright ASME, 2009). 30

2.16 1-D Damaged element. (Reproduced from [57], copyright Springer, 1996). . . . 31

2.17 Degradation factor hyperbolic variation for increasing stress exposure values for different characteristic parameters β, ξ, and different residual values η_r. 33

2.18 Stress-strain relation for an idealized linear damage evolution. 35

2.19 Crack propagation in a homogeneous orthotropic medium and in a fiber-matrix material. (Reproduced from [108], copyright TU Delft, 2010). 37

4.1 Computation framework of the proposed DPM. 44

4.2 Main dimensions of the ABSLJ model. Dimensions are to scale. 45

4.3 Characteristic regions of the ABSLJ. 45

4.4 Illustration of the ABSLJ characteristic dimensions, boundary conditions and loading. 47

4.5 Displacement *vs.* load control procedures and convergence graphical representation based in a displacement prescribed (in red) and load prescribed (in green) procedures. 50

4.6 a) Full (2x2x2) integration point scheme in a brick element - C3D8 b) Reduced (1x1x1) integration point scheme in in a brick element - *C3D8R* 51

4.7 Illustration of shear locking phenomenon in a 2D linear element with four nodes and four integration points. Blue thick lines represent the element under shear locking when subjected to a bending load. Orange lines represent the real behavior. 52

4.8 Improper hourglass control in a femur loaded in a 3-point bending load case. . 53

4.9 Four mesh refinement configurations in the spew region, with different minimum element sizes, from the coarsest to the finest: a) M1 - coarsest - $el_{sz} = 0.5mm$; b) M2 - coarse - $el_{sz} = 0.375mm$; c) M3 - fine - $el_{sz} = 0.125mm$; d) M4 - finest - $el_{sz} = 0.0625mm$. 58

4.10 Selected paths for the stress analysis: a) adhesive length; b) joint thickness; c) adherend layer length. 59

4.11 Examples of the variation of tensile matrix failure index (MFT) along time in the top, and Young's modulus perpendicular to the fibers (E_2) along time in the bottom, for different damage progression models: a) Hashin 3D + Sudden degradation; b) Puck + Puck PDL; c) Puck + Puck CSE.) 62

4.12 Flowchart of the implemented UMAT. 65

4.13 Illustration of the effect of viscosity on the evolution of the regularized damage variable ($\Delta t = 0.01[s]$). (Reproduced from [109], copyright TU Delft, 2017) . . 66

4.14 Final mesh configuration: a) top view; b) lateral view. The smallest element, at the spew region is 0.0625mm long. 70

5.1 Load-displacement curve for the different mesh configurations. The displacements were taken at the adherend tips. 73

5.2 a) Stress component σ_1 along the adhesive length path [figure 4.10 a)] of FESAL4, for the different mesh configurations; b) Zoomed stress distribution in the spew region. 74

5.3 Relative error of the stress component σ_1 along the adhesive semi-length path [figure 4.10 a)] of FESAL4, for the different mesh configurations with respect to M4. 75

5.4 a) Stress component σ_1 along the length of the first lamina (+45°) path [figure 4.10 a)] of FESAL4, for the for different mesh densities; b) Zoomed stress distribution at the adherend's tip; c) Zoomed stress distribution in the spew region; d) Zoomed stress distribution at the stress discontinuity at the singularity. . . . 76

5.5 Relative error of the stress component σ_1 along the length of the first lamina (+45°) path [figure 4.10 a)] of FESAL4, for the for different mesh densities with respect to M4. 77

5.6 Force-displacement curves for the different layup configurations with a prescribed displacement of $\delta_x = 0.5mm$. The displacements were taken at the adherend tips. 78

5.7 Normal stress in the direction parallel to the fibers σ_1 along the adhesive length. 79

5.8 Peel stress σ_2 along the adhesive length. 80

5.9 Longitudinal-transverse shear stress τ_{12} along the adhesive length. 80

5.10 Normal stress in the direction parallel to the fibers σ_1 along the adherend-adhesive-adherend out-of-plane path. 82

5.11 Peel stress σ_2 along the adherend-adhesive-adherend out-of-plane path. 83

5.12 Longitudinal-transverse shear stress τ_{12} along the adherend-adhesive-adherend out-of-plane path. 83

5.13 Inplane shear stress τ_{13} along the adherend-adhesive-adherend out-of-plane path. 84

5.14 Normal stress in the direction parallel to the fibers σ_1 along: a) the first ply length and 2) the second ply length. 85

5.15 Out-of-plane stress σ_2 along: a) the first ply length and 2) the second ply length. 87

5.16 Longitudinal-transverse shear stress τ_{12} along: a) the first ply length and 2) the second ply length. 88

5.17 Experimental (solid lines) *vs.* FEA load-displacement curves (dashed lines), initial failure (IF) and ultimate failure (UF) events for the $[45/90/-45/0]_{2s}$ configuration. The displacements were measured at the extensometer arms positions: 60mm apart, adjacent to the overlap area. 91

5.18 Experimental (solid lines) *vs.* FEA load-displacement curves (dashed lines), initial failure (IF) and ultimate failure (UF) events for the $[90/-45/0/45]_{2s}$ configuration. The displacements were measured at the extensometer arms positions: 60mm apart, adjacent to the overlap area. 91

5.19 Experimental (solid lines) *vs.* FEA load-displacement curves (dashed lines), initial failure (IF) and ultimate failure (UF) events for the $[0/45/90/-45]_{2s}$ configuration. The displacements were measured at the extensometer arms positions: 60mm apart, adjacent to the overlap area. 92

5.20 Experimental (solid lines) *vs.* FEA load-displacement curves (dashed lines), initial failure (IF) and ultimate failure (UF) events for the $[45/0/-45/0]_{2s}$ configuration. The displacements were measured at the extensometer arms positions: 60mm apart, adjacent to the overlap area. 92

5.21 FEA load-displacement curves, damage initiation and ultimate failure events for the four different tested laminates. 93

5.22 Experimental *vs.* FEA damage initiation loads for the four different tested laminates. 94

5.23 Experimental *vs.* FE model ultimate loads for the four different tested laminates. 95

5.24 Experimental *vs.* FEA logarithmic longitudinal strain ε_x maps in the joint region at: a) damage initiation; b) average load value between damage initiation and ultimate failure; c) ultimate failure. The DIC results relate to layup $[0/45/90/-45]_{2s}$ - specimen 5. 96

5.25 Experimental *vs.* FEA logarithmic shear strain ε_{xy} maps in the joint region at: a) damage initiation; b) average load value between damage initiation and ultimate failure; c) ultimate failure. The DIC results relate to layup $[0/45/90/-45]_{2s}$ - specimen 5. 97

5.26 Failure index (FI), Young's modulus (E) and damage (d) maps in the adhesive of the $[0/45/90/-45]_{2s}$ at: a) damage initiation; b) average load value between damage initiation and ultimate failure; c) ultimate failure and d) final failure. . 99

5.27 Failure index maps of the $[0/45/90/-45]_{2s}$ at the ultimate failure: tensile fiber failure index (FFT) and tensile matrix failure index (MFT) for different adherend failure criteria. 101

6.1 Damage propagation in XFEM using the phantom nodes concept: a) before partitioning and b) after partitioning of cracked element. (Reproduced from [16], copyright Elsevier, 2011). 106

P.2 Stress concentration factor around a hole in an orthotropic plate. (Reproduced from [52], copyright Wiley, 2015). 119

P.3 Geometry and material parameters of the single-lap joint for: a) 1-D bar model and b) 1-D beam model. (Reproduced from [105], copyright Elsevier, 1998). . 120

P.4 Normalized adhesive shear stress distributions of thick-adherend single-lap joint comparison: a) improved 1-D bar model (Goland and Reissner with adherend shear), 1-D bar model (Volkersen), original 1-D beam model (Goland and Reissner) and b) improved 1-D beam model with the edge moment M_0 (Goland and Reissner with adherend shear), 2-D FEM model and original 1-D beam model (Goland and Reissner). (Reproduced from [105], copyright Elsevier, 1998). . . 121

P.5 Shear stress distribution in a ABSLJ from finite-element models with and without spew and from Goland and Reissner analytical solutions [31]. 123

P.6 Transverse normal (peel) stress distribution in a ABSLJ from finite-element models with and without spew and from Goland and Reissner analytical solutions [31]. 123

P.7 a) Effect of adhesive brittleness and overlap length on: a) the peel stresses of balanced ABSLJ (Reproduced from [39], copyright NASA, 1974); b) the shear strength of ABSLJ. (Reproduced from [38], copyright NASA, 1973). 124

P.8 Effect of the adherend stiffness imbalance on the adhesive peel stresses in ABSLJ. (Reproduced from [38], copyright NASA, 1973). 125

P.9 a) Transversely isotropic material illustration (2-3-plane is the plane of of isotropy); b) Laminate section before and after deformation due to normal displacement and bending. (Reproduced from [20], copyright Oxford University Press, 2006). 127

P.10 a) Resultant forces and moments in a lamina; b) Multidirectional laminate with coordinate notation of individual plies. (Reproduced from [20], copyright Oxford University Press, 2006). 131

P.11 General orthotropic lamina element: a) stresses in the load coordinate system; b) projection of the stresses in the laminate coordinate system onto the 1-direction material system; projection of the stresses in the laminate coordinate system onto the 2-direction material system. (Reproduced from [76], copyright NASA, 1994). 134

P.12 Kinking bands originated from fiber compressive failure. (Reproduced from [81], copyright SAGE, 2005). 136

P.13 Features prone to delamination owing to: out-of-plane loading [a) lug fitting and b) rib-to-skin joint], geometry [c) taper and d) curved section in bending] and discontinuities [e) ply drop and f) free edge]. (Reproduced from [113], copyright The Royal Society, 2012). 136

P.14 Comparison of failure criteria with test data: a) boron-epoxy off-axis specimens; b) glass-epoxy off-axis specimens. θ angle is defined from load axes to material axes (Reproduced from [42], copyright ASME, 1980). 138

P.15 Master fracture surface (for $\sigma_1 = 0$) for UD material in the (σ_n, τ_{nt}, τ_{nl}) stress space with fracture resistances $R_{\perp}^{(+)A}$, $R_{\perp\parallel}^{A}$ and $R_{\perp\perp}^{A}$ of the stress action plane. The (σ_2,τ_{21}) fracture curve follows a contour line (from a to c) and then a boundary line of a cross-section (from c to d). Compare with figure P.16. (Reproduced from [84], copyright Elsevier, 1998). 139

P.16 Fracture curve (τ_{21}, σ_2, for $\sigma_1 = 0$), representing three different fracture modes A, B, C. The curve is generated by two ellipses and one parabola. (Reproduced from [84], copyright Elsevier, 1998). 139

P.17 Example of Newton-Raphson method implementation for a function $y = sin(x)-$ 0.7 with an initial guess of $x_0 = 1.2$ and a tolerated error of $\epsilon_{tol} = 0.0001$. . . . 142

P.18 Example of Newton-Raphson method implementation for a function $y = 10cos(x)+$ $1/x$ with an initial guess of $x_0 = 0.05$ and a tolerated error of $\epsilon_{tol} = 0.0001$. . . 142

P.19 Graphical example of Newton–Raphson method applied to solve nonlinear equilibrium equations in Abaqus. 144

P.20 Flowchart of framing UMAT in a generic Abaqus/Standard simulation. 147

P.21 Normal and shear stress values along the adhesive path length: a) normal stress in the direction parallel to the fibers σ_1; b) peel stress (*i.e.* in the out-of-plane direction) σ_2; c) normal stress in the inplane transverse direction σ_3; d) longitudinal-transverse shear stress τ_{12}; e) inplane shear stress τ_{13}; f) transverse shear stress τ_{23}. 151

P.22 Normal and shear stress values along the adherend-adhesive-adherend out-of-plane path: a) normal stress in the direction parallel to the fibers σ_1; b) normal stress in the out-of-plane direction σ_2; c) normal stress in the inplane transverse direction σ_3; d) longitudinal-transverse shear stress τ_{12}; e) inplane shear stress τ_{13}; f) transverse shear stress τ_{23}. 152

P.23 Normal and shear stress values along the bottom adherend's first layer: a) normal stress in the direction parallel to the fibers σ_1; b) normal stress in the out-of-plane direction σ_2; c) normal stress in the inplane transverse direction σ_3; d) longitudinal-transverse shear stress τ_{12}; e) inplane shear stress τ_{13}; f) transverse shear stress τ_{23}. 153

P.24 Normal and shear stress values along the bottom adherend's second layer: a) normal stress in the direction parallel to the fibers σ_1; b) normal stress in the out-of-plane direction σ_2; c) normal stress in the inplane transverse direction σ_3; d) longitudinal-transverse shear stress τ_{12}; e) inplane shear stress τ_{13}; f) transverse shear stress τ_{23}. 154

P.25 Comparison between theory's original [24] and obtained Von Mises failure envelopes for a random isotropic material (principal stresses only). The stresses are normalized by the yield strength of the material. 155

P.26 Comparison between theory's original [42] and obtained Hashin's failure envelopes for an (unspecified) orthotropic material under biaxial (σ_2 and σ_3) loading. $Y^T = 45MPa$; $Y^C = 240MPa$; $S^T = 55MPa$. 156

P.27 Comparison between theory's original [85] and obtained Puck's failure envelopes for a E-Glass/LY556/HT907/DY063 material under biaxial loading: 0° GFRP lamina under combined σ_2 and τ_{12} stresses. Strength values: $Y^T = 35MPa$; $Y^C = 114MPa$; $S^L = 72MPa$. 157

P.28 Comparison between theory's original [85] and obtained Puck's failure envelopes for a E-glass/MY750 epoxy material under biaxial loading: 0° GFRP lamina under combined σ_1 and σ_2 stresses. Strength values: $X^T = 1280MPa$; $X^C = 800MPa$; $Y^T = 40MPa$; $Y^C = 145MPa$; $S^L = 73MPa$; $E_1 = 45600MPa$; $E_{f1} = 72400MPa$; $\nu_{12} = 0.278[-]$; $\nu_{f12} = 0.22[-]$. 158

P.29 Comparison between theory's original [82] and obtained LaRC05's failure envelope (case 2) for a T300/PR319 material under combined loading: 0° CFRP laminate under combined σ_2 and τ_{12} stresses. Strength values: $X^C = 950MPa$; $Y^T = 40MPa$; $Y^C = 125MPa$; $S^L = 97MPa$; $\eta_L = 0.082[-]$. 159

P.30 Comparison between theory's original [83] and obtained LaRC05's failure envelope (case 5) for a E-glass/MY750 epoxy material under triaxial loading: 90° GFRP laminate under combined σ_2 and $\sigma_1 = \sigma_3$ stresses. Strength values: $Y^T = 40MPa$; $Y^C = 145MPa$; $S^L = 73MPa$; $\eta_L = 0.082[-]$; $\alpha_0 = 50°$. 160

P.31 Young's modulus degradation over time in some elements of the adhesive. . . . 161

List of abbreviations

Abbreviation	Full form
ABSLJ	Adhesively Bonded Single Lap Joint
ADP	Adhesive Ductility Parameter
AE	Acoustic Emission
CAE	Complete Abaqus Environment
CDM	Continuum Damage Model
CFRE	Carbon Fiber Reinforced Epoxy
CFRP	Carbon Fiber Reinforced Polymer
CLT	Classical Laminate Theory
CSE	Constant Stress Exposure
CT	Compute Tomography
CZM	Cohesive Zone Model
DIC	Digital Image Correlation
DPM	Damage Progression Model
FE	Finite Element
FEA	Finite Element Analysis
FEM	Finite Element Method
FESAL	Finite Element Stress Analysis Layup
FF	Fiber Failure
FFC	Compressive Fiber Failure
FFT	Tensile Fiber Failure
FRP	Fiber Reinforced Polymer
IFF	Inter-Fiber Failure
MFC	Compressive Matrix Failure
MFT	Tensile Matrix Failure
NL	Non-Linear
PDA	Progressive Damage Analysis
PDL	Predefined Degradation Law
QI	Quasi-Isotropic
SLJ	Single Lap Joint
UD	Uni-Directional
UMAT	User MATerial subroutine
VCCT	Virtual Crack Closure Technique
WWFE	World Wide Failure Exercise
XFEM	eXtended Finite Element Method
e.g.	*exempli gratia* (for example)
et al.	*et alia* (and others)
i.e.	*id est* (in other words)
vs.	*versus* (against)

List of symbols

Latin

Symbol	Description	Units
$[A]$	Inplane coupling matrix	$[N/m]$
A	Area	$[m^2]$
$[B]$	Inplane-out-of-plane coupling matrix	$[N]$
B	Width of the body (in the VCCT example)	[m]
$[C]$	Stiffness matrix	$[Pa]$
$[D]$	Out-of-plane coupling matrix	$[N.m]$
d	Damage variable	[-]
∂	Partial derivative	[-]
E	Young's modulus	$[Pa]$
E_{1b}	Longitudinal bending stiffness	$[Pa]$
E_{1m}	Longitudinal membrane stiffness	$[Pa]$
E_s	Burst energy in AE sensor	$[J]$
F	Force	[N]
f_E	Puck's stress exposure	[-]
G	Shear modulus	$[Pa]$
G_c	Fracture energy	$[J/m^2]$
h	Height from the neutral axis	$[m]$
$\{K\}$	Curvature vector	$[1/m]$
k	Stiffness	$[N/m]$
K_c	Fracture toughness	$[Pa.m^{\frac{1}{2}}]$
$\{M\}$	Moment per unit width vector	$[N]$
$m_{\sigma f}$	Mean magnification factor of the transverse stress for the fibers	[-]
$\{N\}$	Force per unit width vector	$[N/m]$
$[Q]$	Reduced stiffness matrix	$[Pa]$
$[S]$	Compliance matrix	$[1/Pa]$
S	Shear strength of the lamina	[Pa]
spw	Spew dimension	[-]
$[T]$	Transformation matrix	[-]
t	Thickness of the laminate	$[m]$
w	Width of the laminate	$[m]$
X	Strength of the lamina in the fiber direction	$[Pa]$
Y	Strength of the lamina in the transverse direction	$[Pa]$
z	Z-coordinate w.r.t. the neutral axis	$[m]$

Greek

Symbol	Description	Units
α	Scarf angle	[-]
β	Puck's proportional constant that control the decay rate of η	[-]
γ	Shear strain	[-]
γ_e	Elastic strain energy	$[J/m^2]$
γ_p	Plastic strain energy	$[J/m^2]$
δ	Displacement/separation	$[m]$
Δ	Change in a variable	[-]
$\{\varepsilon\}$	Strain vector	[-]
ε	Normal strain	[-]
η	Degradation factor	[-]
η_L	LaRC05's slope coefficient for longitudinal shear strength	[-]
η_T	LaRC05's slope coefficient for transverse shear strength	[-]
θ	Transformation angle / inclination of the potential fracture plane	[-]
μ_{vr}	Viscous regularization coefficient	[-]
ν	Poisson ratio	[-]
ξ	Puck's exponential constant that control the decay rate of η	[-]
π	Mathematical constant 'Pi'	[-]
$\{\sigma\}$	Stress vector	$[Pa]$
σ	Normal stress	$[Pa]$
τ	Shear stress	$[Pa]$
ψ	LaRC05's angle of a kink-band plane	$[-]$

Subscripts and superscripts

Symbol	Description
$\cdot_{12}$	In the material coordinate system
$\cdot_a$	Adhesive related quantity
$\cdot^C$	Compressive mode
$\cdot_d$	Damaged quantity
$\cdot_f$	Fiber related quantity
$\cdot_{FF}$	Puck's fiber failure
$\cdot_{I,II,III}$	Fracture modes I, II and III, respectively
$\cdot_{ij}$	Generic indices of a matrix
$\cdot_{IFF}$	Puck's inter-fiber failure
$\cdot^i$	Iteration number
$\cdot_k$	Ply number on the laminate / increment number
$\cdot^k$	Increment number
$\cdot^L$	Longitudinal mode
$\cdot_m$	Matrix related quantity
$\cdot_{ply}$	Ply related quantity
$\cdot_s$	Shear related quantity
$\cdot^T$	Tensile / transverse mode
$\cdot_{ult}$	Ultimate quantity
$\cdot_{xy}$	In the load/laminate coordinate system

1

Introduction

Over the last decades, aerospace industry has been gradually embracing Fiber Reinforced Polymers (FRPs) and adhesively bonded joints as main material [90, 92] and joint method [6, 62, 97, 102, 114], respectively. While composite materials overcome their metal counterparts in terms of: higher specific properties, improved durability, less sensitivity to fatigue and resistance to corrosion [63]; adhesive bonded joints, in turn, outperform bolted and riveted joints providing: a more structurally efficient method for load transfer, lower stress concentrations, better fatigue performance, reduced weight [16, 45] and vibration damping [66].

On ground of ease of manufacturing, Adhesively Bonded Single Lap joints (ABSLJ) in particular, have been widely studied [101], nonetheless, its mechanical analysis is far from being trivial. The anti-symmetric configuration and the significant transverse displacements caused by the eccentric load path makes this joint configuration inherently inefficient [38, 68] inducing high stress concentrations at the overlap ends. In this critical region, the longitudinal-transverse shear stress component and all normal components experience a sudden grow, namely the out-of-plane component in the adhesive (commonly named as peel stresses) and in the adherends (commonly named as interlaminar stresses). The analysis becomes even more complex when the adherends are made of Fiber Reinforced Polymeric (FRP) materials given their anisotropic behavior.

A FRP composite material is made of a combination of two very distinct phases that can be specifically tailored to comply with a broad range of design requirements and to achieve a desirable mechanical performance for a given aerospace application [36, 47, 74]. The fiber reinforcement is the backbone of the material, defining the strength and stiffness in its direction [20]. On the other hand, the matrix (the continuous phase) protects, bonds, supports and transfers the local stresses from one fiber to the other through shear mechanisms [47]. Multidirectional laminates are composed of multiple layers stacked together of Uni-Directional (UD) material (each layer is commonly designated as 'ply' or 'lamina') oriented in different directions resulting in complex mechanical interactions [30]. When the composite structure is loaded, a stress field develops throughout the whole laminate, being the local stresses different from ply to ply, particularly between differently oriented plies. Raising the load level up to the strength of a given lamina will trigger a damage phenomenon, most likely starting with matrix cracking.

Both the academia and the industry have been striving for accurate failure prediction in FRP through the development and implementation of failure theories [110] that aim to fully describe the non-linear constitutive behavior caused by the characteristic failure mechanisms since damage initiates, followed by its propagation until ultimate failure.

The institutionalized philosophy regarding damage tolerance in composite structures for aerospace applications has been extremely conservative, leading to over-designed solutions [74]. The reality is that most of composite structures sustain a substantial amount of damage prior to ultimate failure [7, 32]. It is therefore vital to accurately predict when damage initiates (by means of appropriate failure criteria) and how damage propagates (captured by a suitable material property degradation models) [2, 30], in order to fully understand the constitutive behavior of composite materials, enabling at the same time the possibility of a tailored efficient composite design for specific technical and economic objectives.

Initially conceived to model damage in isotropic and homogeneous materials, Continuum Damage Models (CDMs) have been quite popular and effective in this endeavor to model damage in FRP, owing to the versatility and convenience of implementation in a Finite Element (FE) environment. However, as Forghani *et al.* [29] emphasize, extending the concepts of CDMs to orthotropic materials is not straightforward. Over the years, several authors proposed new composite's damage models, tending to gradually incorporate new enriching physical considerations rather than relying purely on phenomenological relations. Amongst the mainstream models, Hashin [42], Puck [85] and LaRC05 [82] failure criteria excel in terms of predictive capabilities. Concerning damage propagation, CDMs assume the effect of the damage by the selective degradation of the engineering constants of the material. In the scope of material degradation models, two main approaches can be found: sudden degradation models which instantaneously degrade a given elastic property to a smaller percentage, once damage is detected, without subsequent reduction; and gradual degradation models that based on a predefined evolution law or based on the assumption that the failure index remains constant find the progressively reduced value of the elastic parameters.

This document is structured in a logical manner, sequentially addressing the defined research subquestions: The following chapter 2 presents and discusses, in a systematized manner, relevant findings in the literature. This chapter is subdivided in three sections: an review on adhesively bonded structures and the influence of geometrical; an overview on the constitutive relations of FRP composite materials and an outline over the progression damage analysis, including an overview on state-of-the-art CDM. This culminates in chapter 3, where the research question and objective are formulated. It follows chapter 4 in which the research methodology is defined for the preliminary studies and the damage progression study, including: numerical ABSLJ model definition, numerical considerations, User MATerial subroutine (UMAT), verification and validation. It follows, chapter 5 that presents and discusses the results of the preliminary studies: a) the mesh convergence study; b) the stress study, comparing four adherend layups under a prescribed displacement along four pre-defined paths. Still in this chapter, the DPM is validated against an existing experimental campaign. From this discussion, conclusions are drawn and presented in chapter 8 along with several recommendations for further development of this topic.

2

Literature study

2.1. Adhesively bonded joints

Adhesive bonding can be described as the joining process in which materials (the adherends) are bonded by means of an interface substance (the adhesive), holding the adherends together by surface attachment. The forces that enable this surface attachment are a combination of microscopical mechanical locking and chemical bonding [70].

In bonded joints, the adhesive is subjected to shear and normal stresses in the out-of-plane direction (also known as peel stresses). The main function of the adhesive is to transfer the loads from one adherend to another [19]. It is through the formation of chemical bonds (mainly of the covalent type and intermolecular forces, which play a less determinant role) between the adherend surface atoms and the adhesive compounds that this load transfer mechanism takes place [6].

Composite parts for aerospace applications are either bolted/riveted or bonded for joining purposes. Adhesively bonded methods present several advantages over conventional mechanically fastened joining counterparts [50, 65, 96]. Applying bolted joints in composites is undesirable for the following reasons: a) the anisotropic behavior of FRP leads to high stress concentrations[1]; b) the brittleness of the composite material allows little stress relieve through plasticity at the critical locations of the loaded hole's edge and c) UD laminates present low through-the-thickness strength leading to (interlaminar) delamination [11]. By contrast, adhesively bonded joints show: a) continuity with regards to load transfer; b) enhanced strength-to-weight ratio, c) improved damage tolerance and d) ease fabrication at lower costs [6]. Appendix B - table P.1 summarizes in a table the advantages and disadvantages of both methods.

2.1.1. Adhesively bonded joint types

Adhesively bonded joints are used in many configurations as shown in figure 2.1 a). The designer should be able to find a compromise among competing requirements. If on the one

[1]For a laminate only containing 0°oriented uni-directional (UD) plies, the stress concentration factor at 90°of the hole's edge is almost 7 (see appendix A - figure P.2).

hand a joint should have a simple and smooth geometry and be cheap to produce, on the other it should effectively sustain static and/or cyclic loads during the aircraft operational period [40].

Some joint configurations might be excluded from the design options due to limited strength [figure 2.1 b)] or owing to non-compliance with more specific requirements such as aerodynamic smoothness. The inherent geometric step in adhesively bonded single lap joints (ABSLJ) might induce laminar–turbulent transition in a surface that is intended to be in laminar regime. Not exclusively but also for this reason, ABSLJ are not used in wing covers.

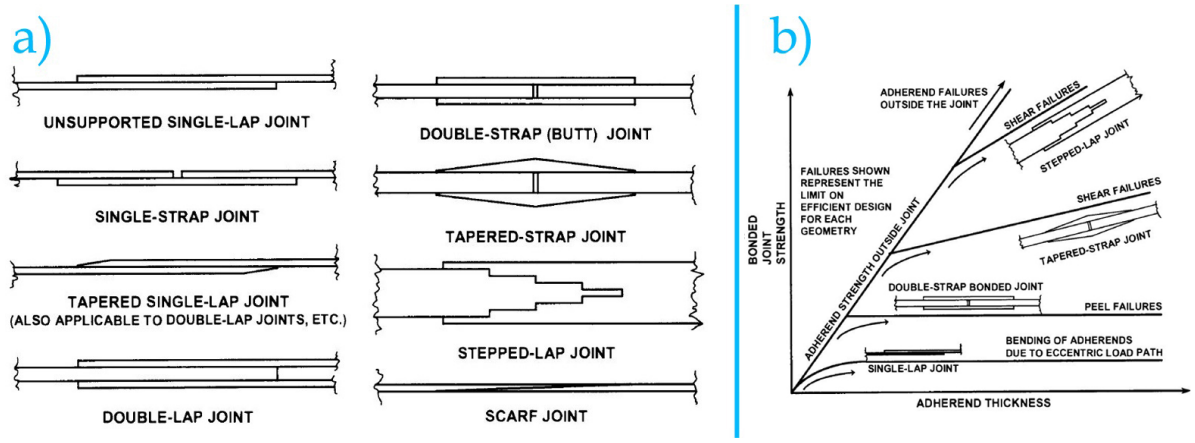

Figure 2.1: Adhesively bonded joint types: a) different designs; b) joint strength *vs.* adherend thickness. (Reproduced from [40], copyright Kluwer, 2003).

An overview on the different joint types

Single lap joint

Either by analytical, finite difference or finite element methods, the ABSLJ is the most extensively studied joint design [41, 112]. Furthermore, the ABSLJ is the simplest adhesively bonded joint to produce [41, 68]. Nevertheless, its stress analysis is not trivial.

Owing to load path eccentricity, unsupported SLJ are inherently inefficient [39]. In practical terms, owing to the anti-symmetric geometry of the joint (*i.e.* the offset in the line of action of the load), high bending and peel stresses develop at the lap ends, which causes the joint to rotate. The use of alignment tabs dramatically improves the strength of the joint [38] due to the fact that it reduces the load path eccentricity, hence mitigating the detrimental effects caused by the non-uniform peel and shear stresses. Section 2.1.3 explore in detail the parameters that influence this joint type strength.

The longitudinal-transverse shear is known for its 'bathtub' distribution along the bond length. The reason for the peak shear stresses at the adhesive overlap ends relates to strain mismatch between the adherends, at those regions. At the adherend lap start (red region in figure 2.2), where the stress concentration is located, the strains are greater than the strains experienced by the corresponding lap end (green region in figure 2.2) of the other adherend which is, in reality, lightly loaded. By contrast, in the center of the bondline, the adhesive experiences small shear stresses, considering that the smaller mismatch between the adherends' strains. Yet, the effect of the simple shear in the adhesive central elements should be considered.

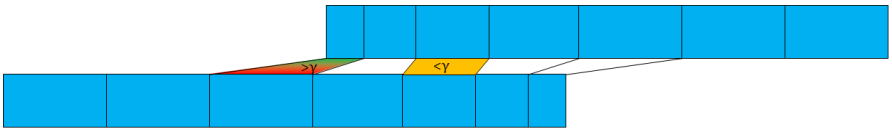

Figure 2.2: Illustration of the high shear strain experience by the adhesive at the lap ends.

Single strap joint

When compared to other joint configurations, the single strap joint counts with relatively little research in terms of stress analysis. Given that it is an asymmetric joint (with respect to the 1-2 plane) and particularly for thick adherends, when loaded develops high adhesive peel stresses and associated through-thickness adherend interlaminar stresses [see figure 2.3 a)] that affect the adhesive shear stress distribution. The abrupt eccentricity at the butt region results in high bending moments in the middle of the splice plate [40]. This joint type is commonly used for repair procedures in the automotive and aerospace industries [112].

Double lap joint

Considering that double lap bonded joint is symmetric (with respect to the 1-2 plane), one might think that the analysis only involve extensional deformations of the adherends. Yet, reality is that the load path is also eccentric[2], meaning that peel stresses are also present in this configuration due to the induced moment about the neutral axis which, by its turn, was created by the shear load acting in the bonded face of the adherend at a distance $t/2$ (for a symmetric layup). Thus, peel stresses do develop at the lap ends, which might be significant and determinant, specially for thick adherends [see figure 2.3 a)].

Despite the existence of peel stresses, these play a lesser role (when compared to ABSLJ), hence the strength of these joints is much less sensitive to the influence of the overlap length [38]. Based on this, it expectable that, for the same lap length, the strength of this joint is always more than double of its ABSLJ counterpart [112].

Double strap and tapered-strap joints

Hart-Smith [40] states that for sufficiently thick outer adherends, double strap bonded joints are subjected to peel strength cutoffs (see figure 2.3), *i.e.*, beyond a certain adherend thickness, the strength of the joint is no longer governed by the adherend strength but instead by the peel stress state. These peel stresses are originated due to abrupt changes in the joint axial stiffness at the thickness transition, ultimately leading to a through-thickness (interlaminar) failure.

The tapered-strap bonded joint overcomes this limitation, by gradually reducing the thickness of the splice plates (outer adherends) ends. Even though tapering significantly improves the peel strength of the joint, the shear strength is generally not affected by it, which explains the gradual increase of the joint strength with the adherend thickness, up to a shear

[2]The load that flows axially through the central adherend splits in two directions just before it reaches the overlap region, acquiring a vertical component.

governed failure, as opposed to the (untapered) double strap bonded joint whose failure is peel dominated [see figure 2.1 b)].

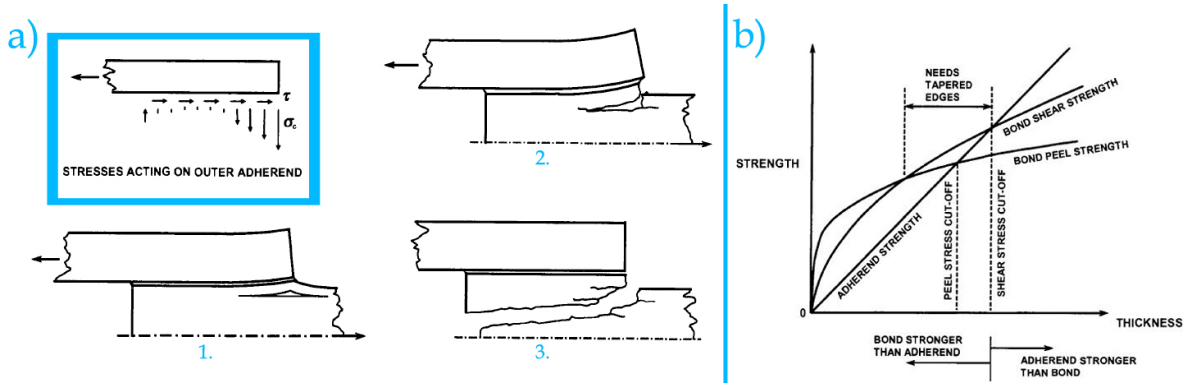

Figure 2.3: Effect of high peel on thick adherends: a) failure sequence; b) governing failure modes in function of adherend thickness. (Reproduced from [40], copyright Kluwer, 2003).

Stepped-lap and scarf joint

The stepped-lap and the scarf joints are the most efficient configurations in the sense that the stress concentration at the lap ends is minimized, which obviously results in a stronger joint. These configurations are recommended for thicker adherends (rule of thumb: $t > 6.35[mm]$ [40]), considering that the stiffness is relatively constant throughout the lap length, avoiding the development of peel stresses lap ends. Scarf and stepped-lap[3] are frequently use in the repair of aerospace composite parts, ensuring aerodynamic smoothness [36] that might be crucial for performance purposes, as explained before.

Scarf joints have the remarkable feature of being flush and co-linear. The shear and normal stresses in this joint type are dependent on the adherend thickness and scarf angle [36] which also define the overlap length. Yet, due to the fact that the tips of the adherends have a finite thickness (which leads to a stress concentration) and due to the stiffness imbalance between the adherends, the structural efficiency of such joints is smaller than the theoretical. Hence, it is of vital importance to maintain the stiffness constant throughout the whole lap length even if two different materials are being joint[4].

Despite the huge advantage of having a null load path eccentricity which translates into null bending moments under a tensile load case, leading to constant peel and shear stress distributions over the overlap length, there is a trade-off that needs to be addresses regarding the scarf angle α value. If α is not small enough, then the tensile projection[5] of the force acting on the adhesive will be significant which might compromise the joint's loading capability, attending to the fact that adhesives are rather inefficient under a tensile loading [45]. On the other hand, an excessively small α might cause manufacturing issues or/and an extremely long overlap region. Figure 2.4 illustrates the load decomposition on one adherend of a scarf joint.

[3] If produced flush as opposed to the illustration of a stepped-lap joint shown in figure 2.1 a).
[4] In practice to ensure stiffness balance in the case of two different materials, the geometrical stiffness compensates the imbalance in the material stiffness.
[5] The force acting on the scarf inclined overlap section can be decomposed in two components: a shear component $F_{shear} = F.cos(\alpha)$ and a tensile component $F_{tension} = F.sin(\alpha)$.

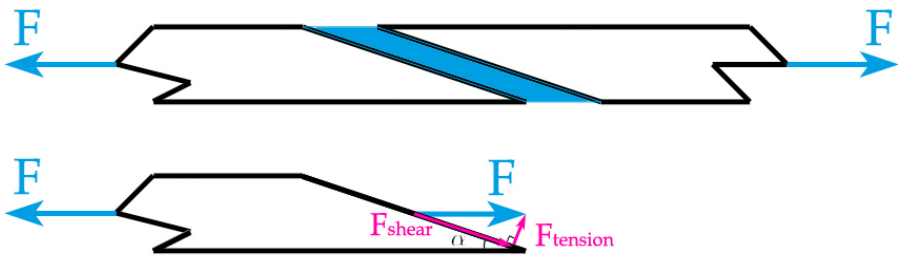

Figure 2.4: Tensile and shear projections of the forces acting in the adherend of a scarf joint.

While the strength of the scarf joint increases as the scarf angle decreases, the strength of the stepped-lap joint, for a fixed number of steps, is barely affected. The latter's strength is improved by maximizing the number of steps [36].

2.1.2. Failure modes in FRP adhesively bonded joints

The failure modes are determined by several factors, namely: quality of the bond, specimen geometry and load case [6]. Although not explicitly referred by the author, the failure mode is affected by the adherend properties - material and geometrical. Take the previous charts in figures 2.1 b) and 2.3 b) and consider a tapered-strap joint configuration loaded in tension until failure, with rather thin and compliant adherends, each composed by the following layup: $[90]_{2s}$ bonded using a brittle adhesive. Now, only changing the adherend properties, consider a thicker and stiffer pair of adherends with the following layup: $[0/0/0/45/-45/45/-45/90]_{2s}$. Most likely, the failure modes would not be the same. Based on the referenced figures, in the first case an adherend failure would be expected, whereas a shear failure would be the likely scenario, in the latter case.

The standard practice for classifying failure modes in adhesively bonded FRP joints (ASTM D5573) [3] identifies and characterizes seven classes of failure modes, described and illustrated in the following table:

Table 2.1: Definition and illustration of the failure modes classified by ASTM D5573. (Adapted from [3]).

Failure mode (Abbreviation)	**Definition**	**Illustration**
Adhesive (or interfacial) failure	Separation appears to be at the adhesive-adherend interface.	
Cohesive failure	Separation is within the adhesive.	
Thin-layer cohesive (or interphase) failure	Failure similar to cohesive failure, except that the failure is very close to the adhesive-adherend interface, characterized by a 'light dusting' of adhesive on one adherend surface and a thick layer of adhesive left of the other.	
Fiber-tear failure	Failure occurring exclusively within the fiber reinforced plastic (FRP) matrix, characterized by the appearance of reinforcing fibers on both ruptured surfaces.	
Light-fiber-tear failure	Failure occurring within the FRP adherend, near the surface, characterized by a thin layer of the FRP resin matrix visible on the adhesive, with few or no glass fibers transferred from the adherend to the adhesive.	
Stock-break failure	Break of the FRP adherend outside the adhesively bonded-joint region, often occurring near it.	
Mixed failure	Any combination of two or more of the previous six classes.	

Even though this practice accomplishes its goal in presenting a comprehensive definition of possible failure modes in FRP adhesively bonded joints, it does not explain the cause of each of the presented failure modes. For that, theoretical stress analysis models and finite element models validated by empirical results, were developed in order to provide a good understanding of the critical parameters that lead to a particular failure mode.

2.1.3. Parameters influencing the single lap bonded joint strength

The structural performance of an adhesively bonded joint is affected by several parameters, such as: 1) manufacturing bonding process; 2) surface preparation, 3) geometrical parameters [subdivided in 3.1) bondline thickness, 3.2) joint configuration and 3.3) overlap length] and 4) material properties [subdivided in 4.1) adhesive properties and 4.2) adherend material].

Taking into account that the first three parameters are not within the scope of this thesis, brief considerations about the influence of some of the these on the joint strength are presented in appendix D.

2.1.3.1. Adhesive properties

In a review paper [10] published in 2017, Budhe *et al.* state that in order to satisfy industry demands, advanced adhesive materials are being developed in order to meet the demanding requirements. Thus, the selection process of an adhesive material for a specific application is quite complex since it depends on several factors such as: the adherend characteristics, the curing temperature, the expected environmental condition in service, the type of load in the bonded elements and, of course, the cost [6].

The mechanical properties of an adhesive, particularly the stress-strain curve and the shear modulus define the adhesive behavior [6]. This behavior may range from relatively brittle

to very ductile [see figure 2.5 a)], even though, in reality the shear properties manifest as viscoelastic[6] rather than elastic-plastic, making the mechanical analysis too complex [45]. For reasons of simplification and for sake of practicality, the shear stress-strain curve is idealized through a bilinear elastic-perfectly plastic approximation. Thus the actual highly non-linear (NL) region and the hysteresis energy losses are neglected, yet, the idealization complies with the shear strain energy absorbed by the adhesive, *i.e.*, the area under the actual shear stress-strain curve is equal to the area in the equivalent analytical model. Figure 2.5 b) represents both, the actual behavior and the idealized model which is defined by three parameters: a) the plastic shear stress (maximum) τ_p; b) the elastic shear strain γ_e and c) the plastic shear strain γ_p.

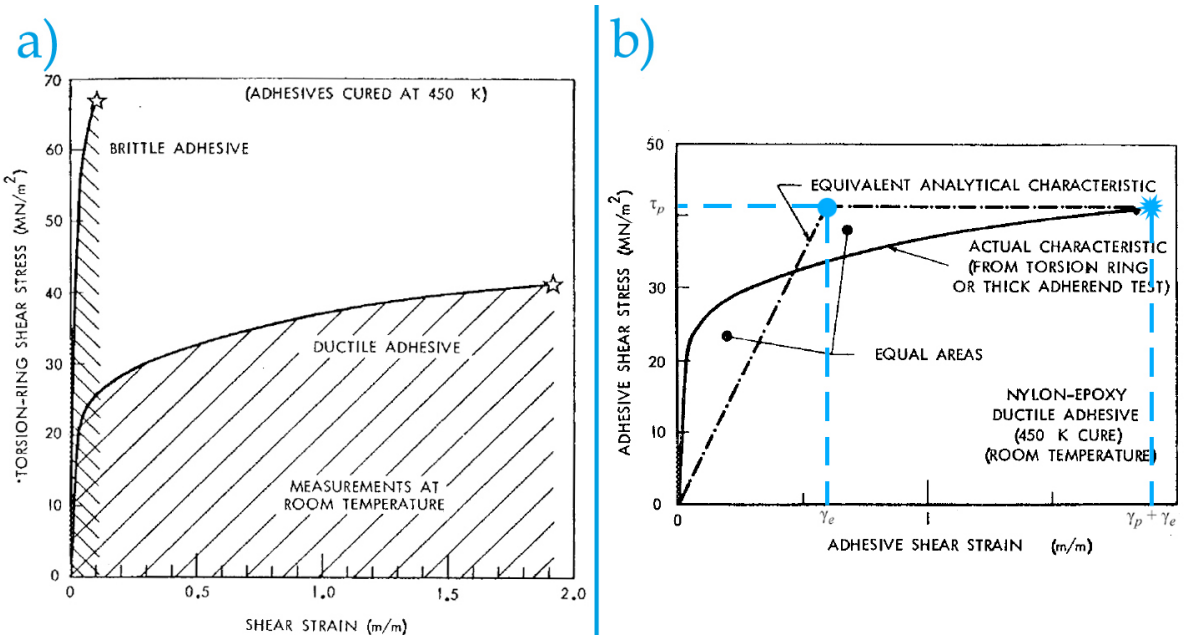

Figure 2.5: a) Comparison of shear stress-strain curves and associated absorbed energies for brittle and ductile adhesives. (Reproduced from [39], copyright NASA, 1974); b) Actual characteristic and idealized adhesive shear stress-strain curves and parameters that characterize the idealized model. The areas bellow both plots are equal, *i.e.*, the energy absorbed by the adhesive is the same in both models. (Adapted from [39]).

2.1.3.2. Effect of adhesive ductility

Adhesive ductility has profound effects on the mechanical behavior of adhesively bonded joints. First of all, a useful parameter should be presented so it gives a good indication of the adhesive's elastic-plastic behavior and toughness. Thus, a conveniently named, Adhesive Ductility Parameter (ADP) relates the plastic shear strain with the elastic shear strain ($ADP = \gamma_p/\gamma_e$). If the ADP is equal to zero it means that the adhesive is purely elastic, *i.e.*, brittle. On the other hand, stating that ADP is equal to ten means that the adhesive is ten times more plastic than elastic, *i.e.*, ductile [45].

Figure 2.5 a) clearly shows that ductile adhesives generally present higher toughness values. Additionally, brittleness increase the magnitude of peel stresses with respect to the average ad-

[6]Viscoelastic materials exhibit both viscous and elastic characteristics when undergoing deformation. Due to the viscous component, hysteresis takes place in the stress–strain curve, *i.e.*, some energy is 'dissipated' during the loading cycle.

herend stresses, especially for short overlaps, fact that naturally decreases the joint efficiency, as shown in appendix E.1 - figure P.7 a). In the same appendix, figure P.7 b) explicitly establishes the relation between the adhesive brittleness and the shear joint efficiency, corroborating the previous conclusions. Plus, the referred chart indicates that the worst case scenario when it comes to joint efficiency, is having a brittle adhesive with an eccentric load path.

It should be emphasized that ABSLJ strength is rarely governed by shear strength, but rather by induced peel stresses due to load path eccentricity that ultimately lead to delaminations due to high through-thickness adherend stresses [38].

2.1.3.3. Adherend material

2.1.3.4. Effect of adherend stiffness imbalance

Any stiffness imbalance between adherends intensifies stress concentration in the adherends which leads to a reduced joint efficiency in comparison to balanced adherends (see figure 2.6 a), and for this reason Hart-Smith [38] suggests that the use of imbalanced SLJ should be avoided. Furthermore, this stiffness imbalance greatly increases the adhesive peel stresses with respect to the average adherend stresses (appendix E.2 - figure P.8).

The author highlights the fact that in imbalanced ABSLJ, the bending moments seen by adherend at the overlap ends are inversely proportional to the adherend axial stiffness, meaning that a thinner/softer adherend will be subjected to higher stress levels induced by bending. Specifically for composite adherends, the author concluded that increasing the bending stiffness parameter $k_b = 12D(1-\nu^2)/(Et^3)$ results in an improved joint efficiency for a given stiffness imbalance value.[7] [38]. In other words, by maximizing the bending stiffness D of both adherends by concentrating the stiffer 0°plies as far as possible from the neutral axis minimizes the detrimental effects of the axial stiffness imbalance between them, as can be observed in figure 2.6 b).

[7]One of the parameters that the author uses to quantify the stiffness imbalance is the 'adherend extensional stiffness ratio' which he abbreviates to ETR (check table 1 in reference [37]).

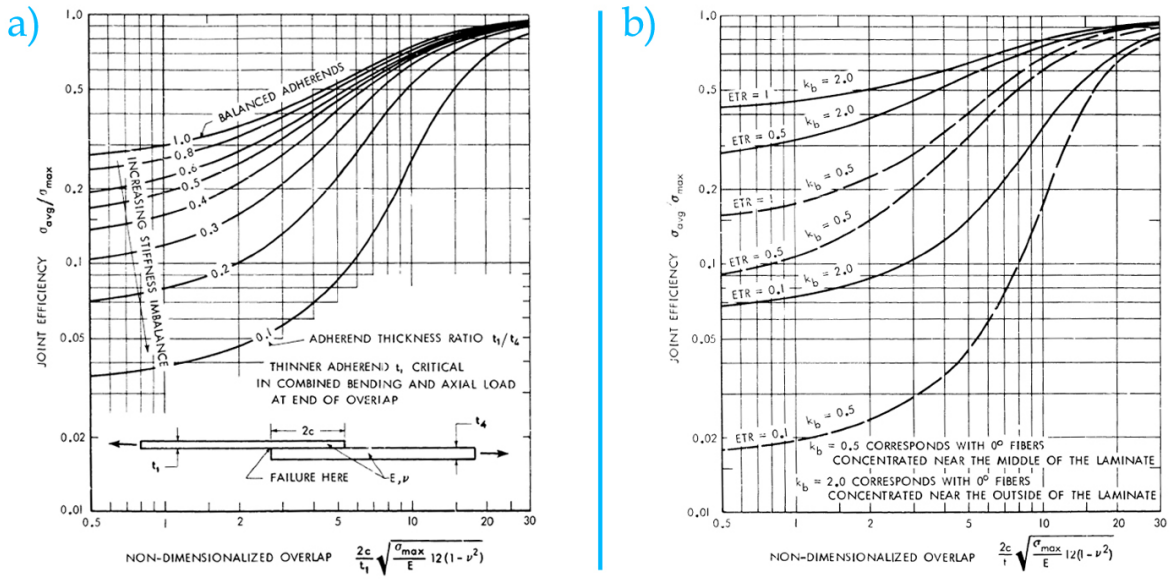

Figure 2.6: Effects of adherend stiffness imbalance on adherend joint efficiency: a) for different adherend thickness ratio; b) for different adherend extensional stiffness ratio and bending stiffness values. (Reproduced from [38], copyright NASA, 1973).

Hart-Smith [38] also studied the effect of the adherend stiffness imbalance on peel (inter-laminar tensile) adhesive stresses for different adherend thickness ratios (see appendix E.2 - figure P.8). The author concluded that this failure mode is more likely for thicker adherends, for the reasons stated before related to the load path eccentricity, and that the adhesive peel stresses for an adherend thickness ratio of $t_1/t_4 = 0.1$ can be as 14 times higher as for an identical adherend case.

2.1.3.5. Effect of stacking sequence

Matthews and Tester [68] experimentally studied the influence of the stacking sequence of Carbon Fiber Reinforced Polymer (CFRP) adherends in the strength of ABSLJ subjected to a quasi-static tensile loading.The tested composite specimens were all symmetric and were laminated using UD CFRP plies oriented at 0°or 45°. Several stacking sequence combinations were built for laminates composed by 6, 8, 10 and 12 plies.

The authors concluded that the strength increased with proportion of 0°plies. Moreover, the 8-ply specimens corroborated Hart-Smith theory that stronger joints have the 0°plies on the outside of the laminate. Yet, for 6-ply layups there was no correlation between experiments and theory, which led the authors to speculate that thinner laminates were more sensitive to experimental inaccuracies, such as specimen alignment and load eccentricity. Finally, a twisting behavior was observed which affected the results leading to an intensification of shear stresses, which by its turn resulted in a premature failure. They associated this twisting behavior with the existence of bending-twisting coupling ($D_{16}, D_{26} \neq 0$). Notwithstanding, the authors did not explicitly related the existence of this coupling with the fact that some of the laminates were not antisymmetric, which is a necessary condition to eliminate bending-twisting couplings.

Using the Finite Element Method (FEM), Aydin [4] assessed the 3D effects of fiber orien-

tation angle of CFRP multidirectional laminates on the stress distributions and on the failure indices of epoxy bonded SLJs. While one of the ABSLJ end was fixed, a pressure of $70MPa$ was applied on the cross section of the other ABSLJ cross-section. Eight layup configurations, each composed by 16 plies, were studied: $[45/-45]_{4s}$, $[55/-55]_{4s}$, $[0/90]_{4s}$, $[30/60]_{4s}$, $[0]_{16}$, $[90]_{16}$, $[90/45/-45/0]_{2s}$, $[90/30/-30/90]_{2s}$. The author concluded that the ply stacking sequence have a significant effects on the stress distribution and failure predictions in the adherend and adhesive. For a prescribed loading, laminates $[0]_{16}$ and $[0/90]_{4s}$ generally showed the lower stress concentrations in both, the adherend and the adhesive. The author justified this result with the fact that in both cases the adhesive's neighboring plies are 0s. As explained before, a higher number of 0s and their remote position from the neutral axis, increases the bending stiffness of the adherend.

2.2. Progressive Damage Analysis (PDA) in composites

Damage can be defined as the development of cavities or cracks at microscopic, mesoscopic and macroscopic levels which results in the deterioration of the mechanical properties of the material [75]. For Ochoa and Reddy [79] the main difficulty in mathematical modeling of damage relates to the different scales involved from the initiation to propagation of damage. First failure always initiates at micro-level and gradually evolves into a macro damage mode [29, 79]. This statement is supported by Kassapoglou [52] who warns for the fact that, even though desirable, analysis on events taking place at the micro-level is extremely complex to perform, instead focus should be redirected to ply-level scale (mesolevel). Nevertheless, disregarding the micro-scale events is neglecting the physical phenomenon of damage initiation, itself. In practice, FRP laminates are idealized as a homogenized orthotropic material, which leads to the loss of micro physical and mechanical information that will detrimentally affect the progressive damage analysis [108].

Catastrophic failure of a composite structure usually takes place due to propagation or accumulation of damage as the load is increased, meaning that the load at which the structure ultimately fails hardly corresponds to the first ply failure load [92]. The following stress-strain curve shows first ply failure and damage propagation events, stages 2 and 3, respectively (figure 2.7).

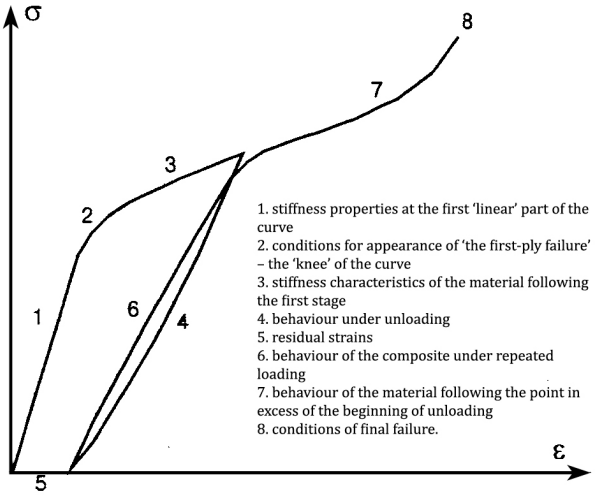

Figure 2.7: Stress-strain curve of an angle-ply composite under loading, unloading and repeated loading. (Reproduced from [120], copyright Elsevier, 2004).

2.2.1. Progressive damage analysis methodology

Typically, researchers follow two approaches in PDA, either analytical (*i.e.*, by means of closed-form solutions) or numerical (*i.e.*, by means of Finite Element Analysis [FEA] solutions). Analytical computations of the stresses and displacements near to the crack tip are only feasible for simple problems. By contrast, for most of real engineering problems which comprise complex geometries, numerical solutions using FEM are required [28, 46]. Leone *et al.* [58] indicate that verification and validation are critical tasks for the development of PDA using FEM. Verification assesses whether the model results are consistent with the fundamental concepts and assumptions of the model under evaluation, by other words, it checks if the model meets its specifications. Validation, by other hand, assesses whether the model accurately represents the physics of the problem when compared to experimental data *i.e.*, whether it fulfills its intended purpose.

Within the paradigm of a numerical approach, Puck and Schürmann [84] identify four fundamental constituent elements for PDA in composites:

1. analysis of strains and stresses ply-by-ply;
2. lamina's fracture criteria;
3. degradation models to include the effects of partial damage, which often does not lead to ultimate failure of the laminate;
4. a routine that simulates the progressive fracture process by applying the above sequences iteratively.

This approach is generally corroborated in the review article conducted by Garnich and Akula [30] and in the extensive NASA report authored by Sleight [92], whereupon the author states that initial lamina failure and respective failure mode can be predicted by applying an appropriate failure criteria. For the subsequent failure prediction (*i.e.*, after damage initiation), Sleight claims that such analysis requires a deep understanding of the failure modes and of the damage propagation mechanisms captured by a material degradation model that adjusts the material properties of the lamina.

One of the most relevant concluding remarks of the world-wide failure exercise (WWFE) [94] was that most of the performed theories provide accurate predictions of the laminate properties at low strains, up to initial failure. From that point on, damage progresses and large NL effects take place, which are not accurately modeled by state-of-the-art methods.

2.2.2. Damage modeling of composites at various scales

Damage initiation and propagation is composite structures is a multi-scale phenomenon that usually starts with microscale cracking of the matrix, that grow to mesoscale cracks and delaminations with further load increase, eventually culminating in macrocracks and fiber failure [29]. In the same manner, the scale of spacial resolution in modeling composites can be discretized in three levels: micro, meso, macro, as shown in figure 2.8.

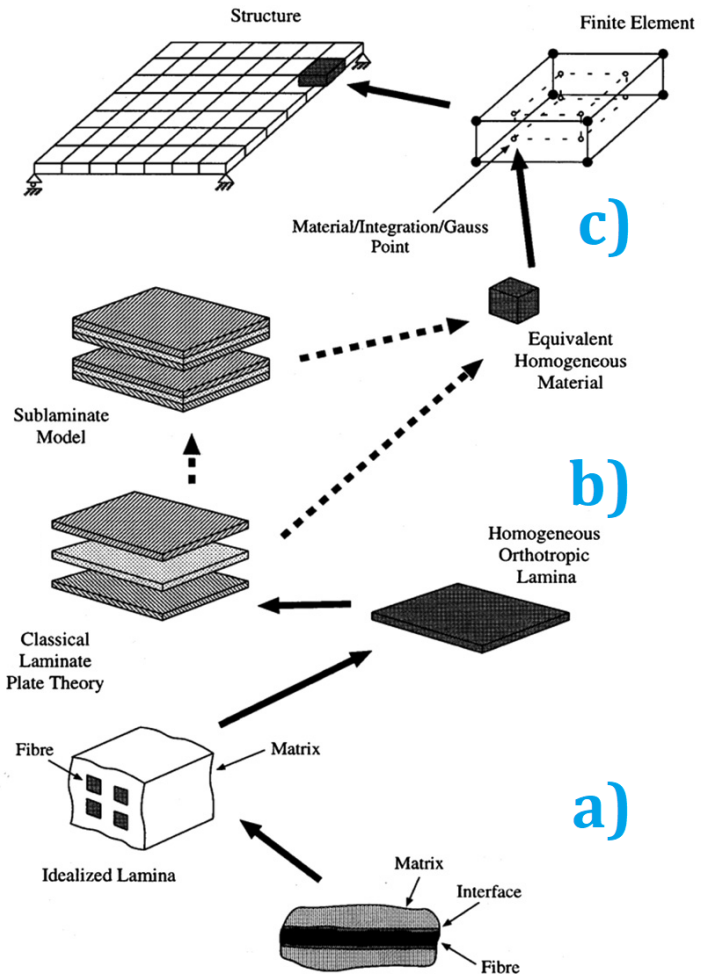

Figure 2.8: Illustration of different modeling approaches of composite materials at the a) microscale, b) mesoscale and c) macroscale. (Reproduced from [86], copyright Elsevier, 2018).

2.2.2.1. Microscale - representative volume element

Microscale models treat both phases of the composite material separately. In such approach, the interaction between the fibers and the matrix is analysed. The 'building block' of this approach consists of fibers in the middle surrounded by matrix material.

While these models have proven successful in predicting the elastic properties of the undamaged material and onset of damage, they presented issues with capturing the evolution of damage. Furthermore, these models proven unable to extrapolate the localized damage to the whole composite structure [86].

2.2.2.2. Mesoscale - ply-based modeling

Modeling composites at the ply-level has been the most popular and extensively applied approach for studying the damage behavior of such structures. The 'building block' of this approach is each lamina that is defined by its homogeneous equivalent properties, typically the engineering constants (which are the required material inputs), that are extracted from experimental tests on UD laminates. The layers are commonly assumed to be perfectly bonded unless interface elements (such as cohesive elements) are used to model interlaminar failure [86].

Ply-based models rely on the assumption that the structural behavior of each ply is independent of its neighbors, thus the interaction of failure mechanisms is typically neglected [29]. Despite its popularity and decent predictive capacity, mesoscale models are usually computationally expensive.

In the framework of mesoscale modeling, appendix F describes and derives the constitutive relations of multi-directional laminates.

2.2.2.3. Macroscale modeling

Forghani *et al.* [29] argue that macroscale models are the only viable and practical approach for simulation of large-scale structures. Even though these models are not focused nor capable of predicting the details of damage events in the layers, they were conceived to predict, in a smeared manner, the overall NL response of the laminate or the structure.

The 'building block' of this approach is the sublaminate of the composite structure.

The driven issues with this approach are the calibration of the macroscopic material properties (recall that the representative volume is the sublaminate) and required level of discretization.

2.2.2.4. Multiscale modeling

Combining the potentials of the analysed approaches by modeling the behavior of composite structures at different scales is the main idea of multiscale modeling. Multiscale models subdivide in two groups: hierarchical and concurrent.

Hierarchical models transfer the predicted global elastic response from the micro-level to the macro-level, meaning that the macroscopic behavior is controlled by the underlying constitutive

relations [86]. Yet, due to homogenization, this approach is unable to predict damage and failure in terms of fracture energy and size effect [29].

By contrast, concurrent multiscale models selectively employ both scales simultaneously. In undamaged areas, the homogenized macromodel is used, while in damaged regions the resolution is increased and the analysis is done under the framework of meso-micro scale.

Even though multiscale failure analysis models are desirable [108], the implementation of such frameworks is limited due to its inherent complexity and immense computational cost. For this reason, researchers and engineers usually target one of the mentioned scales to study the damage behavior and structural response of composite structures [29, 86].

2.2.3. Failure mechanisms in composites

In order to properly analyze progressive damage in composites, it is crucial to characterize the failure modes. Unlike isotropic materials, FRP laminated materials show a panoply of failure mechanisms, which might take place within a ply (intralaminar failure) or between plies (interlaminar failure) [80, 109].

Due to the fact that FRP composites consist of very dissimilar phases (stiff elastic brittle fibers and a compliant yielding matrix), damage takes place according to different damage mechanisms [42, 52]. These may include: matrix cracking, fiber micro-buckling, fiber-matrix debonding, delamination, fiber breakage, or any combination of all these mechanisms [2, 53, 87], as figure 2.9 shows.

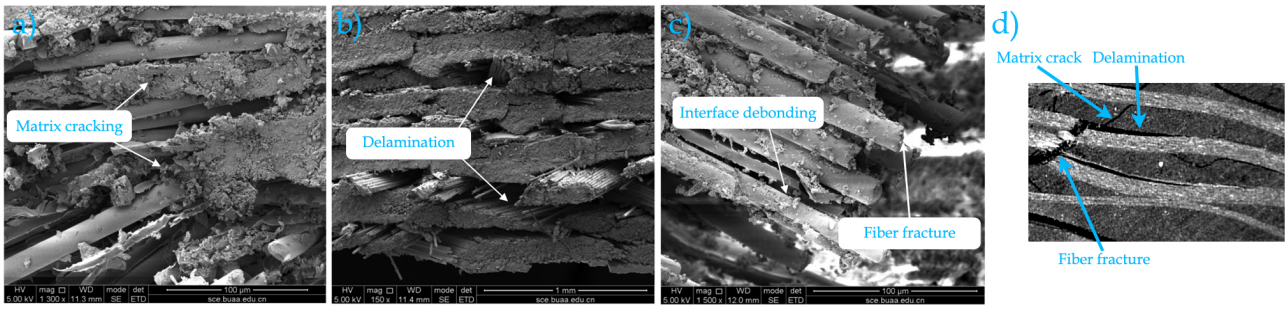

Figure 2.9: Scanning Electron Microscope (SEM) images of damaged E-glass/epoxy multiaxial specimens after impact showing: a) matrix cracks (1300x); b) delaminations (150x); c) interface debonding and fiber fractures (1500x). (Reproduced from [60], copyright TU Delft, 2015). d) Photograph of damaged carbon fiber woven composite showing different failure mechanisms. (Adapted from [18]).

In this regard, Kassapoglou [51] states that, due to the fact that the matrix has much lower strength than the fibers, usually damage starts in form of matrix cracks transverse to the primary load direction, which may multiply, grow and coalesce into delaminations for increased loads. Moreover, local stress concentrations may lead to fiber-matrix (interface) debonding. Further load increase leads to some fibers to break. The load is redistributed throughout the remaining load-carrying capable material until the laminate has no significant residual strength left, ultimately leading to catastrophic failure. Therefore, these different damage mechanisms are able to interact with each other [see figure 2.9 d)], affecting the local mechanical properties of the laminate and consequently leading to a significant reduction of the structure load-carrying capability [87]. The occurrence of these failure modes depends on

the constituent properties, the lamination sequence and loading conditions [30].

In the failure model for FRP under inplane and three-dimensional stress states proposed by Pinho *et al.* [81], five main failure modes of laminated FRP composites were identified and characterized:

2.2.3.1. Fiber Tensile Failure (FFT)

Considering the fibers' high stiffness and strength and the fact that the structure is usually not able to redistribute the load, large amounts of energy are released in a short time period, causing a catastrophic failure [81].

2.2.3.2. Fiber Compression Failure (FFC)

Once again and even though the laminate might experience uniaxial compression, this failure mode is mostly affected by matrix shear behavior, voids and fiber misalignment. Such imperfections usually lead to localized damage modes such as: fiber micro-buckling, matrix shear failure or fiber breakage. As an observable result, kink bands can be easily identified at the micro-scale as shown in appendix G.1 - figure P.12. [81].

2.2.3.3. Matrix Tensile Failure (MFT)

This failure mode is characterized by the fracture plane being usually perpendicular to the load direction (transverse matrix cracking). The strength of this failure mode is greatly affected by structural properties of the surrounding laminae, phenomenon designated by the authors as in-situ effects (see subsection 2.2.4) [81].

2.2.3.4. Matrix Compression Failure (MFC)

Due to the fact that the failure occurs in a given plane angle, most likely not aligned with the load direction, indicates a shear dominant nature of the process [81]. When the crack occurs along the fiber direction, it is called a splitting crack.

2.2.3.5. Delamination

Kassapoglou [52] defines delamination in a laminate as any separation between two adjacent plies. This damage mode is caused by high interlaminar stresses, typically in association with low out-of plane strength[8] [113]. Once delaminated, a composite structure experience a serious reduction in its material properties, particularly in its bending stiffness [81]. Besides degrading the structural properties of composite materials, delaminations are difficult to detect by traditional non-destructive inspection techniques [14].

For both quasi-static and fatigue loading cases, delaminations are a critical damage mode. In quasi-static condition, crack propagates under single fracture modes when the strain energy release rate equals the interlaminar fracture toughness [107]. Even though cyclic loading

[8]Generically, out-of-plane properties are dominated by the matrix properties in the light of the fibers only provide reinforcement in the plane of the laminate.

conditions are beyond the scope of this work, it deserves mention that under these loading conditions, delaminations may grow up to a critical size for load levels well below the ultimate load [14].

Delaminations are driven by through-thickness stresses that exceed the strength of the thin matrix layer between plies [52]. The development of these interlaminar stresses may have five causes [52, 104, 113]:

- **Out-of-plane loading**: the applied load direction has a projected component that is perpendicular to the laminate plane. Lug fittings and rib-to-skin joints [see appendix G.2 - figures P.13 a) and b), respectively] are a paradigmatic example of this failure cause;
- **Structure geometry**: a) tapered laminates generate shear and normal out-of-plane stresses by diffusing the load throughout the changing thickness [see appendix G.2 - figure P.13 c)]; b) curved laminates also originate interlaminar normal stresses when induced moments tend to reduce the curvature. The associated issues become more significant when the ratio thickness to radius increases [see appendix G.2 - figure P.13 d)]; c) lastly, geometries with load path eccentricity induce peel stresses on the adhesive and through-thickness adherend interlaminar stresses, which for the purposes of this thesis is the most significant case [28, 113].
- **Localized interlaminar stresses**: singularities arise at geometrical or material sharp discontinuities where the stresses, theoretically, become infinite. The failure progresses if there is sufficient energy involved driving the propagation process. Classical examples are: cracks, discontinuous plies, ply drops and free edges [see appendix G.2 - figures P.13 e) and f), respectively].
- **Impact**: delamination is a critical damage mode under impact loading [113] that might take place during manufacturing (*e.g.*, bridging of plies), service (*e.g.*, runaway debris and hail damage) or maintenance (*e.g.*, tool dropping) [28, 52]. It can be particularly deceitful for low speed-high mass impacts where almost no evidence of damage can be found on the surface, while inside the laminate matrix cracks and delaminations may be found. Whereas this type of damage has relatively small influence on residual tensile strength [113], it can reduce up to 60% the compression and shear strength [52].
- **Temperature and moisture effects**: the residual stresses originated due to the mismatch between the matrix and fiber thermal expansion coefficients, during the curing process can lead to delaminations [104].

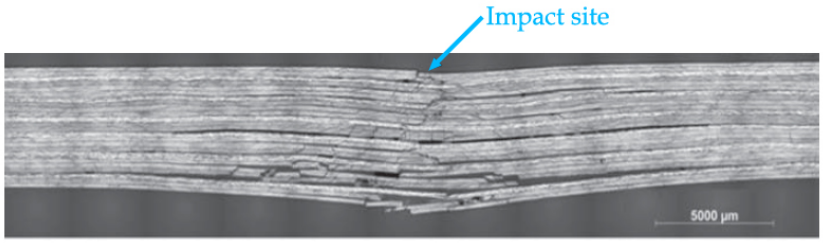

Figure 2.10: Section cut showing the damage created in a quasi-isotropic laminate after 25J impact. (Reproduced from [52], copyright Wiley, 2015).

2.2.4. In-situ strength properties

2.2.4.1. Background theory

Inpired by Dvorak and Laws theory [26, 27], Camanho *et al.* [13] suggest that in order to predict matrix cracking in a laminate subjected to transverse tensile stresses and in-plane shear, the failure criterion should account for in-situ effects.

Figure 2.11 shows how Dvorak and Laws theory (solid line) correlates to experimental data (markers) for different laminates. The thicker UD laminate $[90]_{8s}$ proved to be the weakest, with a lamina strength lower that the UD strength value. However, for a inner 90°ply thickness of $0.125mm$ in the $[0/90_n/0]$ laminate, its strength value is more than the double of the UD strength. This strongly suggests that thin plies are stronger than thick UD laminates.

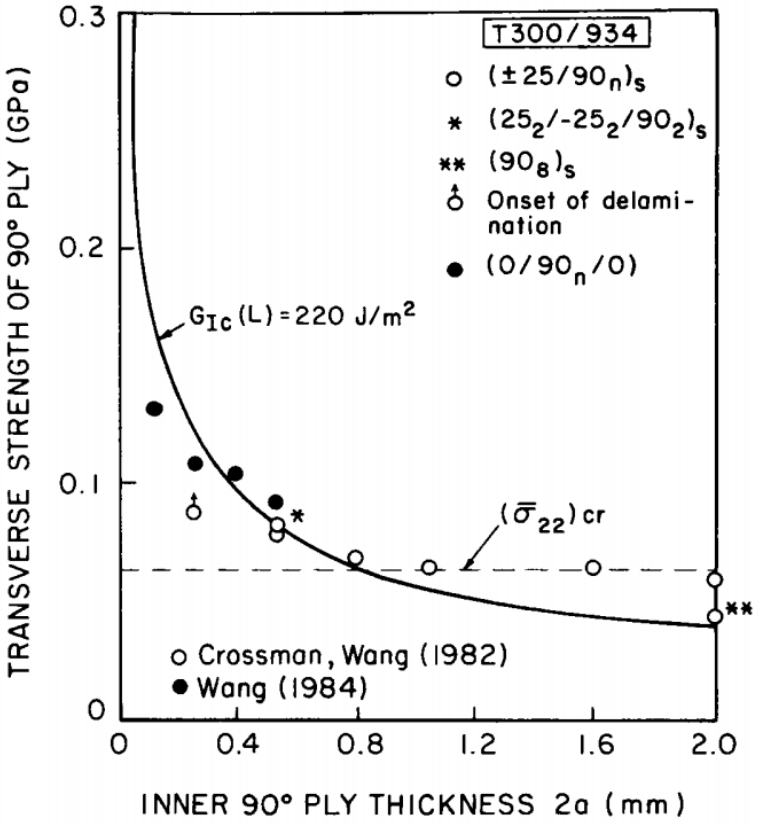

Figure 2.11: Transverse strength of the 90°oriented ply in multidirectional laminates with different numbers of 90°laminae. The dashed line represents the UD strength value. The solid line represents Dvorak and Laws prediction. (Reproduced from [26], copyright Wiley, 1987).

2.2.4.2. In-situ fundamentals

The latter labeled in-situ effect is characterized by higher transverse tensile and shear strengths of a lamina when it is constrained by other laminae with different orientations in a multi-directional laminate, when compared to the strength of the same lamina in a UD laminate [13]. Pinho *et al.* [81] note that this in-situ strength depends not only on the location and orientation of the constraining plies but also the number of clustered plies together. These two last factors can be simply seen as the ply thickness since that, same oriented plies clustered together are in fact a single thicker ply that is constrained by differently oriented plies.

Considering the dependence of these in-situ strengths on factors such as ply thickness and location, Pinho *et al.* [82] emphasize that the foundation for the 'strength enhancement' is structural rather than material.

The authors claim that under the same stress state, the conditions for micro-crack propagation are much more propitious for an UD laminate than for a thin ply in a multi-directional laminate neighbored by different orientations laminae. This stems from the fact that the thickness of the ply and the presence of surrounding plies change the boundary conditions of the fracture mechanics problem for crack propagation [82]. In fact, an UD laminate has a multitude of potential transverse (1-3) fracture planes (parallel to the fibers), where a crack once created can easily propagate in a transverse direction. This statement is supported by Kassapoglou [52], who argues that cracks in FRP grow following an irregular path, which is defined and constrained by the fibers in the adjacent plies that are in different orientations, acting as crack stoppers.

In-situ strength values have been determined by experimental and analytical methods, Yet, in the past, both approaches present accuracy issues in predicting the in-situ shear strength, given the highly NL shear behavior of FRP [13]. Hence, the referenced article proposed an analytical closed-form model that accurately predicts the in-situ shear strength as function of ply thickness and location.

2.2.4.3. Ply classification and in-situ equations

Using fracture mechanics models Camanho *et al.* [13] derived the equations used to calculate the in-situ strength properties for:

- Inner thick plies embedded in a multidirectional laminate where a slit crack firstly propagates in the transverse direction and then in the longitudinal direction;
- Inner thin plies embedded in a multidirectional laminate where a slit crack propagates in the longitudinal direction (the initial crack extends throughout the whole ply thickness).
- Outer thin plies are one-side unconstrained given that they are located on the surface on the laminate. Because of this, the energy release rate is amplified, thus decreasing the in-situ strength.

A ply that is embedded between two plies (inner ply) present greater in-situ strengths than an unbounded outer ply which is more likely to develop surface cracks [91].

The transverse tensile, transverse compressive and in-plane shear strengths are calculated using elastic properties (E_1, E_2 and G_{12}), the fracture toughness (G_{Ic} and G_{IIc}) and plastic flow parameters (shear incremental stiffness under plastic flow K_p and shear stress at which the plastic flow is activated S_{LP}). The diagram contained in figure 2.12 shows in a systematic manner the in-situ property equations. Further details can be clarified in the original article [13], for an extensive clarification and in [91] for a summarized description of the theory.

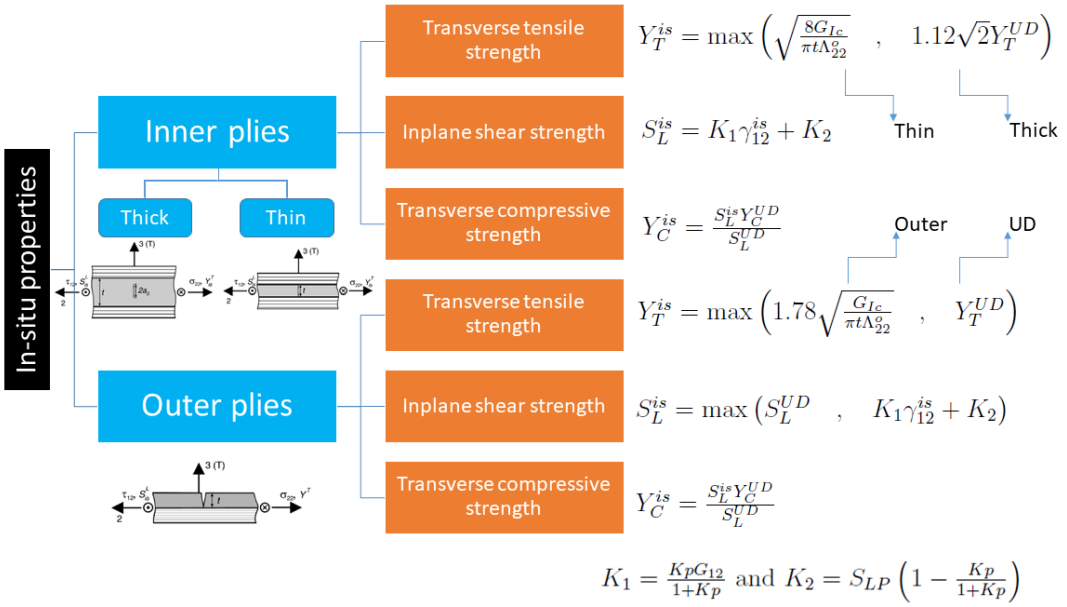

Figure 2.12: Ply classification and related in-situ strength equations.

2.2.5. Continuum damage models (CDM)

The main idea of Continuum Damage Models (CDMs) is to substitute the mechanical behavior of the damaged material in the Fracture Process Zone (FPZ) by associating the implicit failure mechanisms with their overall effects on the elastic properties of the material [86]. In other words, the FPZ is modeled in a smeared manner by degrading the apparent stiffness of the material, *i.e.*, softening the material, in that region [29]. Dávila [21] asserts that the goal of CDM is to develop a framework that accurately describes the material response caused by a progressive damage state . Thus, progressive failure analysis greatly depends on the failure (initiation) criteria and the subsequent material property degradation models [30]. These are the two main ingredients that compose a CDM that is used for PDA of FRP.

These models use the local stress-strain state of an homogenized material and compare it to material allowables by means of a given failure criteria to determine the occurrence of damage initiation. From this point on, CDMs capture the damage propagation by means of a damage state variable that selectively reduces the mechanical properties of the material. Even though these CDMs do not represent the physical damage phenomenon at the microlevel, they provide an appealing and convenient framework for implementation in FEA software [86].

This approach is particularly appealing to simulate intralaminar damage in view of the fact that for multidirectional laminates, this type of damage forms in a more diffused and smeared pattern [29].

2.2.6. Damage initiation criteria

Essentially, damage initiation criteria is materialized by mathematical equations that predict the occurrence of material damage and the associated stress state [30].

Since 1965, when Tsai[9] derived the strength characteristics of anisotropic materials from a generalized distortional work criterion [106], continuous efforts have been done in developing failure criteria to accurately predict the initial failure in UD FRP composite laminates [21, 99]. Presently, most of the damage initiation models are stress/strain based and there is no single theory that accurately predicts failure mode and correspondent load for all loading conditions and for all types of FRP [21].

The main failure criteria can be categorized in three groups [99]:

- Limit criteria: Failure load and mode are predicted by comparing lamina stresses or strains with corresponding strengths separately, *i.e.*, no interaction is considered. Examples are: maximum stress and maximum strain.
- Interactive criteria: Failure load is predicted by using a single quadratic or higher order polynomial equation involving all stress (or strain) components. Failure mode is indirectly determined by comparing stress (or strain) ratios. Examples are: Hill, Tsai-Hill, Tsai-Wu, Hoffman and Yamada-Sun.
- Separate mode criteria: These criteria separates matrix failure criterion from fiber failure criterion. Equations may depend on one or more stress components (may combine normal stresses with shear); in the case of multiple stress components, failure mode is determined by comparing stress (or strain) ratios, as is done with interactive criteria. Examples are: Hashin-Rotem, and Hashin.

Damage initiation is assumed when for a given failure index is equal to one.

2.2.6.1. Hashin failure criteria: a heuristic 3D separate mode failure model

Hashin's three-dimensional failure criteria [42] predict onset and type of damage in a composite lamina [12]. These criteria are expressed in terms of quadratic stress polynomials. This quadratic behavior is chosen, as explained by the author, based on curve fitting considerations alone. Hence, the model is heuristically rather than physically grounded [109].

As mentioned above, due to the fact that a composite material comprises two dissimilar phases, failure mechanisms should be differentiated. Hence, in the author's first effort to establish a failure criteria for FRP, in 1973, Hashin and Rotem [43] distinguished between fiber- and matrix-dominated failure mechanisms. Later, in 1980, Hashin [42] further subdivided each failure mode into tensile and compressive modes [103]. Accordingly, the outcome was established in a piece-wise form, containing four equations that defined the three-dimensional failure criteria for UD fiber composites (see appendix H.1).

Failure predictions of boron-epoxy and glass-epoxy off-axis specimens under tension, based on Hashin's failure criteria showed very good agreement with experimental results (see appendix H.2 - figure P.14).

By contrast, Dávila and Camanho [21] highlight the fact that in the past decade, several studies indicated that the stress interaction proposed by Hashin not always fit the experimental results, particularly in the compressive criteria. The authors note that for a moderate transverse compression ($\sigma_2 < 0$) the apparent shear strength[10] is improved, which is not ac-

[9] Supported by Hill's previous work over the yielding and plastic flow of anisotropic metal, in 1943.

[10] The shear behavior depends on in-plane transverse stress, which in practical terms means that the shear response gets 'stiffer' when compressive transverse stresses are acting [81].

counted in the present criteria but is already taken into consideration in Puck's failure criteria (presented below). Another unaccounted effect is the induced in-plane shear during fiber compression, which significantly reduces the effective compressive strength of the ply [21]. Additionally, Hashin's model is incapable to predict uniaxial stress-strain curves for large strains. Hereupon, the performance of this model in the WWFE-II was ranked among those requiring further development [48].

Even though its clear limitations and the fact that it does not constitute a state-of-the-art damage initiation model, it is undeniable that it established a benchmark for 3D separate mode failure criteria. After more than 35 years since its development, Hashin failure criteria is still being used[11], studied [25] and modified [33].

2.2.6.2. Puck and Schürmann failure criteria: a dominantly phenomenological model with physical considerations failure model

Puck and Schürmann [84] based the description of damage and fracture behavior on phenomenological models but simultaneously placed on physical basis. Their model is not only capable to predict stress levels that lead to crack initiation in a lamina when subjected to a biaxial stress state [93] but also to indicate the direction of the cracks.

Essentially, Puck's failure criteria is divided into two modes: 1) fiber failure (FF), which is further subdivided into two failure modes: tensile and compression (kinking) and 2) inter-fiber failure (IFF) which contains three failure modes, A, B and C.

A note should be done regarding the mismatch between the nomenclature used by the authors and in the context of this work for the failure indices. Puck and Schürmann labeled the failure indices as stress exposure factor in the fibers f_{E_FF} and inter-fibers f_{E_IFF}. In this thesis the former variable corresponds to the fiber failure indices (discriminated by mode, tensile FFT and compressive FFC) and the latter relates to the matrix failure indices (discriminated by mode, tensile MFT and compressive MFC).

Fiber failure (FF)

For a 3D state case, Puck and Schürmann define a fiber failure criterion similar to the maximum stress criterion but extended to the fibers:

$$\sigma_{f1} = E_{f1}\varepsilon_1 + \nu_{f12} m_{\sigma f}(\sigma_2 + \sigma_3)$$

Where σ_{1f} is the stress in the fibers; $m_{\sigma f}$ is a mean magnification factor of the transverse stress for the fibers ($m_{\sigma f} \approx 1.1$ for carbon fibers) and ν_{f12} is the Poisson ration of the fibers in the 2-direction caused by an applied stress in the 1-direction.

Recalling that the strain: $\varepsilon_1 = \frac{\sigma_1}{E_1} - \frac{\nu_{12}}{E_1}(\sigma_2 + \sigma_3)$ and that at tensile failure $\sigma_{f1} = X_f^T = \frac{E_{f1}}{E_1} X^T$, where X_f^T is the tensile strength of the fibers in the longitudinal direction and X^T is the tensile strength of the UD material in the longitudinal direction:

[11] Hashin damage model is built into *ABAQUS®*.

$$\frac{E_{f1}}{E_1}X^T = \frac{\sigma_1 E_{f1}}{E_1} - \frac{\nu_{12}E_{f1}}{E_1}(\sigma_2+\sigma_3) + \nu_{f12}m_{\sigma f}(\sigma_2+\sigma_3)$$

Dividing everything by $\frac{E_{f1}}{E_1}X^T$:

$$f_{E\_FF} \equiv FFT_{Puck} = \frac{\sigma_1}{X^T} - \frac{\nu_{12}}{X^T}(\sigma_2+\sigma_3) + \frac{E_1}{E_{f1}X^T}\nu_{f12}m_{\sigma f}(\sigma_2+\sigma_3) \tag{2.1}$$

The authors did not include complex fiber compressive failure modes such as fiber kinking, instead, the logic used for the fiber tensile mode was simply extended to the compressive mode, using the compressive strength of the UD material in the longitudinal direction X^C instead of X^T, as follows:

$$f_{E\_FF} \equiv FFC_{Puck} = -\left(\frac{\sigma_1}{X^C} - \frac{\nu_{12}}{X^C}(\sigma_2+\sigma_3) + \frac{E_1}{E_{f1}X^C}\nu_{f12}m_{\sigma f}(\sigma_2+\sigma_3)\right) \tag{2.2}$$

Note that for the compressive mode, a minus sign was added due to the fact that all strength values are considered positive, otherwise, the failure index would be negative.

Inter Fiber failure (IFF)

As for the IFF condition, it is based on Mohr-Coulomb fracture hypothesis, which states that fracture is exclusively created by the stresses which act on the fracture plane [84]. In the case of IFF on an inclined plane (at an angle θ_{fp}) parallel to the fibers are: the normal stress σ_n, the transverse-transverse shear stress τ_{nt} and the transverse-longitudinal shear stress τ_{nl} (see figure 2.13).

While a transverse normal tensile stress $\sigma_n > 0$ promotes fracture (mode A), a compressive $\sigma_n < 0$ impedes shear fracture (modes B and C). This is a major improvement with respect to the precedent criteria. Puck and Schürmann included in their IFF condition the benign contribution of compressive normal stresses which add fracture resistance (it can be seen as a supplementary internal friction).

Puck and Schürmann, first developed their physically based phenomenological model [84] for the particular case of a composite material under plane stress conditions. Latter, the same authors generalized the failure criteria to a 3D stress state [85]. Considering that latter is more general, it will be presented first.

Inter Fiber failure (IFF) - 3D stress state

For a generalized 3D stress state of an UD composite element rotated by an angle θ_{fp} from x_2 to the x_n direction[12], Puck and Schürmann, based on the aforementioned Mohr-Coulomb fracture hypothesis, developed the following Inter Fiber failure (IFF) criteria:

[12] x_n is the normal direction to the fracture plane (figure 2.13).

- For a positive, *i.e.*, tensile, normal stress acting on an arbitrary sectional plane with an inclination angle θ, $\sigma_n(\theta) \geq 0$:

$$f_{E\_IFF}(\theta) \equiv MFT_{Puck}(\theta) =$$

$$= \sqrt{\left[\left(\frac{1}{Y^T} - \frac{p^T_{\perp\psi}}{R^A_{\perp\psi}}\right)\sigma_n(\theta)\right]^2 + \left(\frac{\tau_{nt}(\theta)}{R^A_{\perp\perp}}\right)^2 + \left(\frac{\tau_{nl}(\theta)}{S^L}\right)^2} + \frac{p^T_{\perp\psi}}{R^A_{\perp\psi}}\sigma_n(\theta) \tag{2.3}$$

- For a negative, *i.e.*, compressive mode, $\sigma_n(\theta) < 0$:

$$f_{E\_IFF}(\theta) \equiv MFC_{Puck}(\theta) =$$

$$= \sqrt{\left[\frac{p^C_{\perp\psi}}{R^A_{\perp\psi}}\sigma_n(\theta)\right]^2 + \left(\frac{\tau_{nt}(\theta)}{R^A_{\perp\perp}}\right)^2 + \left(\frac{\tau_{nl}(\theta)}{S^L}\right)^2} + \frac{p^C_{\perp\psi}}{R^A_{\perp\psi}}\sigma_n(\theta) \tag{2.4}$$

The stresses acting on the potential fracture plane σ_n, τ_{nl} and τ_{nt} are trivially obtained through a θ rotation along the 1-axis, as shown in figure 2.13 (the transformation equations can be found in appendix H.3). $R^A_{\perp\perp}$ is the fracture resistance of the action plane against its fracture due to transverse/transverse shear stressing and it is given by: $R^A_{\perp\perp} = Y^C/[2(1+p^C_{\perp\perp})]$, where $p^C_{\perp\perp}$ is the slope of (σ_n, τ_{nt}) fracture envelope for $\sigma_n \leq 0$ at $\sigma_n = 0$. Parameters $\frac{p^T_{\perp\psi}}{R^A_{\perp\psi}}$ and $\frac{p^C_{\perp\psi}}{R^A_{\perp\psi}}$ are slope over resistance rotated parameters (for more information, refer to the original article [85]).

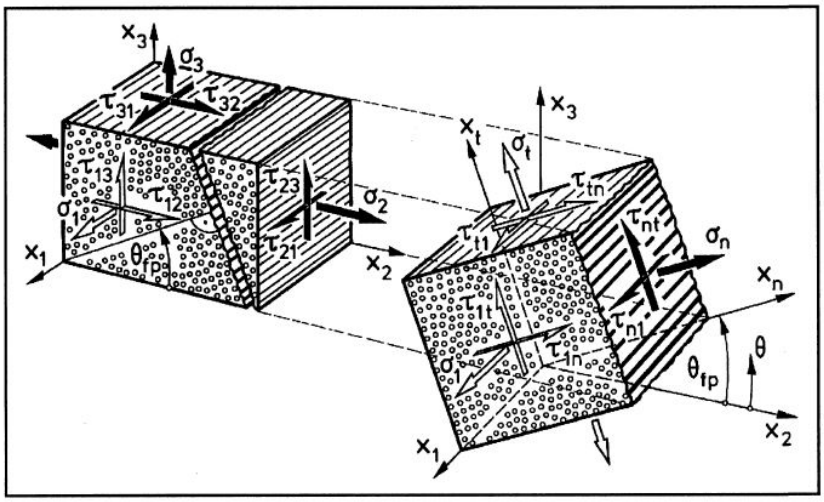

Figure 2.13: Three-dimensional stresses on a UD composite element. (x_1, x_2, x_3) coordinate system is fixed to fiber direction (x_1), laminate mid-surface (x_2) and thickness direction (x_3). The (x_l, x_n, x_t) coordinate system is rotated by an angle θ_{fp} from the x_2 direction to the x_n direction which is normal to the fracture plane. The IFF is only influenced by the three stresses σ_n, τ_{nt}, τ_{nl}. (Reproduced from [84], copyright Elsevier, 1998).

The failure indices $MFT_{Puck}(\theta)$ and $MFC_{Puck}(\theta)$ are obtained through iteration by finding the angle $-90^\circ \leq \theta \leq +90^\circ$ that maximizes these quantities. Based on Mohr-Coulomb fracture hypothesis, Puck and Schürmann labeled the correspondent angle as the fracture plane angle (θ_{fp}). A possible pseudo-algorithm formulation would be:

$$\textit{find}\ \theta_{fp} \quad | \quad max[MFT_{Puck}(\theta)] \quad for \quad \sigma_n \geq 0$$

$$find\ \theta_{fp} \quad | \quad max[MFC_{Puck}(\theta)] \quad for \quad \sigma_n < 0$$

For an IFF, modes B and C imply a compressive normal stress in the fracture plane ($\sigma_n < 0$). The difference relies on the angle of the fracture plane: $\theta_{fp} = 0°$ for mode B and $\theta_{fp} \neq 0°$ for mode C.

Inter Fiber failure (IFF) - plane stress state

For a state of plane stress($\sigma_1, \sigma_2, \tau_{12}$), the condition that differentiates modes B and C can be formulated in the following manner: if the ratio between the modulus of the compressive normal stress in the 2-direction σ_2 and the shear stress τ_{21} is smaller than the ratio between the fracture resistance of the action plane against its fracture due to transverse/transverse shear stressing $R^A_{\perp\perp}$ and the shear stress at the 'turning point' of the (σ_2,τ_{21}) fracture curve (see appendices H.4 and H.5 - figures P.15 and P.16, respectively), then mode B is valid. Otherwise, mode C takes place.

Furthermore, for both mode A and B, the angle of the fracture plane is equal to zero, *i.e.*, fracture plane is parallel to 1-3 plane, whereas for mode C it depends on material properties and the stress level.

Puck's theory entails a very sophisticated modeling of IFF, through the introduction of competing ply cracking modes and fracture plane orientation. Owing to theory's solidity, accurate and reliable predictions are verified, including: theoretical failure envelopes for the UD lamina, final failure envelopes and stress–strain curves for the multidirectional laminates that show very good agreement with the experimental results [93].

Nonetheless, the Puck's model underestimates final failure strains and failure envelopes, where large NL deformations are present. Another drawback of Puck's phenomenological approach is the inclusion of several non-physical material parameters that may be difficult to quantify without considerable experience with a particular material system [21].

2.2.6.3. LaRC03, LaRC04 and LaRC05: three improved physically based failure models

In an effort to develop a damage model for FRP composites containing additional physical features, three successively improved models were created: 1) LaRC03 failure criteria, a six physically-based 2D intralaminar failure criteria; 2) LaRC04 failure criteria, a 3D extended version of its precedent and 3) LaRC05 failure criteria, an improved failure criteria based on a novel NL constitutive model.

In 2003, Dávila and Camanho [21] based on Dvorak's fracture mechanics analysis of cracked plies [26] and Puck's fracture plane concept [84] described an original set of six failure criteria for FRP laminates and named it LaRC03. Unlike most of damage initiation criteria which are predominately heuristically based, LaRC03 present a solid physical framework [109].

Apart from separating the matrix cracking and fiber failure into tensile and compressive modes, the authors further subdivided the compression cases according to the transverse stress state, as it is summarized in the figure 2.14. The criteria for fiber and matrix compression are based on Mohr-Coulomb effective stresses in interaction with the plane of fracture. Still, with respect to fiber compressive failure, the criteria for fiber kinking is highly dependent on the

misalignment angle. The matrix tensile failure criterion is based on fracture mechanics models of matrix cracks and on related in-situ effects [21].

Based on the results of the proposed criteria, the authors concluded that LaRC03 correlate well with experimental results when it comes to failure load envelops and respective failure mode predictions.

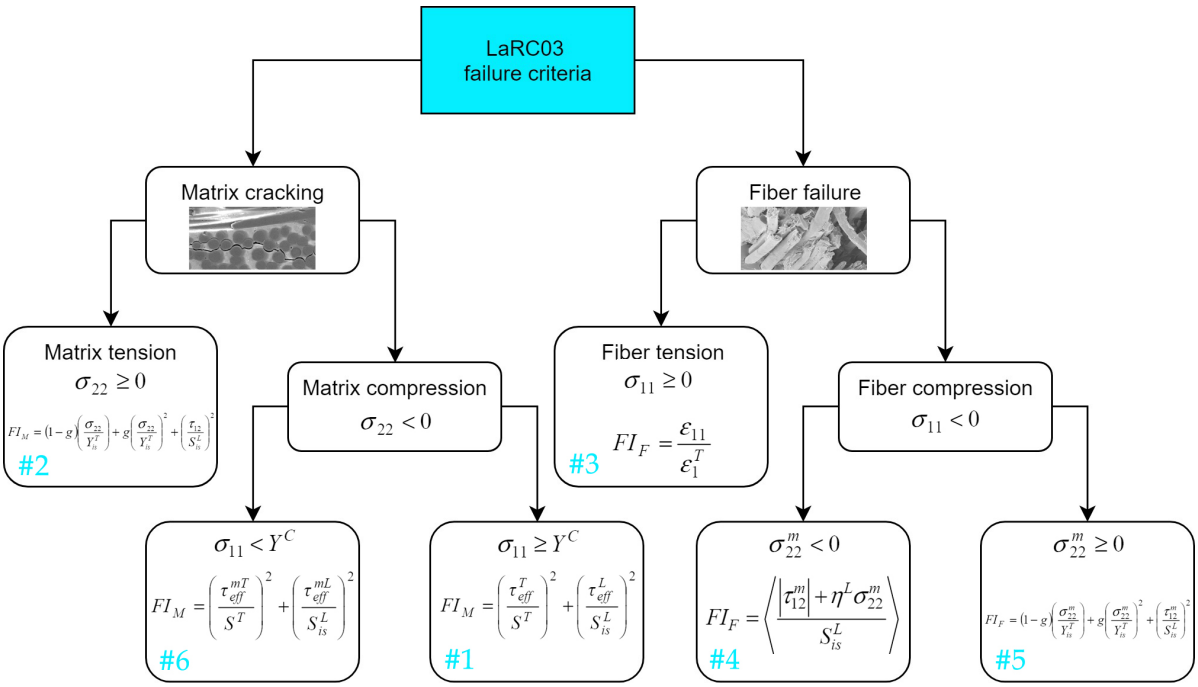

Figure 2.14: Summary of LaRC03 failure criteria (Adapted from [21]).

Two years later, Pinho *et al.* [81] extended LaRC03 failure criteria by generalizing it to a 3D stress state and by incorporating matrix shear non-linearities. This model follows the same physically based approach as its precedent. It also presents the same structure in the sense that it subdivides the matrix and fiber compressive modes according to the transverse stress state.

In spite of the good agreement showed by LaRC04 predictions with respect to experimental data, this model relies on several iterative processes to compute quantities related to the compressive fiber failure, more specifically related to fiber kinking[13], which makes its application computationally expensive.

The updated failure criteria, conveniently named LaRC05 (published in two articles: part A [82] and part B [83]), are founded on a NL pressure-dependent 3D constitutive model, *i.e.*, the yielding response of the resin as well as the effect of the hydrostatic pressure were included in modeling laminated FRP composites subjected to a 3D stress state. The philosophy behind this approach is that failure models and respective criteria should include as much physical phenomena as possible, so that they capture and incorporate the failure processes at micromechanical level, ultimately allowing valid and accurate solutions [82].

[13]Namely the initial misalignment angle and the shear strain in the misalignment frame.

Part B [83] suggests the integration of plasticity theory and some crucial constitutive response features in the 3D stress analysis of UD composites, such as: hydrostatic sensitivity, non-linearity and multi-axial sensitivity.

Similarly to its former models, LaRC05 predicts the failure modes, the fracture plane orientation and the failure load. Moreover, it also accounts for in-situ effects based on fracture mechanics analysis. Yet, it was restructured into three modes failure modes: matrix failure, fiber kinking/splitting and fiber tensile failure.

Owing the inclusion of some assumptions and simplifications, namely in the fiber kinking failure mode, some exhaustive computations of iterative nature of LaRC04 were replaced by closed-form solutions in LaRC05, resulting in a considerable decrease in the associated computational effort.

A summary of the LaRC05 failure criteria is provided:

2.2.6.4. Tensile fiber failure

The FFT index is based on the maximum stress criterion:

$$FI_{FT} \equiv FFT_{LaRC05} = \frac{\sigma_1}{X^T} \tag{2.5}$$

2.2.6.5. Compressive fiber failure - fiber splitting and kinking

Pinho *et al.* [82] describe the compressive fiber failure as fiber splitting or kinking.

According to the authors, it starts with manufacturing defects such as fiber misalignment or for increased compression loads, failure of the neighboring plies resulting in localized high shear stresses which originates fiber splitting. Further load increase generates more bending in the fibers which leads to even more splitting. Finally, the fibers break due to a pernicious combinations of compressive and bending stresses resulting in a kink band [82].

In the model, this differentiation is made based on the magnitude of the longitudinal compressive stress σ_1 with respect to the longitudinal compressive strength value X^C: lower absolute compressive stress values are associated with fiber splitting ($\sigma_1 > -X^C/2$ or in absolute terms $|\sigma_1| < |X^C|/2$), otherwise, fiber kinking is assumed.

The FFC index is calculated based on the following equation:

$$FI_{KINK,SPLIT} \equiv FFC_{LaRC05} = \left(\frac{\tau_{23}^m}{S^T - \eta_T \sigma_2^m}\right)^2 + \left(\frac{\tau_{12}^m}{S^L - \eta_L \sigma_2^m}\right)^2 + \left(\frac{\max(0, \sigma_2^m)}{Y^T}\right)^2 \tag{2.6}$$

Where σ_2^m, τ_{12}^m and τ_{23}^m are the rotated stress components in the misalignment frame; η_L and η_T are the slope coefficients for longitudinal and transverse shear strength, respectively (check the original article [82] for more details regarding the implicit transformations).

2.2.6.6. Matrix failure

Similar to Puck and Schürmann's model, LaRC05 is based on Mohr-Coulomb theory for matrix failure prediction. For both MFT and MFC the suggested failure index equation is:

$$FI_M \equiv MFT_{LaRC05}, MFC_{LaRC05} = \left(\frac{\tau_{nt}}{S^T - \eta_T \sigma_n}\right)^2 + \left(\frac{\tau_{nl}}{S^L - \eta_L \sigma_n}\right)^2 + \left(\frac{\max(0, \sigma_n)}{Y^T}\right)^2 \tag{2.7}$$

Where: σ_n, τ_{nl} and τ_{nt} are the stresses acting on the potential fracture plane. The transformation equations can be found in appendix H.3. The last term only contributes for increasing the failure index value if the normal stress acting on the fracture plane σ_n is tensile, reinforcing the idea that compressive matrix failure delays matrix failure owing to the fact that it tends to close the crack.

This failure criteria show very good agreement with the test cases, earning it a remarkable classification in the WWFE [48] as one of the top performing models in 3D failure analysis. Yet, in order to be a reliable and accurate physically based predictive failure model, it requires extensive characterization of the input material parameters [83].

2.2.7. Material property degradation models

Composite structures have the capability of damage accumulation after damage initiation and before structural collapse [7, 30, 32, 88]. For this reason, the sole use of failure initiation criteria for design purposes results in inaccurate predictions leading to quite conservative design solutions given the considerable residual strength and damaged tolerance that a damaged composite structure exhibits after failure initiates. Thereupon, understanding the NL behavior of quasi-brittle materials due to damage accumulation is paramount, considering that the rate and direction of damage propagation determines the structure's damage tolerance and ultimate failure [64].

Garnich and Akula [30] performed an extensive review on material degradation models for PDA of FRP composites, using the FEM. The authors claim that one of the main challenges in this field is to properly characterize the residual stiffness and strength of the damaged material in a given location. The complexity of modeling PDA in FRP arise from: a) multiple failure modes; b) directionality of failure; c) the interaction between the pristine and the damaged material and d) numerical implementation related issues.

Still in the same article, the researchers classified the studied models as:

- Sudden degradation: all properties are instantaneously reduced to some fraction of the undamaged properties.
- Gradual degradation: one or more properties are reduced in function of other evolving variable, such as strain.

Figure 2.15 clearly schematizes how each approach treats material degradation. While the former group outperforms the latter when it comes to simplicity in the implementation due to its binary nature (the material is either considered undamaged or completely degraded) in characterizing the degraded properties which is translated into computational expediency,

on the other hand, it does not realistically reflect the damage accumulation phenomenon, where the stiffness of the structure changes nonlinearly with damage propagation requiring equilibrium equations to be satisfied at each increment in order to re-establish equilibrium [30].

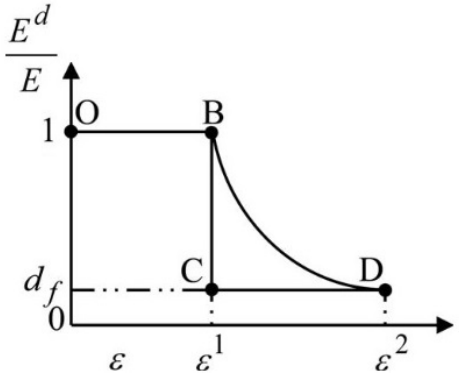

Figure 2.15: Schematic of sudden (path OBCD) and gradual (path OBD) property degradation models. (Reproduced from [30], copyright ASME, 2009).

Given the lack of physical basis and agreement on virtually every material property degradation model resulting in a panoply of different proposals, only three models will be covered in this thesis. Despite the seniority of these models, they created a solid framework on which other authors were inspired to develop further work.

Starting by the classical approach of capturing the effects of damage by reducing the material stiffness by means of a constant internal state variable, Camanho and Matthews [12] proposed a light an easy to implement sudden material degradation model. In the realm of gradual degradation theories, Puck and Schürmann [85] suggest two methods for capturing material degradation that have been recognized as solid, showing good agreement with experimental data [93]. Finally, a linear softening model is suggested as an accurate method in capturing the damage evolution in the adhesive of bonded joints [67].

Within the framework of continuum damage mechanics, the damage state of a material is captured by a damage parameter which, along with the constitutive relations describe the mechanical behavior of the damaged material and the further failure development [30, 75].

Damage in a specimen under uniaxial stress

In order to better understand the physical/mechanical meaning of material damage, the concept of effective stress $\hat{\sigma}$ is introduced through the simplest loading case. Consider a specimen of cross area A, loaded by an applied force F_a, as illustrated in figure 2.16. It is evident that the uniaxial stress is given by:

$$\sigma = \frac{F_a}{A} \tag{2.8}$$

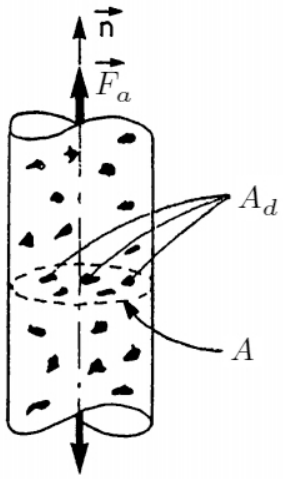

Figure 2.16: 1-D Damaged element. (Reproduced from [57], copyright Springer, 1996).

A bit more subtle to realize is that for a damaged specimen, the effective surface resisting the applied load is the cross-sectional area A minus the cross sectional area of the voids A_d. This means that the effective stress $\hat{\sigma}$ is given by:

$$\hat{\sigma} = \frac{F_a}{(A - A_d)} \tag{2.9}$$

The damage quantity d is defined as the ratio between the cross-sectional area of the voids and the specimen's cross-sectional area[14]:

$$d = \frac{A_d}{A} \tag{2.10}$$

Dividing the numerator and denominator of equation (2.9) by A and inputting this last definition, it simply becomes:

$$\hat{\sigma} = \frac{\frac{F_a}{A}}{\frac{(A-A_d)}{A}} = \frac{\sigma}{1-d} \tag{2.11}$$

For the sake of clarity, the damage parameter ranges from zero to unity, representing, in practical terms the material's damage state:

$$\begin{cases} A_d = 0 \Rightarrow d = 0 \Rightarrow \hat{\sigma} = \sigma & \text{Undamaged material} \\ 0 < A_d < A \Rightarrow 0 < d < 1 \Rightarrow \hat{\sigma} > \sigma & \text{Damaged material} \\ A_d = A \Rightarrow d = 1 \Rightarrow \hat{\sigma} \to \infty & \text{Ultimate failure} \end{cases}$$

Lemaitre [57] uses the strain equivalence principle to define the constitutive behavior of a damaged material. This principle postulates the following:

[14] Matzenmiller *et al.* [69] state that the damage parameter may be seen as the 'loss area'.

> "*Any strain constitutive equation for a damaged material may be derived in the same way as for a virgin material except that the usual stress is replaced by the effective stress.*"

Based on this, the elastic strain ε_e is simply given by:

$$\varepsilon_e = \frac{\hat{\sigma}}{E} = \frac{\sigma}{E(1-d)} \tag{2.12}$$

Hence, the effective elasticity modulus of the damaged material is trivially obtained:

$$\hat{E} = \frac{\sigma}{\varepsilon_e} = E(1-d) \tag{2.13}$$

2.2.7.1. Camanho and Matthews: a sudden method of stiffness reduction

Following a classical approach for modeling the progressive damage of mechanically fastened joints in composite laminates, Camanho and Matthews [12] took into account the effects of damage by selectively and suddenly reducing the engineering constants of the orthotropic material. This stiffness reduction is carried by using an internal state variable d which is multiplied to the initial modulus of the material (E_0 or G_0), when a given failure condition is met.

The following table presents the damage values for each failure mode:

Table 2.2: Constant damage variables of Camanho and Matthews [12] sudden degradation model.

Mode	E_1	E_2	E_3	G_{12}	G_{13}	G_{23}
FFT	0.07	-	-	-	-	-
FFC	0.14	-	-	-	-	-
MFT	-	0.2	-	0.2	-	0.2
MFC	-	0.4	-	0.4	-	0.4

The authors notice that for carbon/epoxy laminates only E_2, G_{12} and G_{23} are considerably affected with increasing crack density [12].

2.2.7.2. Puck and Schürmann material degradation model: two suggested approaches; a predefined degradation law and an iterative method

Puck and Schürmann material degradation model [84, 85] is an extension of the correspondent failure criteria treated in the last subsection 5.6, both composing an integral PDA model.

For this matter, the authors suggest two different methods to degrade the elastic constants:

1. **Predefined Degradation Law (PDL)**: an assumption regarding the function of the degradation parameter η is done, particularly an hyperbolic dependence is adopted:

$$\eta(f_{E\_IFF}) = \frac{1-\eta_r}{1+\beta(f_{E(IFF)}-1)^{\xi}} + \eta_r \tag{2.14}$$

Where η_r is the degradation factor residual value and β and ξ are constants that control the decay rate of the degradation factor. Figure 2.17 shows the hyperbolic variation of η for increasing stress exposure values f_{E_IFF} and the effects of different values for the decay parameters β and ξ. Using this approach implies that the stress exposure factor f_{E_IFF} is free to take any value.

2. **Constant Stress Exposure (CSE)**: this method does not make any assumption regarding the degradation factor behavior. Instead, once damage initiates $f_{E\_IFF} = 1$, the stress exposure factor (authors' nomenclature for failure index) is kept constant at that value and the degradation factor η is found through an iterative process such that the condition $f_{E\_IFF} = 1$ is followed. In practice, when an element reaches a failure index of one (*i.e.* damage initiates), its elastic moduli are degraded making that element bearing less load than it used to be capable of, leading to a load redistributing along the remaining structure.

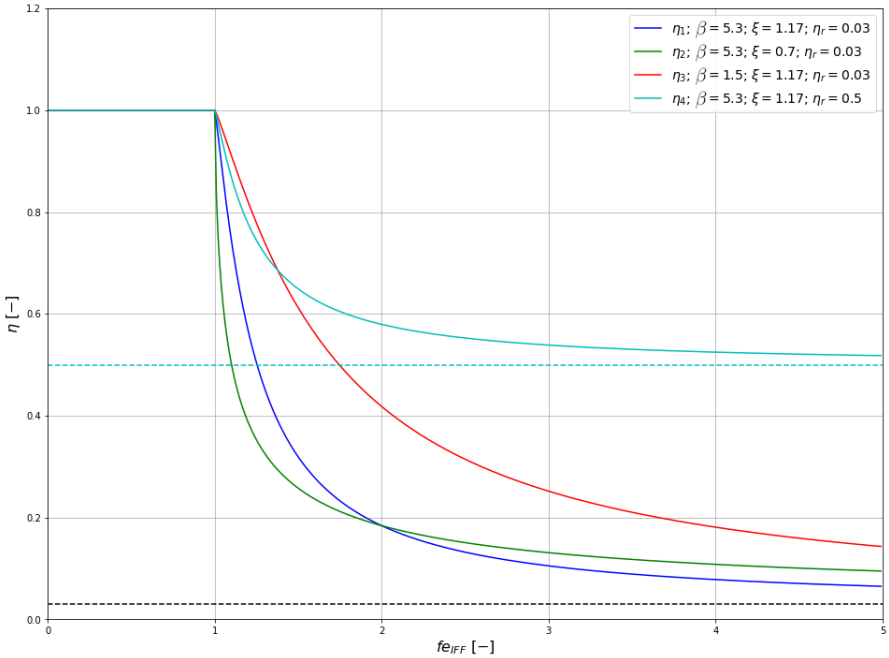

Figure 2.17: Degradation factor hyperbolic variation for increasing stress exposure values for different characteristic parameters β, ξ, and different residual values η_r.

Both methods have advantages and drawbacks. While the second is computationally heavier given that the degradation factor η is found through iteration (using the Newton-Raphson method for fast convergence) and several iterations may be required to ensure a small tolerance error, it is free from any presumption about the evolution of this parameter, thus not requiring any values for the coefficients, which can be especially important for new materials. Furthermore, intuitively, the second approach is more relatable with the physical process of damage.

2.2.7.3. Linear softening law material degradation model: a practical method to model damage evolution

There are several mathematical relations for idealizing the evolution of damage in quasi-brittle materials, such as: linear, bilinear, trapezoidal and exponential [22, 73]. Taking the most simple and convenient, in terms of implementation, the linear softening law (figure 2.18), prior to damage initiation, the material behaves according to its own constitutive relation up to damage onset ($\varepsilon_{eq\_0}, \sigma_{eq\_0}$). From this point onward, for the current *k-th* load (or displacement) increment, the elastic modulus of the material, is degraded according to equation 2.15 until final failure ($\varepsilon_{eq\_u}, \sigma_{eq\_} = 0$).

$$E^k(\varepsilon_{eq}^k) = [1 - d^{k-1}(\varepsilon_{eq}^{k-1})]E_0 \tag{2.15}$$

Where: $d^{k-1}(\varepsilon_{eq}^{k-1})$ is the damage variable for a given equivalent strain state ε_{eq} at the previous *(k-1)-th* load increment and E_0 is the elastic modulus of the undamaged material.

The equivalent strain for an isotropic material is calculated according to:

$$\varepsilon_{eq} = \frac{1}{\sqrt{2}(1+\nu)}\sqrt{(\varepsilon_x - \varepsilon_y)^2 + (\varepsilon_y - \varepsilon_z)^2 + (\varepsilon_z - \varepsilon_x)^2 + \frac{3}{2}(\gamma_{xy}^2 + \gamma_{yz}^2 + \gamma_{zx}^2)} \tag{2.16}$$

The damage variable for the previous *(k-1)-th* load increment is computed as follows:

$$d^{k-1} = \frac{\varepsilon_{eq\_u}(\varepsilon_{eq}^{k-1} - \varepsilon_{eq\_0})}{\varepsilon_{eq}^{k-1}(\varepsilon_{eq\_u} - \varepsilon_{eq\_0})} \tag{2.17}$$

Where: ε_{eq_0} is the equivalent strain at damage onset and ε_{eq_u} is the ultimate equivalent strain.

As can be observed in figure 2.18, there are three possible damage cases:

$$\begin{cases} \text{Elastic region:} \quad d = 0 \quad \text{for:} \quad 0 \leq \varepsilon_{eq} < \varepsilon_{eq\_0} \\ \text{Softening region:} \quad 0 < d < 1 \quad \text{for:} \quad \varepsilon_{eq\_0} < \varepsilon_{eq} < \varepsilon_{eq\_u} \\ \text{Final failure:} \quad d = 1 \quad \text{for:} \quad \varepsilon_{eq} = \varepsilon_{eq\_u} \end{cases}$$

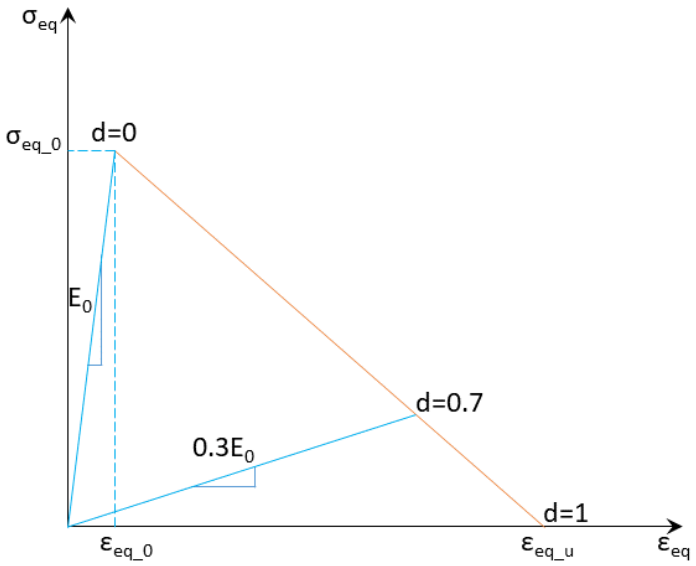

Figure 2.18: Stress-strain relation for an idealized linear damage evolution.

The area under the stress-strain curve is a measure of the critical energy release rate. In order to have dimensional consistency, a characteristic length must be introduced when transforming displacements into strains.

2.2.8. Discussion over modeling intralaminar using the reviewed CDMs

Even though the constitutive behavior of laminated composites is quite complex to model (namely the NL material response), experimental findings show that the incorporation of this complexity in a damage model is vital for the stress field prediction in each lamina. Following this logic, only an extensive incorporation of the underlying physical failure mechanisms will allow a factual determination of the laminate failure load and respective mode. Nevertheless, the relation between the phenomenon complexity and its relevance for the constitutive relation is not trivial to determine [82].

In the sequence of this reasoning, Hashin's damage initiation model generically shows a poor predictive performance given its heuristic nature and deficient incorporation of physical phenomena. Nonetheless, it is easy to implement in a FEA environment and it only requires the material allowables, translating into low computational power. The lack of physical foundation was overcome by Puck's model. Based on Mohr-Coulomb failure theory and phenomenological observations, this model judiciously analyzed and modeled IFF. The fracture plane angle is iteratively determined which adds computational effort to the model. Furthermore, Van Dongen [109] classified its implementation as straightforward, requiring only a few empirical parameters.

All LaRC models are physically based, incorporating unique features such as the in-situ effects (covered in subsection 2.2.4) using fracture mechanics fundamentals for crack growth. LaRC03 considers the classical 2D failure modes but differentiates the compressive failure cri-

teria according to the orthogonal stress state with respect to the associated allowable. LaRC04 expands the precedent theory to 3D, adding, however, considerable computational effort due to exaustive iterative processes. Finally, setting the state-of-the-art damage initiation model, LaRC05 integrates new features such as: the effect of the matrix yielding response and the effect of the hydrostatic pressure. Another noteworthy characteristic of this plasticity theory-based model relates to recognizing unaccounted factors that play a major role in FRP failure prediction, suchlike: edge effects, statistical effects, residual thermal stresses... Explicitly pointing these limitations, raises awareness among the scientific community for further investigation.

However, the main strength of Puck and, particularly, LaRC05 relates to their accuracy in failure predictions. In a comparison among the predictive capabilities of 12 failure criteria and related experimental data for 12 test cases under various 3D states of stress, Puck and LaRC05 excel among the other theories, in both: part A ('blind' predictions, *i.e.*, no access to experimental results) and part B (revised predictions) of the WWFE-II [48]. Both theories obtained grade 'A' (*i.e.*, within $\pm 10\%$ of the experimental value) in approximately 30% of the test cases and grade 'B' (between $\pm 10\%$ and $\pm 50\%$ of the experimental value) in approximately 50% of test cases for part A, making them the best models for part A [48]. LaRC05 also transcended the remaining theories for part B, *i.e.*, where its predictions were compared with experimental results. For more than 95% of the test cases, Pinho's model [82, 83] got at least grade 'B' and got the highest grade for approximately 40% of the test cases [48].

Sudden property degradation models provide an expeditious yet non-realistic solution in modeling continuous isotropic material. Notwithstanding the oversimplification in modeling damage evolution, the sudden approach reveals adequate for modeling fiber failure owing to the catastrophic nature associated with the event of fiber breakage. Considering the mechanical properties of carbon fibers, namely high strength and stiffness, these structural elements are capable of carrying considerably high loads. For an increasing load application, when a fiber breaks, the load that used to be carried by this fiber is redistributed to the remaining fibers that now become overloaded, usually resulting in a sudden failure of the structure. This cascade phenomenon usually takes place in a very short time period. For these reasons, the use of a sudden failure criterion to model fiber failure is adequate.

Accordingly, and having in mind the progressive nature of damage accumulation in the matrix phase of the composite, by means of crack density growth, gradual material degradation models seem to properly represent reality. In this category, Puck's CSE method stand out owing to its independence from experimentally pre-determined parameters. Furthermore, instead of risking an assumption regarding the transverse modulus degradation, its only assumption is that the failure index remains constant and equal to one after damage initiation, which is a sounding assumption. Both Puck's suggested techniques lead to a hyperbolic evolution of the degradation factor and the engineering constants associated with matrix failure.

The consequence of CDM being based on the homogenization assumption and on the stress state is that the resulting smeared crack will always propagate where the stress is highest [108], disregarding the fact that the material is heterogeneous and neglecting the interaction of the different material constituents. In reality, fibers act as crack stoppers [52], as shown in figure 2.19.

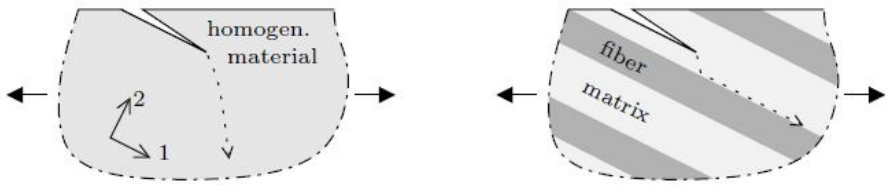

Figure 2.19: Crack propagation in a homogeneous orthotropic medium and in a fiber-matrix material. (Reproduced from [108], copyright TU Delft, 2010).

Despite the shortcomings of CDMs, their convenient and straightforward implementation in a FE framework make them a still popular approach [86]. Because the material is modeled as continuous throughout the damage process, re-meshing is not needed [75]. Furthermore Forghani *et al.* [29] argue that these models offer a better representation of intralaminar damage compared to the discrete approach.

2.3. Conclusions

Several conclusions have been drawn from the literature study:

- Scarf joints are the most efficient joint design since there is no load path eccentricity, thus no peeling stresses develop due to secondary bending. Yet, for a structurally efficient scarf joint, the scarf angle needs to be minimized (so that the tensile [peel] component acting on the adhesive is also minimized) which might lead to manufacturing and requirement issues.
- ABSLJ are inherently structurally inefficient due to: 1) the sudden stiffness 'jump' from the unbonded region to the overlap region and 2) the load path eccentricity. This load eccentricity induces high bending stresses in the adherend's lap ends (where the stress concentration is located due to the sudden change in stiffness), which by its turn contribute for intensifying the already high adhesive peel stresses, correspondent through-thickness adherend interlaminar stresses and longitudinal stresses.
- Generically, increasing the brittleness of the adhesive increases the adhesive peel and shear stresses. Furthermore, ductile adhesives are capable to absorb much more energy than brittle adhesives.
- A stiffness imbalance (either geometrical or material) between the adherends has a detrimental effect on the joint's efficiency, particularly for low values of bending stiffness parameter.
- Laying the 0°oriented plies as far from the neutral axis as possible, increases the bending stiffness parameter which improves the joint efficiency.
- Increasing the overlap length always improves the joint efficiency.
- Under the framework of CLT, composites are analyzed at meso-scale level. Four elastic material constants are needed to characterize the material behavior. The laminate is then subjected to a known load case. Based on these, the strains and stresses are computed and first ply failure is determined according to a given failure criteria.
- Symmetric ($[B]$=0, *i.e.*, no inplane-out-of-plane couplings) and balanced ($A_{16} = A_{26} = 0$, *i.e.*, extension-shear coupling) laminates are preferable for most of aerospace composite designs.

- An anti-symmetric laminate ($D_{16} = D_{26} = 0$, *i.e.*, no bending-twisting coupling) is necessarily balanced and non-symmetric, unless it is composed only by 0°and 90°oriented plies.
- The damage progression methodology comprises four fundamental ingredients: a) stress-strain ply analysis; b) the stresses or strains are compared with the allowables by means of a failure criteria; c) after damage has been detected, the material properties are continuously degraded as damage propagates by means of a material property degradation model; d) a numerical routine that iteratively ensures the reestablishment of equilibrium every time a new failure is detected.
- Damage in FRP composites is complex to describe and analyze. It usually starts with transverse matrix cracks, which is most compliant constituent. These matrix cracks grow, multiply or might coalesce into delaminations which are hard to detect. When the load is sufficiently increased, fibers start to break leading to a catastrophic failure of the structure.
- When analysing failure of multidirectional laminates, the in-situ effects should be accounted, translating into greater longitudinal shear and transverse tensile and compressive strengths. This strength enhancement essentially depends on the ply thickness and location. Generally, an outer unbounded ply is more likely to develop surface cracks, hence its insitu strengths are considered lower than inner plies, but greater or equal to its UD allowables.
- Most of damage initiation models are empirically based and end up neglecting important physical phenomena behind the damage process, leading to inaccurate failure predictions. Contrastingly, LaRC05 and Puck's models incorporate several physical features that translate in reliable failure envelopes and accurate failure predictions when compared against experimental data.
- In the framework of CDM, sudden property degradation models provide a practical and realistic solution to degrade the elastic modulus in the fiber direction, given the typical catastrophic nature of fiber failure. However, this sudden approach is not applicable to model matrix failure propagation, owing to the progressive manner that crack density grows. Gradual property degradation models capture the effects of damage evolution by selectively and gradually reducing the engineering constants related to the matrix.

3

Research question and objective

In the wake of an thorough literature review on the subject of damage progression of FRP ABSLJ, the research question and research objective are the materialization of the research guide and focus of this thesis in light of pushing the state-of-the-art in the present problematic.

3.1. Research question

Main research question

The research core of this thesis work is synthesized in the main research question, which was developed as follows:

Can state-of-the-art Continuum Damage Models (CDMs) accurately predict the global response, damage initiation and propagation until final failure of adhesively bonded single lap joints (ABSLJs), with FRP adherends for different layup configurations, subjected to quasi-static uniaxial tensile loading?

The relevance of addressing this research question relates to the fact that no similar study was found in the literature study where state-of-the-art CDMs were implemented in order to concurrently predict the global response, damage initiation and ultimate loads in ABSLJ with FRP adherends. In conformity with the findings of the WWFE [94], the implemented failure criteria along with the selected material degradation models show a great potential of yielding to realistic predictions. Furthermore the comparison among these proposed models in terms of predictive accuracy may result in valuable conclusions and recommendations for further research in this subject.

Research subquestions

The main research question branches out into narrower and more specific research subquestions. Ultimately, answering all these leads to a final answer to the main research question. For structuring purposes, the subquestions were categorized into: theoretical foundation, preliminary stress study, numerical implementation and comparative analysis.

† Theoretical foundation

In the scope of the theoretical foundation, the following subquestions were addressed in the literature study chapter 2.

The first subset of research subquestions concerns the study of adhesively bonded joints:

a) What are the main types of adhesively bonded joints?
b) How do material properties and geometrical parameters influence the ABSLJ strength under quasi-static tension?
  b.1) How does the stacking sequence in composite adherends influence the ABSLJ strength under quasi-static tension?

The second subset of subquestions relates to an overview on the constitutive relations and mechanical fundamentals of FRP composites:

c) Which equations describe the constitutive behavior of multidirectional composite laminates?
d) How do layup characteristics such: symmetry, balance and anti-symmetry influence the mechanical response of composite laminates?

The third sub-set of research subquestions concerns the theoretical foundation of progressive damage on composite materials:

e) What are the scales for modeling damage in FRP composites?
f) What are the damage mechanisms that characterize failure in FRP composites?
g) By which CDM theories and methods is damage initiation of FRP composites defined and predicted, respectively?
h) By which CDM theories and methods is damage propagation of FRP composites defined and predicted, respectively?

† Preliminary study

In order to understand the mechanical behavior and identify the critical stress regions of ABSLJ with different adherent layup configurations subjected to uniaxial quasi-static uniaxial tensile loading, a preliminary stress study addresses the following subquestions:

i) How do ABSLJs with different adherend layup configuration compare in terms of global behavior (load-displacement curve) for a prescribed displacement?
j) How do stress components distribute in each ABSLJ configuration along: a) the adhesive overlap length; b) through the thickness on the overlap end and c) the adherend first two plies length.

† Numerical implementation

Properly addressing the previous research sub-questions sets a solid theoretical framework and mechanical understanding for the numerical implementation stage. With respect to this stage, the following sub-question is formulated:

k) By which CDMs can intralaminar PDA of composite structures be implemented in FEM?
l) Which numerical configurations better define the problem?

† **Comparative studies**

Having implemented a set of CDMs candidates in four different models and analyzed the respective FE simulation results, in terms of predictive accuracy and versatility, leads to the following research question:

m) How do numerical results obtained by the four implemented CDMs compare with experimental data for different layup configurations?
- *m.1*) In terms of global response, when compared to the data extracted from the tensile testing machines and extensometer.
- *m.2*) Regarding the prediction of damage initiation, when compared to Acoustic Emission (AE) experimental data.
- *m.3*) Regarding the prediction of final failure, when compared to the data extracted from the tensile testing machines.
- *m.4*) Regarding strain maps, when compared to Digital Image Correlation (DIC) experimental data.

3.2. Research objective

Having clearly defined the research question and derived subquestions, the research objective is formulated addressing relevant criteria, regarding: usefulness, feasibility, clarity and informativeness.

To accurately predict the global behavior, damage initiation and ultimate failure loads of ABSLJ with different FRP adherends layup configurations under quasi-static tension by the numerical implementation of state-of-the-art CDMs, comprising valid failure criteria and material degradation models.

4

Methodology

4.1. Computational framework

The proposed DPM comprise the integration and communication amongst different programming interfaces as can be seen in the diagram shown in figure 4.1.

An input python script containing all the information needed to create and configure the FE model operates in an external Python environment. Through parametric modeling, this data is then exported to Abaqus/CAE through Abaqus Scripting Interface which is used to: create the geometrical part, define the material properties, assign sections, create useful sets, mesh the part and define other FE configurations.

Using an implicit integration scheme, the Abaqus/Standard solver uses the Newton-Raphson method to solve the nonlinear equilibrium equations, *i.e.*, it finds the load at each displacement increment (for the case of a prescribed displacement) that guarantees the system equilibrium. During this process, a Fortran user material subroutine is compiled and run defining the material's constitutive behavior. For each displacement increment the state of stress of a given element is evaluated and input to a given failure criteria. Based on whether failure is detected or not, material degradation of the target element takes place.

The output of this analysis is an Abaqus Output DataBase (ODB) file that is opened in Abaqus/Viewer, a subset of Complete Abaqus Environment (Abaqus/CAE) for postprocessing purposes. Most of the output data processing (mostly reading ODB field output date and writing it in raw *.txt* files) was automated using Abaqus Scripting Interface given the repetitive nature of the analysis procedures.

Having the raw data, Python scripts were used to read and write this information by writing it in structured workbook files. Using Python's *matplotlib* library, this data was then plotted into visually appealing graphs.

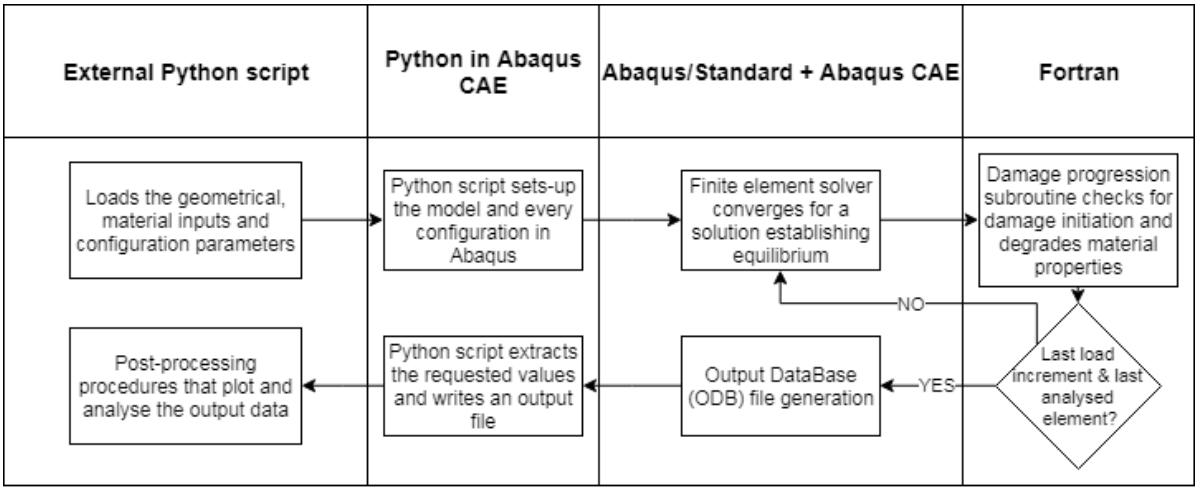

Figure 4.1: Computation framework of the proposed DPM.

4.2. Finite element model definition and configurations

4.2.1. Coordinate system, characteristic dimensions and regions

The coordinate system definition follows the CLT convention. The global/load coordinate system O_{xyz} has the x-axis contained in a plane parallel to the laminae (*i.e.* inplane) and parallel to the longitudinal direction[1]. The z-direction is inplane and parallel to the width of the specimen. The y-coordinate is parallel to the out-of-plane direction. The origin of this reference system is located in the center of the joint length-wise and and thick-wise. In order to ensure only positive width coordinates, the origin was positioned in a lateral face as shown in figure 4.2. Consider the material/local coordinate system as O_{123}: *1*-direction is inplane and along fibers; *3*-axis is inplane and perpendicular to the fibers and *2*-coordinate is in the out-of-plane direction, orthogonal to *1*- and *3*-directions.

The dimensions of the modeled specimen (figure 4.2) were defined based on the *ASTM D5868 - 01(2014)* standard. Table 4.1 summarizes the geometrical parameters and the material properties of the model used to study the stress distribution in the adhesive and adherends.

Both adherends were composed by 16 CFRP UD layers, having 25.4mm (1 inch) of width (w) and lap length ($2c$). The free-length of the adherends (l) was 76.2mm. Regarding the adhesive, its thickness (t_a) was set to 0.125mm and the spew region was defined as an isosceles right triangle with each leg defined eight times higher the ply thickness, *i.e.*, half triangular. Because the spew was assumed half triangular, this implies that the spew width was given by: $spw_w = spw_h + t_a$. Figure 4.4 clearly illustrates these characteristic dimensions.

[1]Which is also parallel to the load application orientation

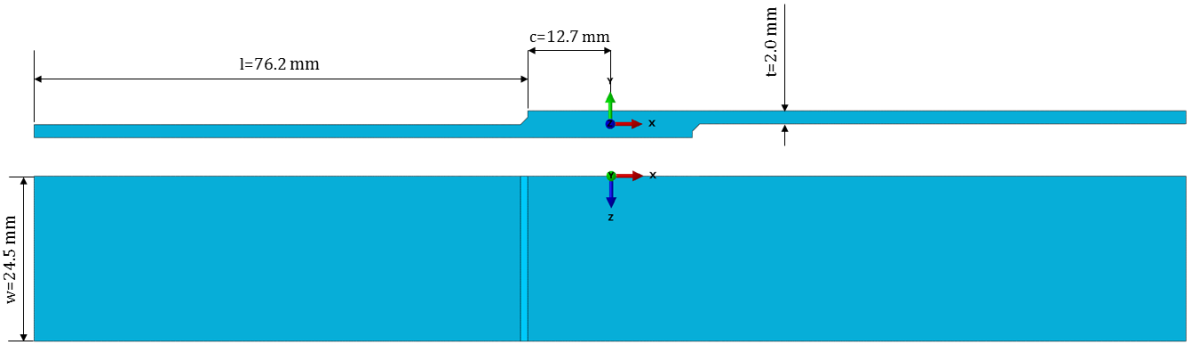

Figure 4.2: Main dimensions of the ABSLJ model. Dimensions are to scale.

Table 4.1: Characteristic dimensions of the adherends and the adhesive.

Adherend geometrical parameters:			**Adhesive geometrical parameters:**		
Number of plies	n_{ply} [-]	16	Adhesive thickness	t_a [mm]	0.125*/0.0625**
Half overlap length	c [mm]	12.7	Spew size***	spw_h/t_{ply} [-]	8
Free-end length	l [mm]	76.2*/87.3**			
Width	w [mm]	25.4			
Ply thickness	t_{ply} [mm]	0.125			

* values used for the preliminary study.
** values used in the experimental study of Kupski *et al.* [55] and for respective validation.
*** measured in number of covered plies.

Several characteristic regions were identified for clarification and coherency purposes. It is important to have a consistent framework such as the one proposed in figure 4.3, considering that further discussions in this work refer to these regions of interest.

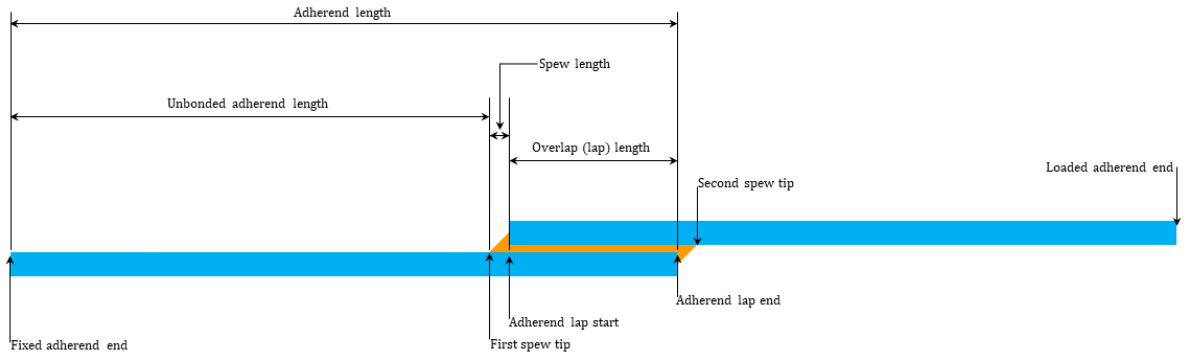

Figure 4.3: Characteristic regions of the ABSLJ.

4.2.2. Material properties

The materials used in the model were UD Carbon Fiber Reinforced Epoxy (CFRE) prepreg tapes for the adherends and epoxy film for the adhesive. Given that the proposed numerical model was validated against experimental data extracted from Kupski *et al.* [55] experimental study, the same materials were used.

The used prepreg tape material was Hexply®F6376C-HTS(12K)-5-35% that contains Tenax®-E HTS45 P12 12K standard modulus fibers. As for the adhesive, Hysol®EA 9695^{TM} 050K AERO was chosen, which presents an areal weight of $240 g/m^2$. The material data were extracted from the referred article [55] and the datasheets of the respective materials. Table 4.2 shows the relevant material properties used, valid at room temperature (23°C).

Table 4.2: Material properties of the adherends - Hexply®F6376C-HTS(12K)-5-35% and the adhesive - Hysol®EA 9695^{TM} 050K AERO. (Adapted from: [55]).

Adherend material properties:			**Adhesive material properties:**		
Longitudinal tensile modulus	E_1 [MPa]	142000	Tensile modulus	E_a [MPa]	2019
Transverse tensile modulus	$E_2 = E_3$ [MPa]	9100	Poisson ratio	ν_a [-]	0.34
Inplane Poisson ratio	$\nu_{12} = \nu_{13}$ [-]	0.27	Tensile strength	X_a [MPa]	48
Transverse Poisson ratio	ν_{23} [-]	0.3	Normal strain at break	ε_{a_ult} [-]	0.11
Inplane shear modulus	$G_{12} = G_{13}$ [MPa]	5200	Shear strain at break	γ_{a_ult} [-]	0.3
Transverse shear modulus	G_{23} [MPa]	3500			
Longitudinal tensile strength	X_T [MPa]	2274			
Longitudinal comp. strength	X_C [MPa]	1849			
Transverse tensile strength	Y_T [MPa]	102			
Transverse comp. strength	Y_C [MPa]	255			
Inplane shear strength	$S_{12} = S_{13}$ [MPa]	63			
Transverse comp. strength	S_{23} [MPa]	35			

4.2.3. Boundary conditions and applied load

All the analysed samples were subjected to the same boundary conditions. The bottom left adherend (figure 4.4) was set as clamped (no displacements nor rotations allowed).

In respect of the load application, it was displacement controlled at the tip of the top right adherend. The loading rate was set to 13mm/min, as suggested in the *ASTM D5868 - 01(2014)* standard.

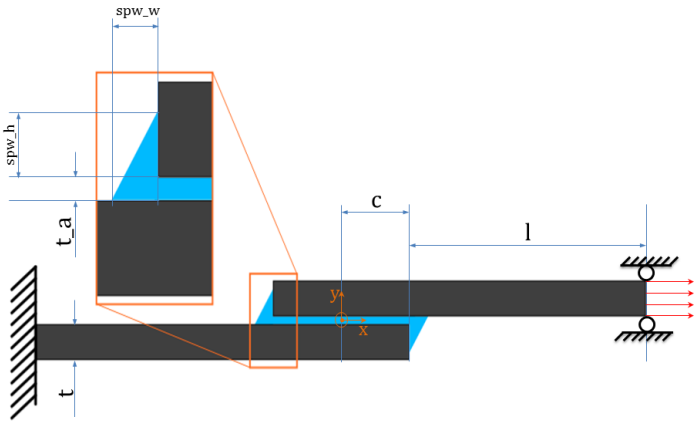

Figure 4.4: Illustration of the ABSLJ characteristic dimensions, boundary conditions and loading.

4.2.4. Assumptions

The subsequent analysis relied on the following set of assumptions:

- The adhesive material is considered to be isotropic, whereas the adherend material is considered to be orthotropic, both requiring the input of the elastic constants.
- Both the adherend and adhesive materials behave linear-elastically. Their constitutive behavior is governed by the local element matrices described in subsection O. In reality, this assumption is an overstatement because this particular adhesive shows some ductility. Because of the complexity of its implementation, plasticity effects were not ignored, *i.e.*, the adhesive was considered brittle.
- Both materials were considered to be homogeneous. This is a bold assumption in the case of the adherend material given its distinctive phase composition, hence not physically representing reality. Yet, this is a common simplification within the meso-level modeling of composites which is assumed for convenience and to alleviate computational cost in the simulation. The attribution of orthotropic properties to the adherend material is done by means of the so-called 'engineering constants'.
- Laminae are perfectly bonded together and to the adhesive, therefore displacements are continuous through the joint thickness.
- Only intralaminar failure was assessed. No interlaminar model was implemented to capture delaminations.
- The spew geometry is idealized as half triangluar.
- No visco-elastic effects were considered nor any other time-dependent effects.

4.2.5. Parametric model generation - Python scripting in Abaqus

While working in Abaqus/CAE, for every performed action, there is a correspondent Python command. This automation of repetitive tasks, is done through Abaqus Scripting Interface[2] where a full model can be generated and/or analysed by means of a python

[2]Abaqus Scripting Interface is an Application Programming Interface (API) used to, among other purposes, create or modify Abaqus models and read from Abaqus output database.

script.

The created script to generate the ABSLJ model not only generates the bulk part based on characteristic dimensions, but it also partitions it by the number of plies so the material orientation can be later assigned based on the fiber orientation intended for each specific lamina. Furthermore, based on the inputs defined by the user, if the UMAT option is turned on, user material properties are attributed to the adherend and adhesive materials including any specific material property used by a given failure criteria, otherwise the materials are simply defined by their engineering constants. The use of insitu strength properties might, as well, be turned on or off.

Many useful sets are created in light of further analysis, namely: bottom and top adherends; numbered individual laminae; characteristic regions such as the lap, spew and free-adherend regions; boundary condition and load application faces; among other useful subsets.

The meshing of the part is also parameterized through seeding of specific edges, specifically: the longitudinal (subdivided in lap, spew and free-adherend regions), the width and the thickness edges of the ABSLJ model. The element type and other mesh configurations are fully configurable.

The boundary conditions and loads are then applied in the predefined face sets and the field output requests is customized.

The versatility of using this API does not end in the model creation as it can be used to read from output database files and write data in a spreadsheet (in formats such *.txt* or *.csv*). The data contained in these spreadsheets can then be post-processed using other python scripts that transform (using mathematical libraries such as *NumPy* or *SymPy*) and plot (using a plotting library named *Matplotlib*) according to the set configurations.

By automating these actions, not only time can be saved but mistakes are more likely avoided for manually repeated action. Section 4.1 elaborates on what each environment does and how they communicate with each other.

4.2.6. Numerical considerations

4.2.6.1. Abaqus Standard *vs.* Explicit

In appendix J - table P.3 summarizes the differences, consequences and potential applications of the two available procedures in Abaqus: Abaqus/Standard, a general-purpose finite element program and Abaqus/Explicit, an explicit dynamics finite element program.

In summary, the implicit scheme finds a solution to a Non-Linear (NL) system of equations iteratively based on the previous and current states of the system, whereas explicit scheme solution is only based on the current state and does not require computationally expensive iteration techniques. Despite its conditional stability, requiring small time steps, the explicit approach is well suited for problems involving severe non-linearities or complex contact condition whereas the implicit approach may fail to converge analysing such problems [86].

Based on the findings of the preliminary stress study (section 5.2), in which a linear global response was found, few iterations are expected. On top of this, in the critical region (lap ends) the mesh was refined making the size of the elements in that region considerable small. An explicit procedure would require an considerably small time increment, thus significantly increasing the required computational power. Taking into account these two important considerations and the trade-off present in table P.3, an Abaqus/Standard procedure has been chosen.

Despite the fact that an implicit procedure is considered to be unconditionally stable, it might still lead to convergence issues.

For some FEA problems it is not trivial to determine, which type of procedure would be more computationally efficient given the number of factors and their respective weights in affecting the computational cost of the analysis. For the present problem and in light of future academic research on the topic, it is recommended that this issue is further investigated.

4.2.6.2. Static, quasi-static *vs.* dynamic loading

Static loads imply that inertial forces are zero, meaning that there is no acceleration in the load application. Slightly different is the quasi-static loading condition that entails a very small acceleration of the load application, which, for the purposes of the analysis, can be neglected.

By contrast, dynamic loading implies cyclic loading in short periods, causing the structure to vibrate. In this loading regime, the inertial forces are considerable.

Both the FEA and the referenced experimental campaign used to validate the DPM were under quasi-static conditions.

4.2.6.3. Load *vs.* displacement control

Generically, mechanical testing of structural elements can be load or displacement controlled. Typically the tensile load tests are displacement controlled at a fixed given displacement rate. This means that the load adjusts according to the stiffness of the structure in order to maintain the displacement rate at a constant value. Conversely, in a load controlled test, a given load rate is imposed and the displacement in the structure is free. A note should be made with respect to the evolution of these controlled variables over time. Standard test methods for lap shear joints define a constant displacement or load rate.

Abaqus, as many other FEA software allow both loading conditions. Similarly to the testing campaign, also the FE simulation was displacement prescribed.

This option avoids the snap-trough instability. This phenomenon happens when for an increasing load, the structure starts to show a softening behavior up to the point that the 'stiffness become negative' ($\frac{\partial F}{\partial u} \leq 0$), followed by a stiffness recovery which, in some cases, might even exhibit a hardening behavior with respect to the initial stiffness (figure 4.5). A load controlled procedure might diverge or neglect the existence of this 'valley-shaped' region, whereas a displacement controlled method is capable of capturing this

phenomenon.

A displacement prescribed method is not able to deal with snap-back behavior (when displacement reverts). Considering the nature of the problem in analysis, the snap-back behavior is not expected to happen.

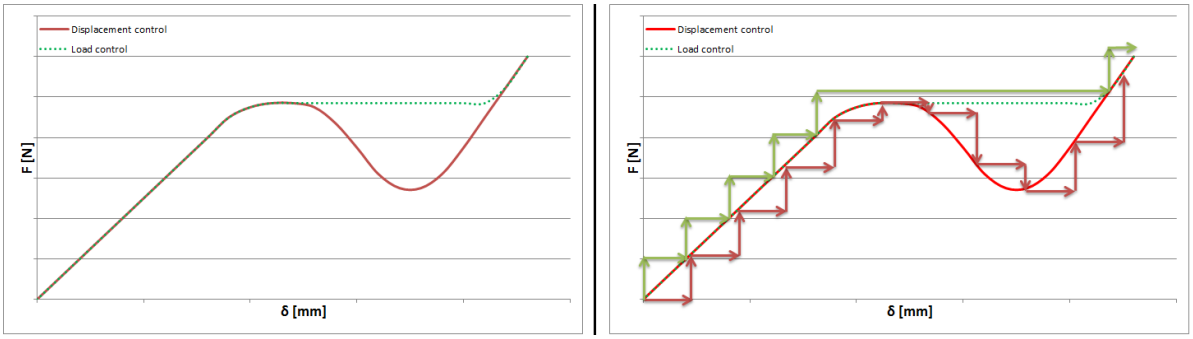

Figure 4.5: Displacement *vs.* load control procedures and convergence graphical representation based in a displacement prescribed (in red) and load prescribed (in green) procedures.

4.2.6.4. Newton-Raphson method

Generic description and algorithm

Generically, the Newton–Raphson method is a root-finding algorithm that sequentially produces better approximations of the roots in real-valued functions. The concept is to start with an initial guess for the root, and take the derivative of the function at that position and compute its x-intercept, leading to a better approximation to the true root. This is done iteratively until an acceptably small error ϵ_{tol} is reached.

The pseudo algorithm for Newton-Raphson implementation can be formulated as follows:

$$
\begin{aligned}
&while \quad |f(x_{n+1})| > \epsilon_{tol} \quad do:\\
&\qquad x_{n+1} = x_n - \frac{f(x_n)}{f'(x_n)}\\
&\qquad if \quad |f(x_{n+1})| \leq \epsilon_{tol} \quad then:\\
&\qquad\qquad return \quad x_{n+1}\\
&\qquad else:\\
&\qquad\qquad x_n = x_{n+1}
\end{aligned}
$$

In appendix K.1 - figures P.17 and P.18 show two graphical representations of Newton-Raphson method implementation. In same appendix - table P.4, presents the root approximation values and the function values obtained for each iteration.

Abaqus nonlinear solver

Abaqus/Standard uses Newton–Raphson method, as a numerical technique to solve nonlinear equilibrium equations. Appendix K.2 summarily explains how the Newton-

Raphson method is implemented in Abaqus for a load controlled case, followed by a graphical representation of the process and the associated algorithm.

Finding Puck's degradation factor through Newton–Raphson method

Puck's constant stress exposure degradation model establishes that once damage initiates, the stress exposure factor (for inter-fiber failure mode) f_{E_IFF}, generally designated as matrix failure index, is kept constant ($f_{E\_IFF} = 1$) and the degradation factor η is iteratively found such that the condition $f_{E\_IFF} = 1$ is maintained. There seems to be an hyperbolic dependence of η on f_{E_IFF} [figure 4.11 c)]. Convergence on finding the roots of such behavior can be easily done by using Newton-Raphson technique.

The pseudo algorithm for the Newton-Raphson implementation to find the degradation factor that sets the stress exposure factor equal to one after damage initiation, can be found in appendix K.3.

4.2.6.5. Solid elements

Considering that a 3D stress state was expected, particularly in the lap region elements, where the out-of-plane stresses could not be neglected, 3D solid elements were used. In fact, the values of this stress component were of the same order of magnitude as the remaining normal stresses (see results in appendix P - figures P.21 - P.24.)

Abaqus/Standard allows the use of reduced integration for first-order brick elements, also referred to as centroid strain elements with hourglass control [1].

The difference between full- and reduced-integration elements lies on the order of integration to generate the element stiffness matrix. While fully integrated linear brick elements (*C3D8*) use eight (2x2x2) integration points, reduced linear brick elements (*C3D8R*) use one (1x1x1) integration points, as illustrated in figure 4.6.

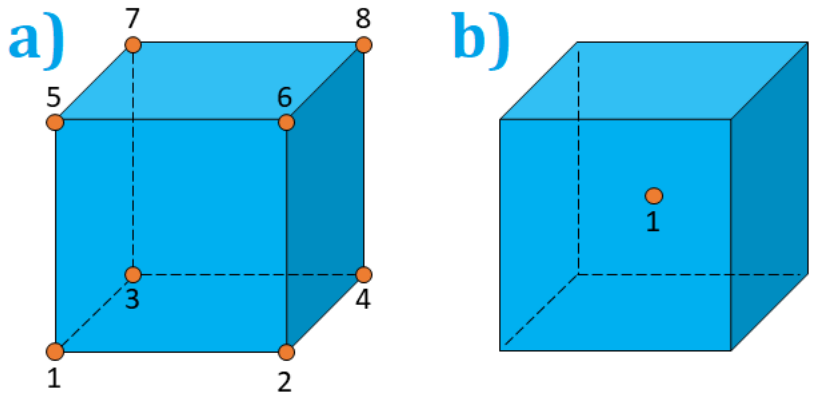

Figure 4.6: a) Full (2x2x2) integration point scheme in a brick element - C3D8 b) Reduced (1x1x1) integration point scheme in in a brick element - *C3D8R*

Reduced-integration significantly decreases the computational effort, particularly in 3D

problems. In some cases its use is recommended over full integration without compromising results accuracy.

Furthermore, some authors suggest that the use of the reduced integration option considerably mitigates the shear locking phenomenon [61, 119]. The reason for this is that this reduced scheme alleviates the shear stiffness. The next subsection treats this shear locking phenomenon in detail.

In this analysis, continuum 3D 8-node elements (also known as hexahedron or even solid brick elements) with reduced integration (*C3D8R*) were used.

4.2.6.6. Shear locking phenomenon

In the present case, a modeling deficiency phenomenon named 'shear-locking' must be considered, particularly when linear quadrilateral (2D) or hexahedron (3D) elements are used. Shear locking is characterized by an unrealistic over-stiff behavior for bending dominated load cases. Rather than showing a bending behavior, the element deforms in shear, thus presenting parasitic shear stresses that physically misrepresents reality (figure 4.7).

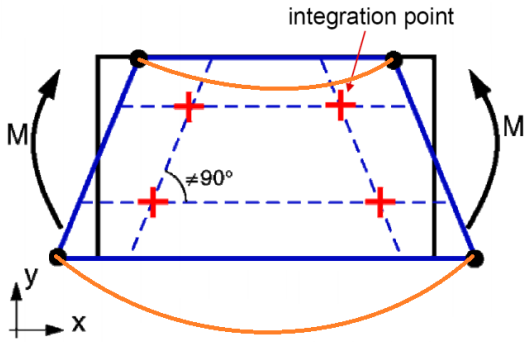

Figure 4.7: Illustration of shear locking phenomenon in a 2D linear element with four nodes and four integration points. Blue thick lines represent the element under shear locking when subjected to a bending load. Orange lines represent the real behavior.

Given that the origin of this error is related to the inherent characteristic of the shape function low degree polynomial [23], using higher order elements mitigates the occurrence of this error.

Additionally, high aspect ratio (AR) elements in the mesh emphasize the shear locking effect, leading to underestimated displacements. In order to alleviate this effect, the AR of the elements was limited to a relatively low value, as detailed in the next point.

4.2.6.7. Element aspect ratio (AR) effects

Dow [23] highlights another cause for over-stiffening behavior, the AR stiffening, again related to an excess of strain energy due to shear. Shear locking and AR stiffening are caused by an analogous mechanism.

Furthermore, high ARs, as well as poorly shaped elements, lead to inaccurate results, especially in regions with strong field gradients.

Aspect ratios between eight and ten are usually the accepted limits within the engineering community, being the latter the limit recommended by Abaqus [1]. As a rule of thumb, elements with an AR lower than five are, generally, considered as good. An AR of one, *i.e.*, a cube when using brick elements is the ideal in terms of minimizing the potential numerical errors. To ensure a proper mesh quality Abaqus has a mesh verification tool that highlights and helps the user to identify elements that do not comply with the AR customized limit.

In the present case, the adhesive thickness was always the bottleneck in terms of element sizing. As a practical example, if the limit aspect ratio is set to an AR of 5, in the lap region, where the stresses are expected to be more critical, having a bondline thickness of $t_a = 0.0625mm$ implies that no element dimension in that region exceeds the length of $0.3125mm$.

4.2.6.8. Hourglass control

Hourglass modes are non-physical modes that are induced by reduced integration. The typical outcome is an unrealistic response of the structure (figure 4.8) due to zero-energy modes of deformation. This happens when all stress components are equal to zero at the element's integration point. Further information regarding the causes of this phenomenon is provided in appendix L.

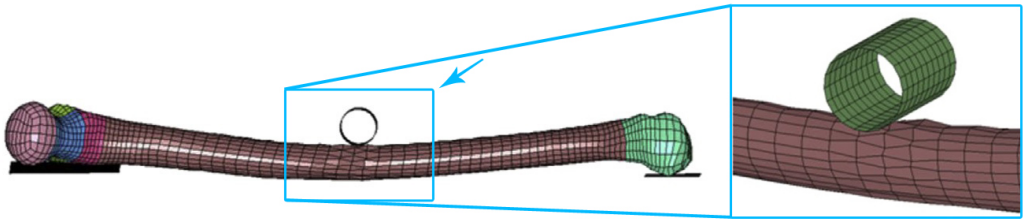

Figure 4.8: Improper hourglass control in a femur loaded in a 3-point bending load case.

In order to mitigate this effect, fictitious elastic stiffness and viscous damping are added. This is done by selecting the most appropriate hourglass control method. Because a first-order reduced-integration was used, an enhanced hourglass control was selected, as suggested in the manual [1]. Another strategy used to avoid this effect is through mesh refinement.

4.3. Preliminary studies

Because CDMs rely on the stress-strain state to capture damage, two preliminary stress studies were performed to: 1) build confidence on the reliability of the predicted stresses; 2) identify regions of troubling convergence; 3) identify critical regions in terms of stress; 4) understand the stress distribution along those critical regions and 5) understand the effect of the layup configuration in the stress distribution.

4.3.1. Adherend layup configurations

Specifically for the preliminary stress study, four layup configurations were used to study the influence of the stacking sequence in the stress distribution in the joint (in both, the adherend layers and the adhesive). To each Finite Element Stress Analysis Layup (FESAL) was attributed a code, as presented in table 4.3.

Table 4.3: Layup configurations used to study the stress distribution in the ABSLJ.

Code	Compacted layup	Extended layup
FESAL1	$[0]_{16}$	[0/0/0/0/0/0/0/0/0/0/0/0/0/0/0/0]
FESAL2	$[0/90]_{s^3}$	[0/90/90/0/0/90/90/0/0/90/90/0/0/90/90/0]
FESAL3	$[+45/\text{-}45]_{4s}$	[+45/-45/+45/-45/+45/-45/+45/-45/-45/+45/-45/+45/-45/+45/-45/+45]
FESAL4	$[+45/0/\text{-}45/90]_{s^2}$	[+45/0/-45/90/90/-45/0/+45/+45/0/-45/90/90/-45/0/+45]

4.3.1.1. FESAL1 - $[0]_{16}$

A laminate composed only by 0°plies is intrinsically symmetric ($B = 0$, no inplane - out-of-plane coupling), balanced ($A_{16} = A_{26} = 0$, no extension - shear coupling) and anti-symmetric ($D_{16} = D_{26} = 0$, no bending - twisting coupling).

This laminate presents high axial and bending stiffness in the longitudinal direction, yet it is 'unprotected' against secondary loads, namely the transverse stresses induced by the Poisson effect. Moreover, it has a relatively low shear rigidity.

Because this laminate is only composed by UD plies, matrix cracks can propagate easily given the absence of other fiber orientations that would arrest its progression. I any event, the implemented model is 'blind' to this fact since the material was idealized as homogeneous at the meso-level.

4.3.1.2. FESAL2 - $[0/90]_{s^3}$

This second laminate is made by 0°and 90°plies stacked together in a triple symmetry configuration. As the first laminate, FESAL2 is intrinsically symmetric, balanced and anti-symmetric.

Even though this laminate is protected against transverse secondary loads by having 90°oriented plies it presents less axial and bending stiffness than its predecessor. On top of this, the change in direction every two plies acts as a crack propagation stopper, which is not captured by CDMs.

4.3.1.3. FESAL3 - $[+45/\text{-}45]_{4s}$

The third laminate is only composed by $\pm 45°$ UD plies. Even though it is symmetric and balanced, it is not anti-symmetric anymore, meaning that to a bending or torsional moment, a twisting or bending deflection will be, respectively, induced.

The absence of 0s and the predominance of 45s make this laminate the most compliant of the group to axial and bending deflections, yet the stiffer to shear.

Regarding the crack propagation, the same logic to FESAL2 applies in this laminate.

4.3.1.4. FESAL4 - $[+45/0/-45/90]_{s^2}$ (QI)

This Quasi-Isotropic (QI) laminate is composed by the classical orientations and has double symmetry. Each ply is offset by 45°with respect to the next, except for the adjacent middle layers. As the previous laminate, FESAL4 is symmetric and balanced but not anti-symmetric.

Even though it is not the stiffer laminate, it presents the best compromise among all the important design considerations, such that: axial and bending stiffness, performance in many directions and alternation in the ply orientation that hinders crack progression. It is, therefore the most balanced configuration.

4.3.1.5. Analysis of the ABD matrices

The constitutive equations for a multi-directional laminate were derived in appendix F.3.6. The $[ABD]$ matrix characterizes the mechanical behavior of the laminate. For each term of the matrix, the respective couplings were characterized. Submatrix $[A]$ represents the inplane axial/shear stiffness; submatrix $[B]$ defines the inplane-flexure coupling and submatrix $[D]$ gives the bending/twisting stiffness.

For each FESAL, the ABD matrix were computed and can be found in appendix I. Table 4.4 summarize the longitudinal axial A_{11} and bending stiffness D_{11} terms for all the laminates and the relative value with respect to the stiffest configuration, FESAL1.

Because FESAL1 has only 0°oriented plies, it has the highest axial and bending stiffnesses, $A_{11} = 285333.0N/mm$ and $D_{11} = 95111.0Nmm$, in the load direction. For both analysed components, these values represent almost the double with respect to FESAL2; as for FESAL3 they are more than three times higher. The QI configuration (FESAL4) is positioned in between these last two, showing 42.2% and 44.4% of the respective stiffness components.

Considering that FESAL2 has the same number of 0°and 90°oriented laminae, the inplane axial stiffnesses have the same value ($A_{11} = A_{22}$). Given that no other ply orientation were used, both the shear and twisting stiffness terms, A_{66} and D_{66}, respectively, have the same values in both laminates. It is worth mentioning that the bending stiffness D_{11} and D_{22} are not the same considering that the relative position of the plies matter for the these terms, hence having the outermost ply 0°oriented in the reason for $D_{11} > D_{22}$. Hence, having stiffer 0°oriented plies as far as possible from the neutral axis, increases the bending stiffness in the direction parallel to the fibers.

As expected, FESAL3 has the highest shear stiffness A_{66} considering that it is composed only by $\pm 45°$ oriented plies, but the lowest axial and bending stiffnesses, $A_{11} = A_{22}$ and $D_{11} = D_{22}$. As mentioned before the QI layup, FESAL4, is the most balanced configuration.

Table 4.4: Axial and bending stiffness values and relatives percentages (to FESAL1) in the main direction for the four considered layups.

Code	A_{11} $[N/mm]$	D_{11} $[Nmm]$
FESAL1	285333.0 (100.0%)	95111.0 (100.0%)
FESAL2	151809.2 (53.2%)	52689.4 (55.4%)
FESAL3	88773.1 (31.1%)	29591.0 (31.1%)
FESAL4	120291.2 (42.2%)	42241.6 (44.4%)

4.3.2. Mesh convergence study

A QI layup configuration (FESAL4, see subsection 4.3.1) under the application of a prescribed displacement of $\delta_x = 0.5mm$ was chosen for the mesh convergence study. The stress component parallel to the fibers σ_1 was the selected variable to perform the convergence study given that it is the dominant stress component. The stresses were compared along two paths defined in the middle of joint's width, namely throughout: the adhesive length and the first ply length. These paths were selected due to their proximity to the stress concentrations, where convergence is most demanding.

The assumed convergence criterion was of $\epsilon_{rel} \leq 0.01$, meaning that convergence was assumed when the relative error between the finest configuration and the others was less or equal than 1%.

The mesh generation was fully parameterized by seeding all model's edges. The edges categories were identified: longitudinal edges (x-direction); width edges (z-direction) and thickness direction (y-direction). In the spew region, the vertical seeding was fixed by the ply thickness. As for the horizontal direction, considering that the spew was defined as an isosceles triangle, the element width also coincided with the ply thickness.

Longitudinal edges seeding

The mesh of the current model was subdivided in three regions and the longitudinal edges were seeded by size according to different bias options:

- Lap region: this region was double bias seeded, meaning that a minimum and a maximum element sizes were defined, at both lap ends and lap center, respectively.
- Spew region: a constant element size was defined for this region equal to the lap region minimum, meaning that no bias seeding was considered.
- Free-adherend region: this region was single bias seeded, meaning that a minimum and a maximum element sizes were defined, at the spew end and the free-adherend end, respectively.

Figure 4.14 provides a good illustration of the bias used in seeding the different regions of the longitudinal edges.

Width edges seeding

As the stress variation along the transverse inplane coordinate was beyond the scope of this thesis, the seeding throughout the width direction had no bias and the element size was kept 3 to 5 times the size of the smallest element. Higher aspect ratios were avoided due to its detrimental effect on results accuracy.

Thickness edges seeding

For all configurations, every ply and adhesive were seeded by element size: one per edge; under the assumption that the stress gradient is weak within the respective structures in the out-of-plane direction.

Mesh configurations

As stated before, the expected critical stress region is located near to the lap ends. For this reason, the mesh of the model was refined in that same region, as shown in figure 4.9. Each mesh was characterized by the length of its smallest element, located at the spew tip, as shown in figure 4.9. The following table shoes the minimum element size used at each mesh configuration and respective total number of elements.

Table 4.5: Minimum size element and total number of elements for each mesh configuration used in the preliminary stress convergence study.

Label	**Coarse level**	el_{sz} $[mm]$	**# of elements**
M1	Coarsest	0.5	85714
M2	Coarse	0.375	155340
M3	Fine	0.125	574600
M4	Finest	0.0625	1735734

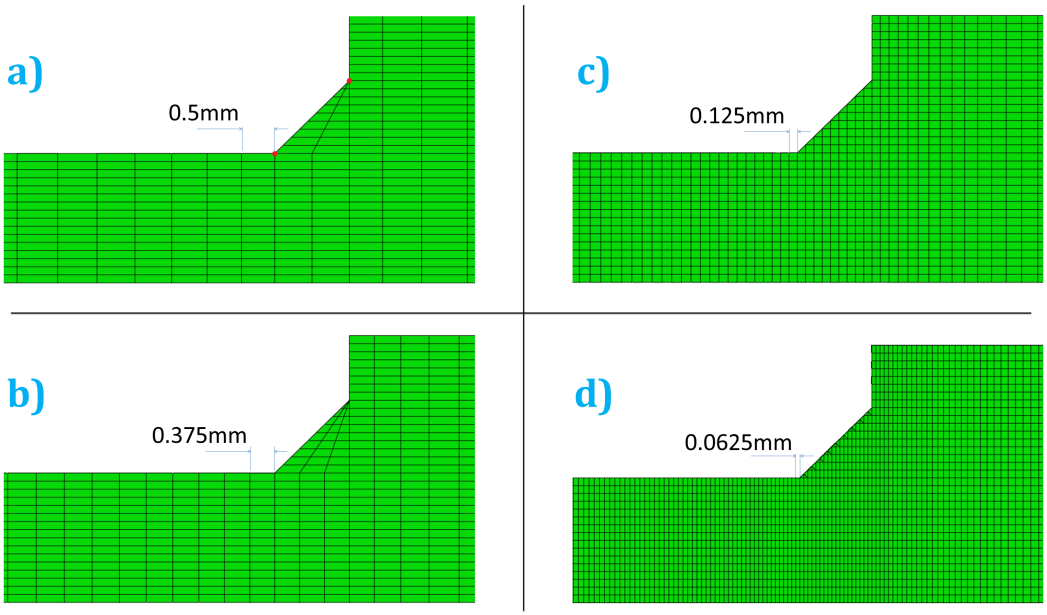

Figure 4.9: Four mesh refinement configurations in the spew region, with different minimum element sizes, from the coarsest to the finest: a) M1 - coarsest - $el_{sz} = 0.5mm$; b) M2 - coarse - $el_{sz} = 0.375mm$; c) M3 - fine - $el_{sz} = 0.125mm$; d) M4 - finest - $el_{sz} = 0.0625mm$.

Two singularities at each lap end were identified, considering the geometry without tangential continuity. Both can be clearly seen in figure 4.9, marked with a red spot. Theoretically, the stresses at the singularities tend to infinity. In the adjacent regions of these sharp corners, convergence is harder to achieve closer to the singularity.

The results of the preliminary mesh convergence study are properly presented in the results chapter under section 5.1.

4.3.3. Preliminary stress study

The present subsection treats the methodology of a preliminary stress study of ABSLJs made of different layup configurations (FESAL 1-4, check 4.3.1) for a prescribed displacement of $\delta_x = 0.5mm$. Effectively, the stress distribution over three paths of interest are presented and discussed in subsection 5.2.

As concluded from the literature survey (section 2.1), in the vicinity of the overlap ends, peak longitudinal and out-of-plane normal stresses as well as peak longitudinal-transverse shear stresses can be found in the adherends and in the adhesive, for two main reasons:

(a) The stiffness 'jump' from the unbonded to the overlap region creates two stress concentration regions[3] on each side of the lap that along with the eccentricity in the load path induce high bending stresses, which rotate the joint overlap region and translate into high longitudinal and transverse normal stresses in the overlap ends;
(b) The strain mismatch between the start of one of the adherends overlap and the

[3]Even though the spew considerably alleviates this undesirable phenomenon, it is still significant.

correspondent end of the other induces high longitudinal-transverse shear stresses in the adhesive at the lap ends, forming the well known bathtub-shaped distribution (see figure 2.2).

4.3.3.1. Selected paths of analysis

The stress analysis was carried along three paths of interest, as shown in figure 4.10, taking into account the stress state of the designated regions:

- Adhesive length (in the x-direction) at the mid-bondline. This is a critical region given that the adhesive transfers the loads from one adherend to the other. Along the bondline length, the stress distribution takes the already mentioned bathtub shape.
- Joint thickness path (in the y-direction) at the adherend lap start. The stress distributions along the joint thickness were analyzed to understand the variation of the stress from the closest to the farthest plies from the adhesive and to identify the adherend free end effect.
- Adherend's first two layers length (in the x-direction) at the middle of the ply. The first two adhesive neighboring plies were assessed, considering their proximity to the stress concentration region, being, for this reason, the most critical.

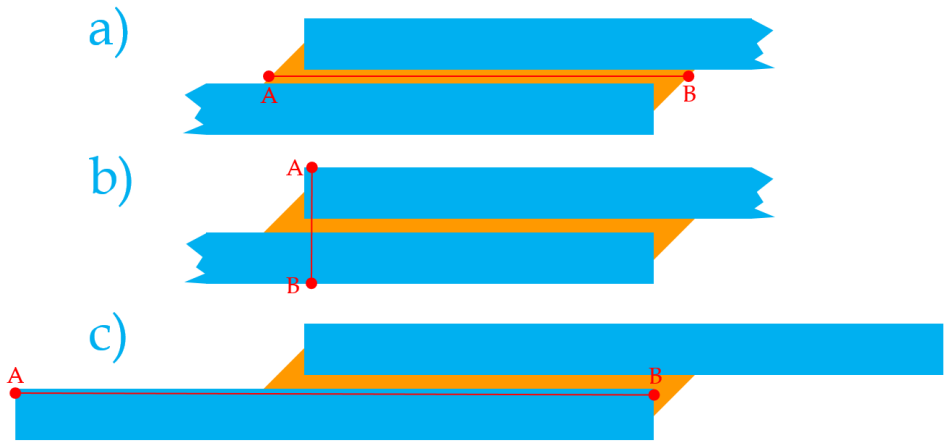

Figure 4.10: Selected paths for the stress analysis: a) adhesive length; b) joint thickness; c) adherend layer length.

The results of the preliminary stress study are properly presented in the results chapter under section 5.2.

4.4. Damage progression model (DPM)

4.4.1. Selected failure criteria and material degradation models

Subsections 2.2.6.1-2.2.7.3 review relevant failure criteria and material degradation models in the scope of consolidated CDMs found in literature. The outcome of that study was

the judiciously selection of three failure criteria combined with three material degradation methods in four combined damage models, summarized in table 4.6:

Table 4.6: Overview of the selected PDA models.

PDA-Adherend	Failure criteria	Material degradation model
CDM1	Hashin 3D [42]	Camanho & Matthews (Sudden) [12]
CDM2	Puck [84, 85]	Puck - Pre-defined damage law (PDL) [84, 85]
CDM3	Puck [84, 85]	Puck - Constant stress exposure (CSE) [84, 85]
CDM4	LaRC05 [82, 83]	Puck - Constant stress exposure (CSE) [84, 85]

4.4.1.1. Motivation for the selected combinations

Adherend models

The first model, Hashin 3D + Camanho & Matthews (a sudden degradation model), was selected as a simplified but well established damage model. Hashin 3D failure criteria [42] has been widely used by the failure analysis community. Despite its simplicity and mainly empiric background, Hashin's model yields to accurate failure predictions. Similarly, sudden material degradation models, such as the one proposed by Camanho & Matthews (Sudden) [12], are also quite simple and of expeditious implementation, ensuring a light computational cost. Hence, the first CDM follows a traditional approach of failure analysis and relies on its simplicity and light computational cost while ensuring decent predictions.

The second and third models, Puck + Puck PDL and Puck + Puck CSE, respectively, were considered by reason of a systemic implementation of Puck's failure analysis model [84, 85]. Being the failure criteria the same, the difference between the two models resides in the determination of the damage degradation parameter approach as thoroughly explained in subsection 2.2.7.2. The purpose of having both CDMs with the same failure criteria but with different material degradation approaches was to test the hypothesis that Puck CSE produces more accurate results in damage propagation regime owing to the fact that it does not make any assumption regarding to the degradation variables evolution.

The objective of CDM4, LaRC05 + Puck CSE was to compare Puck's failure criteria with LaRC05 failure criteria in terms of prediction accuracy of damage onset, taking into consideration that both, CDM3 and CDM4 have the same implemented material degradation model. Based on the WWFE-I [94] and WWFE-II [48] findings, these two failure criteria were considered top performing models in 3D failure analysis, showing very good agreement with experimental results.

Adhesive model

As for the isotropic adhesive material, the well-established von Mises criterion was selected. For the subsequent degradation of the material, the linear softening model, adequately discussed in subsection 2.2.7.3 was selected, taking into consideration the fairly good correlation obtained by other authors [67] when implementing the same material degradation model in the adhesive.

4.4.1.2. Summary of failure criteria governing functions and specific parameters

Table 4.7 summarizes the used functions and values of specific parameters for each failure criteria implemented in the adherends, per failure mode. More details concerning each failure criteria can be found in the literature study subsections 2.2.6.1 - 2.2.6.3, which review the used failure criteria models.

Table 4.7: Failure index equations and specific parameter values for each failure criteria model.

Failure index	Hashin	Puck	LaRC05
FFT	eq.(P.42)	eq.(2.1) | $m_{\sigma f} = 1.1$	eq.(2.5)
FFC	eq.(P.44)	eq.(2.2) | $m_{\sigma f} = 1.1$	*find* ψ | *max*[eq.(2.6)]
MFT	eq.(P.46)	*find* θ | *max*[eq.(2.3)] for $\sigma_n > 0$	*find* θ | *max*[eq.(2.7)] for $\sigma_n > 0$
MFC	eq.(P.47)	*find* θ | *max*[eq.(2.4)] for $\sigma_n < 0$	*find* θ | *max*[eq.(2.7)] for $\sigma_n < 0$

4.4.1.3. Summary of material degradation functions and specific parameters

Table 4.8 summarizes the used functions and values of specific parameters for each material degradation model. More details concerning each material degradation model can be found in the literature study subsections 2.2.7.2 - 2.2.7.3, which review the used material degradation models.

Table 4.8: Degradation factor functions and specific parameter values for each material degradation model.

Degradation factor	Sudden	Puck-PDL	Puck-CSE
$\eta_{E1}(FFT)$	0.07	0.07	0.07
$\eta_{E1}(FFC)$	0.14	0.14	0.14
$\eta_{E2=E3}(MFT)$	0.2	$\eta(MFT)$ = eq.(2.14) | β=5.3;ξ=1.3;η_r=0.03	*find* η | MFT = 1
$\eta_{E2=E3}(MFC)$	0.4	$\eta(MFC)$ = eq.(2.14) | β=5.3;ξ=1.3;η_r=0.03	*find* η | MFC = 1
$\eta_{G12=G13}(MFT)$	0.2	$\eta(MFT)$ = eq.(2.14) | β=0.95;ξ=1.17;η_r=0.03	*find* η | MFT = 1
$\eta_{G12=G13}(MFC)$	0.4	$\eta(MFC)$ = eq.(2.14) | β=0.95;ξ=1.17;η_r=0.03	*find* η | MFC = 1

As table 4.8 shows, the degradation of fiber related properties, namely E_1, was modeled in a sudden manner as proposed in [12], reducing the longitudinal modulus to 7% of the original value for tensile fiber failure and to 14% for compressive fiber failure, for all material degradation models. Fiber failure usually occurs by fiber breakage, resulting in a catastrophic failure of the structure. For this reason, fiber failure propagation was modeled in a sudden way.

Figure 4.11 illustrates an Abaqus output of the damage in an element in the proximity of the adherend overlap region (*i.e.* near to the stress concentration) in a ABSLJ. The top plots show the variation of the tensile matrix failure index over time, whereas the bottom plots depict the correspondent degradation of the Young's modulus perpendicular to the fibers E_2 over time for: a) CDM1, b) CDM2 and c) CDM3.

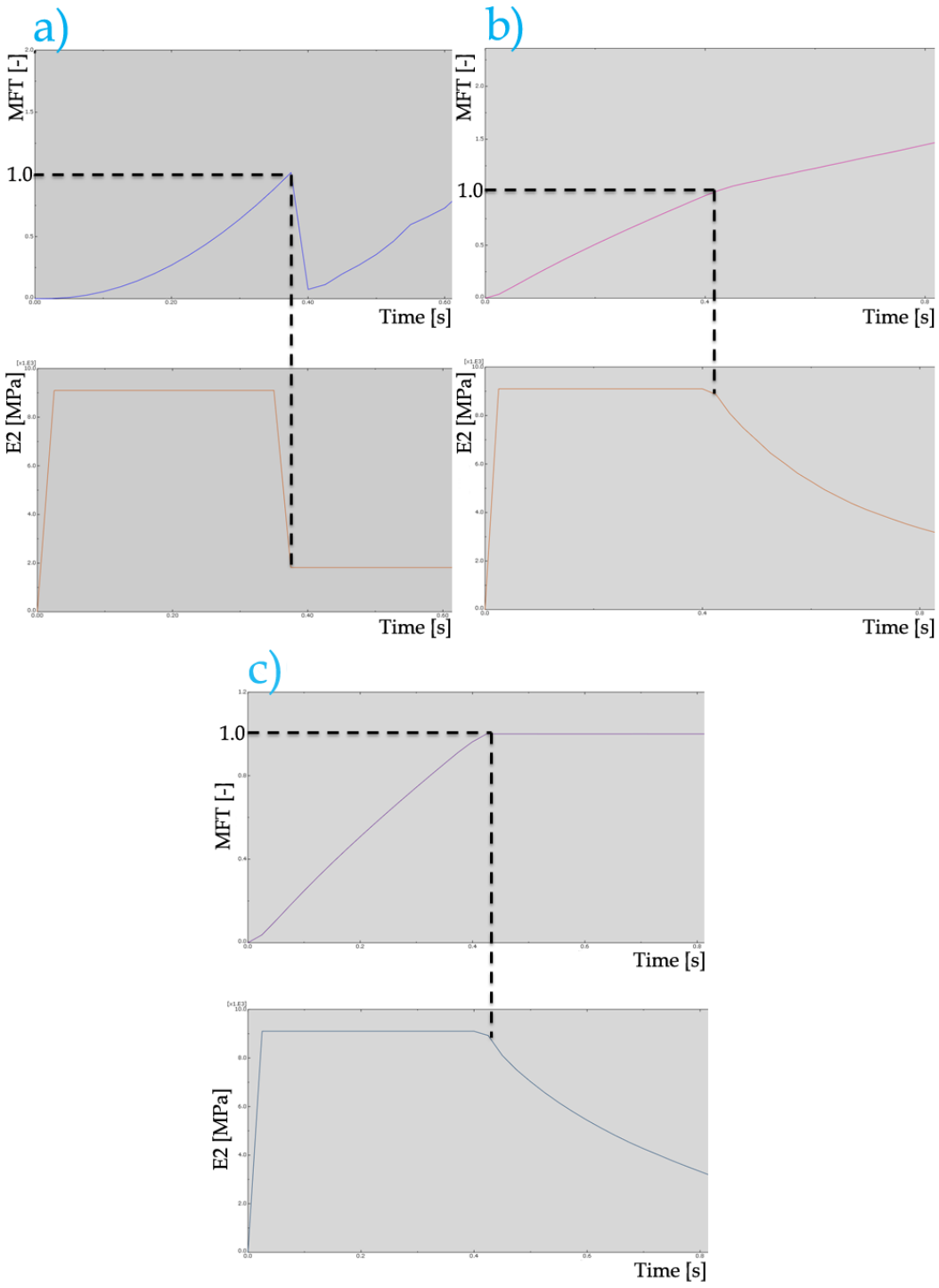

Figure 4.11: Examples of the variation of tensile matrix failure index (MFT) along time in the top, and Young's modulus perpendicular to the fibers (E_2) along time in the bottom, for different damage progression models: a) Hashin 3D + Sudden degradation; b) Puck + Puck PDL; c) Puck + Puck CSE.)

4.4.2. User Material Subroutine (UMAT) implementation

Within an implicit scheme, Abaqus/Standard, the developed DPM was implemented using a User-defined MATerial (UMAT) subroutine. Effectively, UMAT is used to define the mechanical constitutive behavior of the material. Appendix P.20 shows a flowchart of UMAT's framing in a generic Abaqus/Standard simulation.

This subroutine is called for every integration point of the existent elements. Given that eight-node brick element with reduced integration (C3D8R) were selected, UMAT ran once per element.

It must be noted that in UMAT, all strains and stresses are in the local orientation coordinate system.

4.4.2.1. Algorithm

In the framework of FEA of structural problems, the User-defined Material (UMAT) subroutine acts on the constitutive behavior of the element.

Based on the defined material name (string variable recognized by Abaqus/Standard as `CMNAME`): if the string contains '*CFRP*', then adherend's subroutine (UMAT1) is ran, otherwise the adhesive subroutine (UMAT2) is ran. The following steps of the algorithm are common for both, UMAT1 and UMAT2.

The user-defined material properties [`PROPS(NPROPS)`, where `NPROPS` is the number of user-defined material properties, defining the size of the vector `PROPS`] are loaded, read and attributed to UMAT internal variables.

The solver passes the (mechanical elastic) strain vector [`STRAN(NTENS)`, where `NTENS` is the size of the vector] and the strain increment vector [`DSTRAN(NTENS)`], at the beginning of the time increment.

The constitutive behavior of the material is determined by means of the local material Jacobian matrix [`DDSDDE(NTENS,NTENS)`]. Having the local tangent stiffness matrix, the stress vector is computed [`STRESS(NTENS)`]. Appendix (N) demonstrates how these vectors and matrix are computed for a given load increment. After this appended section, the local isotropic and orthotropic local material Jacobian matrices are assembled in appendix (O).

Having the stress vector, a specific failure theory is applied and based on the outputs, for failure indices greater than one, the material elastic properties degrade, otherwise remain the same. Information of the current state must be passed to the subsequent load increment. This is accomplished via solution-dependent state variables [`STATEV(NSTATV)`, where `NSTATV` is the number of state variables].

These state variables are user defined, thus relevant parameters in the failure analysis are requested, such as: the failure indices (FFT, FFC, MFT and MFC), elastic moduli (E_1, E_2, E_3, G_{12}, G_{13}, G_{23}), degradation factor (η) and other failure criteria specific variables (*e.g.* θ_{fp} when Puck is used).

This process is redone for all elements at every time increment. When non-linearities are

present, several iterations may be required in order to meet the convergence criterion. If the solution fails to converge, the time increment is automatically reduced. In the case of the solution still failing to converge for a predefined allowed number of iterations, the simulation stops. Among several plausible reasons, the most likely indicates final failure[4]. In essence, for an increasing prescribed displacement, if the adhesive material gets degraded to a point that cannot continue transferring the loads, numerically this means that there is no correspondent load for that prescribed displacement, hence the equilibrium equation is not satisfied and the solution diverges.

Figure 4.12 shows the flowchart of the implemented UMAT subroutine in the framework of a NL FEA in Abaqus/standard.

[4]A viscous regularization scheme was used to test this hypothesis, as it facilitates convergence. Check the next subsection 4.4.3 for more details.

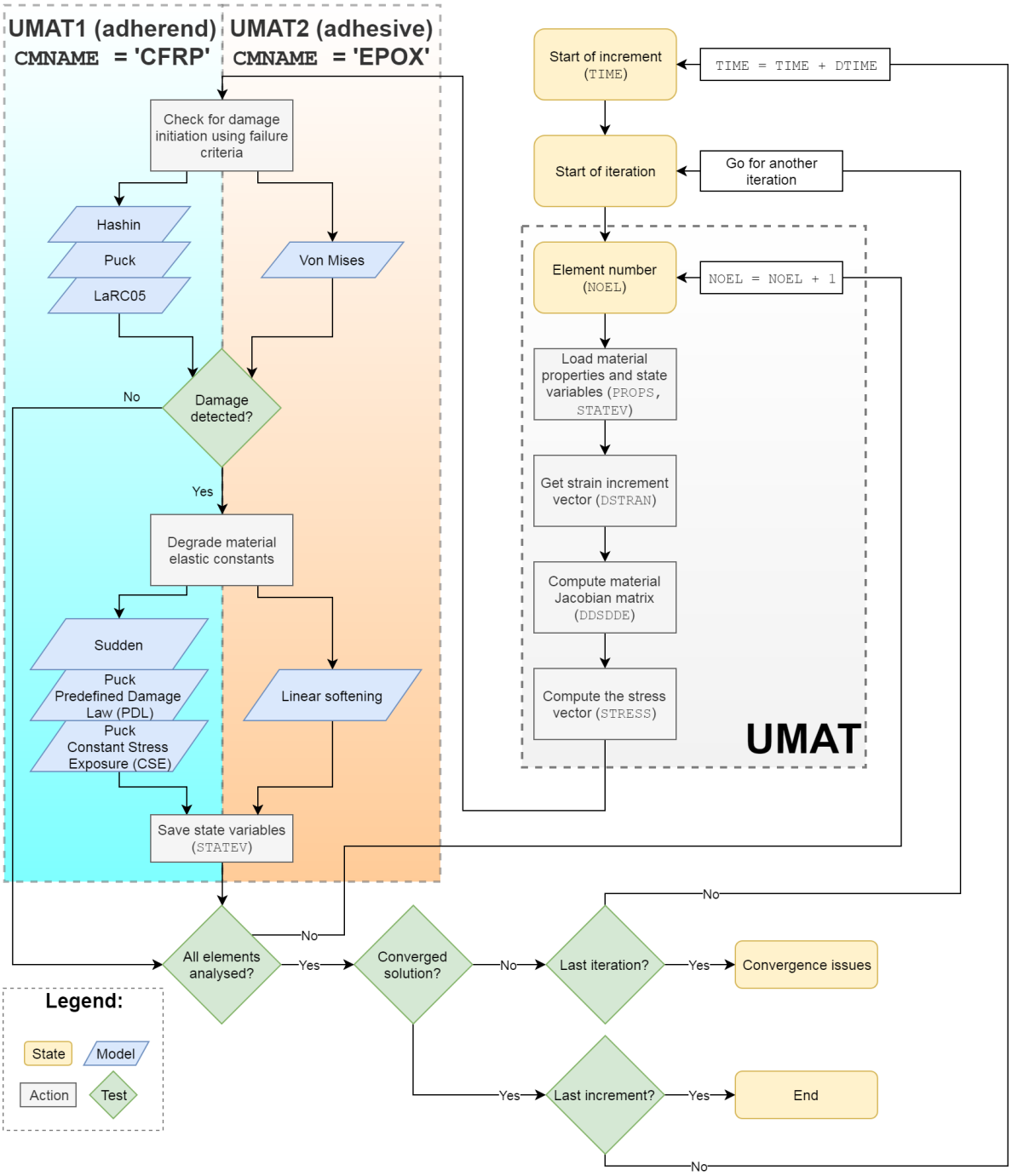

Figure 4.12: Flowchart of the implemented UMAT.

4.4.3. Viscous regularization

In implicit analysis, using material models that exhibit softening behavior and stiffness degradation may lead to convergence issues. Furthermore, the FE predicted softening behavior is sometimes quite irregular, in a step-wise manner.

A viscous regularization scheme can be used to mitigate these difficulties by forcing the

tangent stiffness matrix of the softening material to be positive for sufficiently small time steps [1]. However, high viscous regularization values might pollute the results.

The regularized damage variable is defined by the following evolution equation:

$$\dot{d_v} = \frac{1}{\mu_{vr}}(d - d_v)$$

Expanding the equation, yields to:

$$\frac{d_{v,k} - d_{v,k-1}}{\Delta t} = \frac{1}{\mu_{vr}}(d_k - d_{v,k})$$

Algebraically manipulating the terms, the regularized damage variable becomes:

$$d_{v,k} = \frac{\Delta t}{\Delta t + \mu_{vr}} d_k + \frac{\mu_{vr}}{\Delta t + \mu_{vr}} d_{v,k-1} \tag{4.1}$$

As can be seen from equation 4.1, the regularized damage variable is not only affect by the viscous regularization coefficient but by its relationship with the time increment. Van Dongen [109] elaborated on the practical effects of the $\mu_{vr}/\Delta t$ ratio on the regularized damage parameter. The author presented the variation of the regularized damage variable over time for different $\mu_{vr}/\Delta t$ ratios as shown in figure 4.13. Nunes *et al.* [78] conclude that the used coefficient should be the smallest possible ($\mu_{vr}/\Delta t \to 0$).

In cases of strong mesh dependency and irregular softening behavior, as demonstrated in [78], such undesirable effects could be mitigated by using an appropriate viscous regularization coefficient.

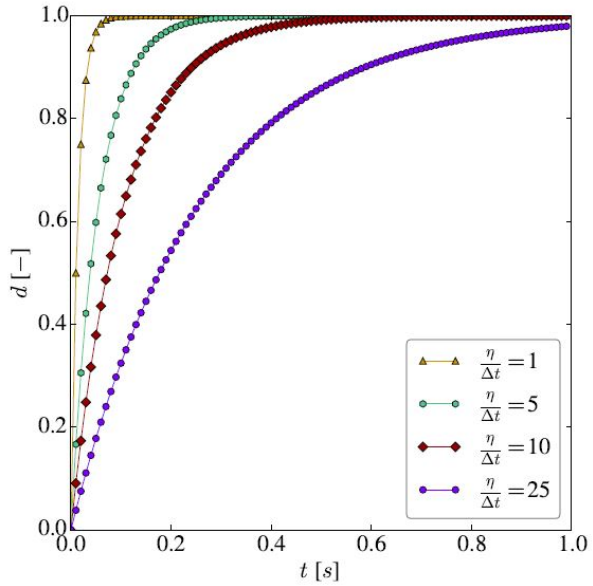

Figure 4.13: Illustration of the effect of viscosity on the evolution of the regularized damage variable ($\Delta t = 0.01[s]$). (Reproduced from [109], copyright TU Delft, 2017)

On the scope of this thesis, considering that the set time increment was of 0.092 seconds, the viscous regularization was set at 0.001, this means that the governing ratio is approximately equal to 0.011 which, according to figure 4.13, should be small enough to not contaminate the results.

4.4.4. Computational cost estimation

The computation power required during a damage progression simulation while using UMAT is dependent on the number of (the symbol # will henceforward be used to denote *number of*) elements, steps, load increments, iterations and the number of requested actions in the UMAT subroutine.

The following equation gives a rough order of magnitude estimate on the number of computations performed by UMAT subroutine in a damage progression simulation:

$$\text{TOTAL \# comp.} = [\text{\# el.}]\times[\text{\# steps}]\times[\text{\# of inc.}]\times[average(\text{\# ite./inc.})]\times[\text{\# UMAT comp.}] \tag{4.2}$$

Where the # UMAT computations is given by the sum of n individual actions plus the sum of s products of the ranges of $q-th$ order nested loops:

$$\text{\# UMAT comp.} = \sum_{m=1}^{n} action_m + \sum_{r=1}^{s}\prod_{p=1}^{q} range_p \tag{4.3}$$

Considering that: the models are composed by approximately one million elements; one step is applied segmented in almost a hundred load increments, most of each requiring one iteration and a UMAT cycle comprises thousands of computations, these coarse values can be inputted into equation 4.4:

$$\text{TOTAL \# comp.} = (\sim 10^6)\times(\sim 10^0)\times(\sim 10^2)\times(\sim 10^0)\times(\sim 10^3) \approx 10^{11} \tag{4.4}$$

This leads to an order of magnitude of 11, meaning that for an entire damage progression simulation it takes roughly several hundred thousand million UMAT computations.

4.4.5. Verification and validation

In the FEM framework, Leone *et al.* [58] indicate that verification and validation are critical tasks for the development of PDA using FEM. Verification assesses whether the model results are consistent with the fundamental concepts (in this case, the failure criteria equations) and assumptions of the model under evaluation. By other words, it checks whether implemented mathematical relations and simulation specifications are according to the conceptual model [116]. Validation, on the other hand, assesses whether the model accurately represents the physics of the problem when compared to experimental data *i.e.*, whether it fulfills its intended purpose.

To ensure that the implementation of the model was correct, several techniques were followed:

- Construction of logic flow diagrams that included each action performed (*e.g.* the UMAT flowchart presented in section 4.4.2.1) and following a 'structured walk-through policy' throughout the code;
- Examination of the simulation outputs for reasonableness for different values of the input parameters;
- Comparing the intermediate global behavior (through load-displacement curves) of the structure with experimental results.

4.4.5.1. Failure envelopes - verification of the implemented failure criteria

The main verification step for the created model was the failure criteria code verification via failure envelope comparison. The procedure consisted in comparing the obtained failure envelopes with the theory's failure envelopes, *i.e.* the ones published by the authors. Each failure envelope was drawn for a given material, of which the strength values were known, under a specific stress state. These can be found in appendix Q along with detailed captions.

Given a set of assumptions (*e.g.* principal stress state $[\tau_{12} = \tau_{13} = \tau_{23} = 0]$, the condition to draw the failure envelopes was setting all the failure indices equal to one and finding the stresses that satisfied this condition. The pseudo-code could be simply formulated as:

$$find(\{\sigma\}) \quad | \quad FFT = FFC = MFT = MFC = 1.0$$

Most failure envelopes required a numerical approach in order to retrieve the data-points required to bound the envelope, owing to: 1) the iterative nature of some criteria, such matrix failure in Puck or LaRC05 models; 2) the fact that the problem to be solved was an indeterminate system of equations (*i.e.*, the number of independent equations was less than the number of unknowns).

The results of this verification step are duly presented in the results chapter under section 5.3. Because of the size of the failure envelopes, these were presented in appendix Q.

4.4.5.2. Validation method

The validation of the model suggested in this thesis will be validated against experimental data obtained by Kupski *et al.* [55]. Details about the methodology followed to test ABSLJs made of different adherend CFRP layup configurations under quasi-static uniaxial tension can be found in the referenced article.

Adherend layup configurantions

Four different adherend layup configurations were tested in this experimental study, three quasi-isotropic and one variant with only 0s and 45s: $[45/90/-45/0]_{2s}$; $[90/-45/0/45]_{2s}$;

$[0/45/90/-45]_{2s}$; $[45/0/-45/0]_{2s}$.

Membrane and bending stiffnesses

Based on CLT, the longitudinal membrane E_{1m} and bending stiffnesses E_{1b} of a laminate were calculated by means of the following formulae:

$$E_{1m} = \frac{1}{ta_{11}} \tag{4.5}$$

$$E_{1b} = \frac{12}{t^3 d_{11}} \tag{4.6}$$

Where t is the thickness of the laminate and a_{11} and d_{11} are the 11 entries of the inverse of the A and D matrices for a symmetric and balanced laminate, respectively. Under these conditions, these entries are given by:

$$a_{11} = \frac{A_{22}}{A_{11}A_{22} - A_{12}^2}$$

$$d_{11} = \frac{D_{22}}{D_{11}D_{22} - D_{12}^2}$$

The longitudinal membrane and bending stiffnesses are measures of how stiff a laminate is to stretching and to bending, respectively in the main direction. Table 4.9 shows the values of the membrane and bending stiffnesses for the four studied laminates.

Owing to the fact that the first three laminates are composed by the same quantity of ply orientations but in a different sequence, their membrane stiffness values are equal. The membrane stiffness value is independent of the sequence. On the contrary, because the $[0/45/90/-45]_{2s}$ layup has a 0°oriented ply as the outermost ply, its bending stiffness is the greatest, even higher than the laminate with 0s instead of 90s ($[45/0/-45/0]_{2s}$). Yet, the $[45/0/-45/0]_{2s}$ layup is the stiffest to stretching in the main direction due to the fact that is has 0s in place of 90s.

Table 4.9: Longitudinal membrane stiffness (E_{1m}) and longitudinal bending stiffness (E_{1b}) for the four tested laminates.

	$[45/90/-45/0]_{2s}$	$[90/-45/0/45]_{2s}$	$[0/45/90/-45]_{2s}$	$[45/0/-45/0]_{2s}$
E_{1m} [MPa]	54622	54622	54622	81113
E_{1b} [MPa]	39653	45996	72424	69391

Mesh configuration

From the analysis of the convergence study, (check the results in section 5.1) the mesh configuration[5] that allowed very small error, even for adjacent regions to the singularity,

[5]As the computational efficiency is out of the scope of this study, the relatively refined mesh that adds computational effort was not of primary concern.

was the mesh with the minimum element size equal to the adhesive thickness ($el_{sz} = 0.0625mm$) which results in a total number of 1002294 elements. From these, 1000836 were hexahedron-shaped elements and 1458 wedge-shaped elements. The latter were located along the diagonal face of the spew.

This configuration ensures a small maximum AR ($\sim 2-3$) on the elements in the critical region, where considerable deformation is expected, which contributes for high results accuracy. In fact, the worst measured AR was of 6.00 and 5.02; the average was of 3.01 and 2.79 for the hexahedron and wedge elements, respectively. Figure 4.14 illustrates the top and lateral view of the final mesh configuration in the damage progression study.

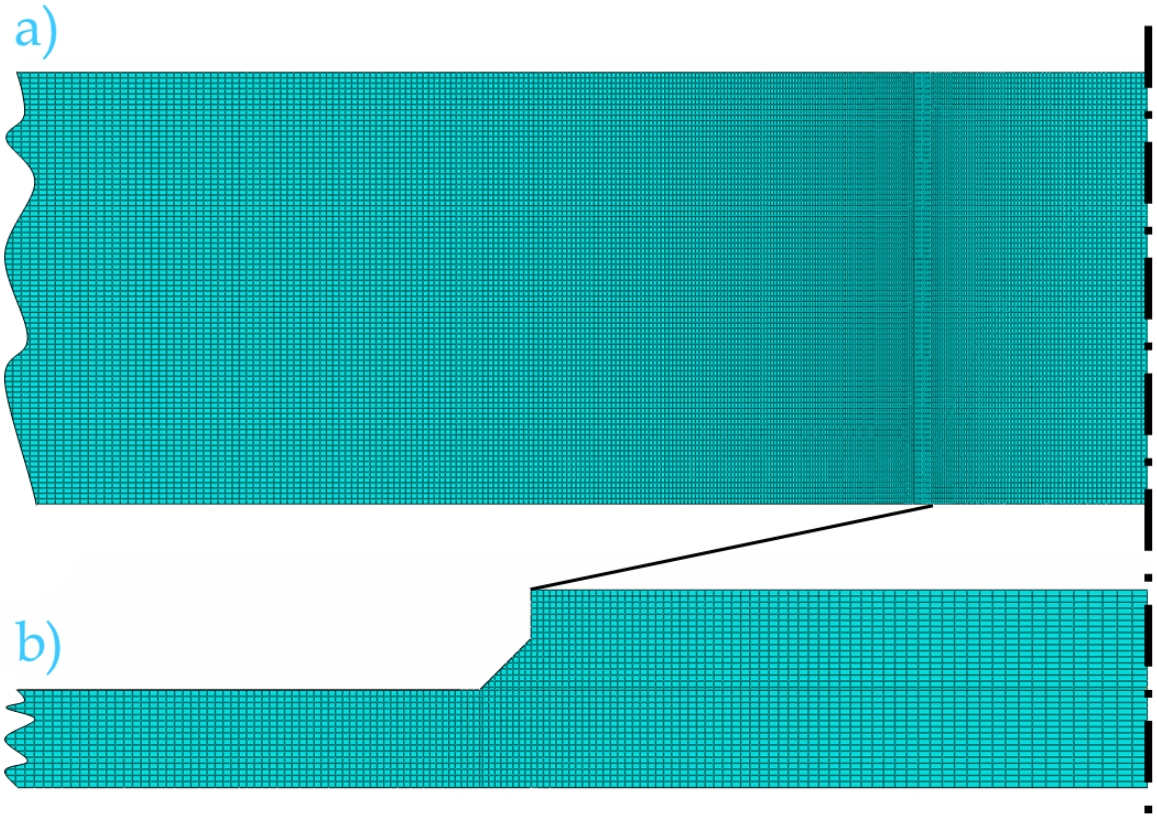

Figure 4.14: Final mesh configuration: a) top view; b) lateral view. The smallest element, at the spew region is 0.0625mm long.

Studied parameters

As part of the endeavour to address the main research question in the stage of comparitative studies, several aspects were studied regarding the response of the joint to damage, namely: a) the global stiffness response, b) the damage initiation load, c) the ultimate load and d) the strain maps.

† Load-displacement curves

During the quasi-static tensile testing, Kupski *et al.* [55] used the load cell in Zwick-Roell AllroundLine Z250 SW to measure the load. For the displacement, a mechanical

extensometer, BTC-EXMACRO.H02 by Zwick-Roell/testXpert II – where the arms were center placed, 60mm apart, (lengthwise and widthwise) on the overlap region.

In the FEA, the loads were obtained by summing the reaction forces in the x-direction in all the nodes contained in the pulled faced. Regarding the displacements, the middle node (thicknesswise and widthwise) on each adherend was found at a distance of $\pm 30mm$ from the center of the joint. The displacement at the top (pulled) adherend was subtracted to the bottom (fixed) adherend at each time increment.

The comparative study of the global behavior of the specimens was of quantitative nature by comparing the stiffness of the linear region. Regarding the initial non-linear region a qualitative analysis was performed.

† Damage initiation load

To capture the damage initiation, Kupski *et al.* [55] employed an acoustic emission (AE) system by Vallen Systeme GmbH was employed which consisted of two VS900-M sensors, that were attached onto the same face of the specimen at $\pm 42.5mm$ from the overlap centre and connected to the AEP4H 34 dB amplifier, as described in the referenced article. The raw data was processed by applying a novel criterion, based on the burst energy. The burst energy is defined as the integration of the squared recorded voltage over a time period. This quantity is meaningful since it accounts for the number of hits and their amplitude over a given time increment.

The defined criterion was based on distinctive burst energy values by comparison with the average value, excluding the events of initial gripping of the specimens (when some matrix cracking occurs) and the final failure when a loud sound is recorded resulting in a quite energetic burst. The criterion was defined as the first event in which the burst energy in one of the sensors at a given time step t (capture frequency at 1 Hz) is greater than 4 times the average of the test in the same sensor:

$$max\left[\frac{nE_{s1}^{t}}{\sum_{ti=0}^{n} E_{s1}^{ti}}, \frac{nE_{s2}^{t}}{\sum_{ti=0}^{n} E_{s2}^{ti}}\right] \geq 4 \tag{4.7}$$

Where: E_{s1}^{t} is the measured energy burst in the time increment t in sensor 1, n is the number of time increments excluding the initial gripping and final failure. The same applies to sensor number 2.

As for the numerical analysis, damage initiation was defined whenever an element exceeded the failure index value of one. Once again, this definition is contestable. The failure indices are calculated based on the element's stress state which can be a problem at singularities due to unreliability of the stress values at those, where convergence was not obtained (even though the error found in the mesh convergence study [section 5.1 - figure 5.2], figure was not too significant). This is assumed as a considerable limitation in this work which deserve a proper reflection on the section of recommendations for future research (section 6.2).

The comparative study of the damage initiation was of quantitative nature.

† Ultimate load

The ultimate failure in both cases (numerical and experimental) was found by the point of maximum load.

The comparative study of the ultimate failure was of quantitative nature.

† Strain maps

The strain field of the overlap area was obtained using the non-destructive testing technique - digital image correlation (DIC) technique [55]. The VIC-3D system by Correlated Solutions, Inc. was used at a 2 Hz frame capture speed and the logarithmic strains were requested.

As for the numerical model, the logarithmic strain maps in the global coordinate system were obtained from the output file. Due to space limitations, only one configuration was analysed.

Considering the generic nature of the information contained in the strain fields, a comparative study of qualitative nature was carried out.

5

Results and discussion

5.1. Preliminary mesh convergence study

5.1.1. Load-displacement curves

The global behavior of the structure does not significantly changed for different mesh configurations as can be observed in figure 5.1. In fact, for all cases, the error at each time step was always lower than 0.15%.

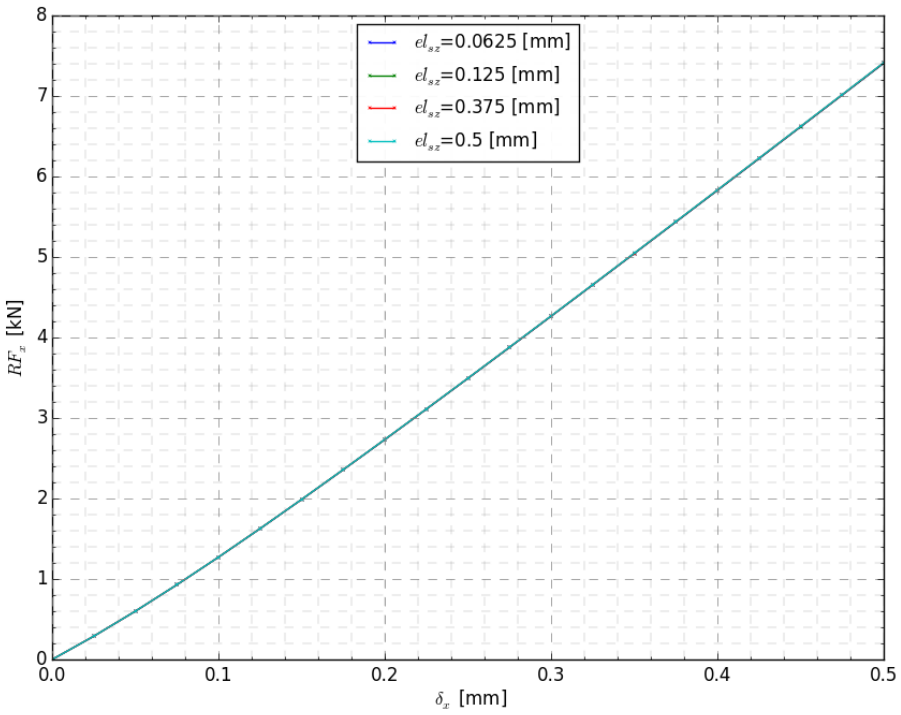

Figure 5.1: Load-displacement curve for the different mesh configurations. The displacements were taken at the adherend tips.

5.1.2. Stress distribution in the adhesive length

The following analysis was performed along the path shown in figure 4.10 a).

Generically, the longitudinal stress component σ_1 in the adhesive's length presents convergence issues in the spew region, considering its proximity to two singularities, as presented in figure 5.2. Particularly, at the spew tips $[x = \pm(c + spw_w)]$, convergence was not obtained, even considering the fact that the relative error dropped from 23.1% to 1.5% from the M1 to the M3 mesh configurations, respectively, having M4 as reference. The fine mesh ensured a relative error less than 1% everywhere else, except at the adhesive tip and at the starting of adherend overlap ($x = \pm c$), where the relative error reached a maximum of 5.6% (figure 5.3).

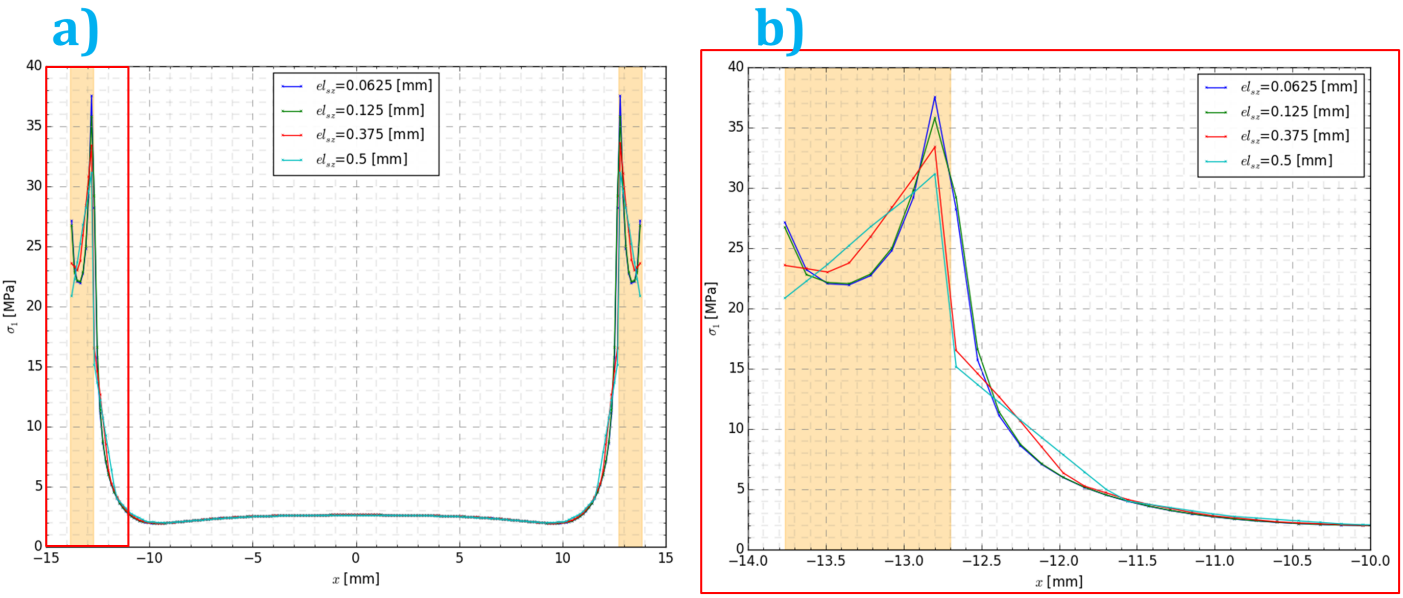

Figure 5.2: a) Stress component σ_1 along the adhesive length path [figure 4.10 a)] of FESAL4, for the different mesh configurations; b) Zoomed stress distribution in the spew region.

Figure 5.3 shows in detail the error oscillation along the adhesive semi-length for the coarser meshes with respect to the M4 discretization and the set mesh convergence criterion. Corroborating the expected scenario of convergence along the the lap's length, M3 showed more accurate results (92.08% of the lap's length showed convergence), followed by the coarse configuration (72.28%) and finally the coarsest configuration (65.35%). The averaged relative errors along the path for the latter sequence were: 0.37%, 2.5% and 4.8%, for M3, M2 and M1, respectively.

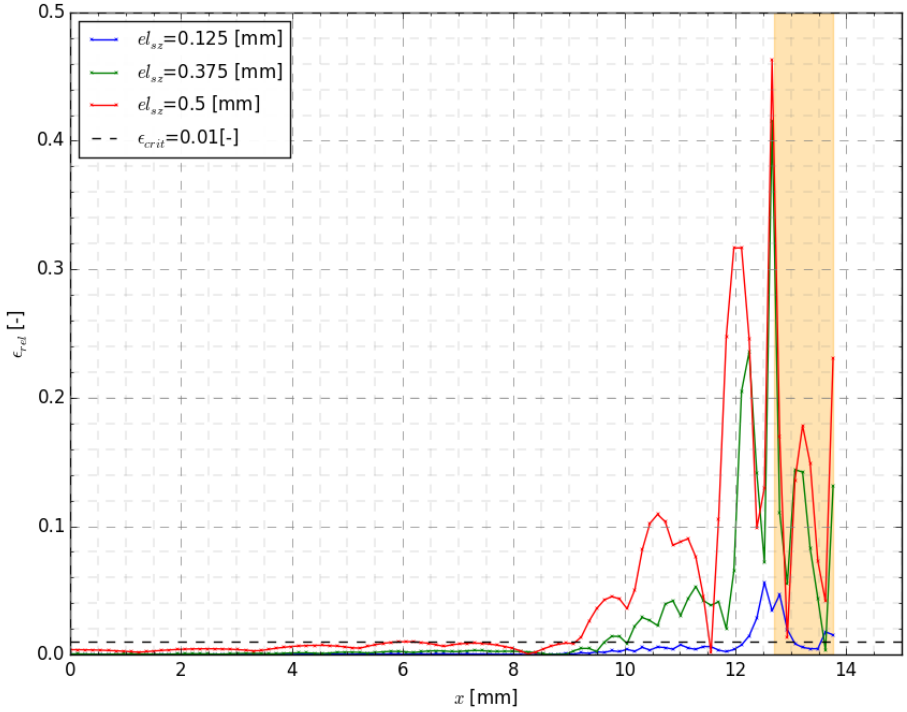

Figure 5.3: Relative error of the stress component σ_1 along the adhesive semi-length path [figure 4.10 a)] of FESAL4, for the different mesh configurations with respect to M4.

5.1.3. Stress distribution along the length of the first two adherend layers

The following analysis was performed along the path shown in figure 4.10 c).

Regarding the stress component parallel to the fibers σ_1 along the first ply's length, three sensitive regions were identified, namely: both adherend tips and the starting of adherend overlap (figure 5.4). While the former are not critical regions, showing relatively low stress levels, the latter is the most critical region. In fact, at the adherend overlap region, the stresses were found to be discontinuous, as figure 5.4 d) suggests. Yet, as the mesh refinement increased, the gap between stress values right before and after the interface coordinate ($x = \pm c$) tended to decrease [figure 5.4 d)]. Furthermore, the M3 configuration was the only configuration that showed an error smaller than 5% despite of its proximity to the singularity.

At the fixed adherend tip, the stresses suggested convergence [figure 5.4 b)], despite the fact that the convergence criterion was not met. Further refinement would be required for a definite conclusion over the convergence in this region.

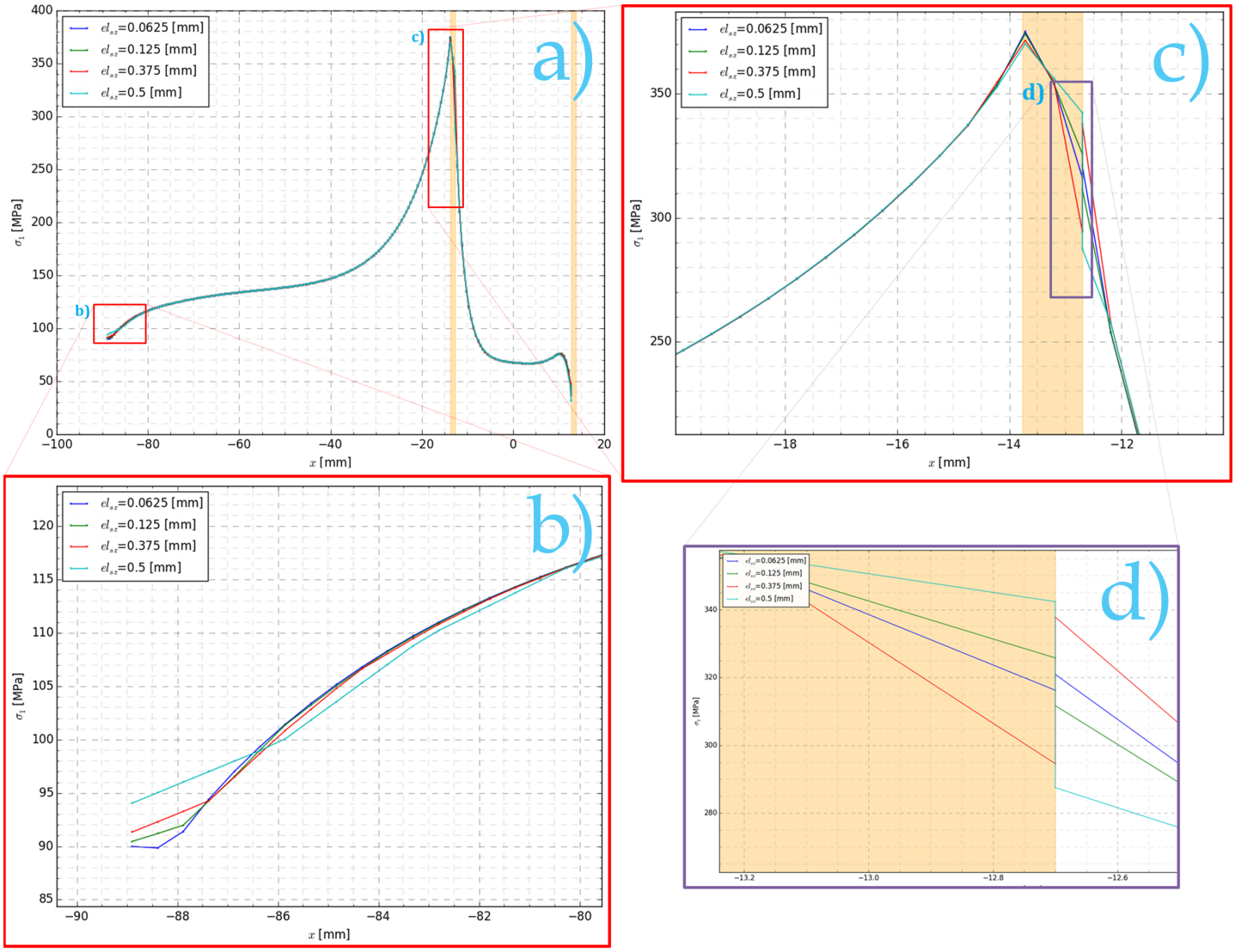

Figure 5.4: a) Stress component σ_1 along the length of the first lamina (+45°) path [figure 4.10 a)] of FESAL4, for the for different mesh densities; b) Zoomed stress distribution at the adherend's tip; c) Zoomed stress distribution in the spew region; d) Zoomed stress distribution at the stress discontinuity at the singularity.

Figure 5.5 shows the distribution of the relative error, explicitly showing three peaks which relate to the above mentioned sensitive regions. As discussed before, the existence of geometrical regions without tangential continuity is the cause for this divergence behavior in the stresses. The convergence criterion was fulfilled in 97.5% of the ply's length for the M3 mesh, in 94.08% of the M2 mesh and in 84.73% of the M1 configuration. For the adherend, the averaged relative errors were considerably lower, 0.20%, 0.32%, 0.66%, for M3, M2 and M1, respectively.

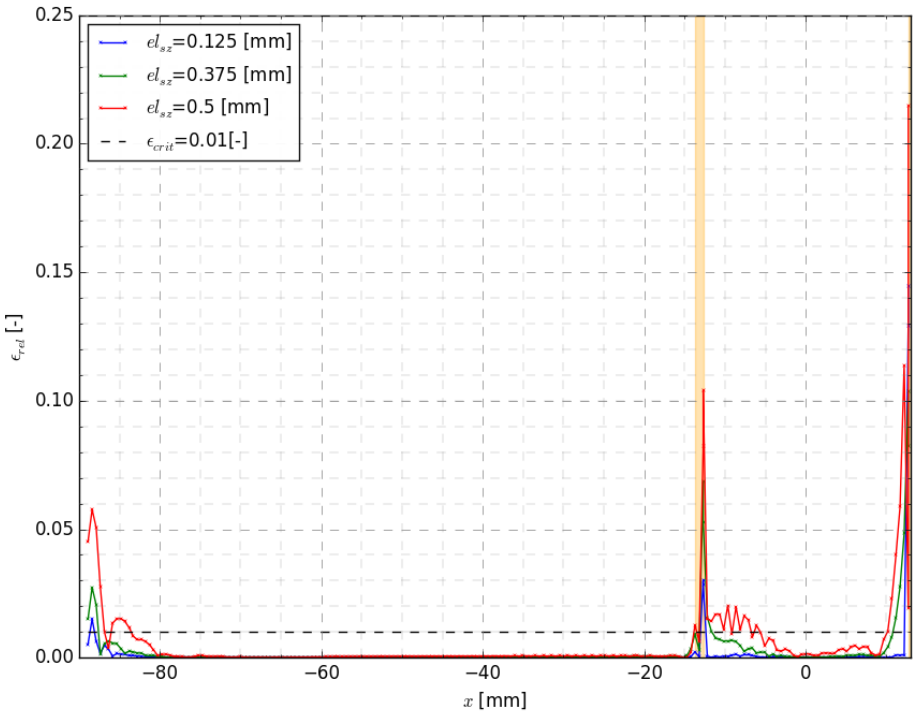

Figure 5.5: Relative error of the stress component σ_1 along the length of the first lamina ($+45^\circ$) path [figure 4.10 a)] of FESAL4, for the for different mesh densities with respect to M4.

Based on the obtained results, the M3 discretization ($el_{sz} = 0.125mm$) was selected as the configuration that was further implemented in this thesis. This refinement allowed a relative error always bellow 5%, with respect to M4, while not costing as much computational power as the finest configuration. Furthermore, the highly structured shape in the spew region ensured a element low aspect ratio, particularly for the smaller elements and a non-distorted shape, both contributing for result accuracy. On top of this, the fact that the elements in the spew have the same length as the ply thickness allowed for a simplified automation of the part meshing.

Another outcome of this mesh refinement study is the determination of the non-convergence regions, *i.e.* locations fairly close to the singularities where convergence was not achieved and these regions (defined by a radius around the singularity and extruded throughout the whole width) have been flagged as not reliable in terms of developed stresses.

5.2. Preliminary stress study

All the normal and shear stress components for the four selected paths are presented in appendix P. In the main body, only the most relevant (in terms of stress values and/or distribution) plots will be shown and analyzed.

5.2.1. Load-displacement curves

For a prescribed displacement of $\delta_x = 0.5mm$ the different laminates show a different carried load. As it is presented in figure 5.6, after an initial slightly non-linear behavior[1], a linear relation takes place until the prescribed displacement is reached. As the reaction load is much bellow the load level to initiate damage, no softening behavior is detected.

Despite the initial slight non-linearity, through a linear interpolation it is possible to extract the stiffness k values for each laminate. As expected, the laminate containing only 0s is the stiffer $k_1 = 38.31kN/mm$, followed by the also anti-symmetric laminate composed only by 0s and 90s which is almost twice compliant $k_2 = 20.76kN/mm$. The laminate containing only 45s is the least stiffer $k_3 = 5.40kN/mm$, by a factor of more than seven, when compared with the first configuration. As expected the QI laminate behaved more compliant $k_4 = 15.02kN/mm$ than the first two laminates but almost 3 times more stiffer than the third configuration.

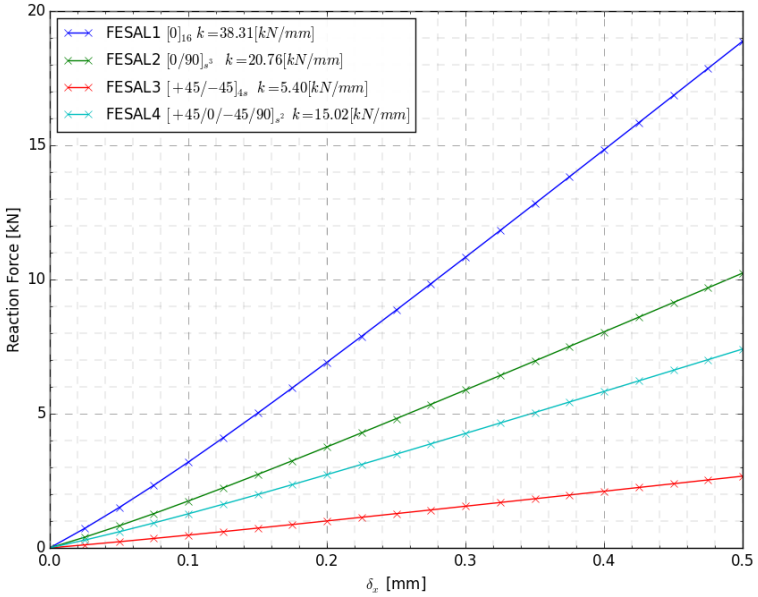

Figure 5.6: Force-displacement curves for the different layup configurations with a prescribed displacement of $\delta_x = 0.5mm$. The displacements were taken at the adherend tips.

5.2.2. Stress distribution along the adhesive length

The following analysis was performed along the path shown in figure 4.10 a).

The normal stress distribution in the adhesive along the lap length showed two very pronounced peaks: one at the spew tips and a generally more pronounced at the lap ends, for all three components σ_1, σ_2 and σ_3. Showing a typical bathtub shape, the longitudinal-transverse shear component τ_{12} distribution (figure 5.9) exhibited a more

[1]Due to the initial non-linear geometric deformation of the structure, characterized by the rotation of the joint.

gradual stress variation *i.e.* much lower stress concentration factors[2], at the starting of the adherend overlap region even if the absolute values of this shear component in that location were higher for the the stiffer laminates when compared with the absolute values of any other normal stress component.

Because of the spew geometry, two peak stress regions can be identified, namely: spew tip and the starting of adherend overlap region. Both are near to singularities (geometrically, sharp corners), meaning that the stresses do not converge with mesh refinement, hence, any interpretation of the stress readings should be carefully done considering that the real stress state might be considerably different.

Addressing the stress component parallel to the load application σ_1 in the adhesive, the stress concentration increases for stiffer adherends, as can be seen in figure 5.7. For FESAL1 (the stiffest) the stress concentration is 10.63 whereas for FESAL3 (the most compliant) is 5.25.

Looking at the peel σ_2 and longitudinal-transverse shear τ_{12} stress distributions in the adhesive (figures 5.8 and 5.9, respectively), an opposite trend is verified when comparing to the longitudinal stress component σ_1. Stiffer configurations showed smaller stress concentrations in the starting of the adherend overlap region.

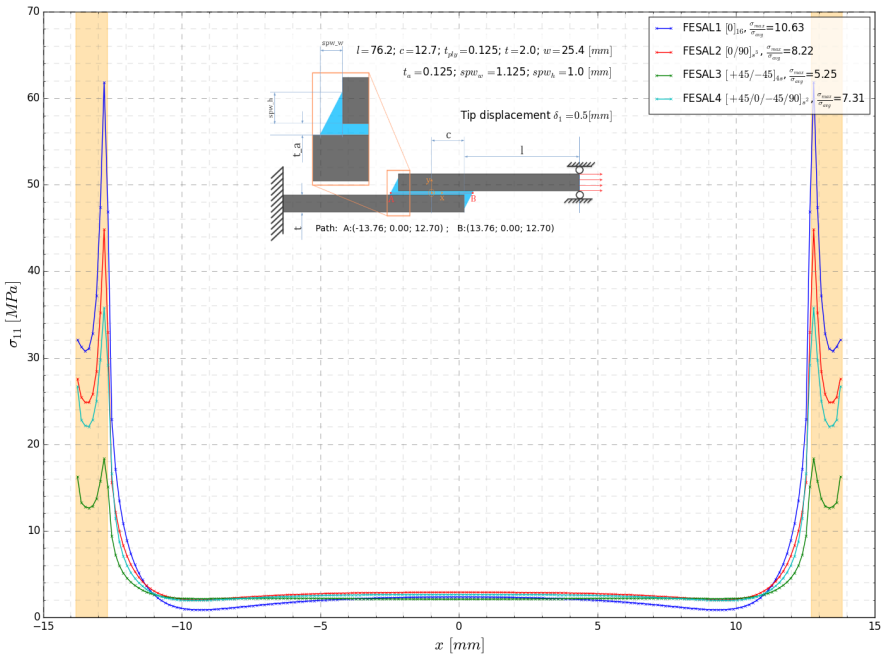

Figure 5.7: Normal stress in the direction parallel to the fibers σ_1 along the adhesive length.

[2]Stress concentration factor is a dimensionless quantity used to quantify how concentrated is in a structure. In mathematical terms it is the ratio of the maximum stress over a reference stress, in this case, the average.

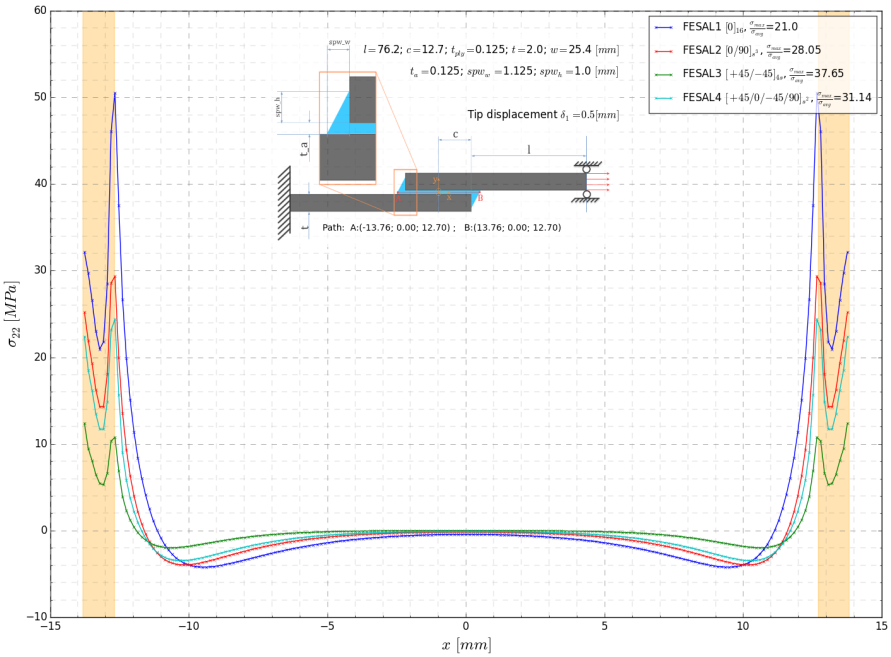

Figure 5.8: Peel stress σ_2 along the adhesive length.

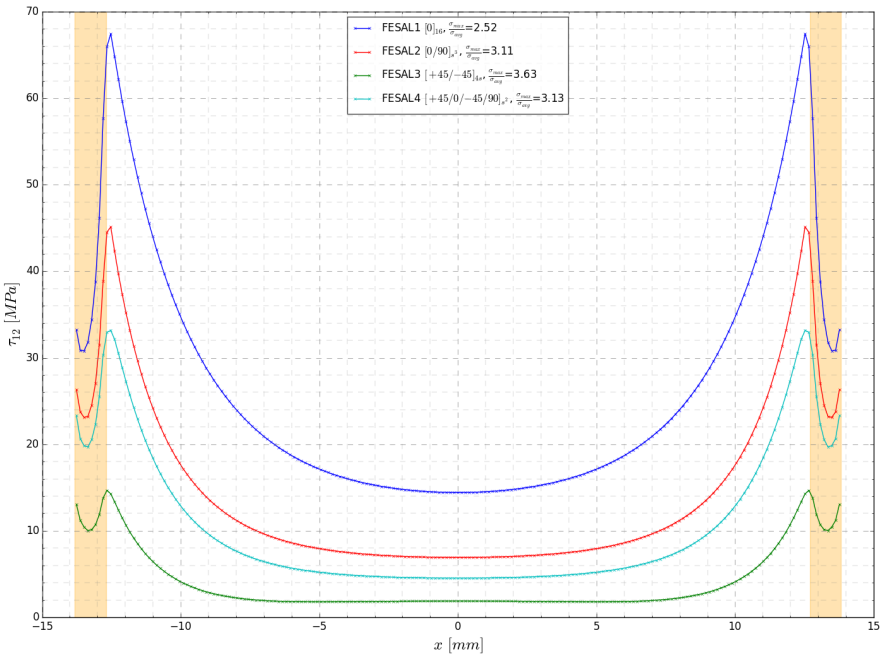

Figure 5.9: Longitudinal-transverse shear stress τ_{12} along the adhesive length.

Another remarkable aspect, common to all so-far analysed stress components is that the ratio between the highest peak located at the lap end and the lower peak located at the

spew tip increases for stiffer adherend configurations.

The inplane shear component τ_{13} and the transverse shear component τ_{23} values were negligible for all laminates. Notwithstanding, for FESAL3 and FESAL4, residual values were recorded for both components, as can be visualized in P - P.21 e) and f) charts. This is related to the fact that the neighboring plies were 45s in both cases, which explains these low, yet existent shear stress values.

Check appendix P - figure P.21 for all stress components along the adhesive length.

5.2.3. Stress distribution along the joint thickness

The following analysis was performed along the path shown in figure 4.10 b).

Along the thickness of the joint path, near to the start of adherend overlap region ($x = -c + \mathrm{d}s$, where $\mathrm{d}s$ is an infinitesimally small length), the stresses vary in step-wise manner. Figure 5.10 illustrates the distribution of σ_1 across the defined path. Because FESAL1 is only composed by 0s, the stress only grows from the bottom layer up to the top adjacent layer to the adhesive, where it reaches a maximum of more than 800 MPa. In the adhesive region, the stresses dramatically drop for less than 50 MPa. In the top adherend, the stresses are more than 4 times lower than to the symmetric ply in the bottom adherend. The reason behind this is related to the fact that the region near to the top adherend's free end is relatively unloaded considering the load path.

As for FESAL2, the 90°oriented plies show residual stress levels, considering that σ_1 is the stress parallel to the fibers (and to the load application), for the 90s, the fibers are perpendicular to the load application, thus, barely carrying any load. This explains the sudden raise in the stress levels for each subsequent 0°oriented lamina, to the stress levels showed by FESAL1 at the same coordinate.

Regarding the peel stress σ_2 distribution along the thickness path (presented in figure 5.11), this component is blind with respect to fiber orientation in terms of the stress distribution shape because the out-of-plane direction is always govern by the matrix properties. Nonetheless, as the stiffer laminates carry more load for a prescribed displacement, these showed greater stress values, as anticipated. Specifically, the FESAL1 reached a maximum stress value of approximately 50 MPa, five times higher than the most compliant laminate with only 45s (FESAL3). From the bottom-most ply of the bottom laminate up to the adhesive the stresses gradually grow in a structured step-wise manner. Contrary to the first stress component distribution, the peel stresses in the adhesive remain at the maximum value. On the lap end of the top adherend, the stresses drop a bit faster than their previous grow and in a less structured manner, due to the reasons explained before that relate to the relatively unloaded state of this region.

Figure 5.12 shows the distribution of the longitudinal-transverse shear stress τ_{12} along the thickness of the joint. FESAL1 show a more gradual because all laminae face in the same direction but steeper growth of this shear stress component up 70MPa, at the adhesive. In contrast, FESAL2 exhibit many sudden variations at the interface of the 0s and 90s, up to the critical value at the adhesive of ∼45MPa. At the 90s, τ_{12} tends to be lower in magnitude. By far, the lowest stress accumulation happened in FESAL3 composed only by 45s, where throughout the path the stress levels kept low, evolving

smoothly up to a maximum of 15MPa, in the adhesive region. The justification behind this relates to the fact that this is the most compliant configuration. Once again, an intermediate behavior between FESAL2 and FESAL3 was found in the QI FESAL4, reaching a maximum of 35MPa in the adhesive. It should be noted that, for all cases, in the bottom-most region of the bottom adherend, negative shear stresses were found meaning a stress in the reverse shear deformation of the contained elements.

The inplane shear stress component τ_{13} (figure 5.13) showed to be negligible in the first two laminates, considering that their composition was limited to 0s and 90s. For other orientations, this inplane shear stress show significant stress levels. As for FESAL3 (only composed by 45s) bottom adherend, the inplane shear stresses grew from 10 MPa to almost 30 MPa, from the bottom-most to the top-most plies, alternating at each lamina (except on the middle of the laminate, given its symmetry) the sign of the stress based on the sign of the fiber orientation. Likewise, for the QI laminate, the considerable shear stress values were only recorded at the 45°oriented plies. For all configurations, the inplane shear stress at the adhesive showed residual values, as expected, taking into consideration the problem's symmetry (with respect to the $1-2$ plane).

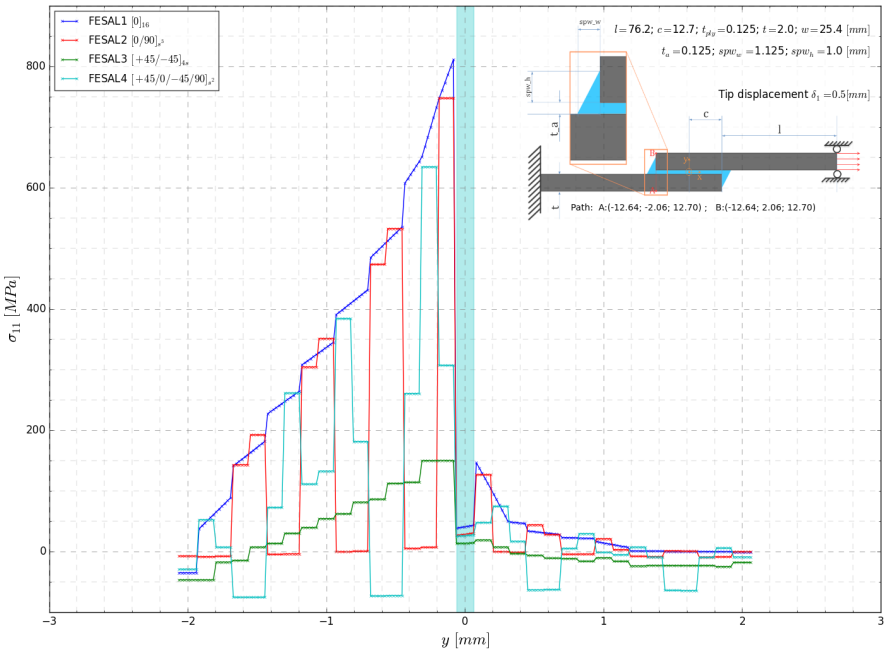

Figure 5.10: Normal stress in the direction parallel to the fibers σ_1 along the adherend-adhesive-adherend out-of-plane path.

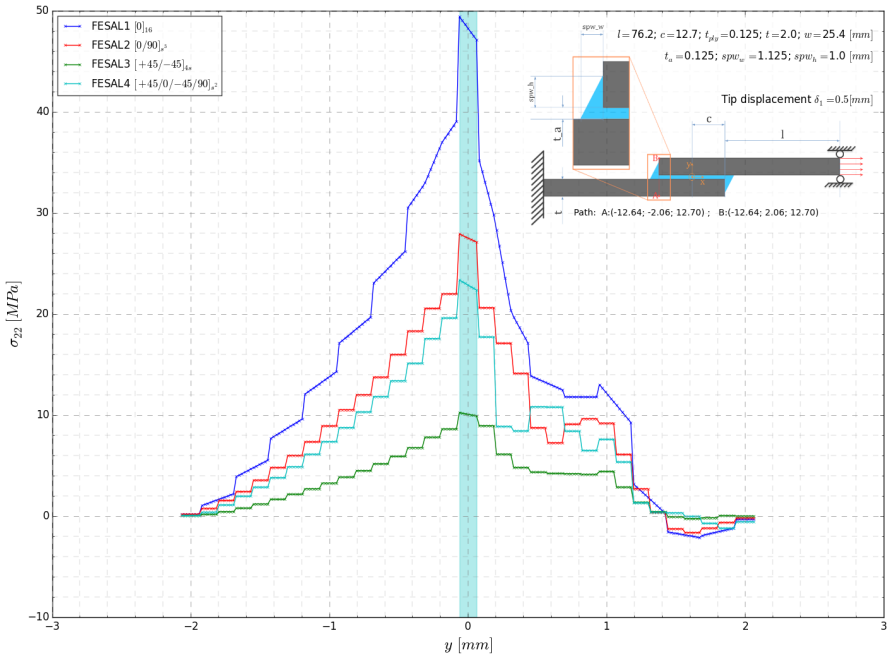

Figure 5.11: Peel stress σ_2 along the adherend-adhesive-adherend out-of-plane path.

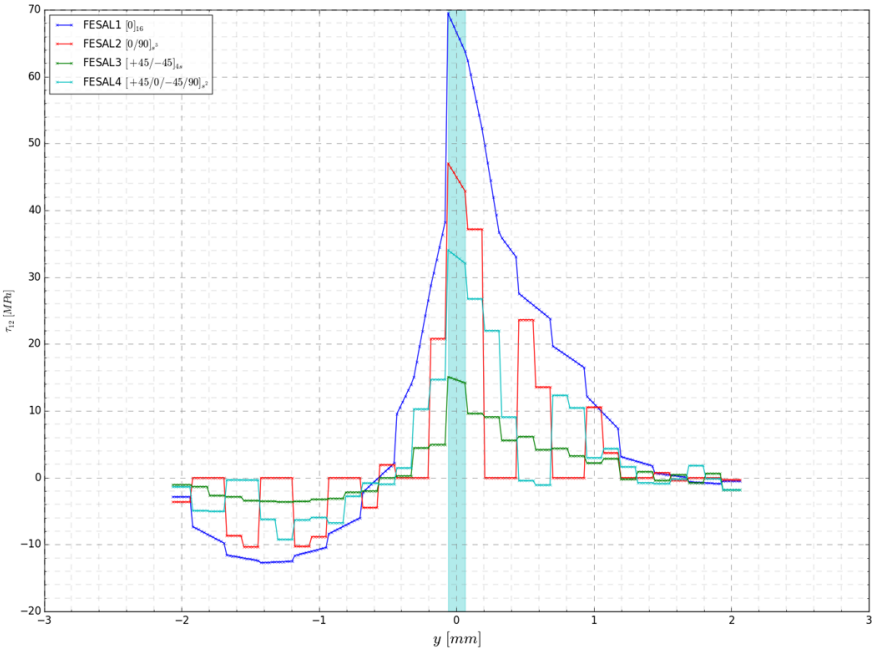

Figure 5.12: Longitudinal-transverse shear stress τ_{12} along the adherend-adhesive-adherend out-of-plane path.

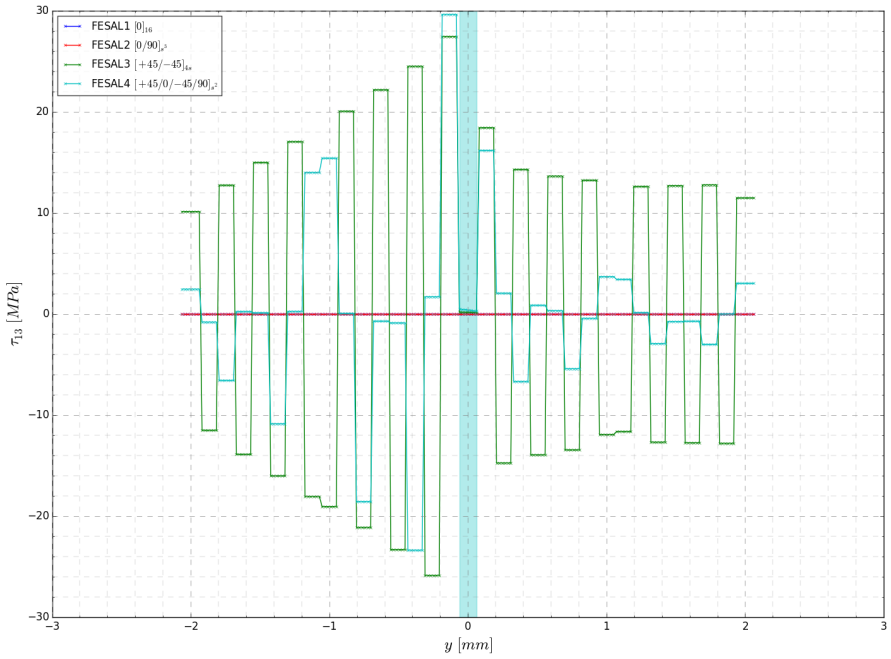

Figure 5.13: Inplane shear stress τ_{13} along the adherend-adhesive-adherend out-of-plane path.

Check appendix P - figure P.22 for all stress components along the adherend-adhesive-adherend out-of-plane path.

It should be borne in mind that, for the adherend-adhesive-adherend out-of-plane path, by integrating each stress component over the cross sectional area, the forces flowing through them are obtained. To be more specific, by integrating σ_x over the width (along the z-direction) and thickness (along the y-direction) of the joint, the correspondent applied load should be found: $F_x = \int_0^w \int_{-(t+t_a/2)}^{t+t_a/2} \sigma_x(y,z)\mathrm{d}y\mathrm{d}z$.

5.2.4. Stress distribution along the length of the first two adherend layers

The following analysis was performed along the path shown in figure 4.10 c).

Figure 5.14 presents the stresses along the fiber direction σ_1 over the first two layers of the adherend. The values of this stress component gradually grow from the fixed tip to the vicinity of the overlap region, where a rapid grow can be observed, for both first two plies. This is particularly true and pronounced for 0°oriented plies. The value of this stress component reaches, approximately, $950MPa$ for the (0°) first plies of FESAL1 and FESAL2.

As for the second ply [figure 5.14 b)], for FESAL1 and FESAL4, both containing 0s as the second ply, this value drops to, approximately, $750MPa$. As anticipated, having a 90°as the second ply orientation, FESAL2 shows a residual (approximately equal to zero) σ_1 value throughout the whole ply length, given that the fibers are perpendicularly oriented

with respect to the load orientation, thus carrying residual amounts of compressive stress due to the Poisson effect. Reference should be made to the stress evolution over the lap region, *i.e.* the region after the adherend overlap, the stresses rapidly drop to values 5 times smaller of the highest peak.

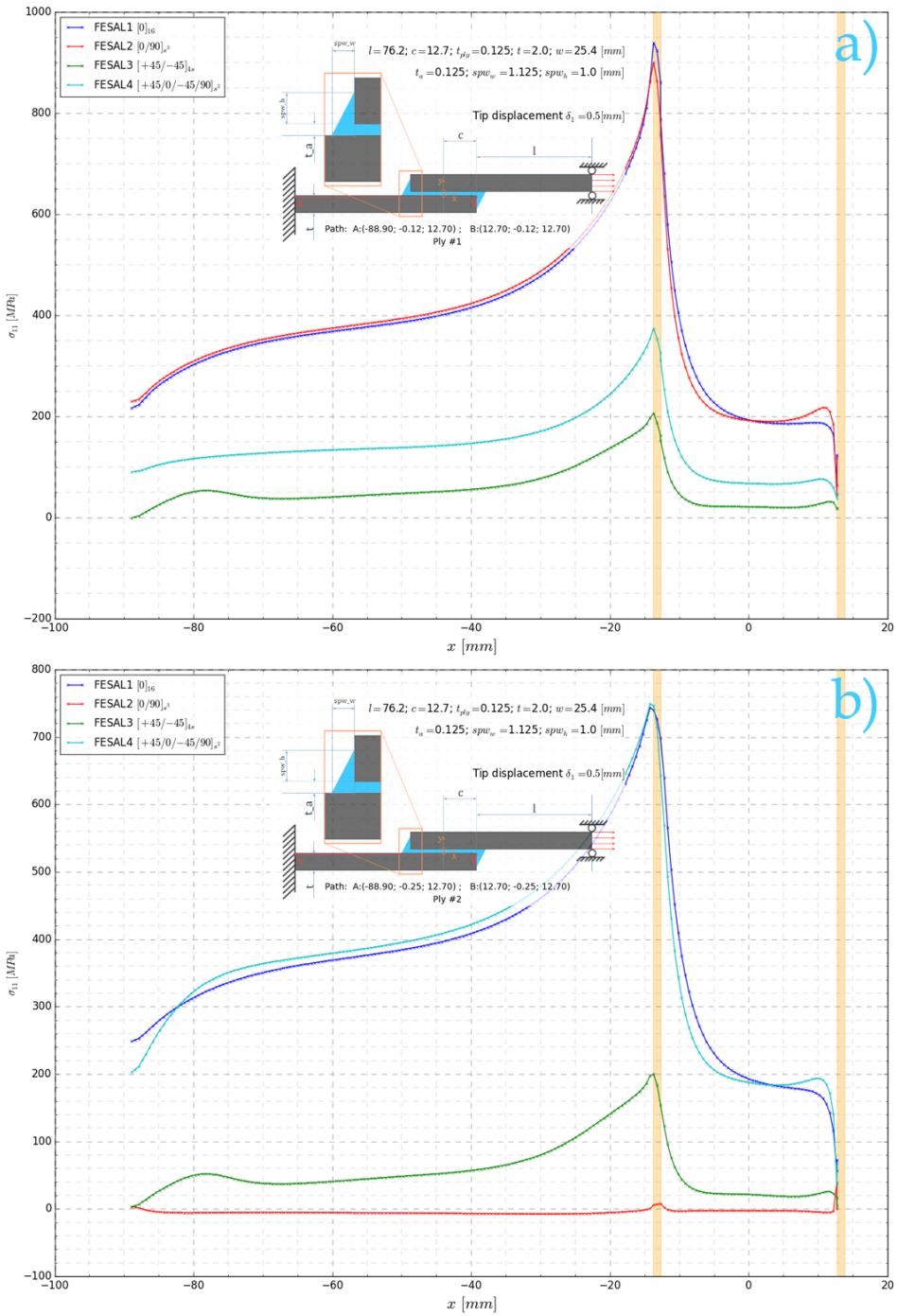

Figure 5.14: Normal stress in the direction parallel to the fibers σ_1 along: a) the first ply length and 2) the second ply length.

Illustrated in figure 5.15, the variation of peel stresses σ_2 in the adherend's plies is, perhaps, one of the most interesting and critical results of this study. The peel stresses are close to $0MPa$ for all laminates in most of the ply's length, except in the vicinity of both spews, where it suddenly reaches very pronounced peaks. This is even especially prominent for 0°plies, where for FESAL1 σ_1 reaches $50MPa$ in the first ply for a $\delta_x = 0.5mm$ prescribed displacement, roughly half of its correspondent transverse tensile strength $Y^T = 102MPa$. After this quite pronounced peak, the stresses dramatically drop to a compressive regime. Over the lap length, the peel stresses stay compressive and low in magnitude (approximately, $-5MPa$ for FESAL1's first ply right after the highest tensile peak). At the middle of the lap length, the plies experience very small peel stress values. The distribution along the lap region is asymmetric, showing higher peaks at the starting of the lap region rather than the its end. The stress concentration is higher for stiffer adherends.

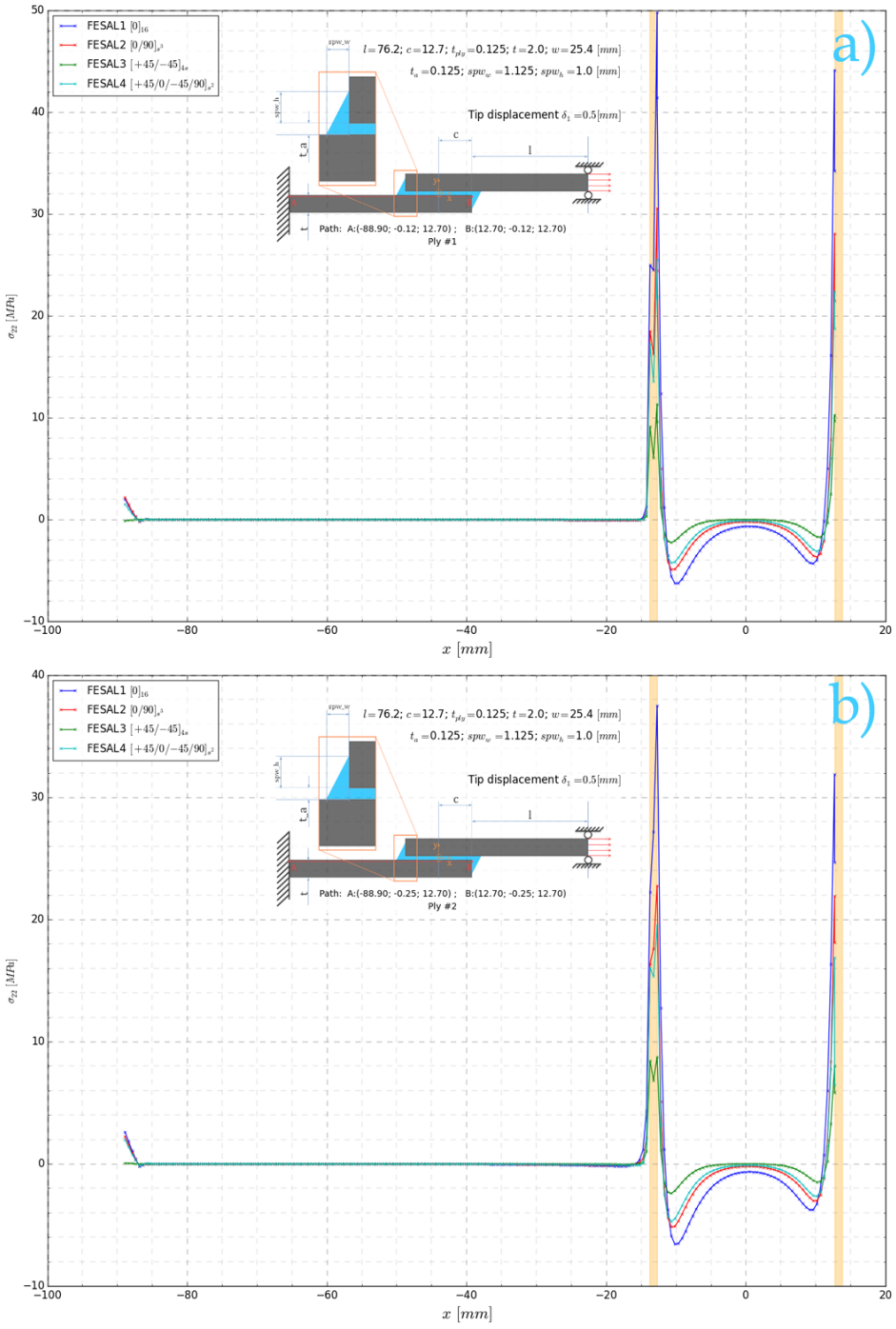

Figure 5.15: Out-of-plane stress σ_2 along: a) the first ply length and 2) the second ply length.

The longitudinal-transverse shear stress τ_{12} distribution along the length of the first two laminae (figure 5.16) shows a similar behavior to the peel stress σ_2 distribution, including the magnitude of the peak stresses. However, several differences were identified: while σ_2 stresses are typically higher on the start of the adherend overlap, τ_{12} stresses are typically higher at the end of the adherend overlap; furthermore, and following the same trend of the stress distribution in the adhesive path, while the peel stresses suddenly increase at the starting of the adherend overlap and then abruptly decrease to a compressive regime over the lap length, tending to zero in the middle of this region, the longitudinal-

transverse shear stress decrease from the first peak more gradually in a bathtub shape, growing to a higher peak at the end of the adherend overlap.

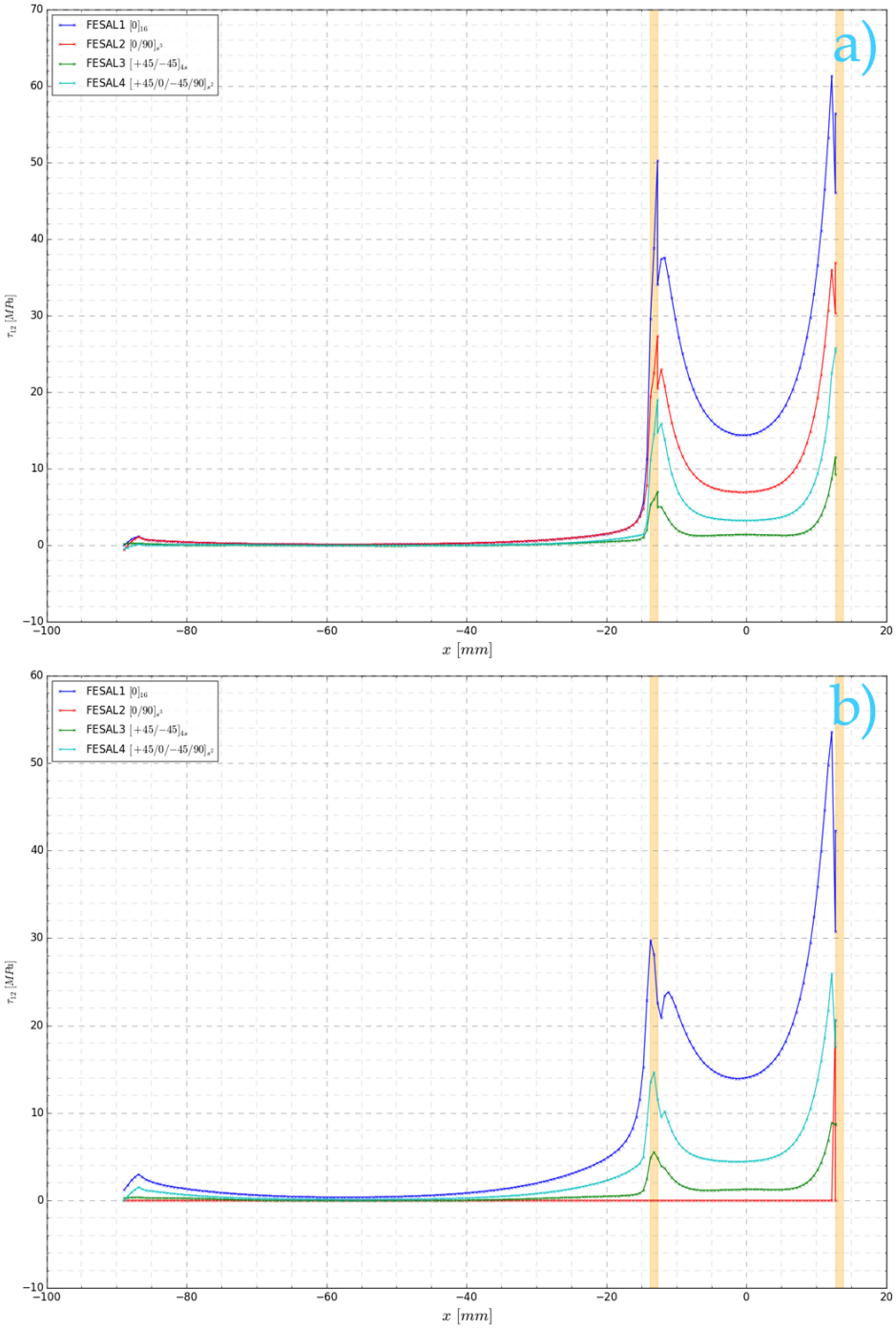

Figure 5.16: Longitudinal-transverse shear stress τ_{12} along: a) the first ply length and 2) the second ply length.

Check appendix P - figures P.23 and P.24 for all stress components along the two first adherend layer paths.

The trend of the transverse inplane stress σ_3 is quite similar to the trend of σ_1 but with the 90s showing the highest peak values (the 3-direction of a 90°oriented ply is aligned with the load x-direction, hence the ply stiffness is dominated by the matrix properties) and one order of magnitude smaller than σ_1 peaks.

Only the 45°oriented plies showed significant inplane shear stress τ_{13} values, which, as already explained, the 45°oriented plies are the ones that better resist to shear deformations.

Every layer orientation developed transverse shear τ_{23} stresses, except for the 0s. Two distinctive peaks were identified in the vicinity of the spew region.

5.3. Verification - failure envelopes

As noted before, the following analysis relates to the failure envelopes presented in appendix Q. The reason behind this relates to the size of the figures where the plots are contained being too large to be placed in the main body of the thesis.

Both von Mises and Hashin failure envelopes, figure P.25 and figure P.26 respectively, show a perfect agreement between the theory and the implemented failure criteria. Recalling that von Mises criterion rely in a single condition, its implementation was trivial.

As for Hashin criteria, this perfect correlation also suggests that the implemented matrix failure criteria (note that the Hashin's fiber mode is independent of the transverse stresses) equations are bug free.

Concerning Puck's failure criteria, when comparing failure envelopes for a GFRP under biaxial loading (σ_2, τ_{12}) a mismatch was found for the compressive matrix mode, particularly in mode C ($\sigma_n < 0$ and $\theta \neq 0$), as can be observed in figure P.27 - the trend defined by the blue markers does not match the theory. After an extensive search errors in the implemented theory, no bug was found in the code. Nonetheless, it should be emphasized that the present problem is a predominantly tensile load case, hence, even considering the Poisson effect, the compressive stresses in the transverse directions do not govern failure (as has been demonstrated in the preliminary stress study results 5.2). Given that the obtained predictions are more conservative than theory's predictions, only if the (unlikely) occurrence of compressive damage is detected, this implementation issue should be further investigated.

Also in conflict with theory, but consistent with the previously analysed failure envelope, is the biaxially loaded (σ_1, σ_2) failure envelope (figure P.28). Additionally to the compressive matrix failure disagreement, two additional features do not conform with the envelopes published by Puck and Schürman:

- First and most important is the rounded regions observed in the theory's failure envelope. There is no apparent reason for the existence of these rounded lines given that the theory does not suggest any interaction between FF and IFF. Both modes are analysed independently, even if both share stress components suchlike σ_2 and σ_3. As explained before, Puck's failure criteria are categorized as separate mode criteria rather than interactive criteria.

- The second aspect relates to the inclination of the FF envelope lines (in green) obtained after implementation, as opposed to the straight vertical lines shown in the article [85]. The authors suggest two ways of calculating FF: 1) as limit criteria, where the stress parallel to the fibers σ_1 is directly compared with the correspondent allowable (X^T for tensile fiber failure and X^C for compressive fiber failure); 2) as a separate mode criteria, by including the Poisson effects of the UD material and the fiber material properties, specifically. The former was used in the theory's failure envelopes and the latter in this work's implemented damage model.

Due to the fact that matrix failure in LaRC05 is also modeled based on Mohr-Coulomb's theory, the biaxial (σ_1, τ_{12}) failure envelope (figure P.29) is similar to Puck's for tensile matrix failure. Because Puck's model has additional considerations regarding the compressive mode, its failure envelope is closed by clearly defined compressive boundary. Contrariwise, LaRC05's compressive side is open, suggesting that (in theory) the material could withstand unrealistically high compressive inplane transverse stresses without failing, as long as the inplane shear stresses were small enough. Yet, with respect to verification, an equivalent (σ_2, τ_{12}) failure envelope was obtained for the implementation of LaRC's theory [82].

As for LaRC05-case 5 (figure P.30) for a GFRP laminate under triaxial normal loading ($\sigma_2, \sigma_1 = \sigma_3$), the obtained failure envelope matched the theory's failure envelope indicating that the matrix failure criterion is implemented correctly.

5.4. Validation

5.4.1. Load-displacement curves: experimental *vs.* FE model

For all laminates, the load-displacement curves of the FE model showed a stiffer behavior when compared against the tested specimens. This is specially true for the beginning of the analysis, at the non-linear region due to the rotation of the joint. At the linear region, this discrepancy is also verified (compare the stiffness k values of the FE model against the tested specimens in figures 5.17 - 5.20).

A possible reason for this over-stiff behavior might be related to the shear-locking behavior, particularly when using solid 3D elements (see subsection 4.7 for more details).

On the other hand, the justification for this response may result from manufacturing defects in the tested specimens. Voids in the adhesive or in the adherend[3] cause a 'more compliant' behavior of the whole structure.

After the ultimate point, the numerical model exhibits a softening behavior rather than a sudden failure, as shown by figure 5.21. This is an effect of the viscous regularization parameter (in this case $\mu_{vr} = 0.001$) in the adhesive material. Even though the use of this parameter does not significantly affect the ultimate load itself, it was found that it predicts a gradual dampened final failure which seemed artificial. As it was explained in more detail in subsection 4.4.3, the use of this parameter alleviates mesh dependency and

[3]The adherends were made of prepreg material cured in an autoclave. No remarks on manufacturing defects on adherends were reported in the article [55], hence the void volume fraction were likely lower than 1%.

ensures the analyst that the ultimate point was reached[4], despite its effect in polluting the results.

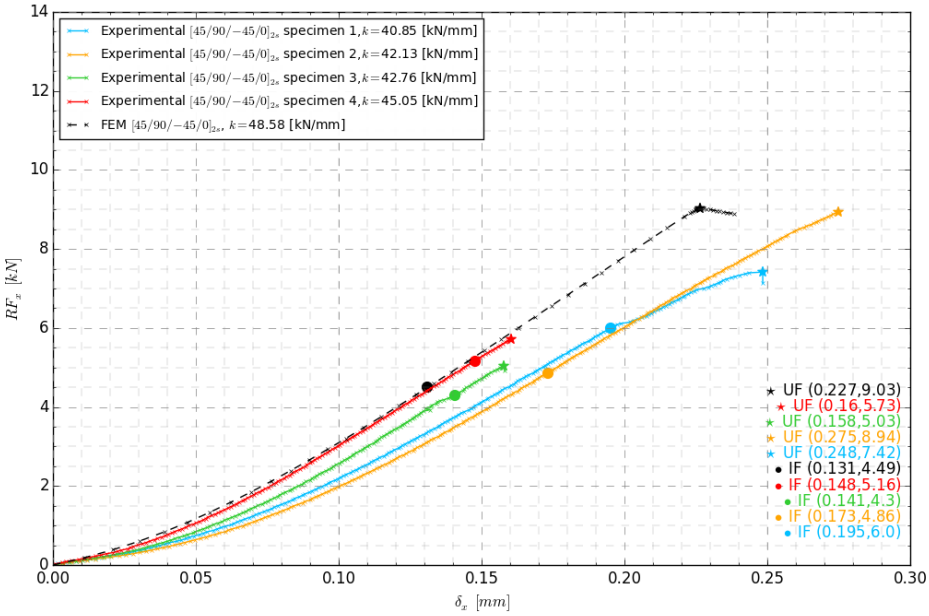

Figure 5.17: Experimental (solid lines) *vs.* FEA load-displacement curves (dashed lines), initial failure (IF) and ultimate failure (UF) events for the $[45/90/-45/0]_{2s}$ configuration. The displacements were measured at the extensometer arms positions: 60mm apart, adjacent to the overlap area.

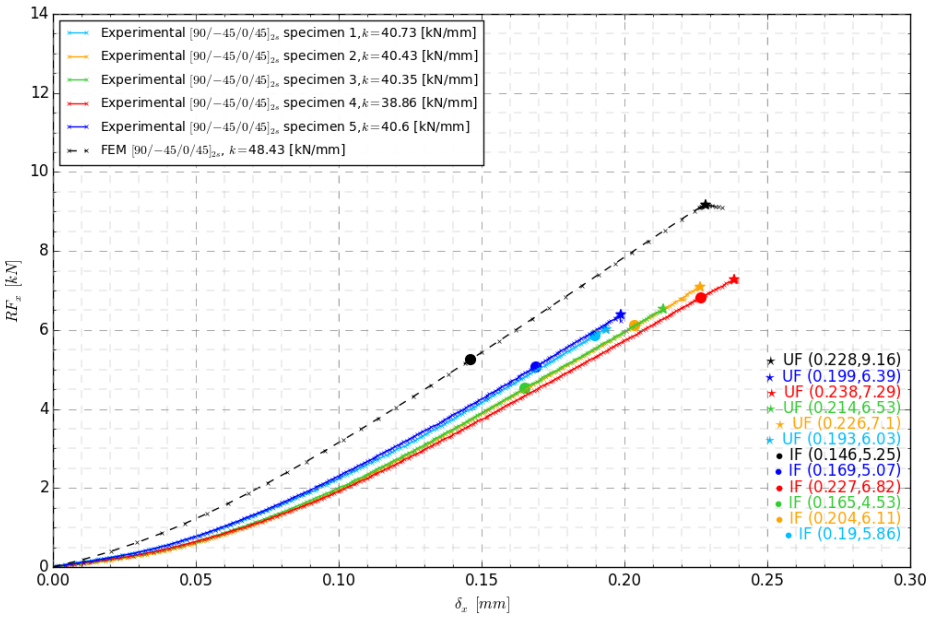

Figure 5.18: Experimental (solid lines) *vs.* FEA load-displacement curves (dashed lines), initial failure (IF) and ultimate failure (UF) events for the $[90/-45/0/45]_{2s}$ configuration. The displacements were measured at the extensometer arms positions: 60mm apart, adjacent to the overlap area.

[4]When viscous regularization was not used, the analysis often terminated with convergence issues without showing any softening behavior or any indication that the ultimate failure was reached. With the use of a viscous parameter, this uncertainty is removed.

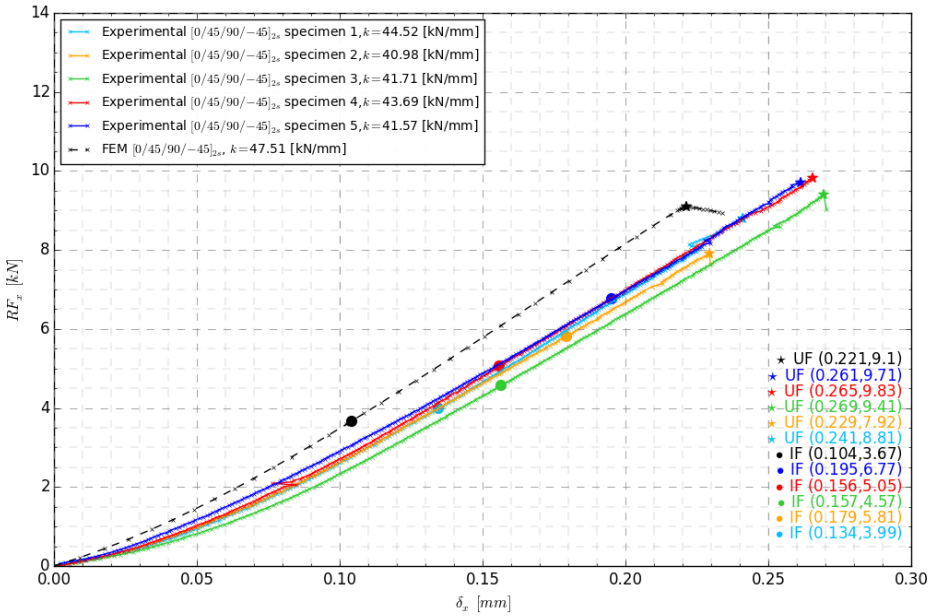

Figure 5.19: Experimental (solid lines) *vs.* FEA load-displacement curves (dashed lines), initial failure (IF) and ultimate failure (UF) events for the $[0/45/90/-45]_{2s}$ configuration. The displacements were measured at the extensometer arms positions: 60mm apart, adjacent to the overlap area.

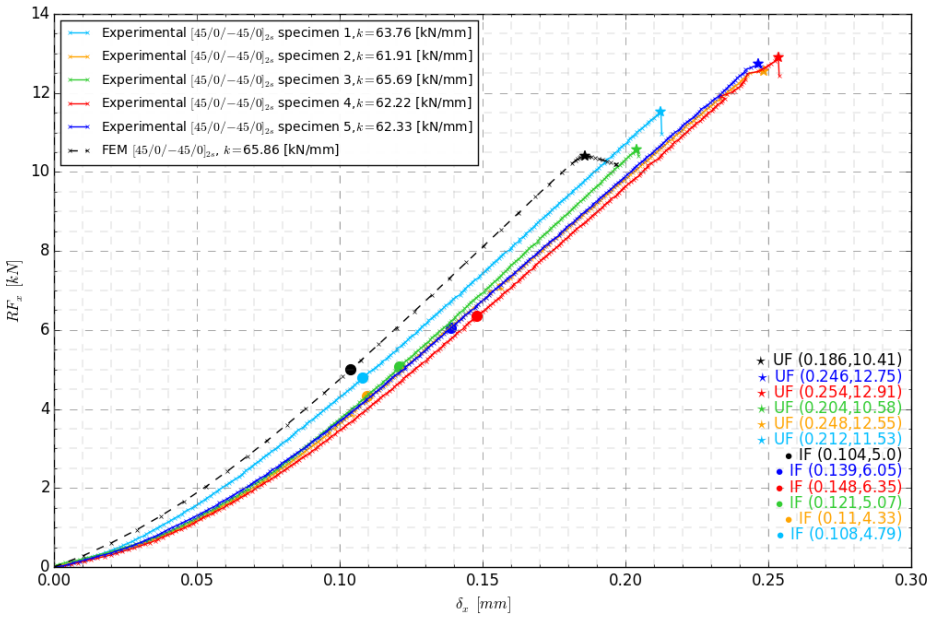

Figure 5.20: Experimental (solid lines) *vs.* FEA load-displacement curves (dashed lines), initial failure (IF) and ultimate failure (UF) events for the $[45/0/-45/0]_{2s}$ configuration. The displacements were measured at the extensometer arms positions: 60mm apart, adjacent to the overlap area.

Figure 5.21 compares the response of all configurations in the same chart. As expected, the laminate with eight 0s ($[45/0/-45/0]_{2s}$) is considerably stiffer than the others given the effect of this lamina orientation on both the longitudinal axial A_{11} and bending D_{11} stiffness components, which govern the material stiffness behavior of the joint.

Regarding the other three QI configurations, as expected, the one with the outermost 0°oriented ply ($[0/45/90/-45]_{2s}$) showed a stiffer behavior in the non-linear region, when compared to the two other configurations ($[45/90/-45/0]_{2s}$ and $[90/-45/0/45]_{2s}$), that presented a quite similar behavior among themselves. According to CLT, the relative position of the 0s in a laminate does not affect the longitudinal membrane stiffness E_{1m} but it does affect the longitudinal bending stiffness E_{1b}, reinforcing the notion that this initial nonlinear region is a bending-dominated problem.

The initial behavior is therefore dominated by the bending stiffness. At the linear region, no significant differences were noted among the three QI configurations considering that their longitudinal membrane stiffness is equal, as shown in table 4.9.

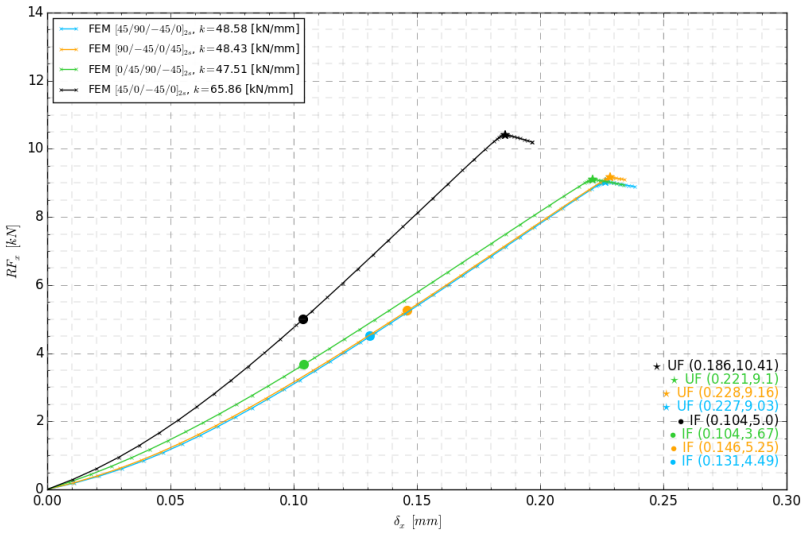

Figure 5.21: FEA load-displacement curves, damage initiation and ultimate failure events for the four different tested laminates.

5.4.2. Damage initiation and ultimate loads: experimental *vs.* FE model

Bar charts, contained in figures 5.22 and 5.23 show that the numerical model predicts generally well the experimentally measured damage initiation and ultimate loads. For all layups, the predicted damage initiation loads were found lower than the experimental averages, particularly for the $[0/45/90/-45]_{2s}$ case where the discrepancy was the highest. Nonetheless, some dispersion was found in the damage initiation and ultimate failure loads of the tested specimens, which is characteristic in the testing of composite materials.

In terms of relative differences, for the four tested configurations: $[45/90/-45/0]_{2s}$, $[90/-45/0/45]_{2s}$, $[0/45/90/-45]_{2s}$ and $[45/0/-45/0]_{2s}$, the PDM under-predicted the damage initiation loads by, 11.5%, 7.5%, 29.9% and 6.1%, respectively, in relation to the AE results. Regarding the ultimate load, the relative differences were quite discrepant: 33.2%, 37.4%, -0.4% and -13.71%, respectively.

Concerning the damage onset discrepancy, a plausible motive for this variability might be related with the used criterion to identify the onset of damage in the acoustic emission and in the numerical model. Regarding the acoustic emission criterion, while the energy burst might be a good parameter to define the onset moment considering that it is based on the number of hits and related amplitude in a given time period, the setting of the quantitative boundary is highly disputable as well as the parameter to which it should be normalized[5]. The condition used in the numerical model is also highly debatable. The first element to overcome the failure index of one might lead to an underestimation of the damage onset owing to the fact that these elements contained singularities, regions at which convergence was not obtained, resulting in a non-credible stress-state that was ultimately used to evaluate the failure index.

As for the ultimate failure, the softer configurations $[45/90/-45/0]_{2s}$ and $[90/-45/0/45]_{2s}$ showed the greater mismatch with the numerical model being less conservative than what was exhibited by the tested specimens. However, it should be noted that the former referred layup presented significant dispersion, probably related to manufacturing defects. By contrast, the laminate with the 0°outer ply showed a very good correlation between the numerical prediction and the experimental results.

In all three QI layups, the predicted ultimate failure was $\sim 9kN$ which seems to indicate that the sequence of a given layup does not influence the ultimate load in the adhesive. For the stiffer laminate ($[45/0/-45/0]_{2s}$), both methods suggest a considerably higher ultimate load but in this case, the numerical model laid on the conservative side. This indicates that by increasing the number of 0s the joint becomes stronger, as already suggest by Matthews and Tester [68].

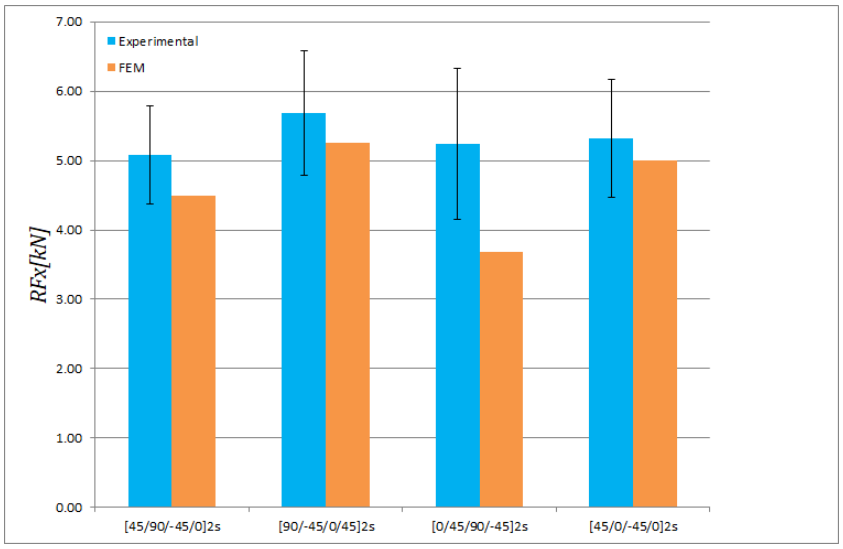

Figure 5.22: Experimental *vs.* FEA damage initiation loads for the four different tested laminates.

[5]Several statistical quantities might be used for this purpose, such as: average, maximum, total...

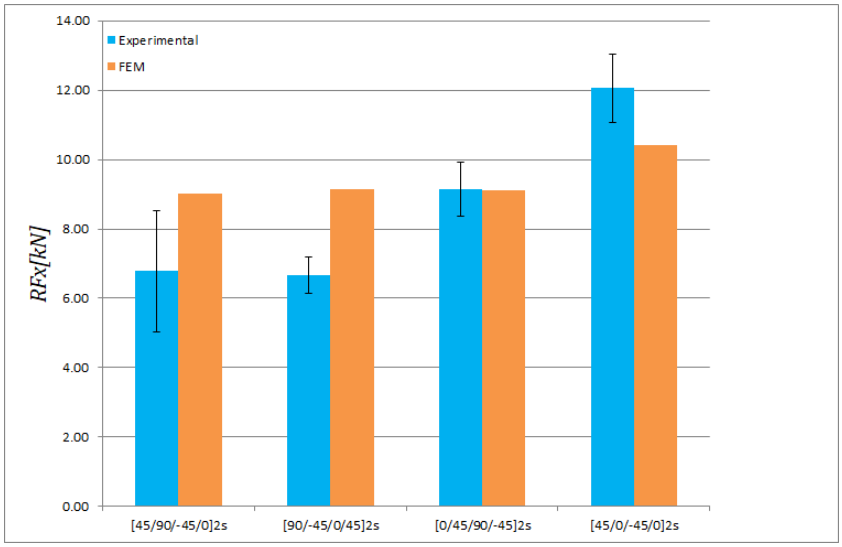

Figure 5.23: Experimental *vs.* FE model ultimate loads for the four different tested laminates.

Other plausible justifications for the mismatch between the numerical and experimental results might be related to: a) manufacturing defects in the tested specimens; b) model 'blindness' with respect to complex fiber-matrix interaction (material is homogenized); c) model incapacity of capturing the interfacial adhesive-adherend mechanical interaction.

The location of the predicted damage can be found in subsection 5.5 - figure 5.26.

5.4.3. Strain maps: experimental *vs.* FE model

Comparison between the DIC (top) and the FE model (bottom) results of the layup $[0/45/90/-45]_{2s}$ are presented in figures 5.24 and 5.25, for logarithmic strains ε_x and ε_{xy}, respectively.

For both analysed variables, the global strain field predicted by the DPM matches the test results. Even though differences were found in the maximum and minimum values for the analysed damage stages, these values were in the same order of magnitude and the gradients agreed.

At the lap ends of the adhesive interface, pronounced maximum tensile and shear values were found in both DIC and FEA for latter stages of damage propagation, as expected for the reasons already elaborated in the preliminary stress study results (appendix P). In contrast, the region around the free corners of the adherends was found practically unloaded, also anticipated considering the geometry of the joint and the load paths.

Negative shear strain ε_{xy} values were found in the opposite faces of the bonded region at the lap ends, meaning an inverse shear deformation, as already verified in the preliminary stress study in figure 5.12. In magnitude, these values were in the same order of magnitude as the maximum positive shear values. At the same region, the longitudinal strain ε_x showed residual values.

The strain maps obtained from the DIC contained some limitations that should be solved in further studies: a) the field area does not cover the entire lap region, *i.e.*, there is no strain information in the borders; b) the resolution should be enhanced for greater accuracy in extracting strain values, especially when zoomed actions are required; c) the speckle pattern should cover the non-bonded adherend region close to the lap ends since this is a critical region fairly close to the stress concentrations.

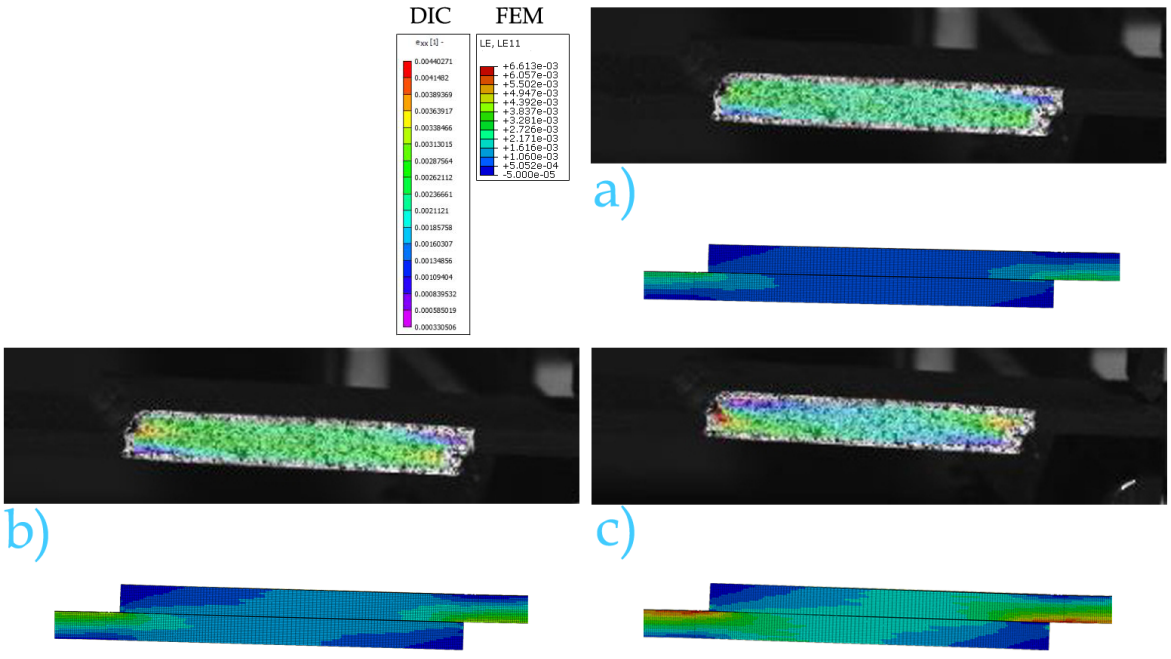

Figure 5.24: Experimental *vs.* FEA logarithmic longitudinal strain ε_x maps in the joint region at: a) damage initiation; b) average load value between damage initiation and ultimate failure; c) ultimate failure. The DIC results relate to layup $[0/45/90/-45]_{2s}$ - specimen 5.

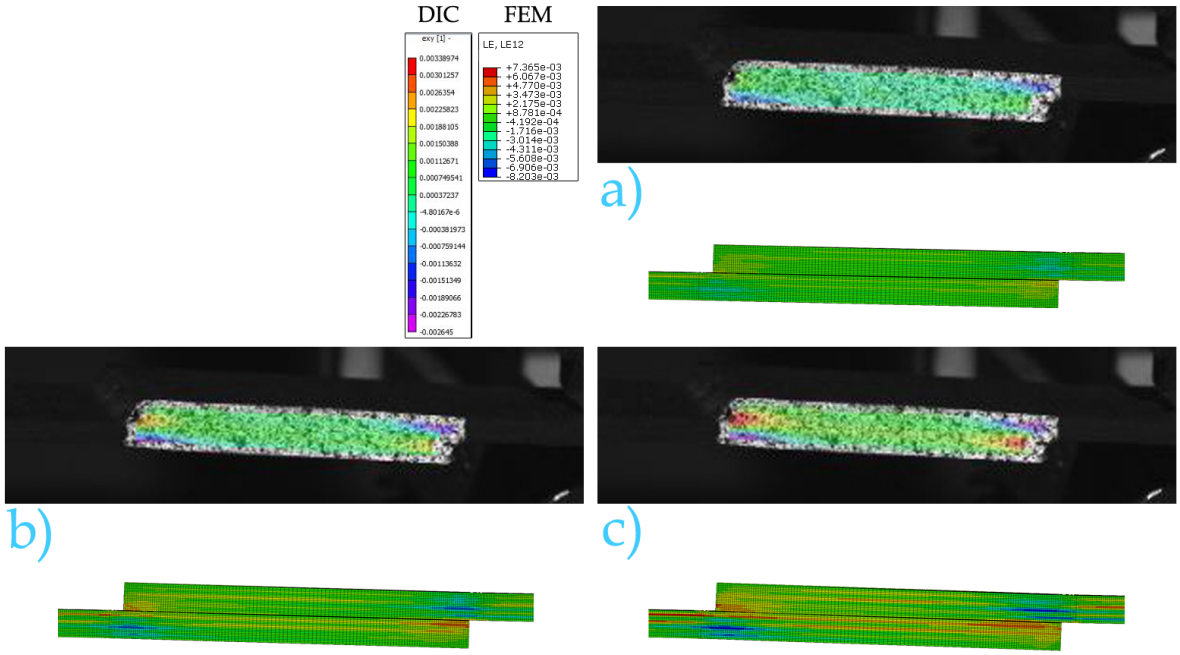

Figure 5.25: Experimental *vs.* FEA logarithmic shear strain ε_{xy} maps in the joint region at: a) damage initiation; b) average load value between damage initiation and ultimate failure; c) ultimate failure. The DIC results relate to layup $[0/45/90/-45]_{2s}$ - specimen 5.

5.4.4. Other remarks

The experimental results presented in the study of Kupski *et al.* [55] present different and complex failure modes for the different tested layups. Based on the available information, namely from mechanical testing, DIC and AE, it is not possible to trace-back the exact location where damage initiated nor exactly how it propagated. Hence, any attempts to pinpoint the damage initiation location in the tested specimens would be, in this case, speculative. In order to retrieve this data from testing, techniques such in-situ Computed Tomography (CT) scanning would have to be used (under the recommendations section, check subsection 6.2.3 where this matter was further developed). For this reason and considering the scope of this work, no comparison was made in terms of failure modes nor damage location. Yet, the following section 5.5 analyses solely within the scope of FEA the found damage maps, particularly the damage initiation region.

Several hypotheses might be formulated to suggest an explanation for the numerical findings that indicate damage initiation and propagation solely the adhesive until final failure:

- The assumption of a brittle adhesive might be contributing for an underestimation of damage due to unaccounted plasticity effects. This means that if the adhesive effectively behaves ductile, it is capable of absorbing more energy than a brittle idealization.
- The used CFRP and adhesive strength values taken from the datasheets might not correspond to the actual strength of the material. Significant discrepancies have been found between the published tested values and the ones declared by

the manufacturers: the adhesive EA 9695 AERO datasheet [44] provide a tensile modulus of 3100 MPa, whereas Kupski *et al.* [55] present 2019 MPa. The same applies to the tensile strength, 76 MPa against 48 MPa, respectively.
- Unaccounted damage modes such as interlaminar failure underestimated failure in the adherends. This hypothesis is less likely given that interlaminar failure is usually preceded of matrix failure that was not detected, yet, it should not be discarded.

From the analysis of the load-displacement curves of the tested specimens, it is noteworthy the scatteredness of the results in terms of stiffness, damage initiation and ultimate failure. This variability is common in the mechanical response of composite structures mostly due to manufacturing defects that lead to material and/or geometric uncertainties [17].

The lack of accuracy in centering the extensometer arms in the joint and 60mm apart might have induced an observational error in the displacement measurements that should not be disregarded.

Another noteworthy aspect of the global response of the tested specimens (figures 5.17 - 5.20) is an irregular and 'shaky' behavior. This can be explained by the activity of other laboratory massive machines during the testing campaign that produce vibrations that contaminate the test outcome.

The gradual softening behavior exhibited by the FE predictions after the ultimate point until the final failure was an artificial effect of the used viscous regularization coefficient of 0.001, since all tested specimen showed a rather sudden final failure. Studying the sensitivity of this parameter is out of the scope of this thesis, however, it was determined that as μ_{vr} increased, a more pronounced fictitious softening behavior was observed associated to a slightly lower ultimate load.

5.5. Failure index, degraded modulus and damage maps in the adhesive

The failure index, degraded modulus and damage maps in the adhesive of the $[0/45/90/-45]_{2s}$ configuration showed a coherent match of the values of these parameters for different stages of damage propagation, as shown in figure 5.26.

At damage initiation [figure 5.26 a)], the failure index (according to the von Mises criterion) in the lap ends reached one. At this moment, the Young's modulus is still not degraded and the damage variable remained equal to zero.

At the average load value between damage initiation and ultimate failure [figure 5.26 b)], the failure index continued to increase around the lap ends and throughout the whole width of the joint. In agreement, the damage variable increased to nearly half unit, consequently degrading the Young's modulus to half of its value.

At the ultimate failure [figure 5.26 c)] significant damage propagation can be identified in the damage maps with $\sim$ 20% of the adhesive area completely degraded. At final failure [figure 5.26 d)] only less than 70% is predicted to carry any load. Appendix R - figure P.31 shows the Young's modulus evolution over time, in selected elements of the

adhesive layer.

On a related note, the maps propagate in a non-symmetric (with respect to the $x-y$ plane) diagonally manner. The reason behind this is the fact that the adherends are non-antisymmetric layups. Based on the CLT (see appendix F for more details) this type of laminates are prone to bending-twisting coupling due to the fact that the entries D_{16} and D_{26} are non zero. Put differently, when the joint undergoes in bending, because of its non-antisymmetric configuration, a twisting response is induced. By its turn, this twisting behavior affects the stress-strain field of the adhesive which governs the damage progression model.

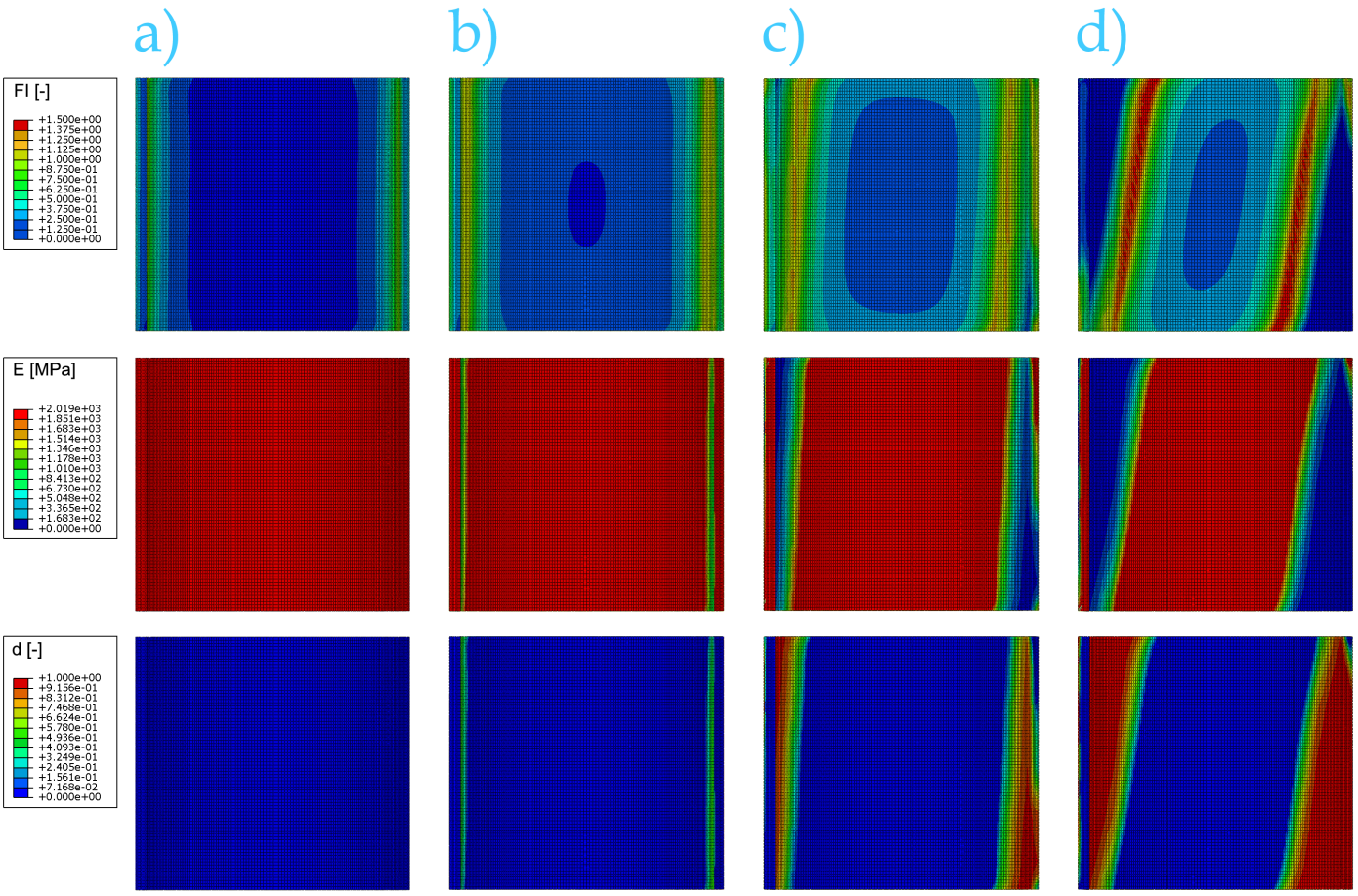

Figure 5.26: Failure index (FI), Young's modulus (E) and damage (d) maps in the adhesive of the $[0/45/90/-45]_{2s}$ at: a) damage initiation; b) average load value between damage initiation and ultimate failure; c) ultimate failure and d) final failure.

5.6. Failure index maps in the adherends at ultimate load

At the ultimate load of the numerical analysis, no damage was detected in the adherends, meaning that before any damage event took place in the matrix or fibers of the composite

plates, the structure reached its ultimate failure due to the damage accumulation in the adhesive. This was not verified in the experiments were damage in the adherends was observed after the tests in all configurations, except in the $[0/45/90/-45]_{2s}$, where mostly cohesive failure of the adhesive was verified. Even though the identified failure modes in the remaining cases suggested complex and coupled failure modes: matrix failure in the adherends, interlaminar failure and interface/cohesive failure, as explained before, no information was provided related to in which phase damage started nor how it propagated. Without the data from methods such in-situ CT scan, further attempts to validate numerical models are not sufficiently solid. Further research in this matter should focus in this validation issue.

The failure index maps of the $[0/45/90/-45]_{2s}$ at the ultimate failure are illustrated in figure 5.27 and the maximum tensile fiber and matrix indices (FFT and MFT, respectively) and correspondent layers are presented in table 5.1.

Regarding the tensile fiber failure, Hashin, based in curve fitting alone, is the most optimistic criterion presenting approximately half of the failure index of Puck and LaRC05 (table 5.1). Following a simplified approach, LaRC05 uses the ratio between the stress component parallel to the fibers with the respective allowable. Added to that ratio, Puck uses the contribution of the fiber properties and the Poisson effect, which has little effect on the failure envelopes as explained by the authors in [85]. The resulting failure indices FFT of these two criteria are, therefore, quite similar.

Both Puck and LaRC05 based the matrix failure criterion on Mohr-Colomb's theory as properly elaborated in sub-section , under the assumption that the fracture plane angle is the one that maximizes the matrix failure index. Despite this, the final formulations of the failure conditions are entirely different, which explains the significant difference among the maximum MFT values found (table 5.1). Hashin, on the other hand is purely heuristically based, resulting in a more pessimistic MFT values.

Because the implemented CDMs rely on the stress state alone, it is predictable that the critical region is located at the lap ends. Furthermore, as for fiber failure, the critical layer is, undoubtedly, the 0°oriented ply next to the adhesive layer; owing to the facts that: 1) this layer contains a singularity which, in practice, results in stress concentration and 2) the fibers are aligned with the applied, making the stress component parallel to fibers σ_1 the dominant component; this can be explained by the high material stiffness E_1 in this direction, which is dictated by the fibers modulus, consequently 'attracting' more stresses.

In its turn, matrix potential failure is predominant in the $\pm 45°$and in the 90°direction; with the former presenting greater deformation. Failure in the plies oriented in these directions is govern by the relationship between a high normal tensile transverse (σ_2 and σ_3) and shear (τ_{12} and τ_{13}) stress state and their respective tensile allowables (Y^T and S^L).

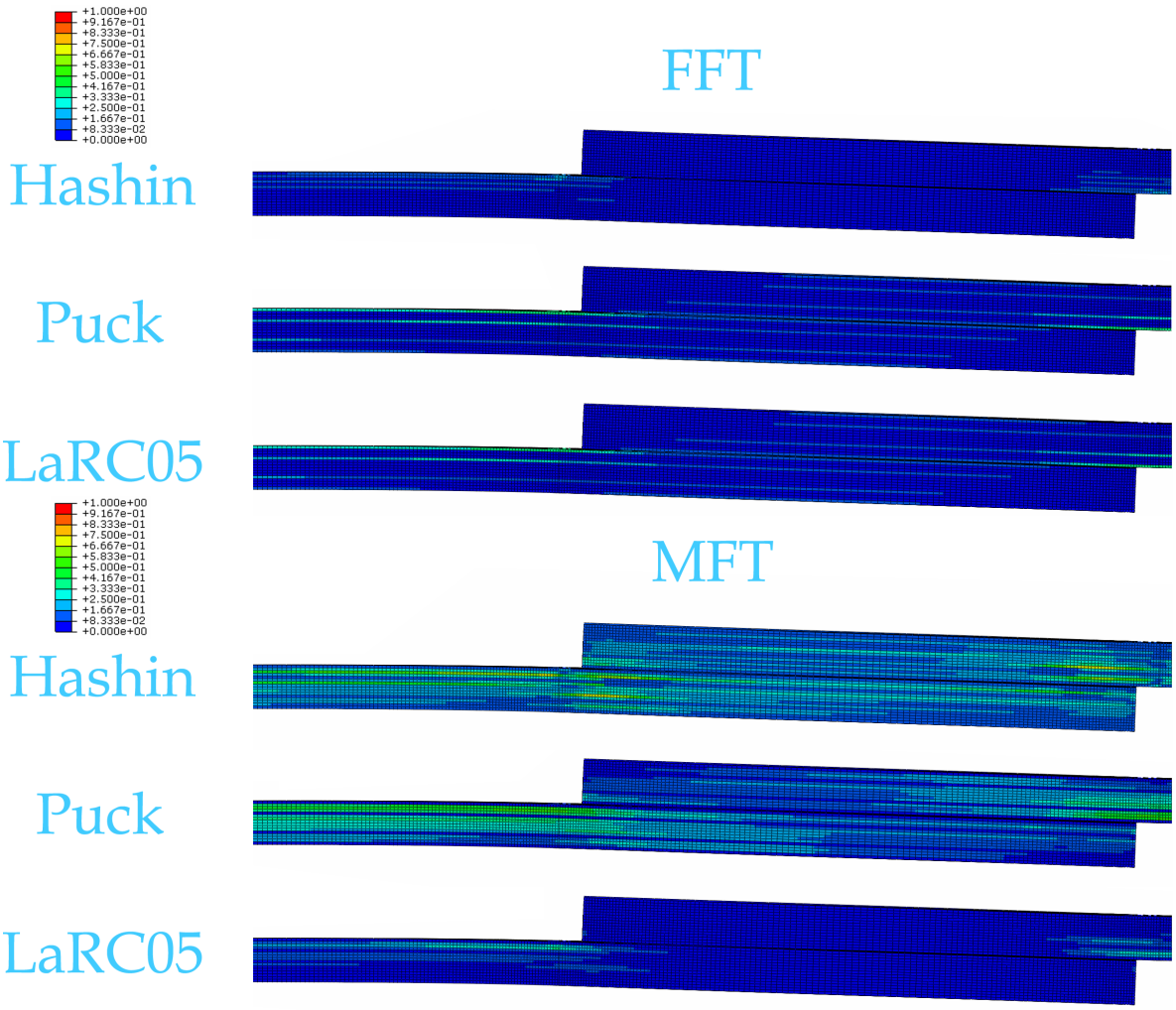

Figure 5.27: Failure index maps of the $[0/45/90/-45]_{2s}$ at the ultimate failure: tensile fiber failure index (FFT) and tensile matrix failure index (MFT) for different adherend failure criteria.

Table 5.1: Maximum failure index values and correspondent layers of the $[0/45/90/-45]_{2s}$ at the ultimate failure for the different failure criteria.

	Hashin	Puck	LaRC05
FFT	0.207	0.409	0.410
At layer(s)	1	1	1
MFT	0.704	0.567	0.342
At layer(s)	3	2,3	2,3

The proposed DPMs seem to under-predict the failure in the adherends. Owing to the fact that the damage degradation models were not activated in the adherends, further analysis in this matter is limited. Notwithstanding, new physically-based features should be added to these models such that the physical phenomena can be modeled in a more realistic manner. Also, despite the underlying challenges, DPMs should be able to capture the interaction between failure modes. For this, a blended approach with fracture mechanics based methods may be a valid solution, as elaborated in the recommendations section 6.2.

6

Conclusions and recommendations

6.1. Conclusions

This thesis aimed to develop and compare DPMs in the framework of CDMs capable of accurately predict the global response, damage initiation, propagation and ultimate failure of ABSLJ made of different FRP layup configurations under an uniaxial quasi-static tensile load. From the analysis of the results, the following conclusions can be drawn:

- The global response of a FRP ABSLJ is firstly non-linear due to the joint's rotation originated by the load eccentricity, which is governed by the structure's antisymmetric geometry. In this region, the longitudinal bending stiffness govern the structural behavior of the ABSLJ, due to the bending-nature problem. After stabilization, the structure is governed by the membrane stiffness and behaves linearly.
- Numerical results using 3D solid elements tend to exhibit a stiffer behavior when compared to tested specimens, particularly in the initial non-linear region. The reasons behind this might relate, among others, to manufacturing defects in the experimental study or shear-locking effects of the 3D solid elements in the numerical model.
- In the numerical predictions, the QI laminates showed quite similar global responses in the linear region ($k = 48.17 \pm 0.9 kN/mm$). This can be explained by the fact that the longitudinal membrane stiffness is independent of the layup sequence. Nonetheless, the $[0/45/90/-45]_{2s}$ case exhibited a slightly stiffer bending behavior due to relative position of the 0s, as the outmost plies, giving it a considerably higher longitudinal bending stiffness which resulted in a stiffer behavior during the initial rotation of the joint.
- The $[45/0/-45/0]_{2s}$ showed a much stiffer behavior ($\sim$35% higher) in the linear region when compared to the other three QI laminates. In spite of having the same total number of plies, in place of 90°oriented laminae, this laminate had 0 (doubling its number in relation to the QI configurations) which resulted in an enhanced longitudinal membrane stiffness.
- The numerical results suggest that the layup sequence of QI adherend layups seem to not significantly affect the ultimate load, *i.e.*, the three QI laminates, with an

equal longitudinal membrane stiffness exhibited similar ultimate loads.

- In contrast, both numerical and experimental results suggest that the load at which damage starts is affected by the neighboring ply of the adhesive. Owing to small sample size and dispersion of the damage initiation loads, it was not possible to establish a clear relationship between the effect of the neighboring ply on this parameter.
- The use of viscous regularization of 0.001 in the adhesive with a time increment of 0.092 seconds seems to be large enough to pollute the results. While its use stabilized convergence and presumably alleviated mesh dependency, its value was high enough to introduce artificial damping effects.
- For the current geometry and materials, numerical predictions suggest that damage started in the adhesive and propagated until final failure of the structure even before any damage event have taken place in the adherends. Conversely, the experimental campaign indicated different and complex failure modes among the tested specimens.
- The predicted strain maps were in agreement with the DIC results for different stages of damage propagation, showing high strain values at the lap ends (due to the stiffness jump of the overlap region) and low strained regions at the unloaded free corners.
- Even for the layup with the 0°outmost lamina, the found damage patterns in the adhesive were not symmetric, in fact were found skewed. This was attributed to the fact that the layups were not anti-symmetric which results in a bending-twisting coupling. The twisting response induced by bending results in an asymmetric pattern.
- The available experimental data, including the load-displacement results from the mechanical testing, AE and DIC results are not sufficient to assess the damage progression in composite structures. New experimental techniques for damage assessment such as in-situ CT-scan mechanical tests are required for a more complete validation of the DPM.

6.2. Recommendations

6.2.1. Continuum damage model

6.2.1.1. Numerical issues

Mesh dependency is one major vulnerability of CDMs. During the softening process, the material tangent stiffness matrix can loose the positive definiteness, becoming ill-posed. At this point, the numerical solutions are mesh dependent which means that the amount of dissipated energy throughout crack propagation tends to zero upon mesh refinement [86]. This issue may be mitigated by using other integral models such as the crack band method or gradient based models.

As mentioned before, another expeditious method to mitigate mesh dependency is by regularizing the damage variable based on the viscous coefficient and time step. The effects of the introduction of viscous regularization for a given time step should be further studied for both the adhesive isotropic material and the adherend anisotropic material.

The spew geometry greatly affects the peak stresses at the lap ends, as suggest Lang and Mallick [56]. The authors concluded that by smoothing the transition of the spew in the adhesive-adherend interface, the stress concentrations were alleviated. A triangular idealization of the spew introduces two sharp corners, *i.e.*, singularities. By using an 'arc-shaped' spew, these singularities are eliminated because tangential continuity in the structure is assured. The authors of the referred article found an overall greatest reduction when an 'arc-shaped' spew is used. When compared to a square-ended spew geometry, an arc geometry achieved a local reduction of 60% in the shear stress, 87% in the peel stress and 35% in the longitudinal stress. In contrast, the configuration used in the present thesis (half triangular) achieved, 45%, 71% and 28% reduction, respectively. It is recommended that the effect of the spew geometry is extended from a stress study to a damage progression study.

6.2.1.2. Plasticity in the adhesive

Because most adhesives present a ductile behavior with a highly non-linear load-displacement response, plasticity should be modeled in the proposed CDMs so that a more realistic behavior of the ABSLJ is obtained. Modeling plasticity is not trivial, thence a literature study on the subject is recommended for a more detailed understanding on the subject.

6.2.1.3. Interlaminar failure

The proposed model is not capable of capturing delaminations which are likely to occur considering the significant peel (associated with mode I fracture) and shear stresses (associated with mode II fracture) at the lap ends regions [62, 98]. Two discrete crack models particularly stand out for modeling delaminations in a FE environment [34, 108].

Particularly, the Virtual Crack Closure Technique (VCCT) is the most widely implemented approach via FEM to simulate delamination within the framework of linear elastic fracture mechanics [89, 110]. This technique determines strain energy release rate based on the assumption that the strain energy released in the expansion process of an infinitesimal crack by a small amount is equal to the amount of the work required to close the crack to its original state [28, 54, 59].

Another popular method in the framework of discrete modeling is the Cohesive Zone Model (CZM) which does not require a pre-existent crack and present no restrictions with regard to the size of the damaged region. For its wider range of application and capability of capturing crack initiation and propagation [89], the CZM is increasingly used for general PDA of composites, specifically for delamination modeling [35, 72, 89, 118]. Moreover, Campilho and Fernandes [15] suggest that this technique is particularly attractive for adhesively bonded joints considering the prime influence of ductility and related stress gradients in the fracture process.

Blending the CDM approach to capture intralaminar failure with one of these methods to model interlaminar failure might result in a more realistic damage progression modeling. On this framework, Van Dongen [110], van Oostrum [111] and Bobeldijk [9] developed relevant work, in fact the materialization of this collective effort was named Progressive Blended Damage Analysis (PBDA) software.

6.2.1.4. Introducing the manufacturing defects in the model

Within the framework of CDMs, the effect of damage is included in the model by degrading the elastic properties of the material. Following this reasoning, also manufacturing defects could be accounted in the model through the introduction of material property penalty factors, *e.g.* the relation between the void content in an adhesive and its effective stiffness could be further studied.

6.2.2. Smeared representation of the crack

One of the main shortcomings of CDMs is that their inability to physically represent the matrix cracking. Instead, this approach results in a smeared representation of damage over the laminate's laminae leading to unrealistic damage patterns [86, 110]. The reason behind this relates to the homogenization of the inherently multi-phased composite material. Consequently, the CDM relies on the association of the damage mechanisms with their overall and 'smeared' effect on the mechanical properties of the material, in practice by means of material property degradation models.

In order to obtain more realistic and accurate damage patterns, an explicit incorporation of discrete cracks in FEM is required. Concerning intralaminar damage, phantom-node eXtended Finite Element Method (XFEM) approach is a major candidate for modeling cracks with arbitrary orientations that might even coalesce into delaminations. With this respect, van der Meer [108] concludes that the XFEM phantom node method accurately captures and models the interaction between matrix cracks and delamination.

Song, Areias and Belytschk developed an efficient and accurate method for modeling arbitrary dynamic crack propagation using phantom nodes [95]. These phantom nodes were introduced to represent the discontinuity of the cracked elements.

If no damage occurs at the element level, then the element is intact and each phantom node is constrained to its corresponding real node. Otherwise, the cracked element splits into two parts. Depending on the orientation of the crack, each part is formed by a combination of some real and phantom nodes, as it is illustrated in figure 6.1.

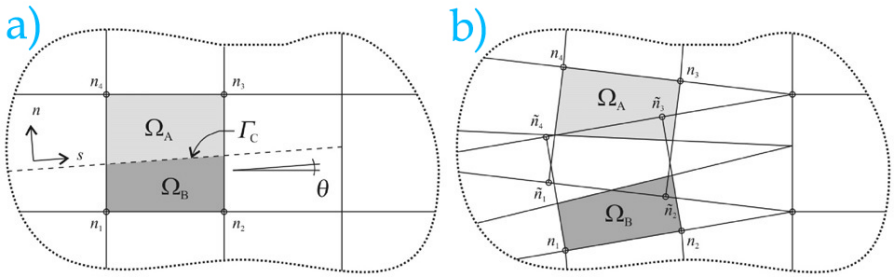

Figure 6.1: Damage propagation in XFEM using the phantom nodes concept: a) before partitioning and b) after partitioning of cracked element. (Reproduced from [16], copyright Elsevier, 2011).

Blending CDMs with discrete methods such as XFEM to capture the multiple crack propagation without the need of mesh updating seems a promising approach towards accurate PDA of FRPs. Nonetheless, Van Dongen *et al.* [110] point out difficulties in its

implementation in Abaqus environment.

6.2.2.1. Insitu strength effects

Considering that the numerical model predicted damage only in the adhesive, the effects of insitu properties in the adherend composite material were not studied. Further studies with relatively weaker adherends should investigate the validity of including these insitu effects.

6.2.3. Experimental studies

6.2.3.1. Sample size

Generically, in order to have a higher confidence level and power of the experimental study to draw conclusions, a larger sample size is required. This is particularly true for the testing of composite structures, which typically show high level of variability in the measured parameters, particularly and relevant to this study: stiffness, damage initiation load and ultimate load.

6.2.3.2. Imaging/scanning of the damage progression

One of the greatest challenges in studying damage progression in FRP composite structures is to detect exactly where the crack initiates and how and where to it propagates. This requires the use of state-of-the-art non-destructive testing methods that provide images or scans of the crack evolution over time.

Techniques such as Computed Tomography (CT) scanning can be used to validate the numerical results presented in sections 5.5 and 5.6, concerning the damage accumulation over time through time-lapse imaging. This non-destructive method provides high resolution 3D imaging of materials by means of combinations of X-ray images taken from different angles that allow a 3D visualisation of the specimen as well as detailed cross-sectional representations of the location and extent of different failure modes.

Yu *et al.* [117] state that in-situ CT scanning promotes the crack event visibility given that the imaging of the composite specimen is performed under load application.

Since in-situ CT scanning can be too expensive and requires specialized testing equipment, a practicable alternative is the ex-situ approach. In concrete terms, while tensile testing the specimen, once damage initiation is detected, the test stops and the specimen is submitted to CT scan test. Having gathered the CT data, the specimen is then submitted to the remaining load until final failure.

For the purpose of validation of models using the discrete crack approach, the use of (high resolution) high speed camera can provide image data regarding the crack growth at the specimen's lateral face. The main limitation of this technique is that no information regarding the interior of the specimen is known, where all the damage action might take place.

Bibliography

[1] ABAQUS. Abaqus Analysis User's Manual, 2014. URL `http://abaqus.software.polimi.it/v6.14/books/usb/default.htm`.

[2] Z. Apalak, M. Apalak, and M. Genc. Progressive damage modeling of an adhesively bonded unidirectional composite single-lap joint in tension at the mesoscale level. *Journal of Thermoplastic Composite Materials*, 19:671–702, 2006. doi: 10.1177/0892705706067487.

[3] ASTM D5573. Standard Practice for Classifying Failure Modes in Fiber-Reinforced-Plastic (FRP). Technical report, ASTM International, 2011.

[4] M. Aydin. 3-D nonlinear stress analysis on adhesively bonded single lap composite joints with different ply stacking sequences. *Journal of Adhesion*, 84:15–36, 2008. doi: 10.1080/00218460801888359.

[5] Alan Baker, Stuart Dutton, and Donald Kelly. *Composite Materials for Aircraft Structures*. American Institute of Aeronautics and Astronautics, Blacksburg, second edition, 2004.

[6] M D Banea and L F M da Silva. Adhesively bonded joints in composite materials: An overview. *Proceedings of the Institution of Mechanical Engineers, Part L: Journal of Materials: Design and Applications*, 2009. ISSN 1464-4207. doi: 10.1243/14644207JMDA219.

[7] B. Bednarcyk, P. Yarrington, C. Collier, and S. Arnold. Progressive Failure Analysis of Composite Stiffened Panels. In *47th AIAA/ASME/ASCE/AHS/ASC Structures, Structural Dynamics & Materials Conference*, Newport, 2006. American Institute of Aeronautics and Astronautics.

[8] G. Belingardi, L. Goglio, and A. Tarditi. Investigating the effect of spew and chamfer size on the stresses in metal/plastics adhesive joints. *International Journal of Adhesion and Adhesives*, 2002. doi: 10.1016/S0143-7496(02)00004-0.

[9] M. Bobeldijk. *A progressive blended fatigue framework for FRPs*. PhD thesis, TU Delft, 2018.

[10] S. Budhe, M. D. Banea, S. de Barros, and L. F.M. da Silva. An updated review of adhesively bonded joints in composite materials. *International Journal of Adhesion and Adhesives*, 2017. ISSN 01437496. doi: 10.1016/j.ijadhadh.2016.10.010.

[11] P. Camanho. Progressive failure analysis of advanced composites. Technical report, INEGI, Porto, 2008.

[12] P. Camanho and F. Matthews. A Progressive Damage Model for Mechanically Fastened Joints in Composite Laminates. *Journal of Composite Materials*, 33(24): 2248–2280, 1999.

[13] P. Camanho, C. Dávila, S. Pinho, L. Iannucci, and P. Robinson. Prediction of in situ strengths and matrix cracking in composites under transverse tension and in-plane shear. *Composites Part A: Applied Science and Manufacturing*, 37:165–176, 2006. doi: 10.1016/j.compositesa.2005.04.023.

[14] P. Camanho, A. Turon, and J. Costa. Delamination propagation under cyclic loading. In S. Sridharan, editor, *Delamination behaviour of composites*, chapter 17, pages 485–513. Woodhead, Cambridge, 2008.

[15] R. Campilho and T. Fernandes. Comparative Evaluation of Single-lap Joints Bonded with Different Adhesives by Cohesive Zone Modelling. In *1st International Conference on Structural Integrity*, pages 102–109. Procedia engineering, 2015. ISBN 9784931136052. doi: 10.1016/j.proeng.2015.08.047.

[16] R. Campilho, M. Banea, A. Pinto, L. Da Silva, and A. De Jesus. Strength prediction of single- and double-lap joints by standard and extended finite element modelling. *International Journal of Adhesion and Adhesives*, 31:363–372, 2011. doi: 10.1016/j.ijadhadh.2010.09.008.

[17] A. Carvalho, T. Silva, and M. Loja. Assessing Static and Dynamic Response Variability due to Parametric Uncertainty on Fibre-Reinforced Composites. *Journal of Composites Science*, 2(6), 2 2018. doi: 10.3390/jcs2010006.

[18] N. Chandarana, D. Sanchez, C. Soutis, and M. Gresil. Early damage detection in composites during fabrication and mechanical testing. *Materials*, 10:685, 2017. doi: 10.3390/ma10070685.

[19] Lucas da Silva, Andreas Ochsner, and Robert Adams. *Handbook of Adhesion Technology*. Springer Heidelberg, Berlin, first edition, 2011.

[20] Isaac Daniel and Ori Ishai. *Engineering mechanics of composite materials*. Oxford University Press, New York, second edition, 2006.

[21] C. Dávila and P. Camanho. Failure Criteria for FRP Laminates in Plane Stress. Technical report, National Aeronautics and Space Administration, Hampton, 2003.

[22] C. Dávila, C. Rose, and P. Camanho. A procedure for superposing linear cohesive laws to represent multiple damage mechanisms in the fracture of composites. *International Journal of Fracture*, 158(2):211–223, 2009. doi: 10.1007/s10704-009-9366-z.

[23] J. Dow. Shear Locking, Aspect Ratio Stiffening, and Qualitative Errors. In *A Unified Approach to the Finite Element Method and Error Analysis Procedures*, chapter 12, pages 271–305. Academic Press, 1999.

[24] N. Dowling. *Mechanical Behavior of Materials*. Pearson, Upper Saddle River, fourth edition, 2012.

[25] A. Duarte, A. Sáez, and N. Silvestre. Comparative study between XFEM and Hashin damage criterion applied to failure of composites. *Thin-Walled Structures*, 115:277–288, 2017. doi: 10.1016/j.tws.2017.02.020.

[26] G. Dvorak and N. Laws. Analysis of Progressive Matrix Cracking In Composite Laminates II. First Ply Failure. *Journal of composite materials*, 21:309–329, 1987.

[27] G. Dvorak, N. Laws, and M. Hejazi. Analysis of Progressive Matrix Cracking in Composite Laminates I. Thermoelastic Properties of a Ply with Cracks. *Journal of composite materials*, 19:216–234, 1985.

[28] P. Elisa. Virtual Crack Closure Technique and Finite Element Method for Predicting the Delamination Growth Initiation in Composite Structures. In P. Tesinova, editor, *Advances in Composite Materials - Analysis of Natural and Man- Made Materials*, chapter 19, pages 463–480. Intech, Rijeka, 2014. URL `www.intechopen.com`.

[29] A. Forghani, M. Shahbazi, N. Zobeiry, A. Poursartip, and R. Vaziri. An overview of continuum damage models used to simulate intralaminar failure mechanisms in advanced composite materials. In P. Camanho and S. Hallet, editors, *Numerical Modelling of Failure in Advanced Composite Materials*, chapter 6, pages 151–173. Woodhead, Vancouver, 2005.

[30] M. Garnich and V. Akula. Review of Degradation Models for Progressive Failure Analysis of Fiber Reinforced Polymer Composites. *Applied Mechanics Reviews*, 62 (1), 2009. doi: 10.1115/1.3013822.

[31] M. Goland and E. Reissner. The stresses in cemented joints. *Journal of Applied Mechanics*, 66:A17–A27, 1944.

[32] P. Gotsisa, C. Chamisa, and L. Minnetyanb. Prediction of composite laminate fracture: Micromechanics and progressive fracture. In M. Hinton, A. Kaddour, and P. Soden, editors, *Failure Criteria in Fibre-Reinforced-Polymer Composites - The World-Wide Failure Exercise*, chapter 3.1, pages 98–120. Elsevier, Farnborough, 2004.

[33] J. Gu and P. Chen. Some modifications of Hashin's failure criteria for unidirectional composite materials. *Composite Structures*, 182:143–152, 2017. doi: 10.1016/j.compstruct.2017.09.011.

[34] P. Harper and S. Hallett. Cohesive zone length in numerical simulations of composite delamination. *Engineering Fracture Mechanics*, 75:4774–4792, 2008. doi: 10.1016/j.engfracmech.2008.06.004.

[35] P. Harper, L. Sun, and S. Hallett. A study on the influence of cohesive zone interface element strength parameters on mixed mode behaviour. *Composites Part A: Applied Science and Manufacturing*, 43:722–734, 2012. doi: 10.1016/j.compositesa.2011.12.016.

[36] B. Harris. *Fatigue in composites - Science and technology of the fatigue response of fibre-reinforced plastics*. Woodhead publishing limited, Cambridge, 1st edition, 2003.

[37] L. Hart-Smith. Adhesive-bonded double-lap joints. Technical report, National Aeronautics and Space Administration, Long Beach, 1973. URL `https://ntrs.nasa.gov/search.jsp?R=19740005082`.

[38] L. Hart-Smith. Adhesive bonded single lap joints. Technical report, National Aeronautics and Space Administration, Hampton, 1973.

[39] L. Hart-Smith. Analysis and design of advanced composite bonded joints. Technical report, National Aeronautics and Space Administration, Long Beach, 1974.

[40] L. Hart-Smith. Adhesively Bonded Joints for Fibrous Composite Structures. In L. Tong and C. Soutis, editors, *Recent Advances in Structural Joints and Repairs for Composite Materials*, chapter 6, pages 173–210. Kluwer, Dordrecht, 1st edition, 2003.

[41] S. Hartshorn. *Structural adhesives - chemistry and technology*. Plenum, New York, 1st edition, 1986.

[42] Z. Hashin. Fatigue Failure Criteria for Unidirectional Fiber Composites. *Journal of Applied Mechanics*, 1980. doi: 10.1115/1.3157744.

[43] Z Hashin and A Rotem. A fatigue failure criterion for fiber reinforced materials. Technical report, Technion - Israel institute of technology, Haifa, 1973.

[44] Henkel. Structural Adhesives - Aerospace Product Selector Guide, 2015. URL `http://www.ntkinternational.com/pdf/361151_ASA13026_structural_RW_06.pdf`.

[45] R. Heslehurst. *Design and analysis of structural joints with composite materials*. DEStech Publications, Lancaster, 2013.

[46] M. Janssen, J. Zuidema, and R. Wanhill. *Fracture mechanics*. Spon Press, New York, 2nd edition, 2002.

[47] Robert Jones. *Mechanics of composite materials*. Taylor & Francis, second edition, 1999.

[48] A. Kaddour and M. Hinton. Maturity of 3D failure criteria for fibre-reinforced composites: Comparison between theories and experiments: Part B of WWFE-II. *Journal of Composite Materials*, 47(6-7):925–966, 2013. doi: 10.1177/0021998313478710.

[49] M. Kanerva, E. Sarlin, M. Hoikkanen, K. Rämö, O. Saarela, and J. Vuorinen. Interface modification of glass fibre-polyester composite-composite joints using peel plies. *International Journal of Adhesion and Adhesives*, 2015. ISSN 01437496. doi: 10.1016/j.ijadhadh.2015.01.016.

[50] E. Kara, A. Kursun, M. Haboglu, H. Enginsoy, and H. Aykul. Fatigue behavior of adhesively bonded glass fiber reinforced plastic composites with different overlap lengths. *Mechanical Engineering Science*, 229(7):1292–1299, 2015. doi: 10.1177/0954406214559111.

[51] C. Kassapoglou. *Design and analysis of composite structures with applications to aerospace structures*. John Wiley and Sons, Delft, 1st edition, 2010.

[52] C. Kassapoglou. *Modeling the Effect of Damage in Composite Structures*. John Wiley and Sons, Delft, 1st edition, 2015.

[53] W. Knauss and L. Gonzalez. Global Failure Modes in Composite Structures. Technical report, NASA, Pasadena, 2001.

[54] R. Krueger. Virtual crack closure technique: History, approach, and applications. *Applied Mechanics Reviews*, 2004. doi: 10.1115/1.1595677.

[55] J. Kupski, S. Freitas, D. Zarouchas, P. Camanho, and R. Benedictus. Composite layup effect on the failure mechanism of single lap bonded joints. *Composite Structures*, 217:14–26, 6 2019. doi: 10.1016/j.compstruct.2019.02.093.

[56] T. Lang and P. Mallick. Effect of spew geometry on stresses in single lap adhesive joints. *International Journal of Adhesion and Adhesives*, 18:167– 177, 1998. doi: 10.1016/S0143-7496(97)00056-0.

[57] J. Lemaitre. *A Course on Damage Mechanics*. Springer, Berlin, 2nd edition, 1996.

[58] F. Leone, C. Dávila, G. Mabson, M. Ramnath, and I. Hyder. Fracture-Based Mesh Size Requirements for Matrix Cracks in Continuum Damage Mechanics Models. Technical report, NASA, Hampton, 2017.

[59] A. Leski. Implementation of the virtual crack closure technique in engineering FE calculations. *Finite Elements in Analysis and Design*, 43:261 – 268, 2007. doi: 10.1016/j.finel.2006.10.004.

[60] D. Li, Y. Qian-Qian, Chuang-Qi Z., N. Jiang, and L. Jiang. Charpy Transverse Impact Failure Mechanisms of 3D MWK Composites at Room and Liquid Nitrogen Temperatures. *Journal of Aerospace Engineering*, 28(4), 2015. doi: 10.1061/(ASCE)AS.1943-5525.0000444.

[61] G. Li, E. Carrera, M. Cinefra, A. de Miguel, G. Kulikov, A. Pagani, and E. Zappino. Evaluation of shear and membrane locking in refined hierarchical shell finite elements for laminated structures. *Advanced Modeling and Simulation in Engineering Sciences*, 6(1), 12 2019. doi: 10.1186/s40323-019-0131-1.

[62] J. Li, Y. Yan, T. Zhang, and Z. Liang. Experimental study of adhesively bonded CFRP joints subjected to tensile loads. *International Journal of Adhesion and Adhesives*, 57:95–104, 2015. doi: 10.1016/j.ijadhadh.2014.11.001.

[63] P. Liu and J. Zheng. Recent developments on damage modeling and finite element analysis for composite laminates: A review. *Materials and Design*, 31:3825–3834, 2010. doi: 10.1016/j.matdes.2010.03.031.

[64] P. Maimí, P. Camanho, J. Mayugo, and C. Dávila. A continuum damage model for composite laminates: Part I - Constitutive model. *Mechanics of Materials*, 39: 897–908, 2007. doi: 10.1016/j.mechmat.2007.03.005.

[65] S. Mall and K. Yun. Effect of Adhesive Ductility on Cyclic Debond Mechanism in Composite-to-Composite Bonded Joints. *The Journal of Adhesion*, 23(4):215–231, 1987. doi: 10.1080/00218468708075408org/10.1080/00218468708075408. URL `http://www.tandfonline.com/action/journalInformation?journalCode=gadh20`.

[66] P. Mallick. *Materials, design and manufacturing for lightweight vehicles*. Woodhead publishing, Cambridge, 298 edition, 2010.

[67] I. Masmanidis and T. Philippidis. Progressive damage modeling of adhesively bonded lap joints. *International Journal of Adhesion and Adhesives*, 59:53–61, 2015. doi: 10.1016/j.ijadhadh.2015.02.001.

[68] F. Matthews and T. Tester. The influence of stacking sequence on the strength of bonded CFRP single lap joints. *International Journal of Adhesion and Adhesives*, 5(1):13–18, 1985. doi: 10.1016/0143-7496(85)90040-5.

[69] A. Matzenmiller, J. Lubliner, and R. Taylor. A constitutive model for anisotropic damage in fiber-composites. *Mechanics of Materials*, 20:125–152, 1995. doi: 10.1016/0167-6636(94)00053-0.

[70] R. Messler. *Joining of Advanced Materials*. Butterworth Heinemann, Stoneham, 1993.

[71] P Molitor, V Barron, and T Young. Surface treatment of titanium for adhesive bonding to polymer composites: a review. *International Journal of Adhesion & Adhesives*, 21:129–136, 2001.

[72] A. Morais. Mode I cohesive zone model for delamination in composite beams. *Engineering Fracture Mechanics*, 109:236–245, 2013. doi: 10.1016/j.engfracmech.2013.07.004.

[73] M. Moslemi and M. Khoshravan. Cohesive zone parameters selection for mode-I prediction of interfacial delamination. *Journal of Mechanical Engineering*, 61:507–516, 2015. doi: 10.5545/sv-jme.2015.2521.

[74] A. Mouritz. *Introduction to aerospace materials*. Woodhead Publishing, Cambridge, 2012.

[75] S. Murakami. *Continuum Damage Mechanics - A Continuum Mechanics Approach to the Analysis of Damage and Fracture*. Springer, Nagoya, 2012.

[76] A. Nettles. Basic Mechanics of Laminated Composite Plates. Technical report, National Aeronautics and Space Administration, Huntsville, 1994.

[77] K. Norman. User-defined material model for progressive failure analysis. Technical report, NASA, Hampton, 2006.

[78] F. Nunes, N. Silvestre, and J. Correia. Progressive Damage Analysis of Web Crippling of GFRP Pultruded I-Sections. *Composite Structures*, 21(3):578–590, 2017. doi: 10.1061/(ASCE)CC.

[79] O. Ochoa and J. Reddy. *Finite Element Analysis of Composite Laminates*. Kluwer Academic Publishers, Dordrecht, 1992.

[80] A. Orifici, I. Herszberg, and R. Thomson. Review of methodologies for composite material modelling incorporating failure. *Composite Structures*, 86:194–210, 2008. doi: 10.1016/j.compstruct.2008.03.007.

[81] S. Pinho, C. Dávila, P. Camanho, L. Iannucci, and P. Robinson. Failure Models and Criteria for FRP Under In-Plane or Three-Dimensional Stress States Including Shear Non-Linearity. Technical report, National Aeronautics and Space Administration, Hanover, 2005.

[82] S. Pinho, R. Darvizeh, P. Robinson, C. Schuecker, and P. Camanho. Material and structural response of polymer-matrix fibre-reinforced composites. *Journal of Composite Materials*, 46(19-20):2313–2341, 2012. doi: 10.1177/0021998312454478.

URL http://jcm.sagepub.com/http://jcm.sagepub.com/http://jcm.sagepub.com/http://jcm.sagepub.com/http://jcm.sagepub.com/http://jcm.sagepub.com/http://jcm.sagepub.com/http://jcm.sagepub.com/.

[83] S. Pinho, G. Vyas, and P. Robinson. Material and structural response of polymer-matrix fibre-reinforced composites: Part B. *Journal of Composite Materials*, 47 (6-7):679–696, 2013. doi: 10.1177/0021998313476523.

[84] A. Puck and H. Schürmann. Failure analysis of FRP laminates by means of physically based phenomenological models. *Composites Science and Technology*, 58: 1045–1067, 1998. doi: 10.1016/B978-008044475-8/50028-7.

[85] A. Puck and H. Schurmann. Failure analysis of FRP laminates by means of physically based phenomenological models. *Composites Science and Technology*, 62: 1633–1662, 2002. URL www.elsevier.com/locate/compscitech.

[86] J. Reiner and R. Vaziri. Structural Analysis of Composites With Finite Element Codes: An Overview of Commonly Used Computational Methods. In P. Beaumont and C. Zweben, editors, *Comprehensive Composite Materials II*, chapter 8.4, pages 61–84. 2017.

[87] A. Riccio. *Damage Growth in Aerospace Composites*. Springer, Naples, 2015.

[88] P. Saha, K. Bakshi, and D. Chakravorty. First Ply Failure Analysis of Laminated Composite Cylindrical Shells. In Wrexham Glyndŵr University, editor, *2nd International Conference on Advanced Composite Materials and Technologies for Aerospace Applications*, pages 127–132, Wrexham, 2012. ResearchGate. URL https://www.researchgate.net/publication/309428026.

[89] C. Sarrado, A. Turon, J. Renart, and I. Urresti. Assessment of energy dissipation during mixed-mode delamination growth using cohesive zone models. *Composites Part A: Applied Science and Manufacturing*, 43:2128–2136, 2012. doi: 10.1016/j.compositesa.2012.07.009.

[90] C. Schuecker and H. Pettermann. Fiber Reinforced Laminates: Progressive Damage Modeling Based on Failure Mechanisms. *Arch Comput Methods Eng*, 15:163–184, 2008. doi: 10.1007/s11831-008-9016-z. URL http://www.adoptech.

[91] C. Silva and P. Camanho. *Mechanics of Hierarchical Nanoengineered Aerospace Composite Materials*. PhD thesis, Universidade do Porto, 2017.

[92] D. Sleight. Progressive Failure Analysis Methodology for Laminated Composite Structures. Technical report, National Aeronautics and Space Administration, Hampton, 1999. URL https://ntrs.nasa.gov/search.jsp?R=19990052628.

[93] P. Soden, A. Kaddour, and M. Hinton. Predictive capabilities of nineteen failure theories and design methodologies for polymer composite laminates. Part B: Comparison with experiments. In M. Hinton, A. Kaddour, and P. Soden, editors, *Failure Criteria in Fibre-Reinforced-Polymer Composites - The World-Wide Failure Exercise*, chapter 6.1, pages 1073–1222. Elsevier, Farnborough, 2004.

[94] P. Soden, A. Kaddour, and M. Hinton. Recommendations for designers and researchers resulting from the world-wide failure exercise. In M. Hinton, A. Kaddour, and P. Soden, editors, *Failure Criteria in Fibre-Reinforced-Polymer Composites - The World-Wide Failure Exercise*, chapter 7.1, pages 1223–1251. Elsevier, Farnborough, 2004. ISBN 978-0-08-044475-8.

[95] J. Song, P. Areias, and T. Belytschko. A method for dynamic crack and shear band propagation with phantom nodes. *International Journal for Numerical Methods in Engineering*, 67:868–893, 2006. doi: 10.1002/nme.1652.

[96] M. Song, J. Kweon, J. Choi, J. Byun, M. Song, S. Shin, and T. Lee. Effect of manufacturing methods on the shear strength of composite single-lap bonded joints. *Composite Structures*, 92:2194–2202, 2010. doi: 10.1016/j.compstruct.2009.08.041.

[97] S. Srinivas. Analysis of bonded joints. Technical report, NASA, Hampton, 1975.

[98] F. Stuparu, D. Constantinescu, C. Picu, M. Sandu, D. Apostol, and S. Sorohan. Cohesive and XFEM evaluation of adhesive failure for dissimilar single lap joints. In Elsevier, editor, *21st European Conference on Fracture*, pages 316–325, Catania, 2017. doi: 10.1016/j.engfracmech.2017.05.029.

[99] C. Sun, B. Quinn, J. Tao, F. Cotr, and D. Oplinger. Comparative evaluation of failure analysis methods for composite laminates. Technical report, Federal Aviation Administration, West Lafayette, 1996. URL `www.tc.faa.gov/its/act141/reportpage.html`.

[100] J. Sun, K. Lee, and H. Lee. Comparison of implicit and explicit finite element methods for dynamic problems. *Journal of Materials Processing Technology*, 105: 110–118, 2000.

[101] J. Tang, I. Sridhar, and N. Srikanth. Nondimensional analysis of single lap joint subjected to out-of-plane loading. *International Journal of Solids and Structures*, 62:229–238, 2015. doi: 10.1016/j.ijsolstr.2015.02.035.

[102] L. Tong. Bond shear strength for adhesive bonded double-lap joints. *International Journal of Solids and Structures*, 31(21):2919–2931, 1994. doi: 10.1016/0020-7683(94)90059-0.

[103] E. Totry, C. González, and J. LLorca. Failure locus of fiber-reinforced composites under transverse compression and out-of-plane shear. *Composites Science and Technology*, 68:829–839, 2008. doi: 10.1016/j.compscitech.2007.08.023.

[104] A. Travesa. *Simulation of delamination in composites under quasi-static and fatigue loading using cohesive zone models*. PhD thesis, University of Girona, Girona, 2006.

[105] M. Tsai, D. Oplinger, and J. Morton. Improved theoretical solutions for adhesive lap joints. *International Journal of Solids and Structures*, 35(12):1163–1185, 1998. doi: 10.1016/S0020-7683(97)00097-8.

[106] Stephen Tsai. Strength characteristics of composite materials. Technical report, NASA, Newport Beach, 1965.

[107] D. Tumino and B. Zuccarello. Fatigue delamination experiments on GFRP and CFRP specimens under single and mixed fracture modes. In *Procedia Engineering*,

pages 1791–1796, Como, 2011. Elsevier. ISBN 3909355366. doi: 10.1016/j.proeng.2011.04.298.

[108] F. van der Meer. *Computational Modeling of Failure in Composite Laminates*. PhD thesis, TU Delft, 2010.

[109] B. Van Dongen. *Progressive damage modelling of FRPs using a blended stress-strain and fracture mechanics approach in FEM*. PhD thesis, TU Delft, 2017.

[110] B. van Dongen, A. van Oostrum, and D. Zarouchas. A blended continuum damage and fracture mechanics method for progressive damage analysis of composite structures using XFEM. *Composite Structures*, 184:512–522, 2018. doi: 10.1016/j.compstruct.2017.10.007.

[111] A. van Oostrum. *Application of fracture mechanics in a blended numerical framework for progressive damage analysis of CFRPs in FEM*. PhD thesis, TU Delft, 2017.

[112] J. Vinson and R. Sierakowski. *The Behavior of Structures Composed of Composite Materials*. Kluwer, New York, 2nd edition, 2004.

[113] M. Wisnom. The role of delamination in failure of fibre-reinforced composites. *Philosophical Transactions of the Royal Society A: Mathematical, Physical and Engineering Sciences*, 370:1850–1870, 2012. doi: 10.1098/rsta.2011.0441.

[114] J. Xará and R. Campilho. Strength estimation of hybrid single-L bonded joints by the eXtended Finite Element Method. *Composite Structures*, 183:397–406, 2017. doi: 10.1016/j.compstruct.2017.04.009.

[115] K. Yang. Element Stiffness Matrix. In *Basic Finite Element Method as Applied to Injury Biomechanics*, chapter 4, pages 151–230. Academic Press, Detroit, 2017.

[116] C. Yin and A. McKay. Introduction to modeling and simulation techniques. In *The 8th International Symposium on Computational Intelligence and Industrial Applications and The 12th China-Japan International Workshop on Information Technology and Control Applications*, Tengzhou, 2018. White Rose. ISBN 078034278X. doi: 10.1145/268437.268440. URL `http://portal.acm.org/citation.cfm?doid=268437.268440`.

[117] B. Yu, S. Bradley, C. Soutis, and P. Withers. A comparison of different approaches for imaging cracks in composites by X-ray microtomography. *Philos Trans A Math Phys Eng Sci.*, 374:2071, 2016.

[118] Z. Yuan and J. Fish. Are the cohesive zone models necessary for delamination analysis? *Computer Methods in Applied Mechanics and Engineering*, 310:567–604, 2016. doi: 10.1016/j.cma.2016.06.023.

[119] C Zienkiewicz and R. Taylor. Reduced integration technique in general analysis of plates and shells. *International journal for numerical methods in engineering*, 3: 275–290, 1971.

[120] P. Zinoviev, S. Grigoriev, O. Lebedeva, and L. Tairova. The strength of multilayered composites under a plane-stress state. In M. Hinton, A. Kaddour, and P. Soden, editors, *Failure Criteria in Fibre-Reinforced-Polymer Composites - The World-Wide Failure Exercise*, chapter 3.12, pages 379–401. Elsevier, Farnborough, 2004.

APPENDICES

A. Influence of the stacking sequence on the stress concentration factor around a hole in a laminate loaded in tension

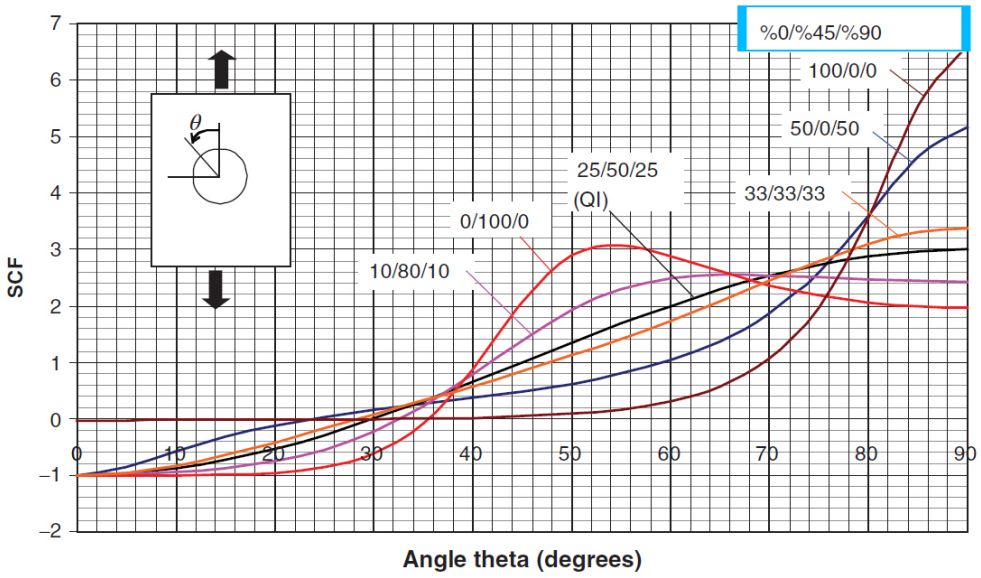

Figure P.2: Stress concentration factor around a hole in an orthotropic plate. (Reproduced from [52], copyright Wiley, 2015).

B. Trade-off between adhesively bonded joints and mechanically fastened joints

Table P.1: Comparison of the advantages and disadvantages between adhesively bonded joints and mechanically fastened joints. (Adapted from [5]).

Advantages	Disadvantages
Adhesively bonded joints	
Small stress concentration in adherends	Limits to adherend thickness
Stiff connection	Inspection other than for gross flaws difficult
Excellent fatigue properties	Prone to environmental degradation
No fretting problems	Sensitive to peel and through-thickness stresses
Sealed against corrosion	Residual stress problems when joining to metals
Smooth surface contour	Cannot be disassembled
Relatively lightweight	May require costly tooling and facilities
Damage tolerant	Requires high degree of quality control
Advantages	**Disadvantages**
Mechanically Fastened joints	
Extensively studied and reliable joint	Considerable stress concentration
(Bolts) can be disassembled	Prone to fatigue cracking in metallic component
No thickness limitations	Hole formation can promote other composite damage
Simple joint configuration	Composites' s relatively poor bearing properties
Simple manufacturing process	Pone to fretting in metal
Simple inspection procedure	Prone to corrosion
Less sensitive to temperature and humidity changes	May require extensive shimming
Provides through-thickness reinforcement; not sensitive to peel stresses	
No major residual stress problem	

C. Tsai *et al.* improved analytical solution: 1-D bar and 1-D beam formulations, expressions and comparison plots

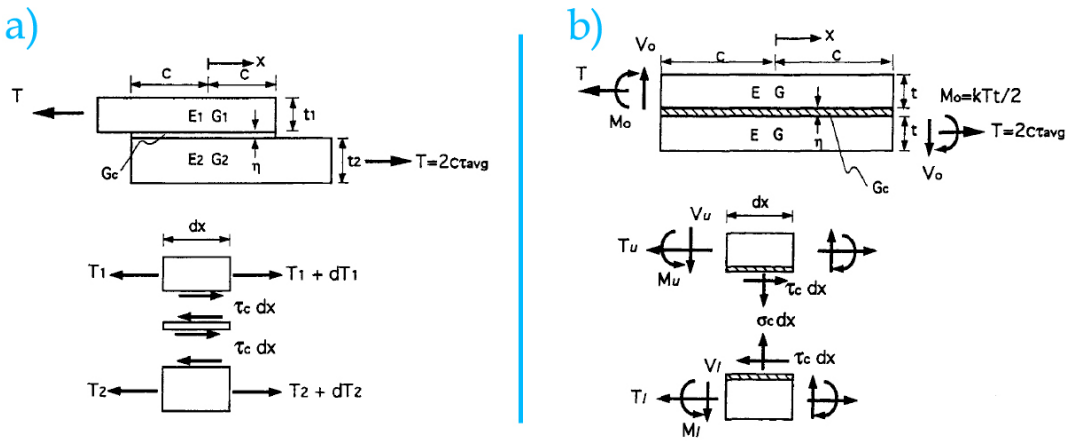

Figure P.3: Geometry and material parameters of the single-lap joint for: a) 1-D bar model and b) 1-D beam model. (Reproduced from [105], copyright Elsevier, 1998).

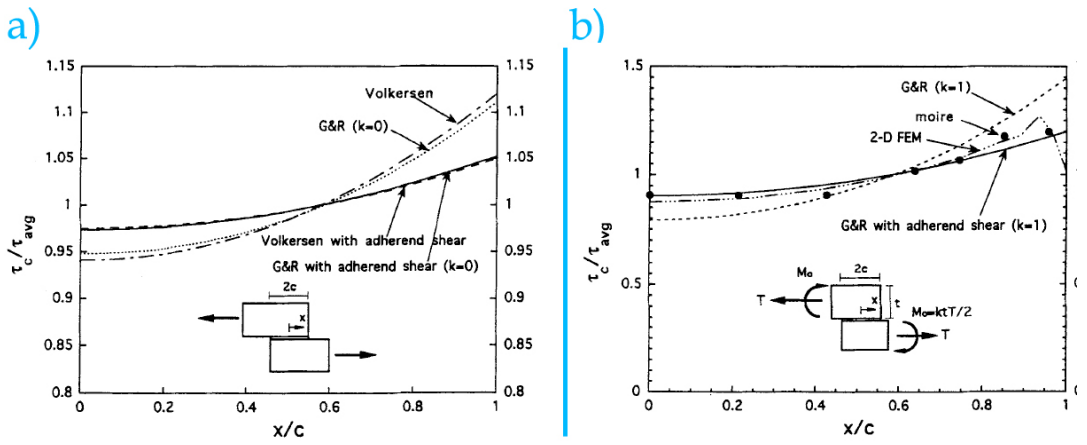

Figure P.4: Normalized adhesive shear stress distributions of thick-adherend single-lap joint comparison: a) improved 1-D bar model (Goland and Reissner with adherend shear), 1-D bar model (Volkersen), original 1-D beam model (Goland and Reissner) and b) improved 1-D beam model with the edge moment M_0 (Goland and Reissner with adherend shear), 2-D FEM model and original 1-D beam model (Goland and Reissner). (Reproduced from [105], copyright Elsevier, 1998).

D. Considerations on other parameters that influence the joint strength

D.1. Manufacturing bonding process

The manufacturing process influences the failure process, the failure mode and the joint strength of a bonded structure [10].

There are essentially four bonding processes:

- Co-curing: both structural elements are simultaneously cured; the use of adhesive is optional;
- Co-bonding: one uncured adherend is cured together with an already cured adherend using an adhesive layer between both;
- Secondary bonding: both already cured composite substrates are bonded by means of an adhesive layer;
- Multi-material bonding: same as previous but with a combination of metal and composite adherends.

Song *et al.* [96] investigated the effects of manufacturing methods on the shear strength of composite ABSLJ and they found that by decreasing order the processes are sorted as follows: co-cured without adhesive > secondary bonded > co-cured with adhesive > co-bonded.

D.2. Surface preparation

Bond strength can be significantly improved by surface treating the adherends prior to bonding [6].

Generally, surface treatments are required to turn the surface receptive to the applied adhesive. Hence, the main goal of treatment is to provide to the surface desirable physical and chemical properties [19]. A clean surface is a necessary but not sufficient condition for bond durability [6].

The main functions of surface preparation are summarized in the following list [19]:

- To remove and/or prevent the formation of contaminants (such as: oils, dusts) and weak layers (such as: weak oxides - in the case of metals adherends) on the adherend surface; this is accomplished by the using a proper degrease agent;
- To maximize the degree of molecular contact between the adhesive and the adherends by increasing the surface energy of the last, thus improving their wetting and by introducing specific functional groups;
- Create a specific structure on the adherend surface that extends the surface area and promotes interlocking mechanisms; these two last functions may be accomplished through mechanical processes, such as abrasion or by using peel ply, however according to the outcomes of a referenced research [49], the found fracture toughness values for peel ply surface treated specimens were 70-80% lower when compared to abraded treated specimens;

In summary, surface treatments decrease water contact angle, increase surface tension resulting in a improved bond strength [71]. Apart from a high surface energy adherends, a low surface energy adhesives are desirable for a maximized wetting.

It is worth mentioning that a particular surface treatment highly depends on the requirements and service conditions of the bond [19].

D.3. Geometric parameters

D.3.1. Bondline thickness

In a literature review article, Budhe *et al.* [10] collected the results from several studies regarding the influence of the bondline thickness on the joint strength and fracture energy for specimens under mode I (using double-cantilever beam [DCB], tapered DCB [TDCB] and butt joints), mode II (using end-notched flexure [ENF] joints) and mixed-mode loading (using single lap bonded joints [ABSLJ]).

It was found that for polymeric adhesives (excluding elastomers), the strength decreases with an increasing bondline thickness, which was attributed to the fact that thicker bondlines contain more defects. Regarding the fracture energy, it was found that it increases with the thickness of a ductile adhesive (the reverse applies for a brittle adhesive). According to the authors, no generalized relation is possible to establish between strength and adhesive thickness given the influence of the other governing parameters.

D.3.2. Joint configuration

An efficiently designed joint presents a constant stress distribution throughout its bonded area. For most of joint configurations, including the simplest and most studied ABSLJ, this is not the case. Instead, both: the shear stress and the transverse normal (peel) stress

distributions present high peaks at the lap ends. Commonly, the shear stress distribution is, by analogy, refereed as 'bathtub' shaped. The following plots, presented in figure P.5 and P.6, show the shear stress distribution and peel stress in a ABSLJ, respectively, from finite element models and from Goland and Reissner analytical solutions.

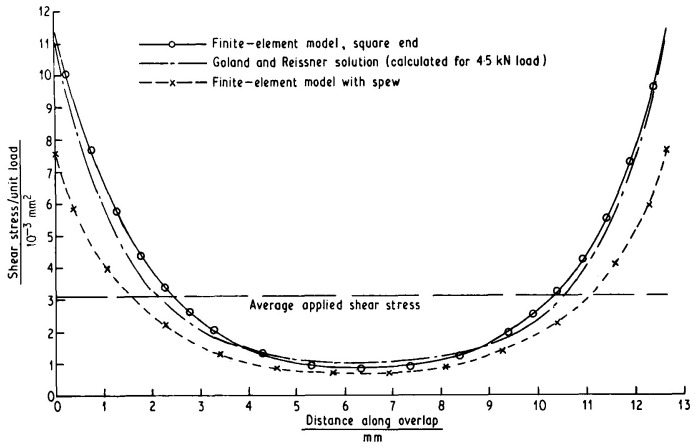

Figure P.5: Shear stress distribution in a ABSLJ from finite-element models with and without spew and from Goland and Reissner analytical solutions [31].

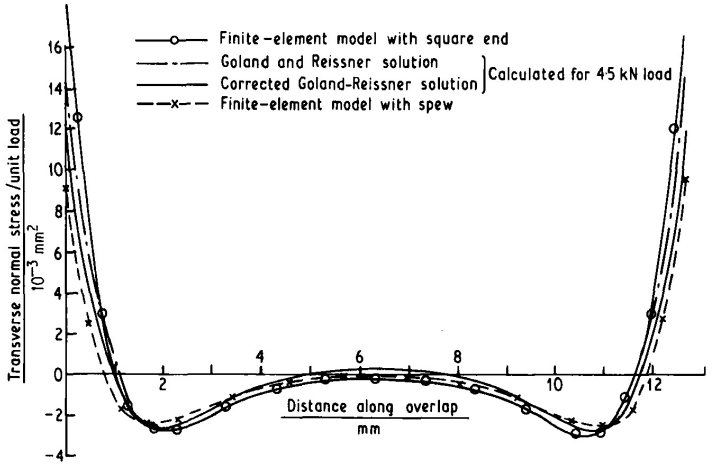

Figure P.6: Transverse normal (peel) stress distribution in a ABSLJ from finite-element models with and without spew and from Goland and Reissner analytical solutions [31].

One strategy commonly use to significantly reduce the peak stresses and thus increase the joint strength is the inclusion of spew. Spew is defined as the portion of adhesive that is squeezed out from the lap area and forms a bead at the lap ends [56]. Two referenced researches [8, 56] investigated how the spew geometry affects the peak stresses and stress distribution in adhesively bonded ABSLJ through a finite element analysis. The authors concluded that spews significantly contribute for stress reduction, particularly the peel stresses (up to $\sim 70\%$ of peak reduction for a half triangular spew geometry [56]) should not be neglected in the stress analysis of single-lap joints. Furthermore, it was concluded that increasing the size of the spew also reduces peak stress concentrations.

E. Effect of the adhesive and adherend properties on the joint strength

E.1. Effect of the adhesive ductility

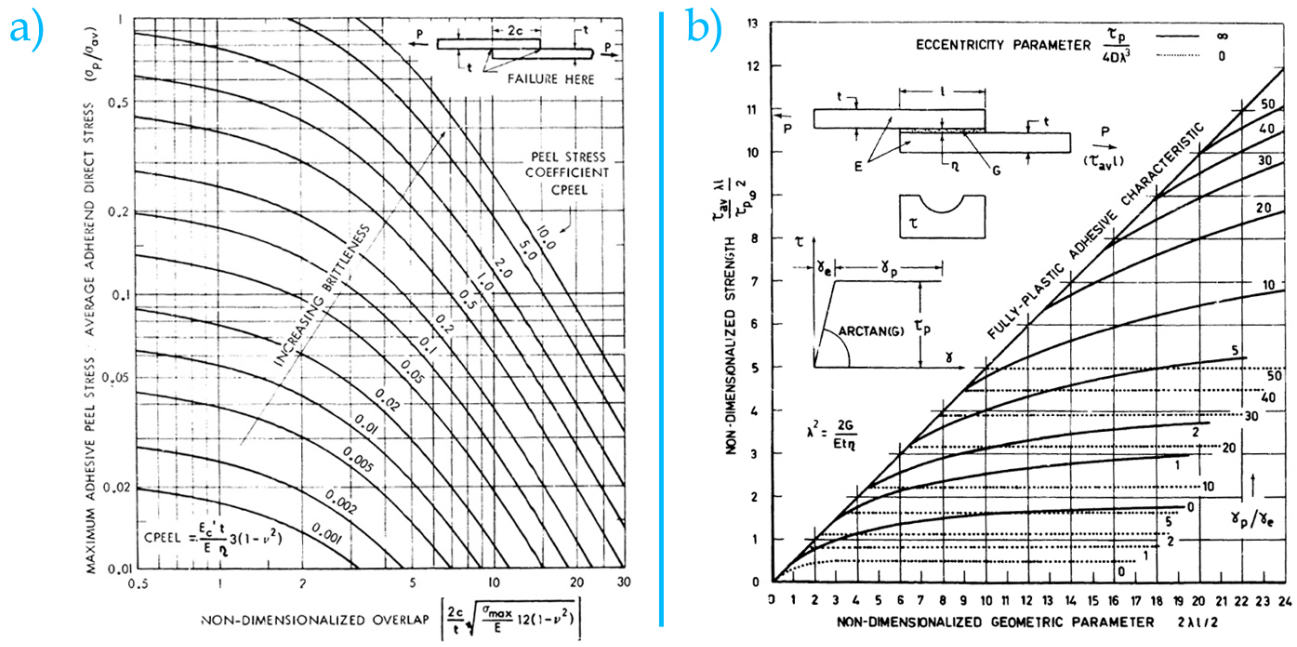

Figure P.7: a) Effect of adhesive brittleness and overlap length on: a) the peel stresses of balanced ABSLJ (Reproduced from [39], copyright NASA, 1974); b) the shear strength of ABSLJ. (Reproduced from [38], copyright NASA, 1973).

E.2. Effect of the adherend stiffness imbalance on the adhesive peel stresses

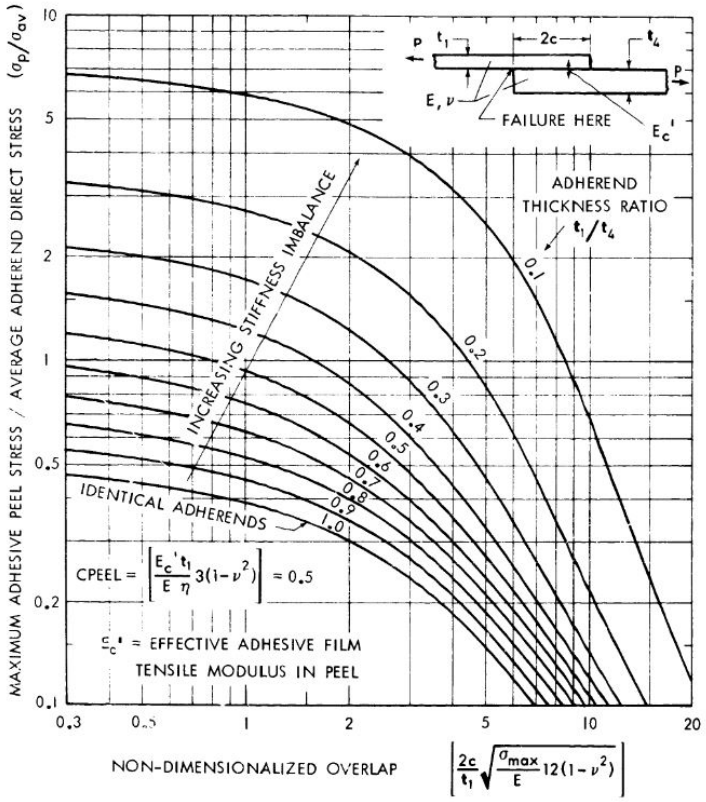

Figure P.8: Effect of the adherend stiffness imbalance on the adhesive peel stresses in ABSLJ. (Reproduced from [38], copyright NASA, 1973).

F. Constitutive relations for anisotropic materials: an overview

A constitutive model describes the material stress-strain relationship. Quasi-brittle materials, such FRP laminates exhibit a broad linear-elastic region, after which due to inherent material non-linearities or due to damage events, the material presents a NL behavior which might be more or less pronounced according to the material properties and layup configuration.

This chapter is dedicated to derive the stress-strain relations in FRP laminates. First, the constitutive relations of a thin lamina under plane stress conditions are derived. Then, the stresses and strains in the material coordinates are transformed into stresses and strains in the laminate/load coordinate system. It follows the formal definition of the invariant stiffness matrix, displacements, strains, resultant forces and moments. With all the ingredients set-up, the constitutive equations for a laminate are assembled together in one matrix equation, relating the applied loads on the laminate to its associated strains. The coupling implication of some popular laminate configurations are summarized in a table. Finally, a generic algorithm to find the first ply failure load is presented.

F.1. Stress-strain relations (3D)

F.1.1. General anisotropic material

The generalized Hooke's law, which relates the stresses σ_i to the strains ε_j through the stiffness components C_{ij} on a general anisotropic three-dimensional cubic element[1] can be written in contracted notation as [20, 47, 51]:

$$\sigma_i = C_{ij}\varepsilon_j \tag{P.1}$$

$$\text{where: } i, j = \{1, 2, 3, 4, 5, 6\}$$

Energy considerations require additional symmetries:

$$C_{ij} = \frac{\partial^2 W}{\partial \varepsilon_i \partial \varepsilon_j} = \frac{\partial^2 W}{\partial \varepsilon_j \partial \varepsilon_i} = C_{ji} \tag{P.2}$$

Reducing the number of independent elastic constants from 36 to 21. The compliance matrix S_{ij} is obtained by inverting the stiffness matrix:

$$\varepsilon_j = S_{ji}\sigma_i \tag{P.3}$$

F.1.2. Orthotropic material

Taking the particular case of an orthotropic material which presents three mutually perpendicular planes of material symmetry, leads to the following considerations [20]:

- No normal stress - shear strain coupling;
- No shear stress - normal strain coupling;
- No coupling between a shear stress acting on one plane and a shear strain on a different plane.

$$\begin{Bmatrix} \varepsilon_1 \\ \varepsilon_2 \\ \varepsilon_3 \\ \gamma_{23} \\ \gamma_{31} \\ \gamma_{12} \end{Bmatrix} = \begin{bmatrix} S_{11} & S_{12} & S_{13} & 0 & 0 & 0 \\ S_{12} & S_{22} & S_{23} & 0 & 0 & 0 \\ S_{13} & S_{23} & S_{33} & 0 & 0 & 0 \\ 0 & 0 & 0 & S_{44} & 0 & 0 \\ 0 & 0 & 0 & 0 & S_{55} & 0 \\ 0 & 0 & 0 & 0 & 0 & S_{66} \end{bmatrix} \begin{Bmatrix} \sigma_1 \\ \sigma_2 \\ \sigma_3 \\ \tau_{23} \\ \tau_{31} \\ \tau_{12} \end{Bmatrix} \tag{P.4}$$

The compliance coefficients S_{ij} are defined in terms of the elastic engineering material constants:

$$\begin{cases} S_{11} = \frac{1}{E_1}; \quad S_{22} = \frac{1}{E_2}; \quad S_{33} = \frac{1}{E_3}; \\ S_{12} = -\frac{\nu_{12}}{E_1}; S_{13} = -\frac{\nu_{12}}{E_1}; S_{23} = -\frac{\nu_{23}}{E_2}; \\ S_{44} = \frac{1}{G_{23}}; S_{55} = \frac{1}{G_{13}}; S_{66} = \frac{1}{G_{12}} \end{cases} \tag{P.5}$$

[1] Symmetry of the stress $\sigma_{ij} = \sigma_{ji}$ and the strain $\varepsilon_{ij} = \varepsilon_{ji}$ was assumed, reducing from 81 to 36 independent elastic constants

The orthotropic material assumption reduces the number of independent elastic constants from 21 to 9.

F.1.3. Transversely isotropic material

Assuming a transversely isotropic material, that is a special case of orthotropic material when one of its principal planes (the 2-3-plane, known as plane of isotropy) has infinite planes of symmetry, *i.e.*, within planes parallel to the plane of isotropy, the material properties are the same in all directions. The most popular example is an unidirectional [UD] FRP lamina, as shown in figure P.9 a):

$$\text{Transversely Isotropic} \begin{cases} S_{12} = S_{13} \\ S_{22} = S_{33} \\ S_{55} = S_{66} \\ S_{44} = 2(S_{22} - S_{23}) \end{cases}$$

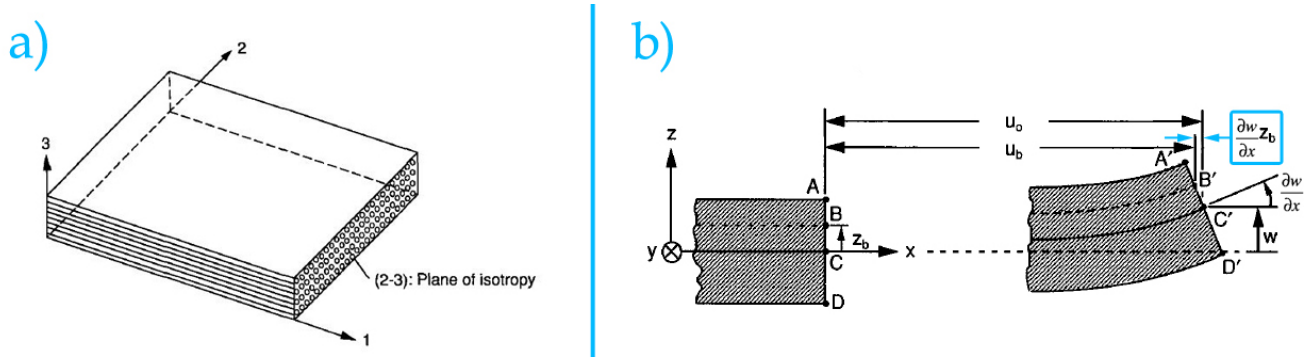

Figure P.9: a) Transversely isotropic material illustration (2-3-plane is the plane of of isotropy); b) Laminate section before and after deformation due to normal displacement and bending. (Reproduced from [20], copyright Oxford University Press, 2006).

$$\begin{Bmatrix} \varepsilon_1 \\ \varepsilon_2 \\ \varepsilon_3 \\ \gamma_{23} \\ \gamma_{31} \\ \gamma_{12} \end{Bmatrix} = \begin{bmatrix} S_{11} & S_{12} & S_{12} & 0 & 0 & 0 \\ S_{12} & S_{22} & S_{23} & 0 & 0 & 0 \\ S_{12} & S_{23} & S_{22} & 0 & 0 & 0 \\ 0 & 0 & 0 & 2(S_{22} - S_{23}) & 0 & 0 \\ 0 & 0 & 0 & 0 & S_{66} & 0 \\ 0 & 0 & 0 & 0 & 0 & S_{66} \end{bmatrix} \begin{Bmatrix} \sigma_1 \\ \sigma_2 \\ \sigma_3 \\ \tau_{23} \\ \tau_{31} \\ \tau_{12} \end{Bmatrix} \tag{P.6}$$

This leads to a relation that depends on only 5 independent elastic constants (E_1, E_2, G_{12}, ν_{12} and ν_{23}):

$$\begin{cases} S_{11} = \frac{1}{E_1} \\ S_{22} = \frac{1}{E_2} \\ S_{12} = -\frac{\nu_{12}}{E_1} \\ S_{23} = -\frac{\nu_{23}}{E_2} \\ S_{66} = \frac{1}{G_{12}} \end{cases} \tag{P.7}$$

F.2. Stress-strain relations for a thin lamina (2D): plane stress state

The previous relation can be further simplified if a state of plane-stress is assumed. This assumption implies that the thickness of the laminate is much smaller when compared its other two in-plane dimensions [51]. Thus, the out-of-plane stresses σ_3, τ_{23} and τ_{31} are considered negligible in relation to the in-plane stresses.

Inserting these assumptions into matrix equation (P.6) results in null out-of-plane shear strains: $\gamma_{23} = 0$ and $\gamma_{31} = 0$. Using the in-plane equations (ε_1, ε_2 and γ_{12}) leads to the stress-strain matrix equation for a transversely orthotropic ply under plane stress:

$$\begin{Bmatrix} \varepsilon_1 \\ \varepsilon_2 \\ \gamma_{12} \end{Bmatrix} = \begin{bmatrix} S_{11} & S_{12} & 0 \\ S_{12} & S_{22} & 0 \\ 0 & 0 & S_{66} \end{bmatrix} \begin{Bmatrix} \sigma_1 \\ \sigma_2 \\ \tau_{12} \end{Bmatrix} = \begin{bmatrix} \frac{1}{E_1} & -\frac{\nu_{12}}{E_1} & 0 \\ -\frac{\nu_{12}}{E_1} & \frac{1}{E_2} & 0 \\ 0 & 0 & \frac{1}{G_{12}} \end{bmatrix} \begin{Bmatrix} \sigma_1 \\ \sigma_2 \\ \tau_{12} \end{Bmatrix} \tag{P.8}$$

$$\{\varepsilon\}_{12} = [S]_{12}\{\sigma\}_{12}$$

Inverting the reduced compliance matrix S, results in the reduced stiffness matrix Q.

$$\begin{Bmatrix} \sigma_1 \\ \sigma_2 \\ \tau_{12} \end{Bmatrix} = \begin{bmatrix} Q_{11} & Q_{12} & 0 \\ Q_{12} & Q_{22} & 0 \\ 0 & 0 & Q_{66} \end{bmatrix} \begin{Bmatrix} \varepsilon_1 \\ \varepsilon_2 \\ \gamma_{12} \end{Bmatrix} = \begin{bmatrix} \frac{E_1}{1-\nu_{12}\nu_{21}} & \frac{\nu_{12}E_2}{1-\nu_{12}\nu_{21}} & 0 \\ \frac{\nu_{12}E_2}{1-\nu_{12}\nu_{21}} & \frac{E_2}{1-\nu_{12}\nu_{21}} & 0 \\ 0 & 0 & G_{12} \end{bmatrix} \begin{Bmatrix} \varepsilon_1 \\ \varepsilon_2 \\ \gamma_{12} \end{Bmatrix} \tag{P.9}$$

$$\{\sigma\}_{12} = [Q]_{12}\{\varepsilon\}_{12}$$

This constitutive relation only depends on only 4 independent elastic constants (E_1, E_2, G_{12} and ν_{12}):

F.3. Constitutive equations of multi-directional laminates

Assumptions

The overall behavior of a multidirectional laminate is dependent on the stacking sequence and properties of the individual layers [20]. This behavior is predicted within the framework of the classical laminate theory (CLT) which is valid under the following assumptions:

(a) Each lamina of the laminate is quasi homogeneous and orthotropic.
(b) Strain-displacement and stress-strain relations are linear.
(c) The laminate and its laminae are in plane stress conditions ($\sigma_z = \tau_{yz} = \tau_{zx} = 0$).
(d) Straight lines normal to the middle surface remain straight and normal to that surface after deformation. This implies that transverse shear strains γ_{zx} and γ_{yz} are zero.
(e) All displacements are small compared with the thickness of the laminate ($|u|,|v|,|w| \ll h$).
(f) In-plane displacements vary linearly through the thickness of the laminate, i.e., u and v displacements in the $x-$ and $y-$directions are linear functions of z.
(g) Normal distances from the middle surface remain constant, that is, the transverse normal strain ε_z, is zero. This implies that the transverse displacement w is independent of the thickness coordinate z.

F.3.1. Transformation of stress and strain equations

Assuming that a lamina is loaded at a arbitrary angle, other than 0° and 90°. The immediate consequence is that the loading direction do not coincide with the principal material direction. For a θ oriented ply, where θ is measured positive counterclockwise (CCW) from the x-axis (usually parallel to the main laminate direction or to the main load, justifying O_{xy} being named the laminate/load coordinate system), to the 1-axis (parallel to the fiber direction, justifying O_{12} being named the material coordinate system). Appendix F.4 demonstrates the stress and strain transformations from the laminate/load coordinate system to the material coordinate system, in equations (P.39) and (P.40), respectively:

$$\begin{Bmatrix} \sigma_1 \\ \sigma_2 \\ \tau_{12} \end{Bmatrix} = \begin{bmatrix} cos^2\theta & sin^2\theta & 2cos\theta sin\theta \\ sin^2\theta & cos^2\theta & -2cos\theta sin\theta \\ -cos\theta sin\theta & cos\theta sin\theta & (cos^2\theta - sin^2\theta) \end{bmatrix} \begin{Bmatrix} \sigma_x \\ \sigma_y \\ \tau_{xy} \end{Bmatrix} \tag{P.10}$$

$$\{\sigma\}_{12} = [T]\{\sigma\}_{xy}$$

$$\begin{Bmatrix} \varepsilon_1 \\ \varepsilon_2 \\ \gamma_{12} \end{Bmatrix} = \begin{bmatrix} cos^2\theta & sin^2\theta & 2cos\theta sin\theta \\ sin^2\theta & cos^2\theta & -2cos\theta sin\theta \\ -cos\theta sin\theta & cos\theta sin\theta & (cos^2\theta - sin^2\theta) \end{bmatrix} \begin{Bmatrix} \varepsilon_x \\ \varepsilon_y \\ \gamma_{xy} \end{Bmatrix} \tag{P.11}$$

$$\{\varepsilon\}_{12} = [T]\{\varepsilon\}_{xy}$$

Invariant stiffness matrix

The invariant stiffness matrix relates the lamina strains with the lamina stresses in the laminate/load coordinate system O_{xy}. It is trivially obtained by: firstly inserting equation (P.9) into inverted equation (P.10):

$$\{\sigma\}_{xy} = [T]^{-1}[Q]_{12}\{\varepsilon\}_{12} \tag{P.12}$$

And secondly inserting equation (P.11) into the matrix product:

$$\{\sigma\}_{xy} = [T]^{-1}[Q]_{12}[T]\{\varepsilon\}_{xy} \tag{P.13}$$

The product of the first 3 matrices on the right side of the equation is conveniently stored in a single 3x3 matrix, named invariant stiffness matrix $[Q]_{xy}$:

$$[Q]_{xy} = [T]^{-1}[Q]_{12}[T] \tag{P.14}$$

Retaking equation (P.13) already with the invariant stiffness matrix, results in the expanded relation:

$$\begin{Bmatrix} \sigma_x \\ \sigma_y \\ \tau_{xy} \end{Bmatrix} = \begin{bmatrix} Q_{xx} & Q_{xy} & Q_{xs} \\ Q_{xy} & Q_{yy} & Q_{ys} \\ Q_{xs} & Q_{ys} & Q_{ss} \end{bmatrix} \begin{Bmatrix} \varepsilon_x \\ \varepsilon_y \\ \gamma_{xy} \end{Bmatrix} \tag{P.15}$$

$$\{\sigma\}_{xy} = [Q]_{xy}\{\varepsilon\}_{xy}$$

F.3.2. Definition of displacements, strains

F.3.3. Displacements

The total inplane displacements u and v at any point of the laminate are given by the sum of the normal displacements [first terms on right side of equations (P.16) and (P.17)] and the displacements introduced by bending[2] [see figure P.9 b)], as follows:

$$u = u^0 - z\frac{\partial w}{\partial x} \tag{P.16}$$

$$v = v^0 - z\frac{\partial w}{\partial v} \tag{P.17}$$

F.3.4. Strains

The normal strains ε_x and ε_y are the deformations in terms of relative displacements. In mathematical terms each displacement is derived with respect to its respective coordinate:

$$\varepsilon_x = \frac{\partial u}{\partial x} = \frac{\partial u^0}{\partial x} - z\frac{\partial^2 w}{\partial x^2} \tag{P.18}$$

$$\varepsilon_y = \frac{\partial v}{\partial y} = \frac{\partial v^0}{\partial y} - z\frac{\partial^2 w}{\partial y^2} \tag{P.19}$$

The first term in the right side of both equations is identified as the midplane strain ε^0 and the negative second derivative that multiplies with distance z is called curvature K.

The shear strain γ_{xy} is given by:

$$\gamma_{xy} = \frac{\partial u}{\partial y} + \frac{\partial v}{\partial x} = \frac{\partial u^0}{\partial y} + \frac{\partial v^0}{\partial x} - 2z\frac{\partial^2 w}{\partial x \partial y} \tag{P.20}$$

Assembling the normal and shear strains into matrix form:

$$\begin{Bmatrix} \varepsilon_x \\ \varepsilon_y \\ \gamma_{xy} \end{Bmatrix} = \begin{Bmatrix} \varepsilon_x^0 \\ \varepsilon_y^0 \\ \gamma_{xy}^0 \end{Bmatrix} + z \begin{Bmatrix} K_x \\ K_y \\ K_{xy} \end{Bmatrix} \tag{P.21}$$

$$\{\varepsilon\}_{xy} = \{\varepsilon\}_{xy}^0 + z\{K\}_{xy}$$

Inputing the last equation into (P.15):

$$\begin{Bmatrix} \sigma_x \\ \sigma_y \\ \tau_{xy} \end{Bmatrix} = \begin{bmatrix} Q_{xx} & Q_{xy} & Q_{xs} \\ Q_{xy} & Q_{yy} & Q_{ys} \\ Q_{xs} & Q_{ys} & Q_{ss} \end{bmatrix} \begin{Bmatrix} \varepsilon_x^0 \\ \varepsilon_y^0 \\ \gamma_{xy}^0 \end{Bmatrix} + z \begin{bmatrix} Q_{xx} & Q_{xy} & Q_{xs} \\ Q_{xy} & Q_{yy} & Q_{ys} \\ Q_{xs} & Q_{ys} & Q_{ss} \end{bmatrix} \begin{Bmatrix} K_x \\ K_y \\ K_{xy} \end{Bmatrix} \tag{P.22}$$

$$\{\sigma\}_{xy} = [Q]_{xy}\{\varepsilon\}_{xy}^0 + z[Q]_{xy}\{K\}_{xy}$$

[2] The contribution of the displacements induced by bending are negative because for the upper part of the neutral axis of an upwards deflected beam [see figure P.9 b)], *i.e.*, at a positive z-coordinate of a beam showing a positive slope $\frac{\partial w}{\partial x}$, both displacements u and v decrease.

F.3.5. Resultant forces and moments

The resultant forces and moments in a given direction and ply in the laminate are constant throughout the edge of the laminate, thus it is convenient to define the resultant forces and moments per unit width. Yet, the stresses are obviously not the same on each lamina (it depends on the ply orientation and [if showing curvature] on the ply position).

Mathematically, the forces per unit width N acting on the laminate [see figure P.10 a)] in a particular direction are given by the integral of the stress in the respective direction over the thickness t of the laminate:

$$\begin{Bmatrix} N_x \\ N_y \\ N_{xy} \end{Bmatrix} = \int_{-\frac{t}{2}}^{\frac{t}{2}} \begin{Bmatrix} \sigma_x \\ \sigma_y \\ \tau_{xy} \end{Bmatrix} dz \tag{P.23}$$

The resultant moments per unit width M [see figure P.10 a)] are given by:

$$\begin{Bmatrix} M_x \\ M_y \\ M_{xy} \end{Bmatrix} = \int_{-\frac{t}{2}}^{\frac{t}{2}} z \begin{Bmatrix} \sigma_x \\ \sigma_y \\ \tau_{xy} \end{Bmatrix} dz \tag{P.24}$$

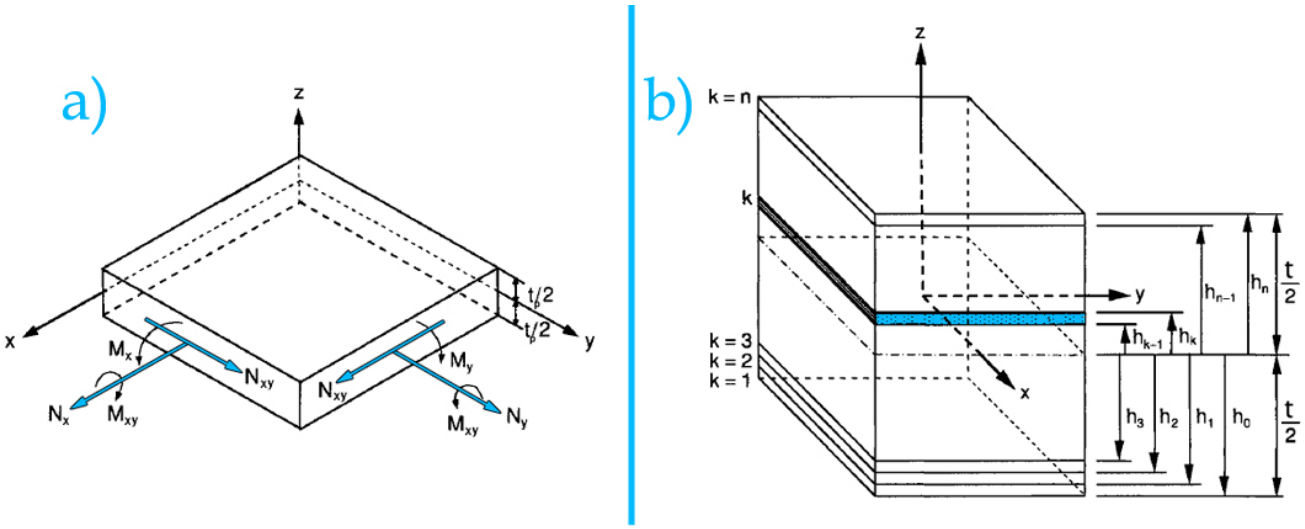

Figure P.10: a) Resultant forces and moments in a lamina; b) Multidirectional laminate with coordinate notation of individual plies. (Reproduced from [20], copyright Oxford University Press, 2006).

F.3.6. Constitutive equations for a laminate

Considering the discontinuities in the stresses between plies, these integrals must be performed over each k ply and then summed for n number of plies [see figure P.10 b)] . Inputing equation (P.22) into the two previous expressions:

$$\begin{Bmatrix} N_x \\ N_y \\ N_{xy} \end{Bmatrix} = \sum_{k=1}^{n} \int_{h_{k-1}}^{h_k} \left(\begin{bmatrix} Q_{xx} & Q_{xy} & Q_{xs} \\ Q_{xy} & Q_{yy} & Q_{ys} \\ Q_{xs} & Q_{ys} & Q_{ss} \end{bmatrix}_k \begin{Bmatrix} \varepsilon_x^0 \\ \varepsilon_y^0 \\ \gamma_{xy}^0 \end{Bmatrix} + z \begin{bmatrix} Q_{xx} & Q_{xy} & Q_{xs} \\ Q_{xy} & Q_{yy} & Q_{ys} \\ Q_{xs} & Q_{ys} & Q_{ss} \end{bmatrix}_k \begin{Bmatrix} K_x \\ K_y \\ K_{xy} \end{Bmatrix} \right) dz \tag{P.25}$$

$$\begin{Bmatrix} M_x \\ M_y \\ M_{xy} \end{Bmatrix} = \sum_{k=1}^{n} \int_{h_{k-1}}^{h_k} \left(z \begin{bmatrix} Q_{xx} & Q_{xy} & Q_{xs} \\ Q_{xy} & Q_{yy} & Q_{ys} \\ Q_{xs} & Q_{ys} & Q_{ss} \end{bmatrix}_k \begin{Bmatrix} \varepsilon_x^0 \\ \varepsilon_y^0 \\ \gamma_{xy}^0 \end{Bmatrix} + z^2 \begin{bmatrix} Q_{xx} & Q_{xy} & Q_{xs} \\ Q_{xy} & Q_{yy} & Q_{ys} \\ Q_{xs} & Q_{ys} & Q_{ss} \end{bmatrix}_k \begin{Bmatrix} K_x \\ K_y \\ K_{xy} \end{Bmatrix} \right) dz \tag{P.26}$$

Tanking into account that the midplane strains ε^0 and curvatures K do not depend on z and that the invariant stiffness matrix $[Q]_{xy}$, as the name indicates, is also constant on the integration over the thickness, all these quantities can be taken outside of the integral[3]:

$$\{N\}_{xy} = \sum_{k=1}^{n} \left([Q]_{xy}^k \{\varepsilon\}_{xy}^0 \int_{h_{k-1}}^{h_k} dz + [Q]_{xy}^k \{K\}_{xy} \int_{h_{k-1}}^{h_k} z dz \right)$$

$$\{M\}_{xy} = \sum_{k=1}^{n} \left([Q]_{xy}^k \{\varepsilon\}_{xy}^0 \int_{h_{k-1}}^{h_k} z dz + [Q]_{xy}^k \{K\}_{xy} \int_{h_{k-1}}^{h_k} z^2 dz \right)$$

Performing the integrals results in the final expressions:

$$\boxed{\{N\}_{xy} = \sum_{k=1}^{n} \left([Q]_{xy}^k \{\varepsilon\}_{xy}^0 (h_k - h_{k-1}) + \frac{1}{2} [Q]_{xy}^k \{K\}_{xy} (h_k^2 - h_{k-1}^2) \right)} \quad \left[\frac{N}{m}\right] \tag{P.27}$$

$$\boxed{\{M\}_{xy} = \sum_{k=1}^{n} \left(\frac{1}{2} [Q]_{xy}^k \{\varepsilon\}_{xy}^0 (h_k^2 - h_{k-1}^2) + \frac{1}{3} [Q]_{xy}^k \{K\}_{xy} (h_k^3 - h_{k-1}^3) \right)} \quad \left[N\right] \tag{P.28}$$

Given that the midplane strains and curvatures are not part of the summations, the invariant stiffness matrices and the distance terms can be transformed into three convenient submatrices:

$$[A_{ij}] = \sum_{k=1}^{n} [Q_{ij}]_{xy}^k (h_k - h_{k-1}) \tag{P.29a}$$

$$[B_{ij}] = \frac{1}{2} \sum_{k=1}^{n} [Q_{ij}]_{xy}^k (h_k^2 - h_{k-1}^2) \tag{P.29b}$$

$$[D_{ij}] = \frac{1}{3} \sum_{k=1}^{n} [Q_{ij}]_{xy}^k (h_k^3 - h_{k-1}^3) \tag{P.29c}$$

Where A_{ij} are extensional stiffnesses relating inplane loads to inplane strains; B_{ij} are inplane-flexure coupling relating inplane loads to curvatures and moments to inplane-strains; D_{ij} are bending or flexural laminate stiffnesses relating moments to curvatures.

[3]From this point on, the derivation will be displayed in the compact format.

Assembling these three last submatrices into one general constitutive matrix that relates in-plane forces and moments to midplane strains and curvatures:

$$\begin{Bmatrix} N_x \\ N_y \\ N_{xy} \\ M_x \\ M_y \\ M_{xy} \end{Bmatrix} = \begin{bmatrix} A_{11} & A_{12} & A_{16} & B_{11} & B_{12} & B_{16} \\ A_{12} & A_{22} & A_{26} & B_{12} & B_{22} & B_{26} \\ A_{16} & A_{26} & A_{66} & B_{16} & B_{26} & B_{66} \\ B_{11} & B_{12} & B_{16} & D_{11} & D_{12} & D_{16} \\ B_{12} & B_{22} & B_{26} & D_{12} & D_{22} & D_{26} \\ B_{16} & B_{26} & B_{66} & D_{16} & D_{26} & D_{66} \end{bmatrix} \begin{Bmatrix} \varepsilon_x^0 \\ \varepsilon_y^0 \\ \gamma_{xy}^0 \\ K_x \\ K_y \\ K_{xy} \end{Bmatrix} \tag{P.30}$$

In a compact format:

$$\left\{\begin{array}{c} N \\ \hline M \end{array}\right\} = \left[\begin{array}{c|c} A & B \\ \hline B & D \end{array}\right] \left\{\begin{array}{c} \varepsilon^0 \\ \hline K \end{array}\right\} \tag{P.31}$$

Partially inverting, in order to obtain the midplane strains from the applied loads:

$$\left\{\begin{array}{c} \varepsilon^0 \\ \hline M \end{array}\right\} = \left[\begin{array}{c|c} A^* & B^* \\ \hline C^* & D^* \end{array}\right] \left\{\begin{array}{c} N \\ \hline K \end{array}\right\} \tag{P.32}$$

Where:

$$[A^*] = [A]^{-1} \tag{P.33a}$$
$$[B^*] = -[A]^{-1}[B] \tag{P.33b}$$
$$[C^*] = [B][A]^{-1} \tag{P.33c}$$
$$[D^*] = [D] - [B][A]^{-1}[B] \tag{P.33d}$$

Fully inverting equation (P.31) results in the most commonly used form of the laminate constitutive equations:

$$\left\{\begin{array}{c} \varepsilon^0 \\ \hline K \end{array}\right\} = \left[\begin{array}{c|c} a & b \\ \hline c & d \end{array}\right] \left\{\begin{array}{c} N \\ \hline M \end{array}\right\} \tag{P.34}$$

Where:

$$[a] = [A^*] - [B^*][D^*]^{-1}[C^*] \tag{P.35a}$$
$$[b] = [B^*][D^*]^{-1} \tag{P.35b}$$
$$[c] = -[D^*]^{-1}[C^*] \tag{P.35c}$$
$$[d] = [D^*]^{-1} \tag{P.35d}$$

F.3.7. Corollary of the classical laminate theory

The following table presents special laminate configurations and its coupling implications.

Table P.2: Special laminate configurations and its consequences in the mechanical behavior of the composite structure.

Property	**Generic layup example**	**Effects on couplings**	**Null elements**	**Examples of practical consequences**
Symmetry - lamination sequence is symmetric about the midplane	$[\theta/\phi]_s$	No extension - bending coupling	[B]=0	An applied shear does not develop curvatures
Balanced - for every theta oriented ply there is a -theta oriented ply	$[\theta/\text{-}\theta/\text{-}\phi/\phi]$	No extension - shear coupling	$A_{16}; A_{26} = 0$	An applied tension does not develop shearing behavior
Anti-symmetric - balanced pairs of plies located symmetrically with respect to the midplane of the laminate	$[\theta/\text{-}\phi/\phi/\text{-}\theta]$	No bending - twisting coupling	$D_{16}; D_{26} = 0$	An applied bending does not develop twisting behavior

These are commonly used configurations in design of composite structures and materials. Noteworthy is that an anti-symmetric laminate is necessarily balanced and non-symmetric, unless it is composed only by 0°and 90°oriented plies.

For the vast majority of aerospace applications, laminates are designed to be symmetric and balance, given that extension-bending and extension-shear couplings, respectively, are generally undesirable (*e.g.*, non-symmetric laminate show warpage due to cooldown after curing).

F.4. 2-D transformation of stresses and strains in the lamina

The stresses and strains in the material coordinate system are transformed from the load coordinate system obtained through a free body diagram on the generally orthotropic lamina [see figure P.11 a)].

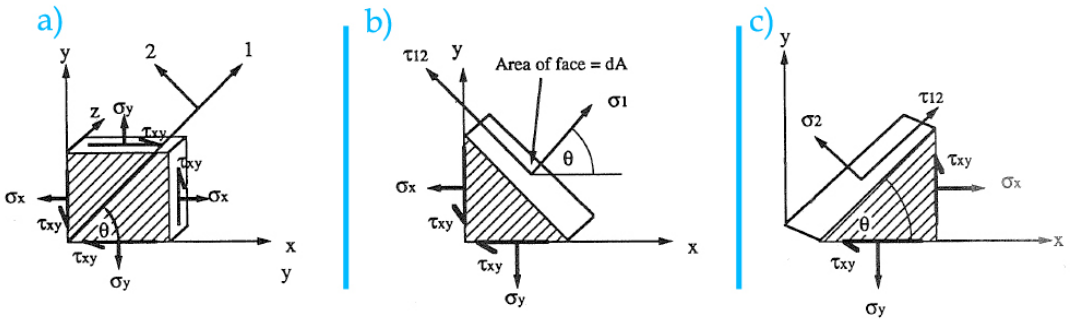

Figure P.11: General orthotropic lamina element: a) stresses in the load coordinate system; b) projection of the stresses in the laminate coordinate system onto the 1-direction material system; projection of the stresses in the laminate coordinate system onto the 2-direction material system. (Reproduced from [76], copyright NASA, 1994).

From the free body diagram - P.11 figure b) in the 1-direction, material stress σ_1 is

obtained:

$$\sum F_1 = \sigma_1 dA - \sigma_x (dA\, cos\theta) cos\theta - \sigma_y (dA\, sin\theta) sin\theta - \tau_{xy} (dA\, cos\theta) sin\theta - \tau_{xy} (dA\, sin\theta) cos\theta = 0$$

$$\sigma_1 = \sigma_x cos^2\theta + \sigma_y sin^2\theta + 2\tau_{xy} sin\theta cos\theta \tag{P.36}$$

From the free body diagram - P.11 figure c) in the 2-direction, material stress σ_2 is obtained:

$$\sum F_2 = \sigma_2 dA - \sigma_x (dA\, sin\theta) sin\theta - \sigma_y (dA\, cos\theta) cos\theta + \tau_{xy} (dA\, cos\theta) sin\theta + \tau_{xy} (dA\, sin\theta) cos\theta = 0$$

$$\sigma_2 = \sigma_x sin^2\theta + \sigma_y cos^2\theta - 2\tau_{xy} sin\theta cos\theta \tag{P.37}$$

From the free body diagram - P.11 figure c) in the 1-direction, material stress τ_{12} is obtained:

$$\sum F_2 = \tau_{12} dA + \sigma_x (dA\, sin\theta) cos\theta - \sigma_y (dA\, cos\theta) sin\theta - \tau_{xy} (dA\, cos\theta) cos\theta + \tau_{xy} (dA\, sin\theta) sin\theta = 0$$

$$\tau_{12} = -\sigma_x sin\theta cos\theta + \sigma_y sin\theta cos\theta + \tau_{xy} (cos^2\theta - sin^2\theta) \tag{P.38}$$

Writing equations (P.36-P.38) in a matrix form:

$$\begin{Bmatrix} \sigma_1 \\ \sigma_2 \\ \tau_{12} \end{Bmatrix} = \begin{bmatrix} cos^2\theta & sin^2\theta & 2cos\theta sin\theta \\ sin^2\theta & cos^2\theta & -2cos\theta sin\theta \\ -cos\theta sin\theta & cos\theta sin\theta & (cos^2\theta - sin^2\theta) \end{bmatrix} \begin{Bmatrix} \sigma_x \\ \sigma_y \\ \tau_{xy} \end{Bmatrix} \tag{P.39}$$

The previous square 3x3 matrix is conventionally named transformation matrix and denoted by T. Similarly, for the strains:

$$\begin{Bmatrix} \varepsilon_1 \\ \varepsilon_2 \\ \gamma_{12} \end{Bmatrix} = \begin{bmatrix} cos^2\theta & sin^2\theta & 2cos\theta sin\theta \\ sin^2\theta & cos^2\theta & -2cos\theta sin\theta \\ -cos\theta sin\theta & cos\theta sin\theta & (cos^2\theta - sin^2\theta) \end{bmatrix} \begin{Bmatrix} \varepsilon_x \\ \varepsilon_y \\ \gamma_{xy} \end{Bmatrix} \tag{P.40}$$

It is worthwhile to mention that transformation matrix T has a special property. The inverse of the transformation matrix for a θ angle is equivalent to the transformation matrix for a minus θ angle:

$$[T(\theta)]^{-1} = [T(-\theta)] \tag{P.41}$$

G. Failure modes in FRP composites

G.1. Kinking bands

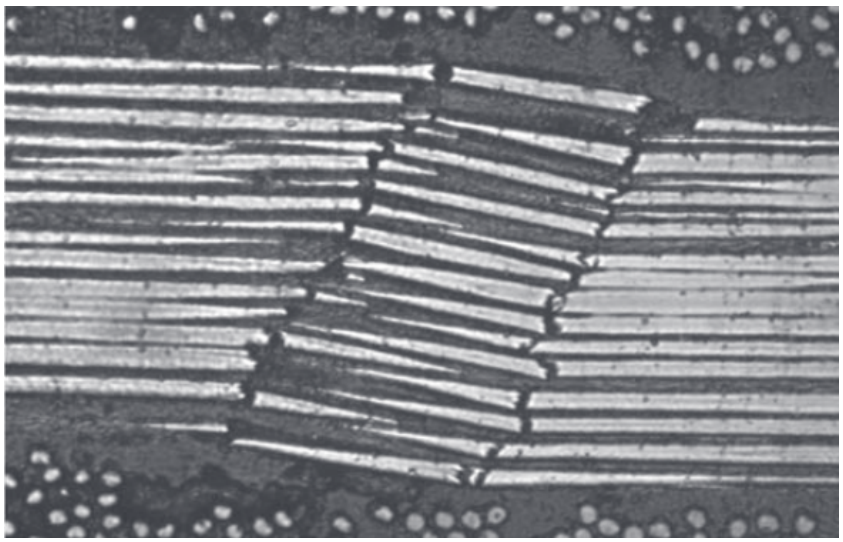

Figure P.12: Kinking bands originated from fiber compressive failure. (Reproduced from [81], copyright SAGE, 2005).

G.2. Features prone to delamination

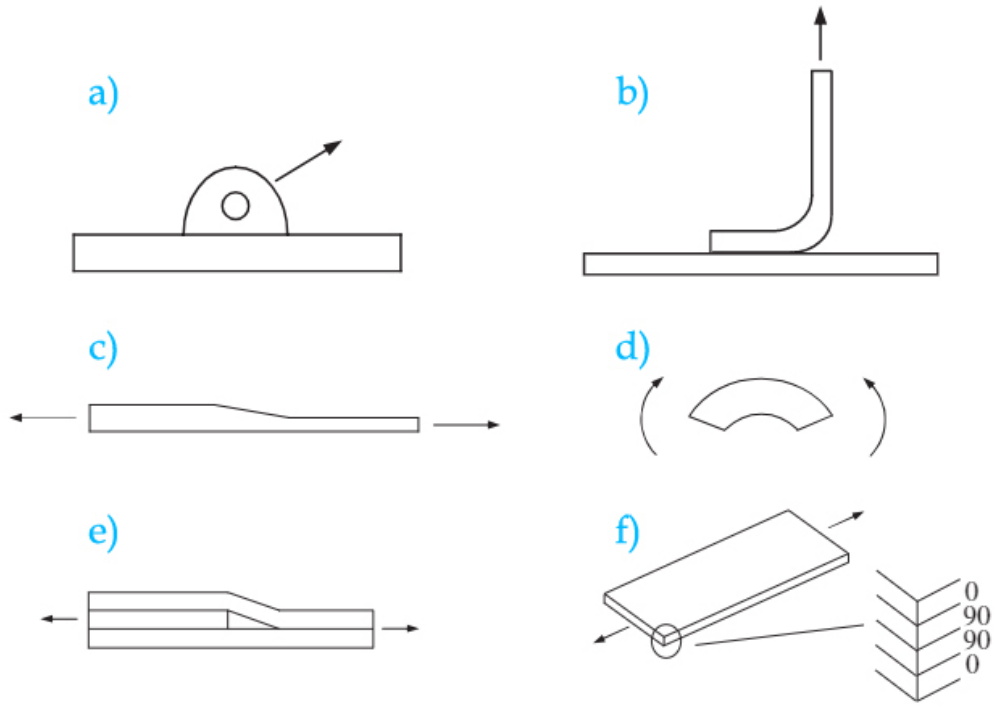

Figure P.13: Features prone to delamination owing to: out-of-plane loading [a) lug fitting and b) rib-to-skin joint], geometry [c) taper and d) curved section in bending] and discontinuities [e) ply drop and f) free edge]. (Reproduced from [113], copyright The Royal Society, 2012).

H. Failure criteria equations and supplementary information

H.1. Hashin's failure criteria equations

† Tensile fiber mode ($\sigma_1 > 0$)

Accounting with shear contribution:

$$\left(\frac{\sigma_1}{X^T}\right)^2 + \frac{1}{(S^L)^2}(\tau_{12}^2 + \tau_{13}^2) = 1 \quad \overset{\text{2D}}{\Longrightarrow} \quad \left(\frac{\sigma_1}{X^T}\right)^2 + \left(\frac{\tau_{12}}{S^L}\right)^2 = 1 \tag{P.42}$$

Disregarding shear contribution:

$$\sigma_1 = X^T \tag{P.43}$$

† Compressive fiber mode ($\sigma_1 < 0$)

$$\sigma_1 = X^C \tag{P.44}$$

† Tensile matrix mode ($\sigma_2 + \sigma_3 > 0$)

$$\frac{1}{(Y^T)^2}(\sigma_2 + \sigma_3)^2 + \frac{1}{(S^T)^2}(\tau_{23}^2 - \sigma_2\sigma_3) + \frac{1}{(S^L)^2}(\tau_{12}^2 + \tau_{13}^2) = 1 \tag{P.45}$$

$$\overset{\text{2D}}{\Longrightarrow} \quad \left(\frac{\sigma_2}{Y^T}\right)^2 + \left(\frac{\tau_{12}}{S^L}\right)^2 = 1 \tag{P.46}$$

† Compressive matrix mode ($\sigma_2 + \sigma_3 < 0$)

$$\frac{1}{Y^C}\left[\left(\frac{Y^C}{2(S^T)}\right)^2 - 1\right](\sigma_2+\sigma_3) + \frac{1}{4(S^T)^2}(\sigma_2+\sigma_3)^2 + \frac{1}{(S^T)^2}(\tau_{23}^2 - \sigma_2\sigma_3) + \frac{1}{(S^L)^2}(\tau_{12}^2+\tau_{13}^2) = 1 \tag{P.47}$$

$$\overset{\text{2D}}{\Longrightarrow} \quad \frac{\sigma_2}{Y^C}\left[\left(\frac{Y^C}{2(S^T)}\right)^2 - 1\right] + \left(\frac{\sigma_2}{2S^T}\right)^2 + \left(\frac{\tau_{12}}{S^L}\right)^2 = 1 \tag{P.48}$$

Where: σ_i is the normal stress in the i direction; τ_{ij} is the shear stress contained in the plane perpendicular to i and in the j direction; X^T is the longitudinal tensile strength; X^C is the longitudinal compressive strength; Y^T is the transverse tensile strength; Y^C is the transverse compressive strength; S^L is the longitudinal shear strength; S^T is the transverse shear strength.

H.2. Comparison between Hashin's failure criteria and experimental results

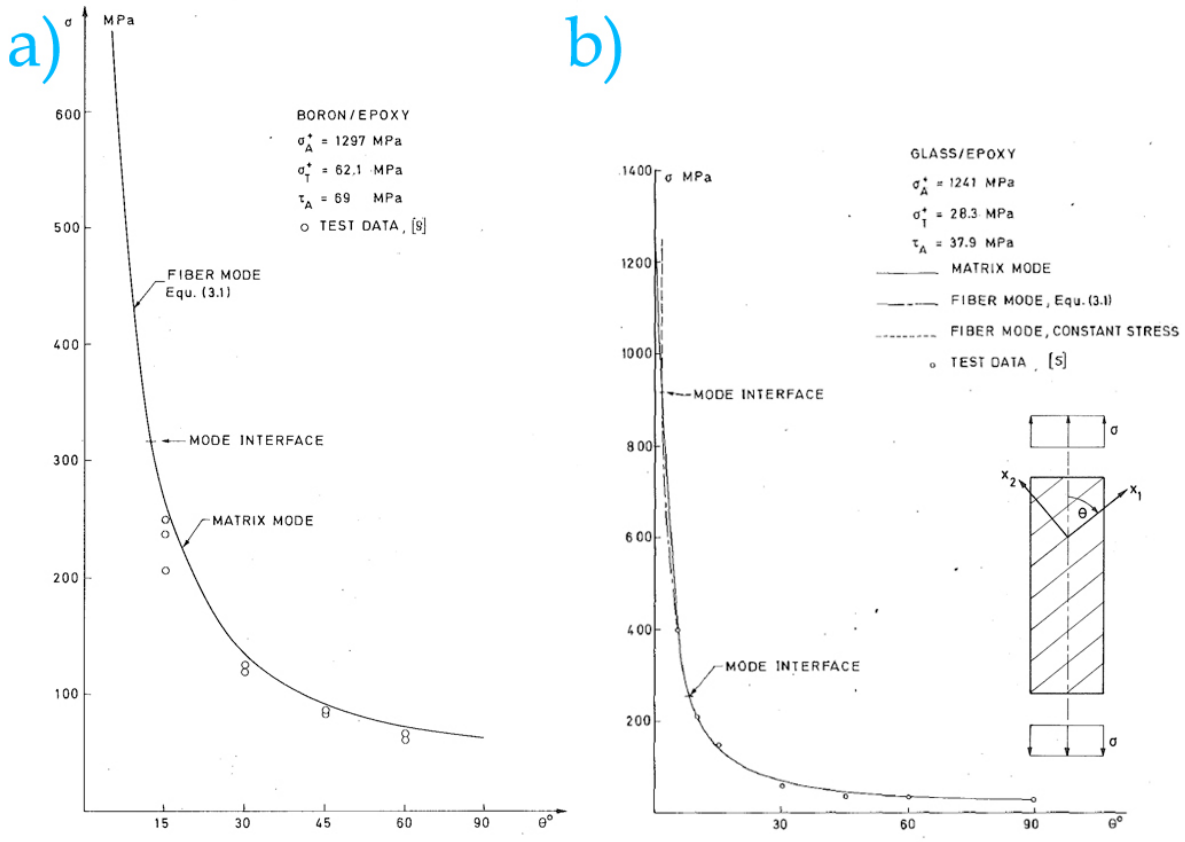

Figure P.14: Comparison of failure criteria with test data: a) boron-epoxy off-axis specimens; b) glass-epoxy off-axis specimens. θ angle is defined from load axes to material axes (Reproduced from [42], copyright ASME, 1980).

H.3. Transformation equations to obtain the stresses acting on an arbitrary sectional plane

$$\begin{cases} \sigma_n(\theta) = \sigma_2 cos^2(\theta) + \sigma_3 sin^2(\theta) + 2\tau_{23} sin(\theta) cos(\theta) \\ \tau_{nt}(\theta) = (\sigma_3 - \sigma_2) sin(\theta) cos(\theta) + \tau_{23}(cos^2(\theta) - sin^2(\theta)) \\ \tau_{nl}(\theta) = \tau_{13} sin(\theta) + \tau_{12} cos(\theta) \end{cases} \tag{P.49}$$

Where σ_n, τ_{nl} and τ_{nt} are, respectively, the normal, the normal/longitudinal shear and the normal/transverse shear stress components acting on the perpendicular plane rotated by an angle of θ.

H.4. Puck's master fracture surface for UD material

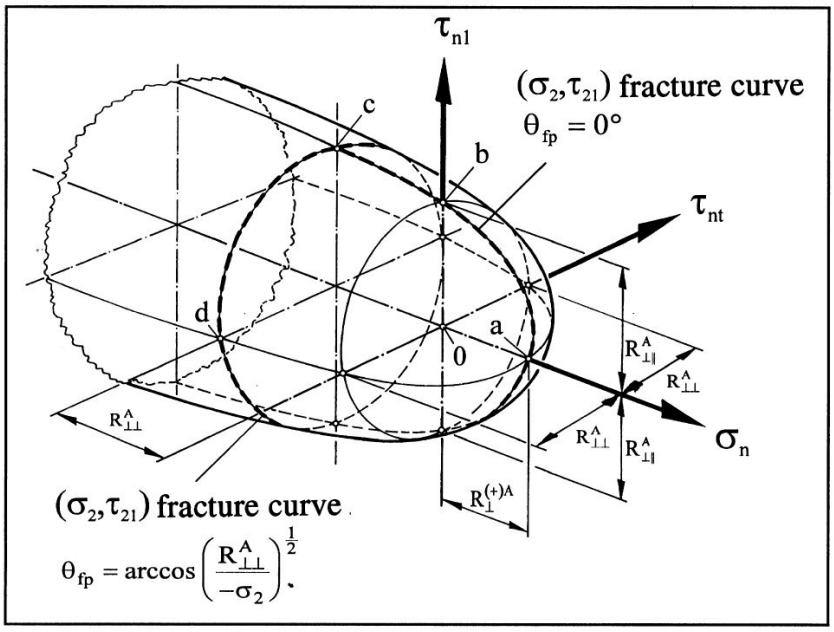

Figure P.15: Master fracture surface (for $\sigma_1 = 0$) for UD material in the (σ_n, τ_{nt}, τ_{nl}) stress space with fracture resistances $R_{\perp}^{(+)A}$, $R_{\perp\parallel}^{A}$ and $R_{\perp\perp}^{A}$ of the stress action plane. The (σ_2,τ_{21}) fracture curve follows a contour line (from a to c) and then a boundary line of a cross-section (from c to d). Compare with figure P.16. (Reproduced from [84], copyright Elsevier, 1998).

H.5. Puck's a-b-c-d fracture surface and associated failure modes to IFF failure type

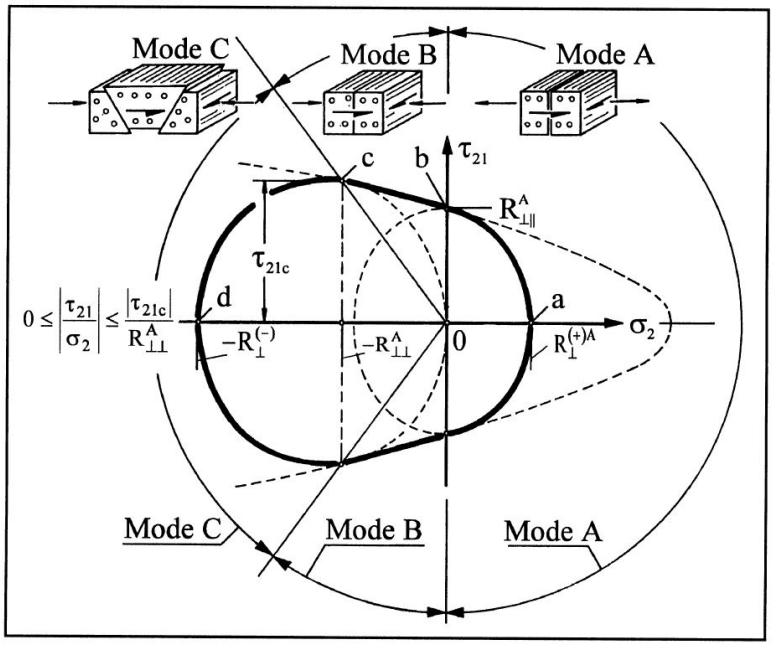

Figure P.16: Fracture curve (τ_{21}, σ_2, for $\sigma_1 = 0$), representing three different fracture modes A, B, C. The curve is generated by two ellipses and one parabola. (Reproduced from [84], copyright Elsevier, 1998).

I. ABD matrices for FESALs

Recalling $[ABD]$ matrix:

$$[ABD] = \begin{bmatrix} A_{11} & A_{12} & A_{16} & B_{11} & B_{12} & B_{16} \\ A_{12} & A_{22} & A_{26} & B_{12} & B_{22} & B_{26} \\ A_{16} & A_{26} & A_{66} & B_{16} & B_{26} & B_{66} \\ B_{11} & B_{12} & B_{16} & D_{11} & D_{12} & D_{16} \\ B_{12} & B_{22} & B_{26} & D_{12} & D_{22} & D_{26} \\ B_{16} & B_{26} & B_{66} & D_{16} & D_{26} & D_{66} \end{bmatrix} \qquad \left[\begin{array}{c|c} [N/mm] & [N] \\ \hline [N] & [Nmm] \end{array}\right]$$

The following matrices are the FESAL1, FESAL2, FESAL3 and FESAL4 $[ABD]$ matrices.

$$[ABD]_{FESAL1} = \begin{bmatrix} 285333.0 & 4937.1 & 0.0 & 0.0 & 0.0 & 0.0 \\ 4937.1 & 18285.4 & 0.0 & 0.0 & 0.0 & 0.0 \\ 0.0 & 0.0 & 10400.0 & 0.0 & 0.0 & 0.0 \\ 0.0 & 0.0 & 0.0 & 95111.0 & 1645.7 & 0.0 \\ 0.0 & 0.0 & 0.0 & 1645.7 & 6095.1 & 0.0 \\ 0.0 & 0.0 & 0.0 & 0.0 & 0.0 & 3466.7 \end{bmatrix}$$

$$[ABD]_{FESAL2} = \begin{bmatrix} 151809.2 & 4937.1 & 0.0 & 0.0 & 0.0 & 0.0 \\ 4937.1 & 151809.2 & 0.0 & 0.0 & 0.0 & 0.0 \\ 0.0 & 0.0 & 10400.0 & 0.0 & 0.0 & 0.0 \\ 0.0 & 0.0 & 0.0 & 52689.4 & 1645.7 & 0.0 \\ 0.0 & 0.0 & 0.0 & 1645.7 & 48516.8 & 0.0 \\ 0.0 & 0.0 & 0.0 & 0.0 & 0.0 & 3466.7 \end{bmatrix}$$

$$[ABD]_{FESAL3} = \begin{bmatrix} 88773.1 & 67973.1 & 0.0 & 0.0 & 0.0 & 0.0 \\ 67973.1 & 88773.1 & 0.0 & 0.0 & 0.0 & 0.0 \\ 0.0 & 0.0 & 73436.1 & 0.0 & 0.0 & 0.0 \\ 0.0 & 0.0 & 0.0 & 29591.0 & 22657.7 & -4172.6 \\ 0.0 & 0.0 & 0.0 & 22657.7 & 29591.0 & -4172.6 \\ 0.0 & 0.0 & 0.0 & -4172.6 & -4172.6 & 24478.7 \end{bmatrix}$$

$$[ABD]_{FESAL4} = \begin{bmatrix} 120291.2 & 36455.1 & 0.0 & 0.0 & 0.0 & 0.0 \\ 36455.1 & 120291.2 & 0.0 & 0.0 & 0.0 & 0.0 \\ 0.0 & 0.0 & 41918.0 & 0.0 & 0.0 & 0.0 \\ 0.0 & 0.0 & 0.0 & 42241.6 & 13136.6 & -2607.9 \\ 0.0 & 0.0 & 0.0 & 13136.6 & 35982.7 & -2607.9 \\ 0.0 & 0.0 & 0.0 & -2607.9 & -2607.9 & 14957.6 \end{bmatrix}$$

J. Abaqus standard *vs.* explicit procedures

Table P.3: Comparison between Abaqus standard and explicit procedures (Adapted from [1, 86, 100]).

Features	Abaqus/Standard	Abaqus/Explicit
Solution technique	Stiffness-based solution through iteration; Newton-Raphson method or its modified forms are used to enforce equilibrium	Explicit time integration; kinematic stress state is obtained from the end of the last time increment
Dependence on the current time increment information	Unknown values are obtained from the current information through iteration methods (such as the Newton-Raphson method). Convergence checking is, therefore, required. If too many iterations are required, this procedure might become too expensive.	Neither iteration nor convergence checking are required. Yet, this procedure is conditionally stable, depending on the smallest element size and the wave speed of the material.
Problem type application	Linear and nonlinear static; Linear dynamic; Low-speed (low frequency response) nonlinear dynamic; Nonlinear heat transfer; Coupled temperature-displacement (quasi-static); Coupled thermal-electrical; Mass diffusion problems; Structural-acoustics	High-speed (short duration) dynamics; Large, nonlinear, quasi-static analyses; Highly discontinuous postbuckling and collapse simulations; Coupled temperature-displacement (dynamic); Structural-acoustics
Mesh refinement cost	Computational cost is proportional to the square of the number of degrees of freedom	Computational cost is proportional to the number of elements and inversely proportional to the smallest element dimension.
Disk space and memory required	If many iterations are needed for convergence, disk and space memory are expected to be large	Typically smaller for more complex geometries and non-linear behavior

K. Newton-Raphson implementation

K.1. Newton-Raphson implementation in two generic examples

The following figures,P.17 and P.18 illustrate two examples of numerical root-finding using the Newton-Raphson method in the functions $y = sin(x) - 0.7$ and $y = 10cos(x) + 1/x$ with an initial guess of $x_0 = 1.2$ and $x_0 = 0.05$, respectively. In the first case case, finding the roots of the respective function would, obviously, be solvable analytically. Yet, for demonstration purposes, the Newton-Raphson method was used as a numerical

technique to solve the root-finding problem for both equations.

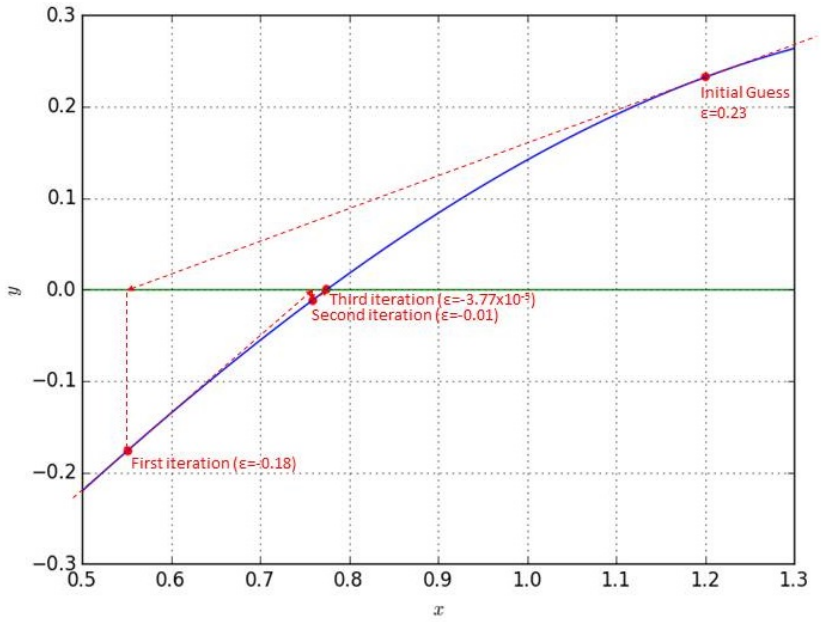

Figure P.17: Example of Newton-Raphson method implementation for a function $y = sin(x) - 0.7$ with an initial guess of $x_0 = 1.2$ and a tolerated error of $\epsilon_{tol} = 0.0001$.

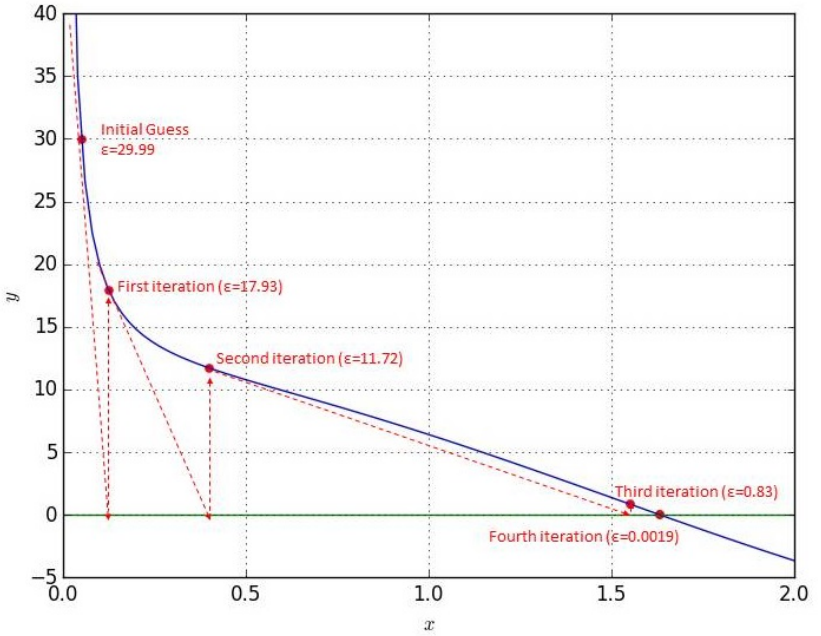

Figure P.18: Example of Newton-Raphson method implementation for a function $y = 10cos(x) + 1/x$ with an initial guess of $x_0 = 0.05$ and a tolerated error of $\epsilon_{tol} = 0.0001$.

Table P.4 presents, for the first analysed case, the root values and respective absolute errors at each iteration.

Table P.4: Root iteration values and respective absolute errors using Newton-Raphson method for a function $y = sin(x) - 0.7$ with an initial guess of $x_0 = 1.2$.

Step number	x_n	$f(x_n)$	$f'(x_n)$	x_{n+1}	$f(x_{n+1})$
Initial (n=0)	1.2000	0.2320	0.3577	0.5513	-0.1762
1^{st} it. (n=1)	0.5513	-0.1762	0.8492	0.7588	-0.0120
2^{nd} it. (n=2)	0.7588	-0.0120	0.7222	0.7753	-3.767E-05

K.2. Newton-Raphson implementation in Abaqus

A body is assumed in equilibrium if the net force acting at every node is equal to zero. By other words, the internal nodal forces $\{f_{int}\}$ must balance the externally applied forces $\{f_{ext}\}$.

$$\{f_{ext}\} - \{f_{int}\} = 0$$

Yet, as numerical methods are of iterative nature, thus leading to approximate results, they require a convergence criterion that defines the method's accuracy. In other words, convergence is achieved when the difference between the external load increment $\{f_{ext}\}^{t+\Delta t}$ and the internal nodal forces $\{f_{int}\}$ at a displacement[4] $(\{a\}^t + \{a\}_i)$ is smaller than the tolerated error $\{\epsilon\}_{tol}$, in this case named residual force $\{r\}_i$:

$$\{r\}_i = \{f_{ext}\}^{t+\Delta t} - \{f_{int}\}(\{a\}^t + \{a\}_i)$$

Initially $i = 0$, the iterated displacement is null $\{a\}_{i=0} = 0$:

$$\{r\}_{i=0}(\{a\}^t + \{a\}_{i=0}) = \{f_{ext}\}^{t+\Delta t} - \{f_{int}\}(\{a\}^t + \{a\}_{i=0})$$

The initial tangential stiffness matrix, which graphically given by the rate of change of the internal nodal forces over the displacement or the residual force over the displacement:

$$[K]_{i=0} = \frac{\partial\{f_{int}\}(\{a\}^t + \{a\}_{i=0})}{\partial a} = -\frac{\partial\{r\}_{i=0}(\{a\}^t + \{a\}_{i=0})}{\partial a}$$

The outcome displacement is given by the sum of the initial displacement with the found displacement increment (graphically, is the horizontal leg of the right triangle, defined by the legs δa_0 and r_0):

$$\{a\}_{i=1} = \{a\}_{i=0} + \{\Delta a\}_{i=0} = \{a\}_{i=0} + [K]^{-1}_{i=0}\{r\}_{i=0}(\{a\}^t + \{a\}_{i=0})$$

If the maximum entry[5] of the residue vector at the found displacement $\{r\}_{i=1}(\{a\}^t + \{a\}_{i=1})$ is smaller than the tolerated error ϵ_{tol}, then convergence is assumed, otherwise, another iteration $i = i + 1$ is required until convergence is achieved. Hence, the convergence criterion may be given by:

[4] Where $\{a\}^t$ is the initial known displacement and $\{a\}_i$ is unknown displacement at the $i - th$ iteration, which will be the output once converge is achieved.

[5] Other criteria may be chosen instead of the maximum value of the vector, *e.g.* the sum of the absolute value of the terms or the square root of the sum of the squares.

$$max[\{r\}_{i=1}(\{a\}^t + \{a\}_{i=1})] < \epsilon_{tol}$$

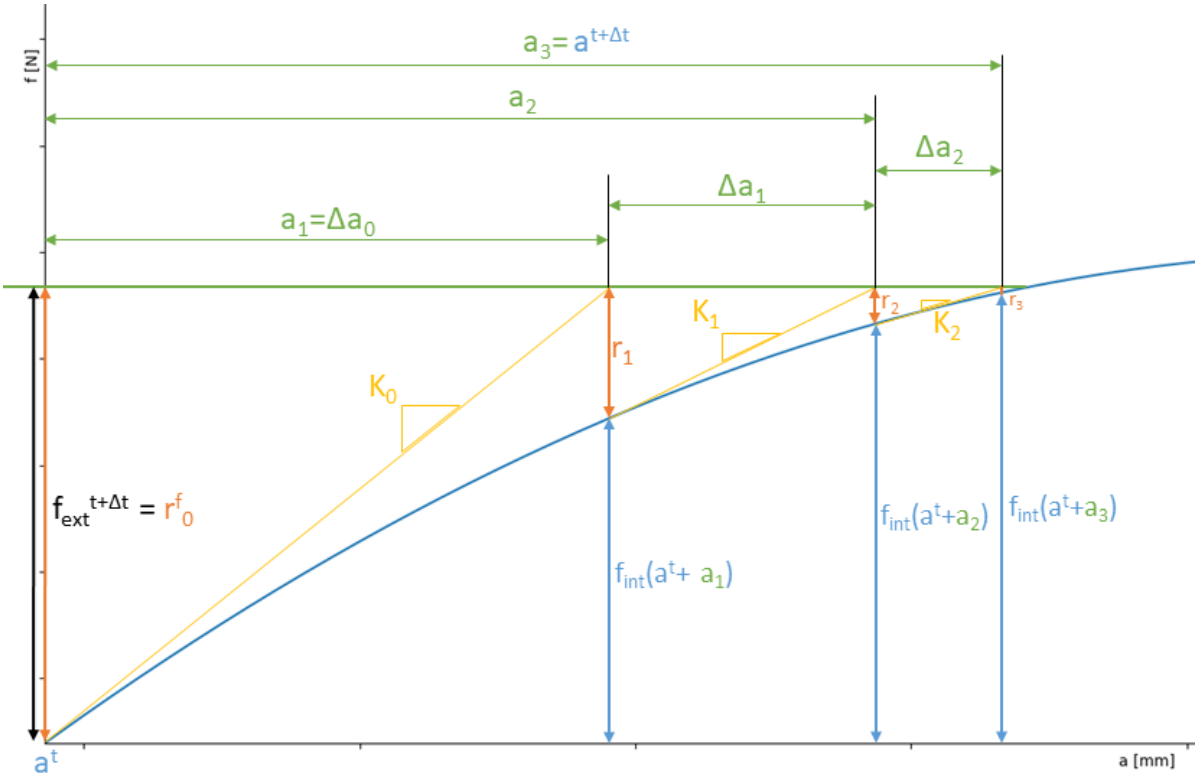

Figure P.19: Graphical example of Newton–Raphson method applied to solve nonlinear equilibrium equations in Abaqus.

The pseudo algorithm for Newton-Raphson implementation in Abaqus/standard can be formulated as follows:

$$
\begin{aligned}
&i = 0 \\
&a_i = 0.0 \\
&while \quad r_i > \epsilon_{tol} \quad do: \\
&\qquad r_i = f_{ext}^{t+\Delta t} - f_{int}(a^t + a_i) \\
&\qquad if \quad r_i \leq \epsilon_{tol} \quad then: \\
&\qquad\qquad return \quad a_i \\
&\qquad else: \\
&\qquad\qquad K_i = compute\_K(a^t, a_i, f_{int}) \\
&\qquad\qquad a_{i+1} = a_i + K_i^{-1} r_i \\
&\qquad i = i + 1
\end{aligned}
$$

K.3. Newton-Raphson implementation in Puck's model

while $|(f_{E\_IFF} - 1)| > \epsilon_{tol}$ *do* :

 # Degraded elastic constants for a given η

$E_2 = \eta * E_{20}$

$G_{12} = \eta * G_{120}$

$E_3 = E_2$

$G_{13} = G_{12}$

 # Degraded elastic constants for an infinitesimal increment on η

$(\eta + \Delta\eta) = \eta + 0.00001$

$E_{2\_\Delta\eta} = (\eta + \Delta\eta) * E_{20}$

$G_{12\_\Delta\eta} = (\eta + \Delta\eta) * G_{120}$

$E_{3\_\Delta\eta} = E_{2\_\Delta\eta}$

$G_{13\_\Delta\eta} = G_{12\_\Delta\eta}$

 # Computation of the constitutive behavior and obtainment of the stress vector

$\{\sigma\} = constitutive(E_2, E_3, G_{12}, G_{13}, \{\varepsilon\})$

$\{\sigma\}_{\_\Delta\eta} = constitutive(E_{2\_\Delta\eta}, E_{3\_\Delta\eta}, G_{12\_\Delta\eta}, G_{13\_\Delta\eta}, \{\varepsilon\})$

 # Failure criteria check

$f_{E\_IFF} = failure_criteria(\{\sigma\}, allowables)$

$f_{E\_IFF\_\Delta\eta} = failure_criteria(\{\sigma\}_{\_\Delta\eta}, allowables)$

 # if convergence is obtained, return current η, otherwise go for a new NR iteration

if $|(f_{E\_IFF} - 1)| \leq \epsilon_{tol}$ *then* :

return η

else :

$$\eta = \eta - (f_{E\_IFF} - 1) * \frac{\Delta\eta}{f_{E\_IFF\_\Delta\eta} - f_{E\_IFF}}$$

L. Hourglass control

The element stiffness matrix is calculated by numerical volume integration of the element shape functions. Typical numerical integration methods are: Riemann integral, trapezoidal rule and Simpson's rule. Yet, these are computationally too expensive. An efficient alternative is by using Gauss quadrature that turns an integration problem into a simplified summation of weighted values evaluated at m integration points. This method dictates that for a polynomial of *2m-1* order, m integration points and weights are used [115]. In FEM, this corresponds to a full integration scheme. As explained before, if a

lower number of Gauss points are used, the integration scheme is reduced.

While this option may significantly reduce the computational time, it also entails undesirable effects, particularly when all nodes have identical displacements, *i.e.* no strains in the element, leading to a so-called zero-energy mode.

A few undesirable scenarios may take in place including: a) deformation by translation or rotation when improper constraints are applied; b) unrealistic strains away from the integration points; c) over-deformed elements for bending problems (especially for concentrated load applications), where the single Gauss point experiences no strain, which means that it produces a zero strain energy. This phenomenon is commonly known as hourglass mode [115].

M. UMAT framing in an Abaqus/Standard simulation flowchart

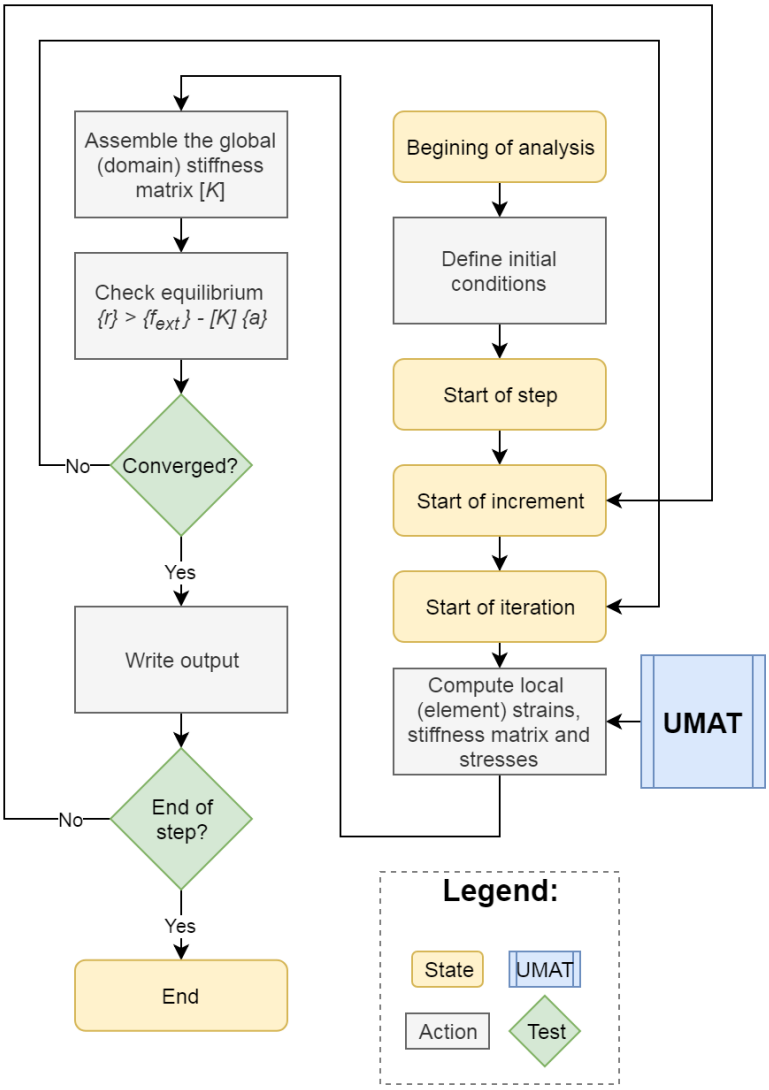

Figure P.20: Flowchart of framing UMAT in a generic Abaqus/Standard simulation.

N. Incremental strain formulation

Abaqus/Standard uses a strain incremental formulation in order to compute the current strain state [77]:

$$\{\varepsilon\}^{k,i} = \{\varepsilon\}^{k-1} + \{\Delta\varepsilon\}^{k,i}$$

This means that the current strain $\{\varepsilon\}^{k,i}$ (at the current $k-th$ load increment and converged at the $i-th$ iteration) is obtained from the sum of the previous strain $\{\varepsilon\}^{k-1}$ (measured from the previous $(k-1)-th$ converged strain at the $i-th$ iteration), plus the current strain increment $\{\Delta\varepsilon\}^{k,i}$. The first term of right side of the equation

(previous strain state) is recognized by Abaqus/Standard within the context of UMAT as `STRAN(NTENS)`; the second term (strain increment) corresponds to `DSTRAN(NTENS)`.

To obtain the current stress state, a similar logic applies:

$$\{\sigma\}^{k,i} = \{\sigma(\{\varepsilon\}^{k-1})\}^{k-1} + \{\Delta\sigma(\{\varepsilon\}^{k,i})\}^{k,i}$$

The incremental stress state is computed using the current local tangent stiffness matrix:

$$\{\sigma\}^{k,i} = \{\sigma(\{\varepsilon\}^{k-1})\}^{k-1} + \left[\frac{\partial\Delta\sigma}{\partial\Delta\varepsilon}\right]^{k,i}\{\Delta\varepsilon\}^{k,i}$$

The local tangent stiffness matrix is also known as the local Jacobian matrix:

$$[J(\{\varepsilon\})]^{k,i} = \left[\frac{\partial\Delta\sigma}{\partial\Delta\varepsilon}\right]^{k,i}$$

The next section O mathematically describes this matrix for isotropic and orthotropic materials.

O. Jacobian matrix computation

O.1. Isotropic material Jacobian matrix

The constitutive behavior of an isotropic material is defined as:

$$\begin{Bmatrix}\sigma_1\\ \sigma_2\\ \sigma_3\\ \tau_{12}\\ \tau_{13}\\ \tau_{23}\end{Bmatrix} = \begin{bmatrix}\lambda+2G & \lambda & \lambda & 0 & 0 & 0\\ \lambda & \lambda+2G & \lambda & 0 & 0 & 0\\ \lambda & \lambda & \lambda+2G & 0 & 0 & 0\\ 0 & 0 & 0 & G & 0 & 0\\ 0 & 0 & 0 & 0 & G & 0\\ 0 & 0 & 0 & 0 & 0 & G\end{bmatrix}\begin{Bmatrix}\varepsilon_1\\ \varepsilon_2\\ \varepsilon_3\\ \gamma_{12}\\ \gamma_{13}\\ \gamma_{23}\end{Bmatrix}$$

Where: $\lambda = \frac{E\nu}{(1+\nu)(1-2\nu)}$; $G = \frac{E}{2(1+\nu)}$ is the shear modulus; E is the Young's modulus and ν is the Poisson ratio of the isotropic material. Inside UMAT, this compliance matrix is the local material Jacobian matrix - `DDSDDE(NTENS,NTENS)`.

O.2. Orthotropic material Jacobian matrix

The constitutive behavior of an orthotropic material is mathematically described by equation P.4. In order to obtain the stress vector as a function of the strains, the compliance matrix is inverted[6]:

[6]Note that the order of the elements of stress and strain vectors was rearranged between equation P.4 which is based in the referenced literature [20], while Abaqus/Standard uses a different convention.

$$\{\varepsilon\} = [S]\{\sigma\} \Leftrightarrow \{\sigma\} = [C]\{\epsilon\} \tag{P.50}$$

The constitutive behavior of an orthotropic material is, therefore, given by:

$$\begin{Bmatrix} \sigma_1 \\ \sigma_2 \\ \sigma_3 \\ \tau_{12} \\ \tau_{13} \\ \tau_{23} \end{Bmatrix} = \begin{bmatrix} \frac{(1-\nu_{23}\nu_{32})E_1}{\chi} & \frac{(\nu_{12}+\nu_{13}\nu_{32})E_2}{\chi} & \frac{(\nu_{13}+\nu_{12}\nu_{32})E_3}{\chi} & 0 & 0 & 0 \\ \frac{(\nu_{12}+\nu_{13}\nu_{32})E_2}{\chi} & \frac{(1-\nu_{13}\nu_{31})E_2}{\chi} & \frac{(\nu_{23}+\nu_{13}\nu_{21})E_3}{\chi} & 0 & 0 & 0 \\ \frac{(\nu_{13}+\nu_{12}\nu_{32})E_3}{\chi} & \frac{(\nu_{23}+\nu_{13}\nu_{21})E_3}{\chi} & \frac{(1-\nu_{12}\nu_{21})E_3}{\chi} & 0 & 0 & 0 \\ 0 & 0 & 0 & G_{12} & 0 & 0 \\ 0 & 0 & 0 & 0 & G_{13} & 0 \\ 0 & 0 & 0 & 0 & 0 & G_{23} \end{bmatrix} \begin{Bmatrix} \varepsilon_1 \\ \varepsilon_2 \\ \varepsilon_3 \\ \gamma_{12} \\ \gamma_{13} \\ \gamma_{23} \end{Bmatrix}$$

Where: $\chi = 1 - \nu_{12}\nu_{21} - \nu_{13}\nu_{31} - \nu_{23}\nu_{32} - 2\nu_{21}\nu_{32}\nu_{13}$.

P. Preliminary FE stress study results for different layup sequences

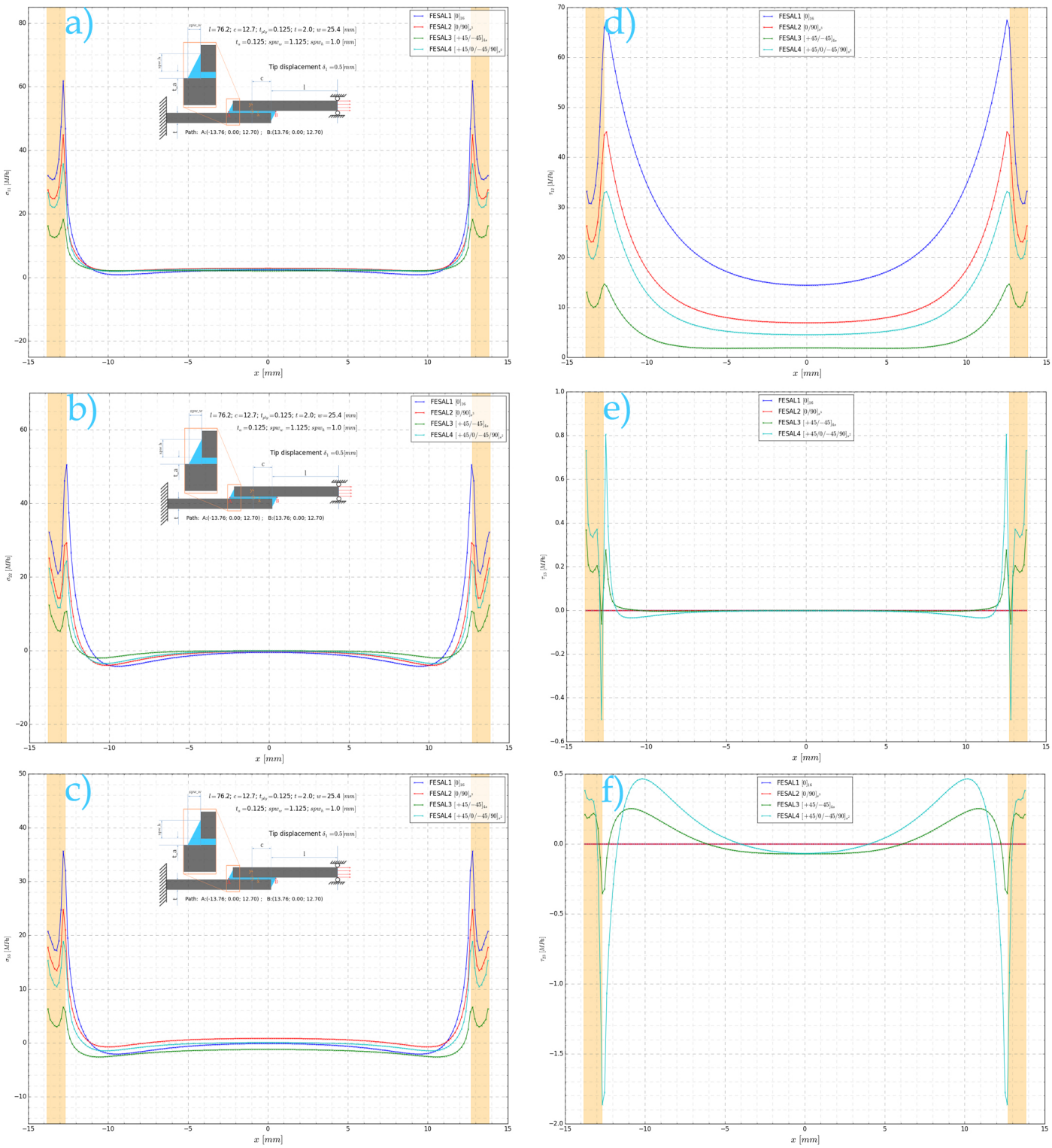

Figure P.21: Normal and shear stress values along the adhesive path length: a) normal stress in the direction parallel to the fibers σ_1; b) peel stress (*i.e.* in the out-of-plane direction) σ_2; c) normal stress in the inplane transverse direction σ_3; d) longitudinal-transverse shear stress τ_{12}; e) inplane shear stress τ_{13}; f) transverse shear stress τ_{23}.

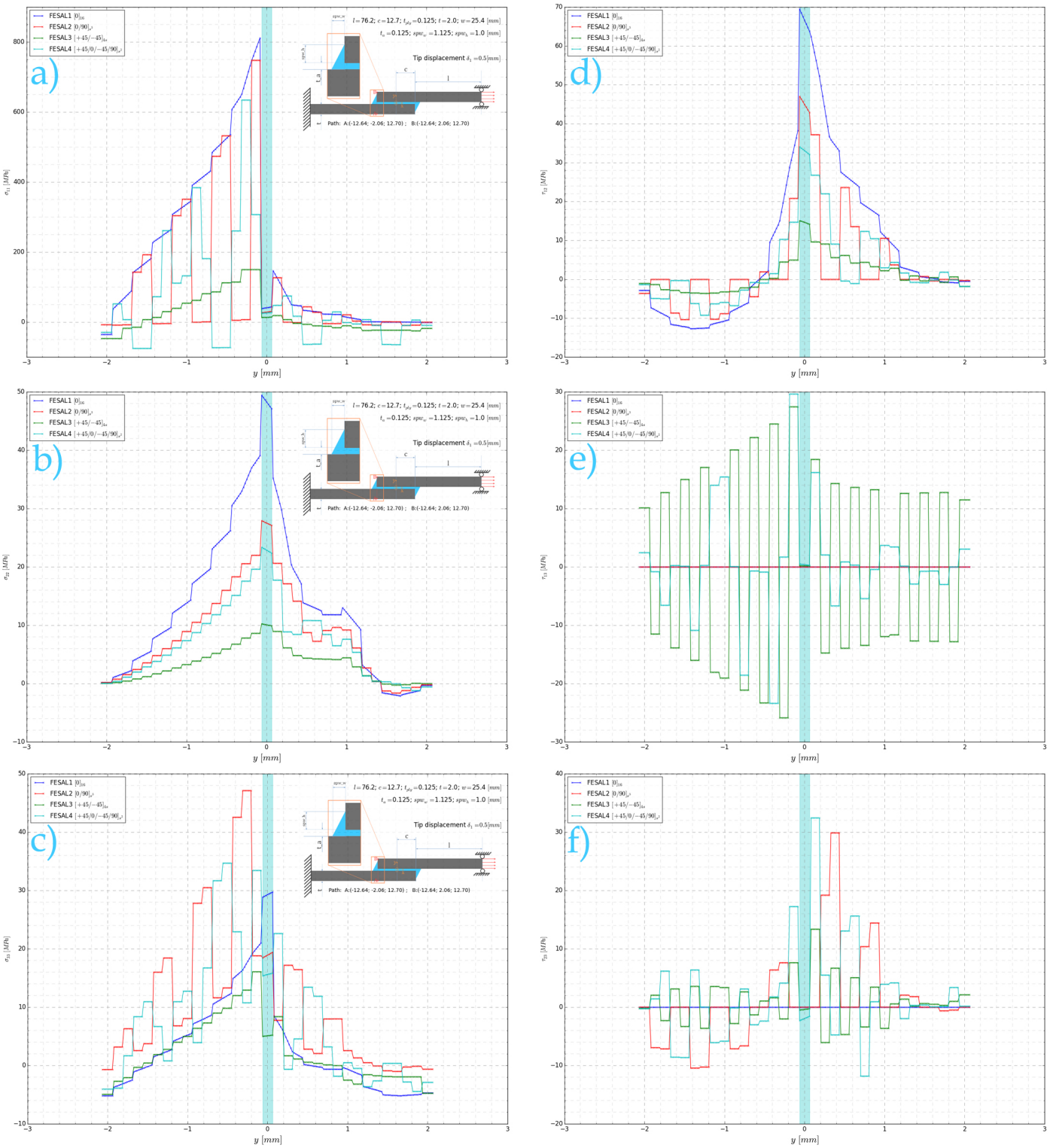

Figure P.22: Normal and shear stress values along the adherend-adhesive-adherend out-of-plane path: a) normal stress in the direction parallel to the fibers σ_1; b) normal stress in the out-of-plane direction σ_2; c) normal stress in the inplane transverse direction σ_3; d) longitudinal-transverse shear stress τ_{12}; e) inplane shear stress τ_{13}; f) transverse shear stress τ_{23}.

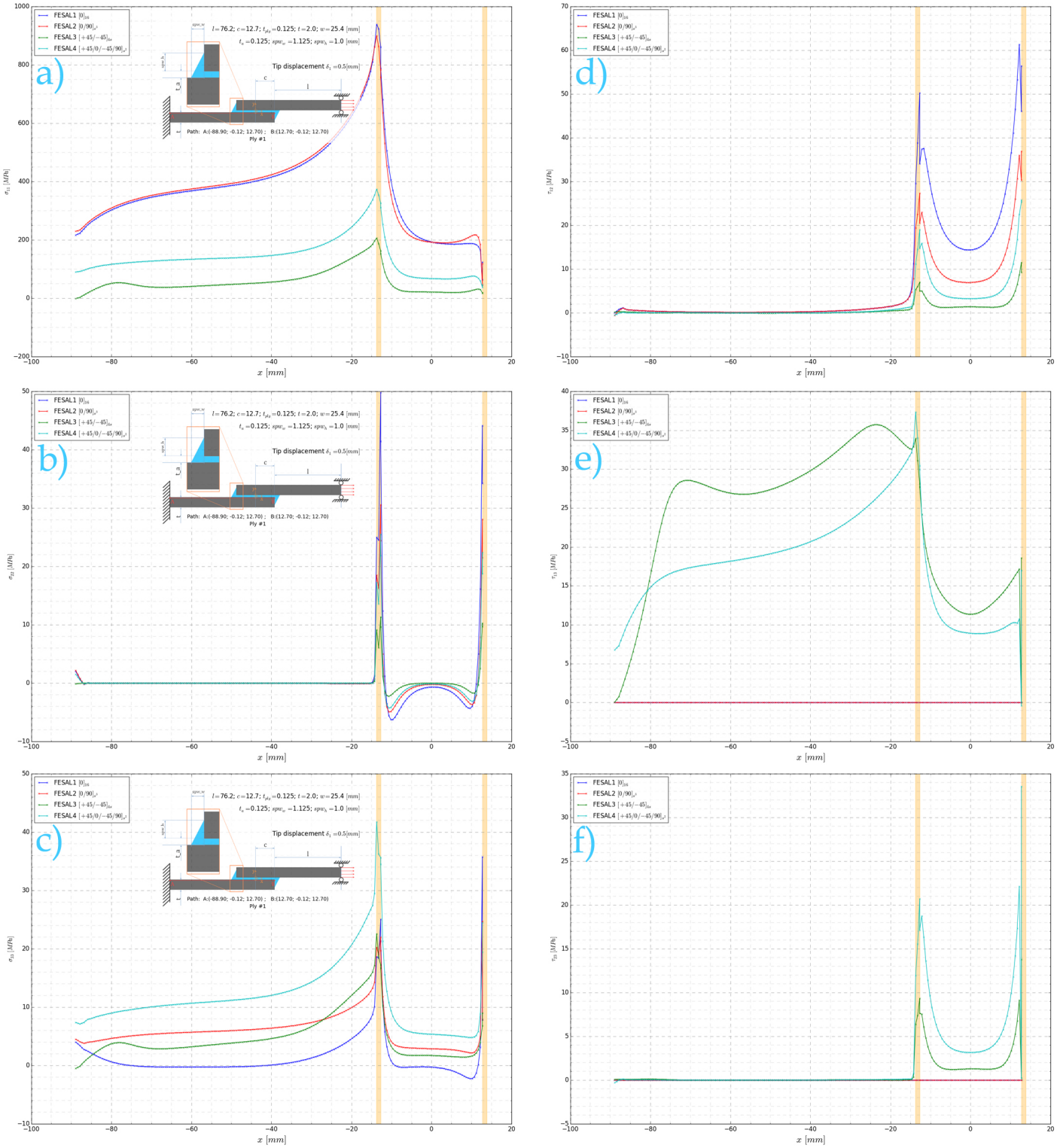

Figure P.23: Normal and shear stress values along the bottom adherend's first layer: a) normal stress in the direction parallel to the fibers σ_1; b) normal stress in the out-of-plane direction σ_2; c) normal stress in the inplane transverse direction σ_3; d) longitudinal-transverse shear stress τ_{12}; e) inplane shear stress τ_{13}; f) transverse shear stress τ_{23}.

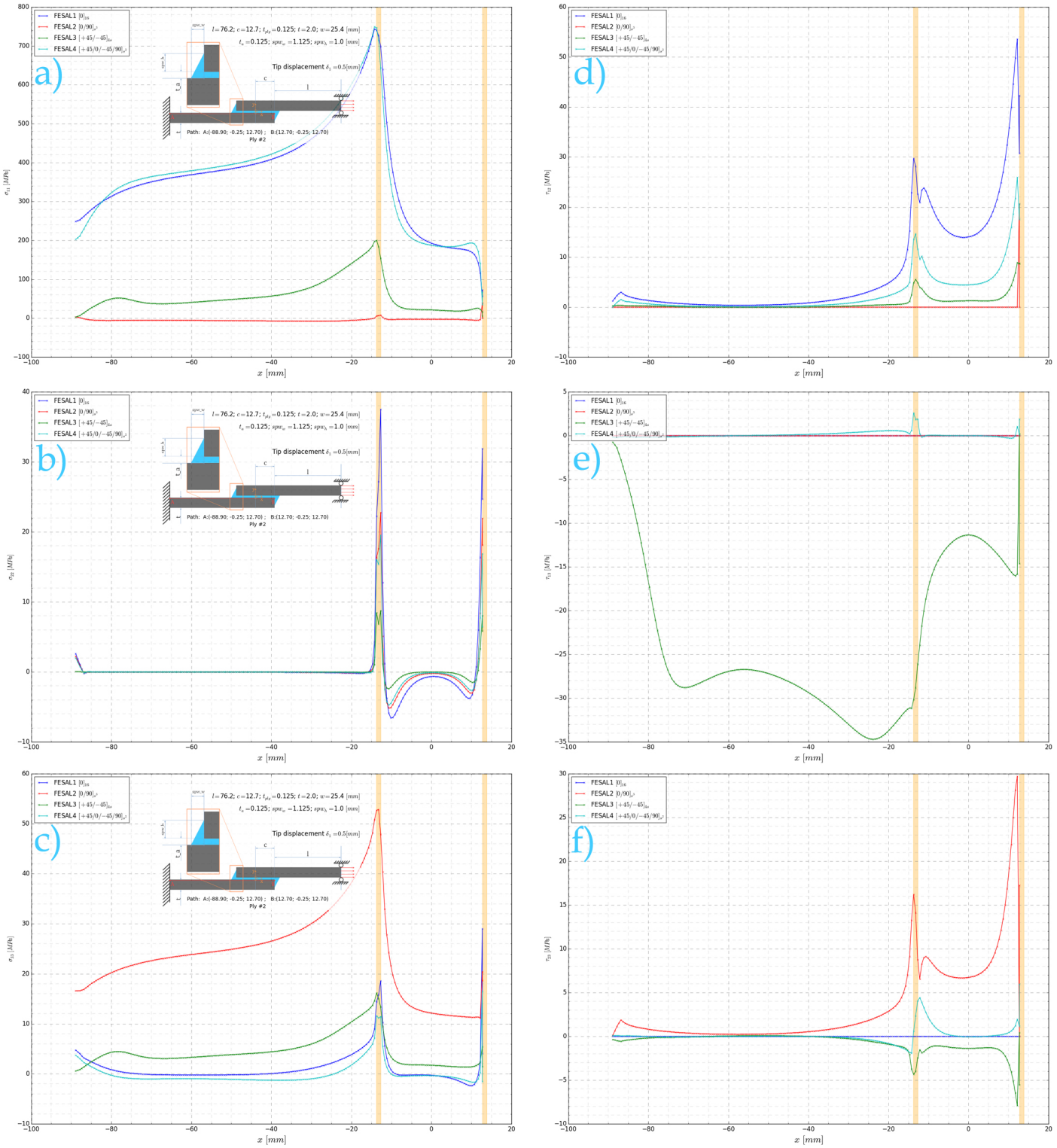

Figure P.24: Normal and shear stress values along the bottom adherend's second layer: a) normal stress in the direction parallel to the fibers σ_1; b) normal stress in the out-of-plane direction σ_2; c) normal stress in the inplane transverse direction σ_3; d) longitudinal-transverse shear stress τ_{12}; e) inplane shear stress τ_{13}; f) transverse shear stress τ_{23}.

Q. Failure criteria code verification: failure envelopes

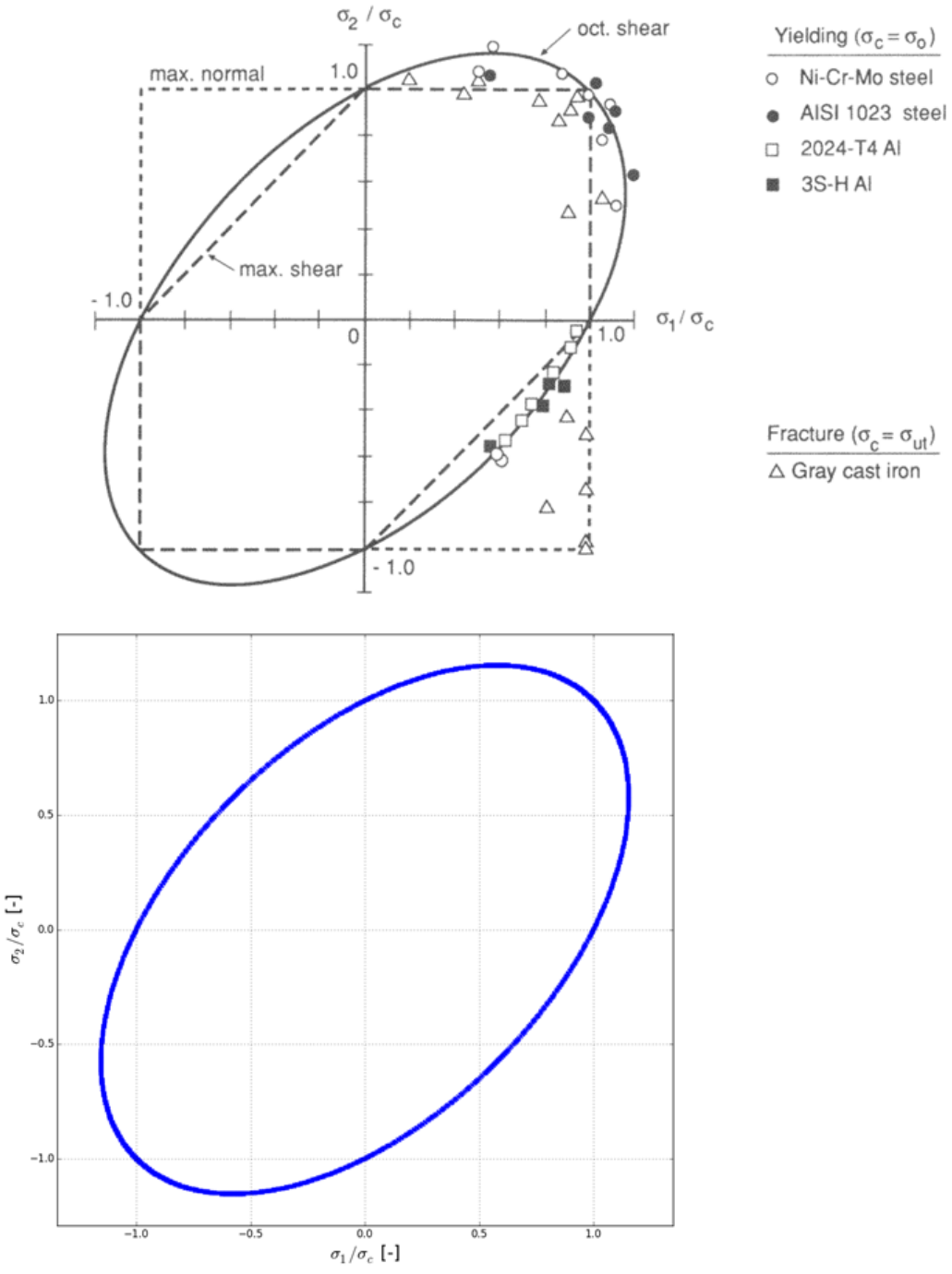

Figure P.25: Comparison between theory's original [24] and obtained Von Mises failure envelopes for a random isotropic material (principal stresses only). The stresses are normalized by the yield strength of the material.

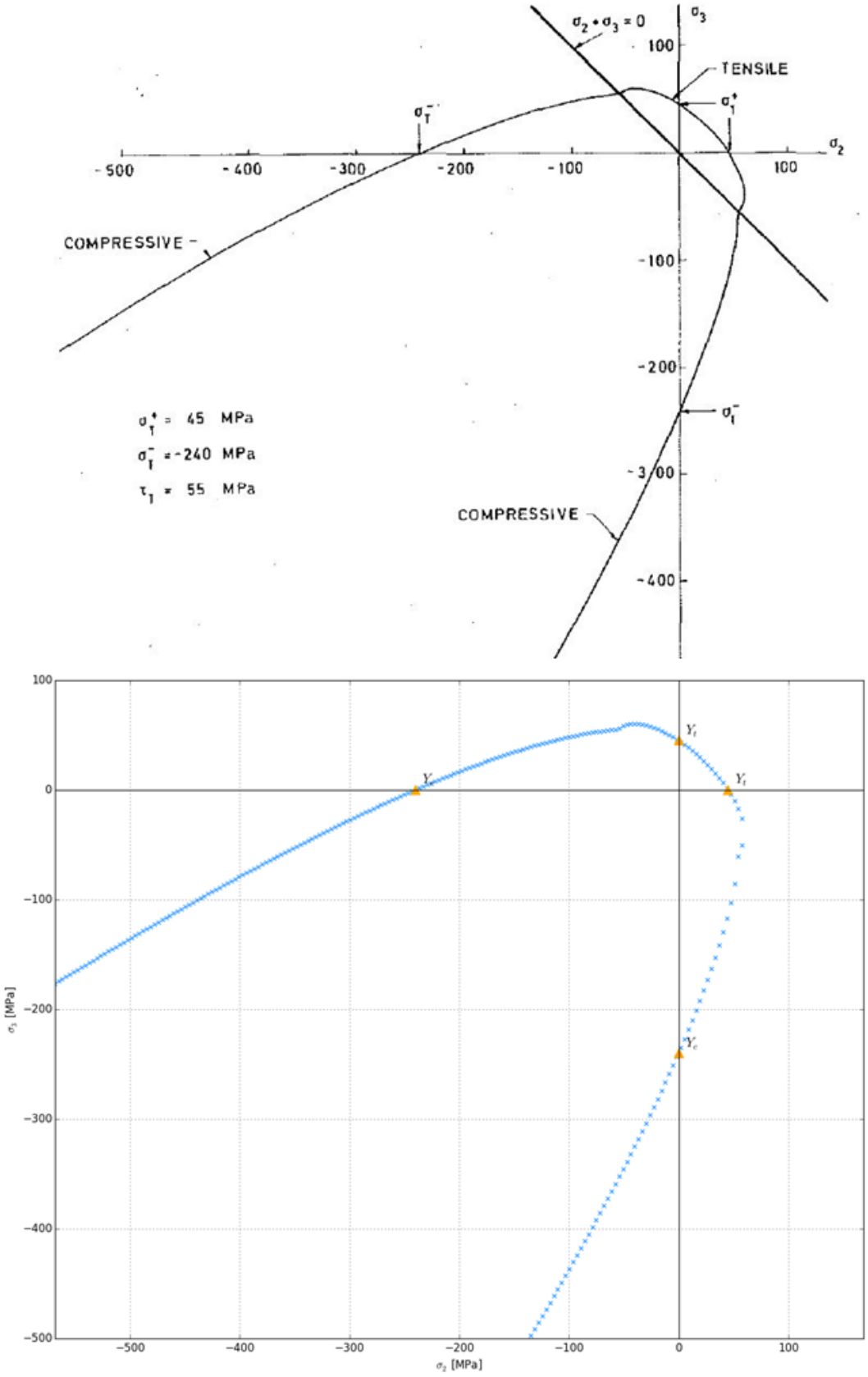

Figure P.26: Comparison between theory's original [42] and obtained Hashin's failure envelopes for an (unspecified) orthotropic material under biaxial (σ_2 and σ_3) loading. $Y^T = 45MPa$; $Y^C = 240MPa$; $S^T = 55MPa$.

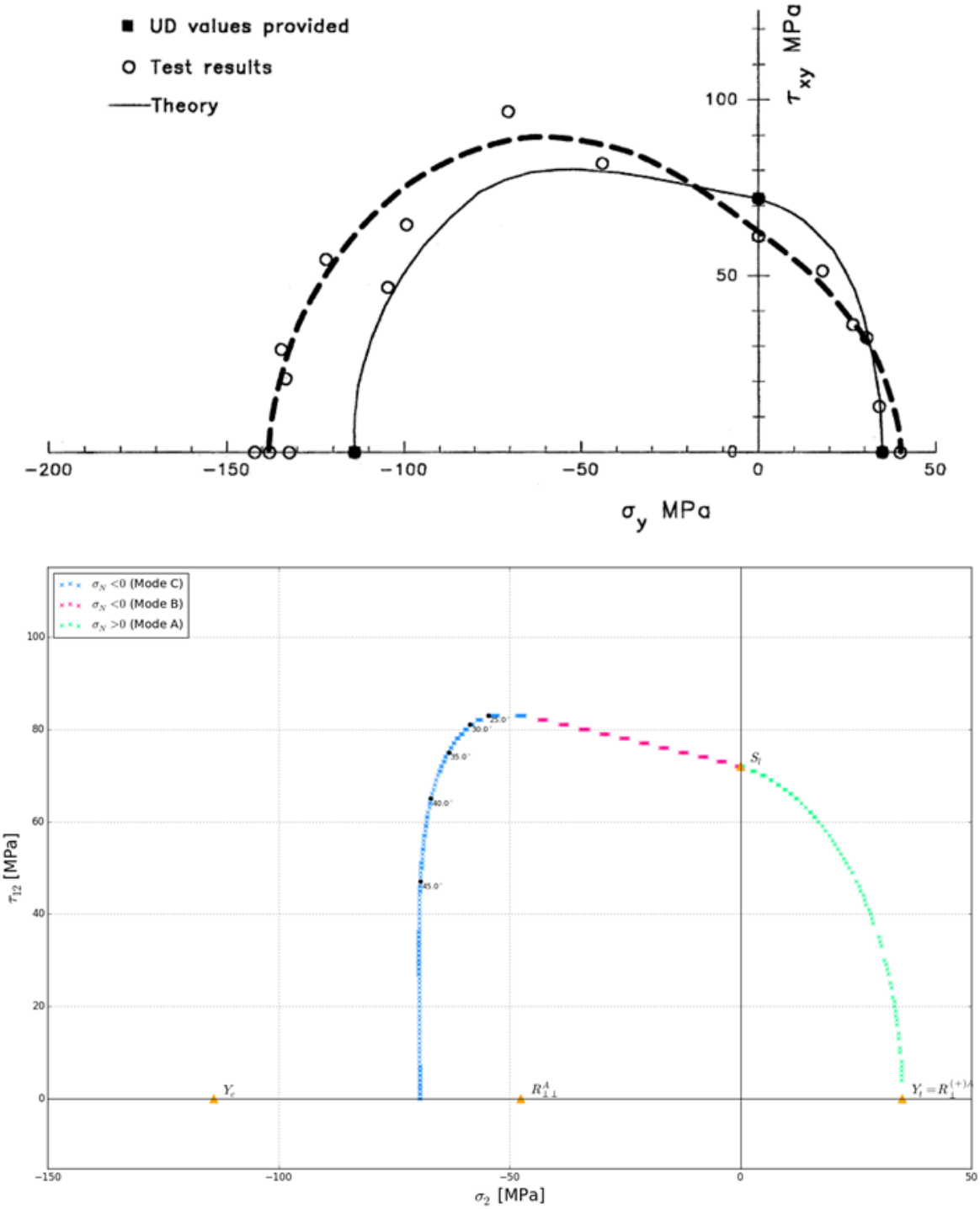

Figure P.27: Comparison between theory's original [85] and obtained Puck's failure envelopes for a E-Glass/LY556/HT907/DY063 material under biaxial loading: 0° GFRP lamina under combined σ_2 and τ_{12} stresses. Strength values: $Y^T = 35MPa$; $Y^C = 114MPa$; $S^L = 72MPa$.

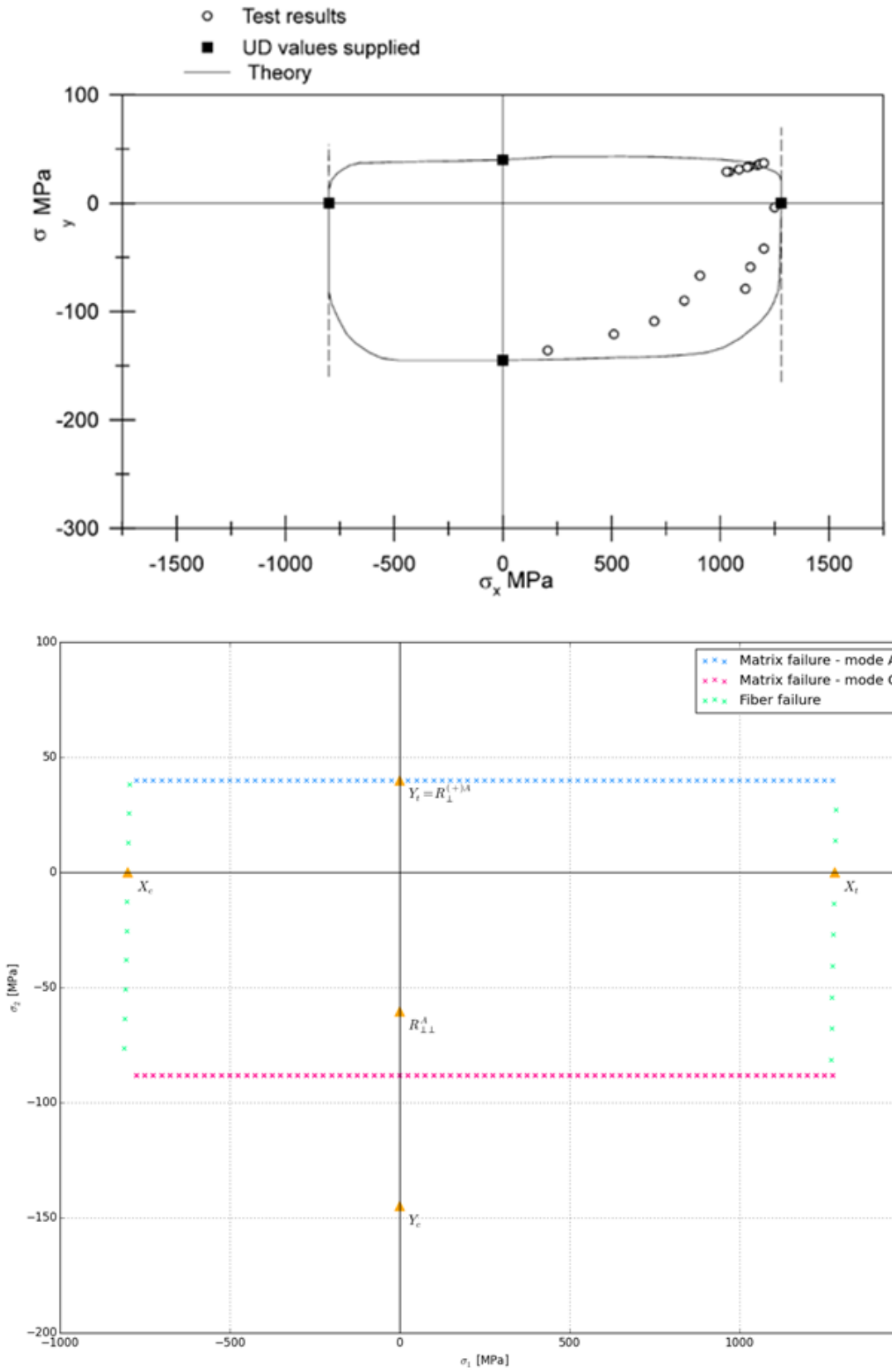

Figure P.28: Comparison between theory's original [85] and obtained Puck's failure envelopes for a E-glass/MY750 epoxy material under biaxial loading: 0° GFRP lamina under combined σ_1 and σ_2 stresses. Strength values: $X^T = 1280MPa$; $X^C = 800MPa$; $Y^T = 40MPa$; $Y^C = 145MPa$; $S^L = 73MPa$; $E_1 = 45600MPa$; $E_{f1} = 72400MPa$; $\nu_{12} = 0.278[-]$; $\nu_{f12} = 0.22[-]$.

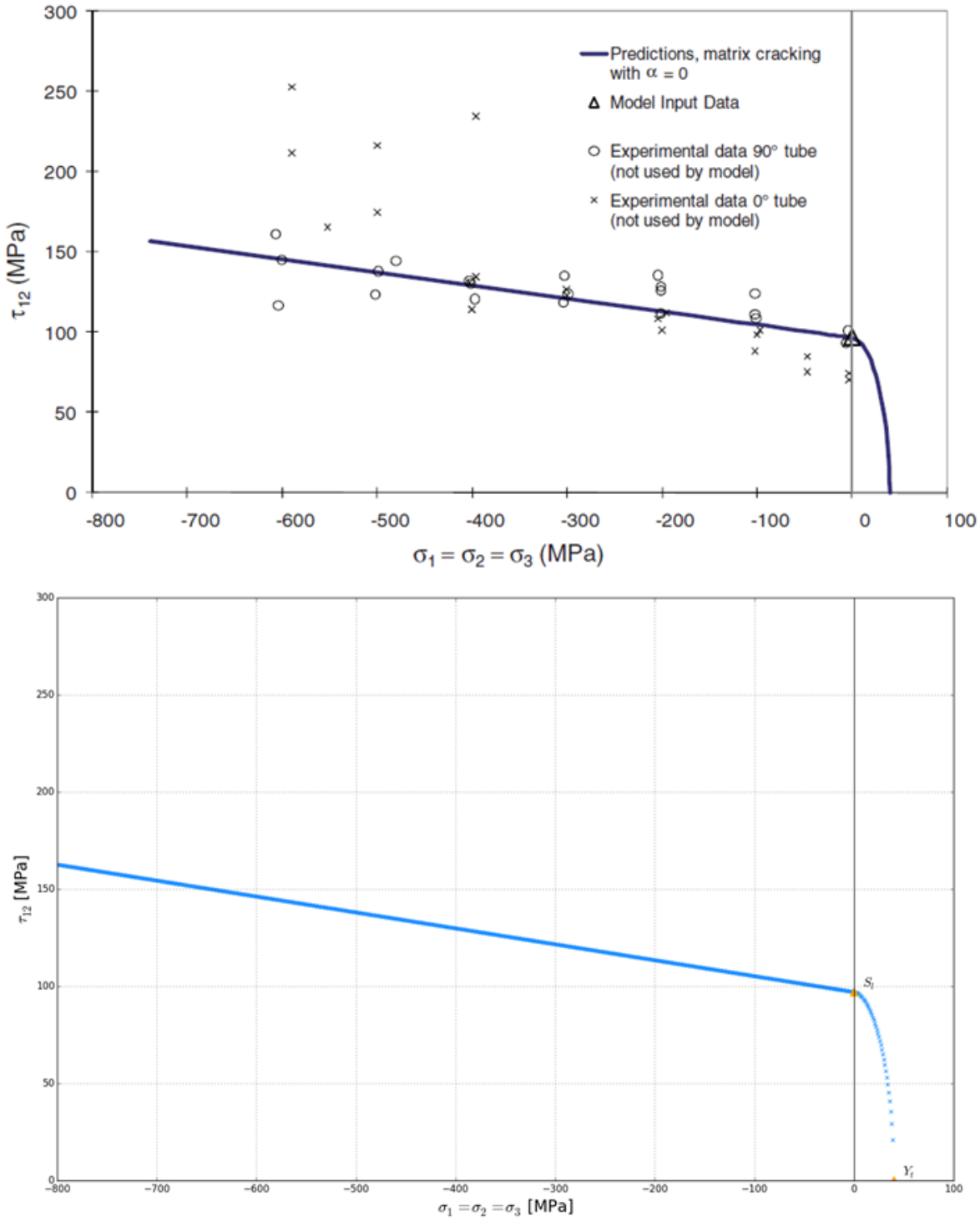

Figure P.29: Comparison between theory's original [82] and obtained LaRC05's failure envelope (case 2) for a T300/PR319 material under combined loading: 0° CFRP laminate under combined σ_2 and τ_{12} stresses. Strength values: $X^C = 950MPa$; $Y^T = 40MPa$; $Y^C = 125MPa$; $S^L = 97MPa$; $\eta_L = 0.082[-]$.

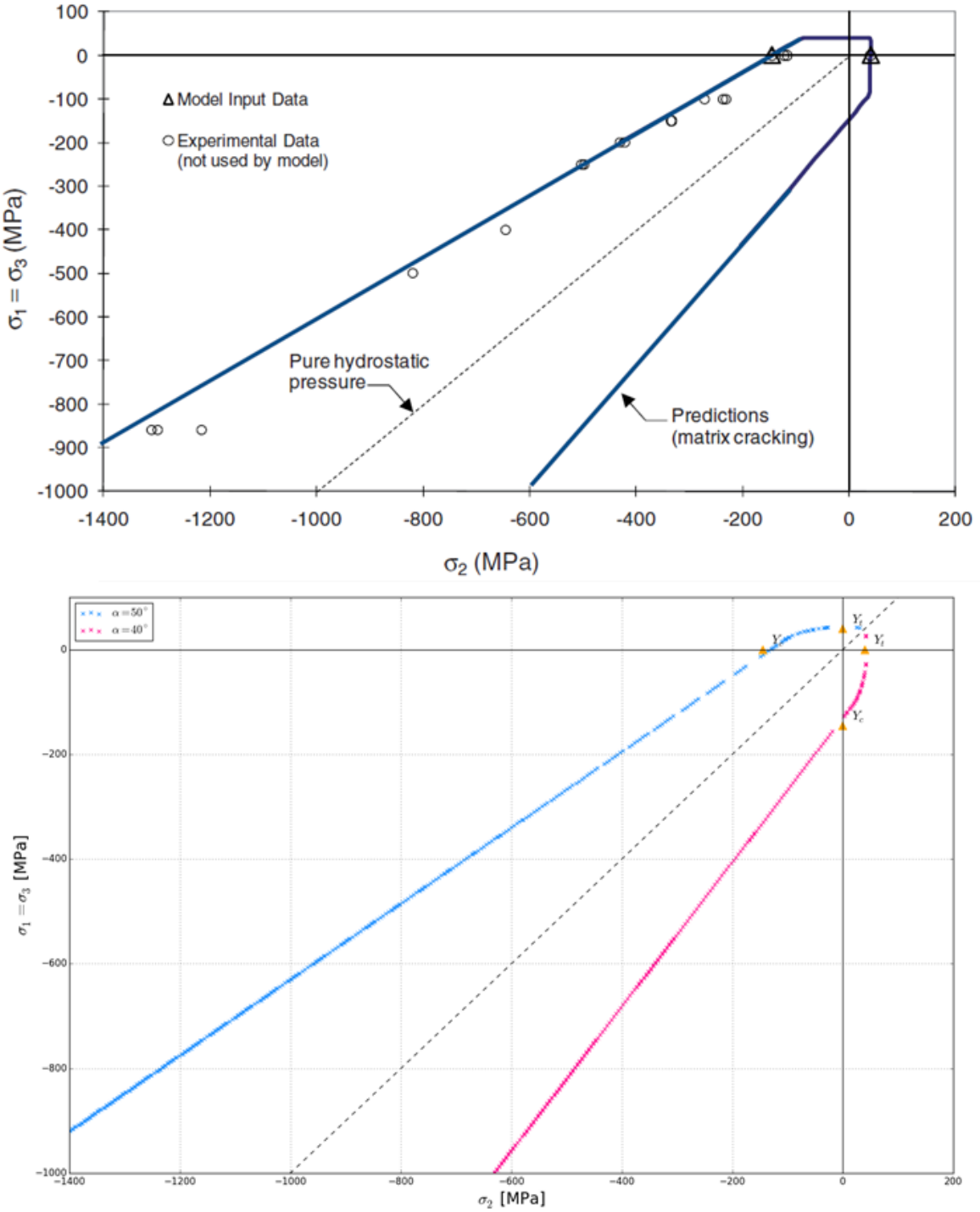

Figure P.30: Comparison between theory's original [83] and obtained LaRC05's failure envelope (case 5) for a E-glass/MY750 epoxy material under triaxial loading: 90° GFRP laminate under combined σ_2 and $\sigma_1 = \sigma_3$ stresses. Strength values: $Y^T = 40MPa$; $Y^C = 145MPa$; $S^L = 73MPa$; $\eta_L = 0.082[-]$; $\alpha_0 = 50°$.

R. Modulus degradation in the adhesive over time

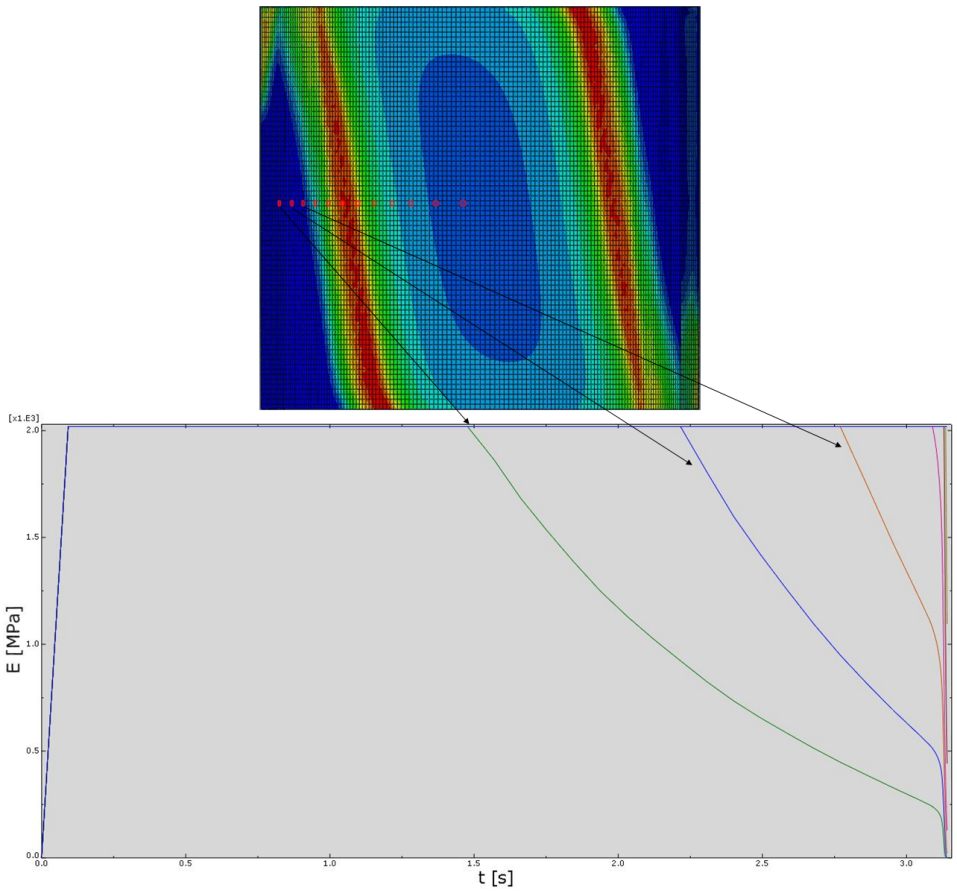

Figure P.31: Young's modulus degradation over time in some elements of the adhesive.